Crystallisation of monoethanolammonium alkylcarboxylates

by

David Richard Booth

Submitted in accordance with the requirements for the degree of

DOCTOR OF PHILOSOPHY

(Chemical Engineering)

The University of Leeds

School of Chemical and Process Engineering

September 2018

The candidate confirms that the work submitted is his/her own, except where work which has formed part of jointly-authored publications has been included. The contribution of the candidate and the other authors to this work has been explicitly indicated below. The candidate confirms that appropriate credit has been given within the thesis where reference has been made to the work of others.

Publication: *Characterisation of monoethanolammonium carboxylates and their acid-soaps*

D. R. Booth, E. Robles, D. York, X. Lai. *Prepared to be submitted.*

This publication contains data/results that will be presented in Chapter 6 of this thesis. The author of this thesis was the lead author of the publication and the other authors inputted ideas and offered guidance and corrections during the preparation of the publication.

Publication: *Crystallisation behaviour of monoethanolammonium carboxylates from aqueous solution*

D. R. Booth, E. Robles, D. York, X. Lai. *Prepared to be submitted*.

This publication contains data/results that will be presented in Chapter 7 and Chapter 8 of this thesis. The data from Chapter 7 included in this publication is the metastable zone width data of MEA laurate and MEA myristate, in-situ Raman measurements of MEA myristate solutions, and off-line characterisation of crystal samples. From Chapter 8, the SAXS/WAXS data collected at I22 at Diamond are included in this publication. The author of this thesis was the lead author of the publication and the other authors inputted ideas and offered guidance and corrections during the preparation of the publication.

Acknowledgements

I would like to thank my supervisors Dr Xiaojun Lai and Eric Robles for their support and guidance throughout my PhD.

I would also like to thank my friends, colleagues, and everyone involved in the Crystallisation group at Leeds for their help, advice, and support during my studies. I'm particularly grateful to Pablo and Boyang for letting me borrow their desks when mine got helpfully moved to the other side of campus from the engineering building. I'd also like to thank Paul and Qi for their help in carrying out the experiments at Diamond and ESRF.

I would like to thank Procter & Gamble and the EPSRC for my Industrial CASE award that enabled the project. In addition, I'd like to thank the Diamond Light Source and the European Synchrotron Radiation Facility (ESRF) for the allocation of beamtime.

Finally, I would like to thank my friends and family for supporting me through my studies. Special thanks goes to my partner Helen for pretending to show an interest when I talked about crystals and soap and for a near constant supply of tea during the writing of this thesis.

Abstract

Monoethanolammonium (MEA) carboxylates are common components of many household cleaning products yet have received relatively little study in literature. They can cause stability problems during product formulation, crystallising out of solution and reducing the products overall performance. A more detailed study on the crystallisation behaviour of MEA carboxylates is therefore carried out using both ex-situ and in-situ characterisation techniques.

MEA carboxylates were produced from even, saturated fatty acids (C12:0 to C18:0) by cooling crystallisation and characterised by powder x-ray diffraction (PXRD), differential scanning calorimetry (DSC), and Fourier-transform infrared spectroscopy (FTIR) and Raman spectroscopy. Soaps are known to also form acid-soap cocrystals, hence a screen for acid-soaps was required for MEA carboxylates. Even saturated fatty acids (C12:0-C18:0) were neutralised to various degrees by MEA and the resulting crystal samples characterised by PXRD, DSC, FTIR, and Raman. The screen indicated a 1:1 acid-soap formed for all the chain lengths studied and whose formation was favoured over forming fatty acid and MEA carboxylate. Binary phase diagrams for the MEA carboxylate – fatty acid systems were generated for the chain lengths studied.

Metastable zone width (MSZW) studies were carried out for MEA laurate and MEA myristate in aqueous solution, revealing non-typical dissolution and crystallisation temperature trends. Ex-situ characterisation and in-situ Raman measurements revealed the 1:1 acid-soap was forming in solution and the observed transitions were its crystallisation and dissolution. The non-typical trends were due to the relative amounts of acid-soap and MEA carboxylate changing with total solution concentration; as concentration increases, the proportion of MEA carboxylate increases leading to a lowering of dissolution temperature.

In-situ simultaneous small- and wide-angle x-ray scattering studies were carried out to characterise the solution structure during crystallisation. No changes were observed on cooling into the MSZW until immediately prior to the onset of crystallisation where a broad WAXS peak at 3.3 Å appeared, suggesting pre-crystallisation ordering in solution. Samples in sealed capillaries indicated a shear-dependence by forming a different, much larger lamellar structure than observed for samples under flow.

Table of Contents

List of Tables

List of Figures

List of Symbols

Chapter 2

x	Solute mole fraction	-
ΔH_f	Enthalpy of fusion	*kJ/mol*
R	Gas constant	*J/mol.K*
T_f	Fusion temperature	*K*
ΔS_f	Entropy of fusion	*kJ/mol.K*
γ	Activity coefficient	-
ΔH_{diss}	Enthalpy of dissolution	*kJ/mol*
ΔS_{diss}	Entropy of dissolution	*kJ/mol.K*
T	Temperature	*K*
c	Concentration	*mol/L*
c^*	Equilibrium concentration	*mol/L*
S	Supersaturation ratio	-
ΔG	Overall free energy change of formation of a cluster	*J*
ΔG_v	Volume free energy change	*J*
ΔG_s	Surface free energy change	*J*
r	Nuclei radius	*m*
ΔG_{crit}	Free energy change for formation of a critically sized cluster	*J*
r_c	Critically sized nucleus radius	*m*
J	Nucleation rate	*/m^3.s*
k_b	Boltzmann constant	*J/K*
A	Pre-exponential factor	-
v_o	Molecular volume	*m^3*
γ_i, γ_{eff}	Interfacial tension and effective interfacial tension	*mJ/m^2*
τ	Induction time	*s*
t_r	Relaxation time	*s*

t_n	Time required to form a nucleus	*s*
t_g	Time required for nuclei growth	*s*
V	Solution volume	*m³*
k_m	Nucleation rate constant	-
ΔC_{max}	Maximum allowable concentration difference	*/m³*
m_o	Nucleation order	-
u_c	Relative critical undercooling	-
T_c	Crystallisation temperature	*K*
T_e	Equilibrium temperature	*K*
R_{hkl}	Crystal growth rate	-
σ	Supersaturation	-
A_i	Growth rate constants where i = 1,2,3,4	-
B	Growth rate constant	-

Chapter 3

L_1	Micellar solution
E, H_1	Hexagonal liquid crystal
D, L_α	Lamellar liquid crystal
S_h	Hydrated surfactant crystals
W	Water
HZ	Fatty acid
MZ	Metal carboxylate
S_{PIL}	Solid protic ionic liquid
S_{FA}	Solid fatty acid
S_{MEA}	Solid MEA
L	Isotropic liquid

Chapter 4

q	Scattering vector	*Å⁻¹*
n	Order of diffraction	-
λ	Wavelength	*Å*

d	Inter-planar spacing	$Å$

List of Abbreviations

MEA	Monoethanolamine
PXRD	Powder x-ray diffraction
SAXS	Small-angle x-ray scattering
WAXS	Wide-angle x-ray scattering
FTIR	Fourier-transform infrared spectroscopy
DSC	Differential scanning calorimetry
MSZW	Metastable zone width
WLM	Wormlike micelle
ATR	Attenuated total reflectance
BCF	Burton Cabrera Frank
CCD	Charge-coupled device
CNT	Classical nucleation theory
IN	Instantaneous nucleation
PN	Progressive nucleation
KBHR	Kaschiev-Borrisova-Hammond-Roberts
RIG	Rough interfacial growth
cmc	Critical micelle concentration
NMR	Nuclear magnetic resonance
DEA	Diethanolamine
TEA	Triethanolamine
MCR	Multivariate curve resolution
ALS	Alternating least squares
SVD	Singular value decomposition
DLS	Dynamic light scattering
DAWN	Data Analysis WorkbeNch

Chapter 1 Introduction

The scientific background and rationale of the project is presented along with the research aims and objectives.

1.1 Research background

The stability of a product throughout its life-cycle is fundamental to its success. There are many mechanisms that could lead to a liquid formulation becoming unstable; components may gradually breakdown or react slowly together over time, solvent could be lost or water absorbed, and components could be sensitive to temperature, humidity, or oxidation. The simplest mechanism is a change in the product temperature that causes the formulation to become supersaturated and crystallisation of a component to occur. This occurs in a range of products from liquid cleaning products such as shampoo and fabric detergents to food products (1).

Liquid cleaning products are complex formulations that can contain numerous dissolved species in mixtures of organic solvent and water (2). In a typical detergent formulation there are multiple types of surfactants present, which in turn can each have a variety of chain lengths and unsaturation, together with other components such as polymers and enzymes. Mixtures of polar organics, such as propylene glycol, and water are the main solvents, but fragrance oils can also act as a solvent. As a result of the complexity of these mixtures, determination or prediction of solubility for components isn't possible or practical. This can lead to product formulations that are supersaturated and therefore thermodynamically unstable at or below room temperature. A thermodynamically unstable solution will crystallise but when this actually occurs is dependent on the kinetics of the process. This provides scope for kinetically stabilising the product through manipulation of the kinetics by changing the product formulation – components such as surfactants within the formulation are likely to inhibit crystallisation. A kinetically stabilised product will remain stable for a period of time but will eventually crystallise given enough time or appropriate conditions.

A liquid cleaning product can be subjected to a variety of temperatures during its lifecycle from manufacturing, transportation, and to storage at the end consumers. Crystallisation stability problems are particularly pronounced during winter, when temperatures fall below 0 °C and the product is subjected to freeze-thaw cycles. The crystals formed in the product become a problem if they don't re-dissolve at ambient temperature as they then have a lasting effect on the product. At best, the crystals merely alter the appearance of the product but at worst it lowers product performance by not delivering active components or comprises product safety by the generation of large, hard-edged crystals. To avoid these issues, liquid cleaning products undergo crystallisation stability testing during their development. This stability testing

can take the form of freeze-thaw cycling but due to the long time-span that the crystallisation problems can occur – anything from days, weeks, to months after formulation – the testing process is time (weeks/months) and resource consuming.

The crystallisation issues can be resolved in a number of ways: development of formulations that are thermodynamically stable at lower temperatures, modification of the crystallisation behaviour, or by improving the stability testing process. Development of stable formulations ultimately resides with determining the solubility of components as a function of all the other components which is not particularly feasible due to the number of components and the interactions between them. Modifying the crystallisation behaviour is primarily concerned with minimising the particle size of the crystallised material to minimise impact. There are potential issues with this approach; initial generation of small crystals and restricting crystal growth, and Ostwald's ripening in which large crystals grow at the expense of smaller crystals (3). Research into the production of nanocrystals for the pharmaceutical industry is well established and could be adapted for liquid cleaning products (4). However, the time-scales for stabilising the particle size will likely be much larger for crystals in liquid cleaning products. The stability testing process has scope for improvement through high-throughput techniques and by accelerating the crystallisation process.

Fundamental to resolving the crystallisation issues is to better understand the crystallisation behaviour of the least soluble components in a typical cleaning product formulation. Fatty acid containing components are known to crystallise out of solution and these are often in the form of soaps, typically sodium carboxylates for water-based formulations and monoethanolammonium (MEA) carboxylates with water and/or polar organic solvents. Sodium carboxylates have been extensively studied with respect to their aqueous phase behaviour (5-14), crystallisation behaviour (15-22), and their acid-soap cocrystals (23-30). In contrast, MEA carboxylates have received relatively little study in literature. Aqueous phase diagrams are available for several carboxylate chain lengths, however these are limited as they do not show the Krafft boundary (31, 32) and there have been no metastable zone width studies reported. The recent interest in MEA carboxylates has been primarily for their ability to form ionic liquids (33-39).

The lack of information in literature is most likely due to the previous lack of industrial drive. The main application of MEA carboxylates is in liquid formulations of cleaning products such as fabric detergents, where the key

parameters are the phase behaviour rather than the crystallisation behaviour. In contrast, sodium soaps have long been used in the form solid soap bars hence the necessity for information regarding their crystallisation and solid phase behaviour.

Recent drives for improving sustainability of formulated products has led to a desire to increase the concentration of liquid cleaning products, reducing product volume and thus reducing the impact of shipping. This has led to a shift towards polar organic co-solvents, which has necessitated the use of soaps with organic counter-ions such as MEA. The increase in concentration of the formulation also increases the likelihood of supersaturated products and therefore the probability that crystallisation will occur. In addition, within industry there is a desire to use a 'global' base formulation which is then tailored to local markets at a late stage, such as by adding region specific fragrances. This 'global' formulation is therefore subjected to a much greater range of ambient conditions, which are also dependent on local customs such as where the product is stored – an unheated outbuilding or within a centrally-heated home will have significant differences in temperature variation. The combined effect of these drives is an increased risk of crystallisation events within cleaning product formulations, which can result in a negative consumer response when the usually clear fabric detergent becomes a turbid suspension of crystals. The net result is an increased need for crystallisation stability testing during product development.

MEA carboxylates were therefore selected for study due to the lack of information in literature regarding their phase and crystallisation behaviour compared to their widespread use in consumer products. Better understanding of these behaviours would enable improvements in product formulation and provide insight into how crystallisation occurs, enabling improvements in stability testing to be developed.

1.2 Aims

The overall aim for the project is to better understand the crystallisation behaviour of MEA carboxylates. This will be addressed through the following objectives:

1. Characterise MEA carboxylates for a range of chain lengths by a number of structural and chemical techniques

2. Investigate the ability of MEA carboxylates to form acid-soap(s), determining their stoichiometry and characterising them structurally and chemically
3. Determine the metastable zone width of MEA carboxylates in aqueous solution, characterising the crystallisation process
4. Elucidate how the solution structure changes as the solution passes into the metastable zone and during the micelle-crystal transition

1.3 Delivery plan

The thesis objectives will be realised through a range of different experimental techniques and activities:

- MEA carboxylates will be produced by cooling crystallisation and characterised to provide structural and chemical data.
- Acid-soaps will be screened for by neutralising fatty acids to various degrees, recovering crystal samples through solvent evaporation, and characterising the resultant crystals through x-ray diffraction and infrared and Raman spectroscopy.
- Crystallisation and dissolution temperatures of MEA carboxylate aqueous solutions will be determined by a polythermal methodology to provide insight into the crystallisation behaviour and the metastable zone width.
- The solution structure of MEA carboxylate solutions will be probed by in-situ time-resolved synchrotron x-ray scattering to determine how the solution structure changes pre-nucleation and during micelle-crystal transition.

1.4 Thesis plan

This thesis contains nine chapters, with each chapter having an individual reference section:

Chapter 1 Introduction: An introduction and background to the research topic and presents the thesis aims and objectives, together with the structure of the thesis.

Chapter 2 Crystallisation Theory: A literature review which covers the fundamentals of crystallisation including nucleation and growth.

Chapter 3 Surfactants, monoethanolammonium carboxylates, and related compounds: provides a review of the literature surrounding the

phase behaviour and crystallisation behaviour of sodium carboxylates, MEA carboxylates, and other carboxylates with similar organic counterions.

Chapter 4 Crystallisation characterisation techniques: covers the fundamentals of the main crystallisation characterisation techniques used with the experimental work of this thesis.

Chapter 5 Materials and methods: describes the materials and experimental methodologies used in the experimental work within this research.

Chapter 6 Synthesis and characterisation of MEA carboxylates and acid-soap complexes: presents the results of the MEA carboxylate characterisation alongside the outcomes of the acid-soap screen.

Chapter 7 Aqueous Phase behaviour of MEA carboxylates: presents the results and analysis of the metastable zone width study of the MEA carboxylates.

Chapter 8 In-situ SAXS/WAXS studies of crystallisation of MEA carboxylates from aqueous solutions: presents the results of the small- and wide-angle x-ray scattering studies into the micelle-crystal transition carried out at Diamond and ESRF.

Chapter 9 Conclusions and future work: summarises the conclusions that can be drawn from this research and describes potential future work.

1.5 References

1. SUMMERTON, E., G. ZIMBITAS, M. BRITTON and S. BAKALIS. Low temperature stability of surfactant systems. *Trends in Food Science & Technology*, 2017, **60**, pp.23-30.
2. STUART, M.C.A., J.C. VAN DE PAS and J.B.F.N. ENGBERTS. Phase behavior of laundry surfactants in polar solvents. *Journal of Surfactants and Detergents*, 2006, **9**(2), pp.153-160.
3. MULLIN, J.W. *Crystallization (Fourth Edition).* Oxford: Butterworth-Heinemann, 2001.
4. WANG, G.D., F.P. MALLET, F. RICARD and J.Y.Y. HENG. Pharmaceutical nanocrystals. *Current Opinion in Chemical Engineering*, 2012, **1**(2), pp.102-107.
5. VOLD, R.D., R. REIVERE and J.W. MCBAIN. A Phase Rule Study of the System Sodium Myristate-Water. *Journal of the American Chemical Society*, 1941, **63**(5), pp.1293-1296.
6. VOLD, R.D. Phase Boundaries in Concentrated Systems of Sodium Oleate and Water. *J Phys Colloid Chem*, 1947, **51**(3), pp.797-816.
7. MCBAIN, J.W., R.D. VOLD and M. FRICK. A phase rule study of the system sodium stearate-water. *Journal of Physical Chemistry*, 1940, **44**(9), pp.1013-1024.
8. MCBAIN, J.W., M.J. VOLD and J.L. PORTER. A phase study of commercial soap and water. *Industrial and Engineering Chemistry*, 1941, **33**, pp.1049-1055.
9. MCBAIN, J.W. and S.A. JOHNSTON. A Note on the Phase Rule Diagram for a Mixture of Sodium Palmitate and Sodium Laurate with Water. *Journal of the American Chemical Society*, 1941, **63**(3), pp.875-875.
10. MADELMONT, C. and K. PERRON. Study of the influence of the chain length on some aspects of soap/water diagrams. *Colloid and Polymer Science*, 1976, **254**(6), pp.581-595.
11. DE MUL, M.N.G., H.T. DAVIS, D.F. EVANS, A.V. BHAVE and J.R. WAGNER. Solution Phase Behavior and Solid Phase Structure of Long-Chain Sodium Soap Mixtures. *Langmuir*, 2000, **16**(22), pp.8276-8284.
12. MONGONDRY, P., C.W. MACOSKO and T. MOADDEL. Rheology of highly concentrated anionic surfactants. *Rheologica Acta*, 2006, **45**(6), pp.891-898.
13. ANTUNES, F.E., L. COPPOLA, D. GAUDIO, I. NICOTERA and C. OLIVIERO. Shear rheology and phase behaviour of sodium oleate/water mixtures. *Colloids and Surfaces A: Physicochemical and Engineering Aspects*, 2007, **297**(1-3), pp.95-104.
14. KING, D.T., D.B. WARREN, C.W. POUTON and D.K. CHALMERS. Using molecular dynamics to study liquid phase behavior: simulations of the ternary sodium laurate/sodium oleate/water system. *Langmuir*, 2011, **27**(18), pp.11381-93.
15. ZHU, S., M. HEPPENSTALL-BUTLER, M.F. BUTLER, P.D. PUDNEY, D. FERDINANDO and K.J. MUTCH. Acid soap and phase behavior of stearic acid and triethanolamine stearate. *J Phys Chem B*, 2005, **109**(23), pp.11753-61.

16. VAN GELDER, R.N.M.R., K.J. ROBERTS, J. CHAMBERS and T. INSTONE. Nucleation of single and mixed straight chain surfactants from dilute aqueous solutions. *J Cryst Growth*, 1996, **166**(1-4), pp.189-194.
17. STUART, M.C., J. VAN ESCH, J.C. VAN DE PAS and J.B. ENGBERTS. Chain-length and solvent dependent morphological changes in sodium soap fibers. *Langmuir*, 2007, **23**(12), pp.6494-7.
18. VAN GELDER, R.N.M.R. *Structuro-kinetic studies of the crystallisation of straight chain surfactants and homologues mixtures*. PhD thesis, University of Strathclyde, 1998.
19. MCBAIN, J.W., M.J. VOLD and S.A. JOHNSTON. The Hydration of Curd Fibers of Sodium Palmitate and Sodium Oleate. *Journal of the American Chemical Society*, 1941, **63**(4), pp.1000-1007.
20. MCBAIN, J.W., O.E.A. BOLDUAN and S. ROSS. X-Ray Diffraction of Sodium Laurate, Palmitate and Stearate at Room Temperature. *Journal of the American Chemical Society*, 1943, **65**(10), pp.1873-1876.
21. ZAWKO, S.A. and C.E. SCHMIDT. Assembly of sodium soap fibers and fibrillar particles triggered by dissolution of sodium chloride crystals. *Soft Matter*, 2010, **6**(14), p.3289.
22. YUAN, Z., W. LU, W. LIU and J. HAO. Gel phase originating from molecular quasi-crystallization and nanofiber growth of sodium laurate–water system. *Soft Matter*, 2008, **4**(8), p.1639.
23. TANDON, P., S. RAUDENKOLB, R.H. NEUBERT, W. RETTIG and S. WARTEWIG. X-ray diffraction and spectroscopic studies of oleic acid-sodium oleate. *Chem Phys Lipids*, 2001, **109**(1), pp.37-45.
24. KRALCHEVSKY, P.A., K.D. DANOV, C.I. PISHMANOVA, S.D. KRALCHEVSKA, N.C. CHRISTOV, K.P. ANANTHAPADMANABHAN and A. LIPS. Effect of the precipitation of neutral-soap, acid-soap, and alkanoic acid crystallites on the bulk pH and surface tension of soap solutions. *Langmuir*, 2007, **23**(7), pp.3538-53.
25. QI, S., D. DEUTSCH and D.Q. CRAIG. An investigation into the interaction between taste masking fatty acid microspheres and alkaline buffer using thermal and spectroscopic analysis. *J Pharm Sci*, 2006, **95**(5), pp.1022-8.
26. HEPPENSTALL-BUTLER, M. and M.F. BUTLER. Nonequilibrium Behavior in the Three-Component System Stearic Acid−Sodium Stearate−Water. *Langmuir*, 2003, **19**(24), pp.10061-10072.
27. LYNCH, M.L., F. WIREKO, M. TAREK and M. KLEIN. Intermolecular Interactions and the Structure of Fatty Acid−Soap Crystals. *The Journal of Physical Chemistry B*, 2001, **105**(2), pp.552-561.
28. LYNCH, M.L. Acid-soaps. *Current Opinion in Colloid & Interface Science*, 1997, **2**(5), pp.495-500.
29. LYNCH, M.L., Y. PAN and R.G. LAUGHLIN. Spectroscopic and thermal characterization of 1:2 sodium soap fatty acid acid-soap crystals. *Journal of Physical Chemistry*, 1996, **100**(1), pp.357-361.
30. HADŽI, D., J. GRDADOLNIK and A. MEDEN. Infrared spectra of, and hydrogen bonding in acid palmitates. *Journal of Molecular Structure*, 1996, **381**(1-3), pp.9-14.

31. WARNHEIM, T. and A. JONSSON. Surfactant Aggregation in Systems Containing Alkanolamines and Fatty-Acids. *J Colloid Interface Sci*, 1990, **138**(2), pp.314-323.
32. WÄRNHEIM, T. and A. JÖNSSON. Phase behavior of alkanolammonium carboxylates. 1992, **88**, pp.18-22.
33. NUTHAKKI, B., T.L. GREAVES, I. KRODKIEWSKA, A. WEERAWARDENA, M.I. BURGAR, R.J. MULDER and C.J. DRUMMOND. Protic Ionic Liquids and Ionicity. *Australian Journal of Chemistry*, 2007, **60**(1), p.21.
34. ÁLVAREZ, V.H., S. MATTEDI, M. MARTIN-PASTOR, M. AZNAR and M. IGLESIAS. Synthesis and thermophysical properties of two new protic long-chain ionic liquids with the oleate anion. *Fluid Phase Equilibria*, 2010, **299**(1), pp.42-50.
35. ALVAREZ, V.H., S. MATTEDI, M. MARTIN-PASTOR, M. AZNAR and M. IGLESIAS. Thermophysical properties of binary mixtures of {ionic liquid 2-hydroxy ethylammonium acetate+(water, methanol, or ethanol)}. *The Journal of Chemical Thermodynamics*, 2011, **43**(7), pp.997-1010.
36. MAXIMO, G.J., R.J.B.N. SANTOS, J.A. LOPES-DA-SILVA, M.C. COSTA, A.J.A. MEIRELLES and J.A.P. COUTINHO. Lipidic Protic Ionic Liquid Crystals. *ACS Sustainable Chemistry & Engineering*, 2014, **2**(4), pp.672-682.
37. SANTOS, D., F. COSTA, E. FRANCESCHI, A. SANTOS, C. DARIVA and S. MATTEDI. Synthesis and physico-chemical properties of two protic ionic liquids based on stearate anion. *Fluid Phase Equilibria*, 2014, **376**, pp.132-140.
38. GREAVES, T.L. and C.J. DRUMMOND. Protic Ionic Liquids: Evolving Structure-Property Relationships and Expanding Applications. *Chem Rev*, 2015, **115**(20), pp.11379-448.
39. TOLEDO HIJO, A.A.C., G.J. MAXIMO, M.C. COSTA, E.A.C. BATISTA and A.J.A. MEIRELLES. Applications of Ionic Liquids in the Food and Bioproducts Industries. *ACS Sustainable Chemistry & Engineering*, 2016, **4**(10), pp.5347-5369.

Chapter 2 Crystallisation Theory

A review of the fundamentals of crystals and the process of crystallisation, from nucleation to crystal growth

2.1 Introduction

Crystallisation is the formation of solid crystals from a vapour, liquid solution, or a liquid melt phase. It begins with the establishment of a driving force which drives the formation of stable clusters of molecules and their growth through a series of processes involving simultaneous mass and heat transfer, controlled by complex variables. This chapter reviews the fundamentals of crystallisation from solubility and supersaturation, to crystal structures and polymorphism, via the processes of nucleation and growth. As a crystallisation process can be broken down into three broad phases - generation of a driving force for crystallisation, nucleation, and growth – an understanding of the complete process is required for true characterisation of a material's crystallisation behaviour. Therefore this review includes solution chemistry, crystal structures, nucleation theory, and crystal growth, focussing on crystallisation from solution.

The chapter begins with the basics of crystal structure and crystallography before moving to the first phase of crystallisation; solubility and supersaturation that drive the overall process. Following this is nucleation covering both classical nucleation and the two-step theory, along with approaches to studying nucleation kinetics. The chapter closes with a review of crystal growth.

2.2 Crystalline state

A crystalline solid possesses a regular repeating three-dimensional pattern in its internal arrangement of atoms, ions, or molecules, which gives the material long-range structural order. If the material doesn't possesses this characteristic long-range order then it is said to be amorphous. Depending on the processing conditions, a given material can often become either crystalline or amorphous. In addition to this, crystals of the same composition can often have different internal arrangements of atoms or molecules giving rise to differences in appearance and physical properties (1).

The simplest representation of a crystal structure is as a repeating point lattice, where each point represents the asymmetric unit – the smallest repeating unit in the structure which can be one or more atoms, ions, or molecules. As each point in the lattice is identical and has identical surroundings, the lattice can be broken down into a smaller repeating unit known as the unit cell. If the unit cell is infinitely repeated in three dimensions the crystal structure will be reproduced. The unit cell is characterised by three

lengths: *a*, *b*, *c*, and three angles; α, β, γ, that are known as the lattice parameters.

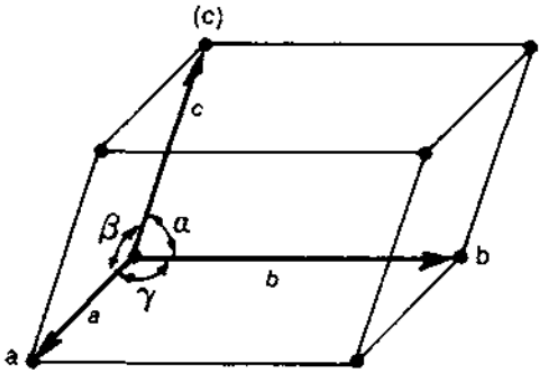

Figure 2.1: A unit-cell (1)

2.2.1 Bravais Lattices and Crystal Systems

There are a number of different lattices and unit cells that could be constructed. However, in 1848 Bravais showed that there were only 14 different point lattices that could be constructed and that they could be further classified into 7 crystal systems as listed in Table 2.1. The lattices can also be divided into either primitive or non-primitive lattices in which primitive lattices only have one lattice point per unit cell and non-primitive have more than one.

Table 2.1: The seven crystal systems, 14 Bravais lattices, and their unit cell parameters (1).

Crystal System	Unit cell parameters	Bravais Lattice
Cubic	$a = b = c$, $\alpha = \beta = \gamma = 90°$	Simple Body-centred Face-centred
Tetragonal	$a = b \neq c$, $\alpha = \beta = \gamma = 90°$	Simple Body-centred
Orthorhombic	$a \neq b \neq c$, $\alpha = \beta = \gamma = 90°$	Simple Body-centred Base-centred Face-centred
Rhombohedral (Trigonal)	$a = b = c$, $\alpha = \beta = \gamma \neq 90°$	Simple
Hexagonal	$a = b \neq c$, $\alpha = \beta = 90°$, $\gamma = 120°$	Simple
Monoclinic	$a \neq b \neq c$, $\alpha = \gamma = 90° \neq \beta$	Simple Base-centred
Triclinic	$a \neq b \neq c$, $\alpha \neq \beta \neq \gamma \neq 90°$	Simple

2.2.2 Polymorphism, Solvates, and Co-crystals

Polymorphism is where a material has more than one crystalline form and although identical in composition different polymorphs can have vastly different physico-chemical properties. These differences in properties such as solubility are due to the different arrangement of molecules within the crystal, particularly the groups exposed at the crystal surfaces, leading to different bonding environments.

Polymorphic materials will often transform between different polymorphs under certain conditions, such as different temperatures or a different solvent. If a material has a number of polymorphs where one polymorph is the most stable form for all temperatures then it is a monotropic system. If the different polymorphs are the most stable form at different temperatures the system is enantiotropic (1). In a polymorphic crystallisation process it is common to find that a metastable polymorphs will crystallise out first and then transform into the more stable form. This phenomenon is known as 'Ostwald's rule of stages' which states that the initial state that is obtained in a process is not the most stable state, but is the least stable state that is closest in energy to the original state. For the case of a polymorphic crystal process, this means that initially a metastable polymorph will form and then transform into more stable forms until it reaches the stable polymorphic form for the given conditions. The time-scale of the metastability can vary from seconds to days or weeks depending on the system and can occur both in the solid state and through a solution-mediated transition.

Polymorphic systems and Ostwald's rule highlight the role thermodynamics and kinetics play in crystallisation. In a crystallisation process, thermodynamics tries to minimise the free energy by forming the most stable polymorph. However, the metastable polymorphs often have only slight differences in energy due to small differences in conformation within their structure. Therefore, if a metastable polymorph is more readily formed, it may form instead of the more stable form due to kinetics. The metastable form does not necessarily have to be a polymorph, it could also be a solvate. A solvate (or hydrate in the case of water) is where solvent molecules are incorporated into the crystal structure. Similarly, multiple chemical species can crystallise together to form co-crystals such as burkeite – a cocrystal of sodium carbonate and sodium sulphate (2).

Cocrystals have become of great interest in crystal engineering, particularly in the pharmaceutical industry, as they provide an alternative route to modifying physico-chemical properties such as improving solubility or stability.

Cocrystals produced from two or more neutral molecules are typically bonded through hydrogen or halogen bonding, whilst those where one of the coformers is a salt are usually bonded through charge assisted hydrogen bonding or coordination bonds (3). In addition to the choice of co-former that cocrystals allow, cocrystals also introduce further complexity as they can also be polymorphic and form solvates (4).

2.3 Solubility and supersaturation

The crystallisation process from a liquid solution depends on the properties of the solute-solvent system and in particular, the solubility of the solute. The solubility is the maximum amount of solute that can be dissolved in a given quantity of solvent at a given temperature to form a homogeneous solution. In an ideal solution the solute-solute and the solute-solvent interactions are equal in strength, which allows the ideal solubility to be predicted from the van't Hoff equation:

$$\ln(x) = \frac{\Delta H_f}{R}\left(\frac{1}{T_f} - \frac{1}{T}\right) \qquad \textbf{(2.1)}$$

Where x is the mole fraction of solute, ΔH_f is the molal enthalpy of fusion, R is the gas constant, T_f is the fusion temperature (melting point), and T is the temperature of the solution. The van't Hoff equation can also be written in the form of eqn. (2.2) as the molal entropy of fusion, ΔS_f, is equal to $\Delta H_f / T_f$. In real systems, the measured solubility often deviates from the ideal solubility due to solute-solute and solute-solvent interactions differing in strength. If the measured solubility is greater, solute-solvent interactions are stronger, whilst if the measured solubility is lower, solute-solute interactions are stronger.

Non-ideal behaviour can be accounted for by taking activity into account and replacing x in eqn. (2.1) with $x\gamma$, where γ is an activity coefficient. Alternatively, the enthalpy and entropy of dissolution, ΔH_{diss} and ΔS_{diss}, can be used in eqn. (2.2) as this takes into account the enthalpy and entropy of mixing, to give eqn. (2.3). This then allows the enthalpy and entropy of dissolution to be calculated from experimentally determined solubility data plotted in $\ln(x)$ vs $1/T$ coordinates (5).

$$\ln(x) = -\frac{\Delta H_f}{RT} + \frac{\Delta S_f}{T} \qquad \textbf{(2.2)}$$

$$\ln(x) = -\frac{\Delta H_{diss}}{RT} + \frac{\Delta S_{diss}}{T} \qquad \textbf{(2.3)}$$

If the amount of dissolved solute in a solution becomes higher than the solubility, e.g if the solution changes temperature, the solution is said to be

supersaturated and becomes metastable. It is this supersaturated state that is the driving force for crystallisation. Supersaturation can be defined as the difference in chemical potential between the supersaturated solution and the solid solute (6). However, supersaturation is usually defined in terms of the concentration difference between the actual concentration, c, and the equilibrium concentration, c^*, the solubility, at the given temperature. It is often described by a supersaturation ratio, S, given by: $S = c / c^*$.

The generation of a supersaturated solution does not instantly result in crystallisation; the solution initially becomes metastable where crystals will form after a finite period of time known as the induction time. If the supersaturation is increased, the solution will pass through the metastable zone and into the labile where crystallisation will occur instantly. Figure 2.2 shows a typical solubility curve, with solubility increasing with increasing temperature. The boundary between the labile and the metastable regions is known as the supersolubility curve, which represents the kinetic limit of metastability (5). The difference between the supersolubility and solubility at a given concentration is the metastable zone width, an important design parameter in crystallisation processes that is dependent on a number of factors including the rate of generation of supersaturation and the rate of agitation (7).

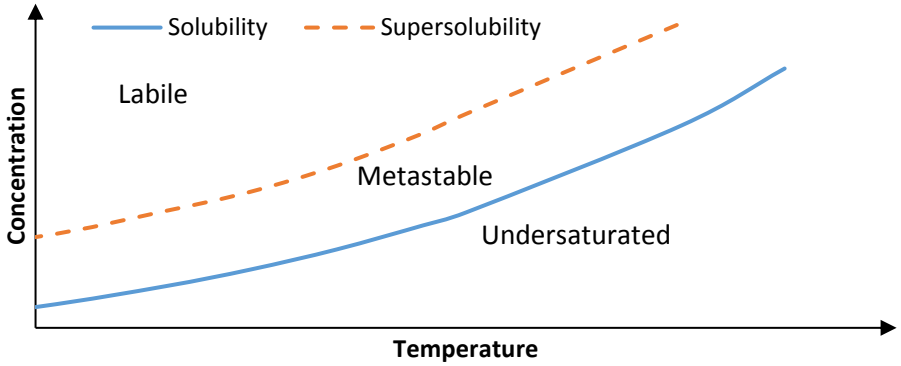

Figure 2.2: A typical solubility-supersolubility diagram

2.4 Nucleation

Nucleation is the starting point for crystal formation, in which solute molecules come together to form clusters or nuclei and pass an energy barrier to become stable, allowing crystal growth to occur. There are a number of nucleation mechanisms possible and these can be categorised as either primary or secondary nucleation. Primary nucleation occurs in the absence of crystalline material and can be further categorised as either homogeneous or heterogeneous nucleation. In primary homogeneous nucleation, nuclei are

formed spontaneously by random collisions of solute molecules in solution whilst in heterogeneous nucleation foreign particles, such as dust, induce nucleation of the solute.

2.4.1 Homogeneous classical nucleation theory

Classical nucleation theory (CNT) was originally developed for condensation of a vapour into a liquid, but has been used “by analogy” to describe crystal nucleation and has become the most widely used description of the process. In CNT, nuclei are formed by addition of molecules from solution to clusters of molecules until either they reach a sufficient size to be stable and are able to grow into macroscopic crystals or until they redissolve (8). This process is often represented as a bimolecular addition process such as in eqn. (2.4) and (2.5).

$$A + A \rightleftarrows A_2 \qquad \textbf{(2.4)}$$

$$A_{n-1} + A \rightleftarrows A_n \qquad \textbf{(2.5)}$$

Classical nucleation theory also makes a number of simplifying assumptions including that the nuclei are spherical and are identical in structure to the macroscopic crystal. It also makes a capillary approximation, neglecting the size/curvature dependence of the surface tension. This has meant that whilst CNT has had success in interpreting nucleation data, it does have shortcomings due to non-realistic assumptions (9).

The thermodynamic description of the process describes the overall free energy change for formation of a cluster, ΔG, as the sum of the volume free energy change, ΔG_v, and the surface free energy change, ΔG_s, as shown in eqn. (2.6) (5). One of the major assumptions of CNT is that the nuclei are spherical, which means that ΔG_s is proportional to the square of the nucleus radius, r^2, whilst ΔG_v is proportional to r^3 (eqn. (2.7)). As ΔG_v is a negative quantity as the solid state is more stable than the supersaturated solution and ΔG_s is a positive quantity due to the creation of a solid-liquid interface, the overall free energy change, ΔG, passes through a maximum as shown in Figure 2.3. This maximum free energy change is the free energy change associated with a critically sized nucleus, ΔG_{crit} (8). Clusters larger than this critical size will continue to grow into crystals as this lowers the free energy, whilst for clusters small than the critical size, they will redissolve to lower the free energy.

$$\Delta G = \Delta G_s + \Delta G_v \qquad \textbf{(2.6)}$$

$$\Delta G = 4\pi r^2 \gamma_i + \frac{4}{3}\pi r^3 \Delta G_v \quad \textbf{(2.7)}$$

$$\frac{d\Delta G}{dr} = 8\pi r\gamma_i + 4\pi r^2 \Delta G_v = 0 \quad \rightarrow -\Delta G_v = \frac{2\gamma_i}{r_c} \quad \textbf{(2.8)}$$

$$\Delta G_{crit} = \frac{16\pi {\gamma_i}^3}{3(\Delta G_v)^2} = \frac{4}{3}\pi \gamma_i {r_c}^2 \quad \textbf{(2.9)}$$

The overall free energy change for a critical nucleus, ΔG_{crit}, shown in eqn. (2.9), can then be derived by describing the volume free energy change in terms of the interfacial tension, γ_i, and the critical radius as in eqn. (2.8) and substituting back into eqn. (2.7).

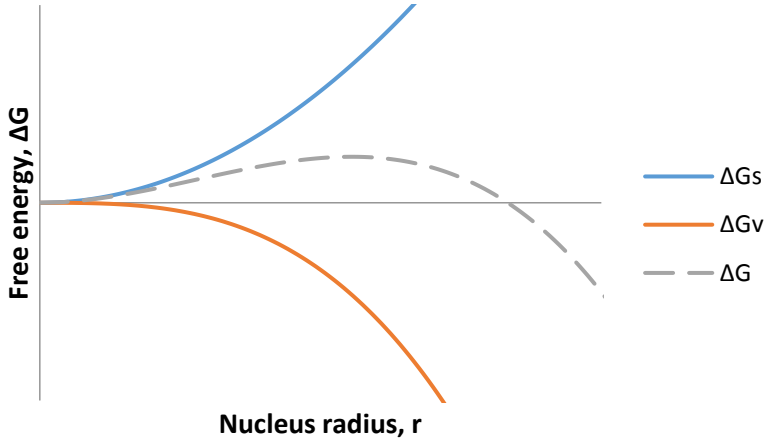

Figure 2.3: The free energy change of forming a nuclei of size, *r*. The maximum corresponds to the critical nucleus size, r_c.

For homogeneous nucleation, the rate of nucleation, J,in terms of number of nuclei formed per unit time per unit volume, can be given by an Arrhenius type rate equation related to the free energy change for a critical nucleus where k_b is the Boltzmann constant and A is the pre-exponential factor (8). Through a Gibbs-Thomson relationship, ΔG_{crit} can be related to the supersaturation as expressed in eqn. (2.11), which leads to expression in eqn. (2.12) for the homogeneous nucleation rate as a function of supersaturation (5).

$$J = Aexp\left[-\frac{\Delta G_{crit}}{k_b T}\right] \quad \textbf{(2.10)}$$

$$\Delta G_{crit} = \frac{16\pi {\gamma_i}^3 {v_o}^2}{3\left(k_b T \ln(S)\right)^2} \quad \textbf{(2.11)}$$

$$J = Aexp\left[-\frac{16\pi {\gamma_i}^3 {v_o}^2}{3{k_b}^3 T^3 (\ln S)^2}\right] \quad \textbf{(2.12)}$$

For heterogeneous nucleation, eqn. (2.12) is still used but with the effective interfacial tension, γ_{eff}, rather than the interfacial tension. This is due to the foreign particles reducing the effective interfacial tension (5).

2.4.2 Secondary nucleation

Secondary nucleation is when solute crystals are already present in the solution, such as in the case of seeding a supersaturated solution with seed crystals of a target polymorph. Secondary nucleation has been well studied and it has been reported in literature that a number of mechanisms exist (1, 5, 10). These include initial breeding, needle/dendritic breeding, contact, attrition, and fluid shear. Initial breeding is where small crystallites are swept off the main crystal surface and become nuclei. This is particularly important in seeded crystallisation processes due to the fines present on seed crystals. Needle or dendritic breeding can occur at high supersaturations where needle or dendritic growth occurs across the crystal surface. These growths are then mechanically detached from the parent crystal and then act as nuclei and grow into separate crystals.

Contact, attrition, and fluid shear are related secondary nucleation mechanisms and a recent review by Agrawal and Paterson proposed a refined classification for these mechanisms as either fluid shear or collision. Collision nucleation occurs due to crystal-crystal or crystal-impeller (or another object in the vessel) and encompasses contact and attrition nucleation. Attrition is where crystal fragments are mechanically generated and detached from the parent crystal due to high velocity collisions such as crystal-impeller collisions. Contact nucleation also occurs due to crystal-impeller collisions but due to crystal-crystal collisions as well. However, contact nucleation occurs due to the removal of an adsorbed solute layer from the crystal-solution interface. Fluid shear is where an adsorbed solute layer is swept away from the crystal interface by shear force (10).

2.4.3 Two-step nucleation

A modern approach to nucleation is two-step nucleation in which a disordered cluster of molecules forms and then re-arranges into an ordered structure (8). In classical nucleation theory it is assumed that a crystalline nucleus forms directly from solution, involving simultaneous transformation in structure and concentration (density). However, in two-step nucleation it is proposed that transformation of these parameters occurs in series, with the initial formation of a dense liquid droplet followed by the formation of a crystalline nucleus within the droplet (11). Much of the evidence for two-step nucleation comes

from work on large molecules such as proteins but there is also evidence for smaller organic molecules such as amino acids (12). The study of two-step nucleation has been carried out by both computational and experimental methods.

Computational studies were among the first to provide evidence of a two-step mechanism. Numerical simulation of homogeneous nucleation of a globular protein showed that close to the liquid-liquid critical point there are large density fluctuations and that the path to forming a nucleus first involves the formation of a liquid-like droplet. It was also noted that the free energy barrier associated for this route was much lower (13).

The two-step nucleation theory has been supported by experimental observations including direct observation of ordered nuclei forming within dense liquid. However, these direct observations have been in protein crystallisation when the dense liquid droplets have been stable rather than metastable – metastable droplets are the more frequent case. It has been inferred that the two-step mechanism applies for metastable droplets by evidence for the existence of metastable droplets and a proposed kinetic law for the two-step mechanism (14). Other experimental evidence for a two-step mechanism includes work on glycine crystallisation involving non-photochemical laser induced nucleation where changing the polarisation state of the laser influences the polymorph nucleated (15). Aqueous solutions of glycine have also been reported to have liquid-like glycine-rich nanoclusters that provide a non-classical nucleation pathway. It was proposed that nucleation occurs within the clusters but that there was a critical size for the nanocluster to grow a sufficiently large glycine crystal that could survive in the more dilute bulk solution (16). Similar solute-rich clusters were proposed to be the location of productive nucleation events of DL-valine (17). It has also been shown that these solute-rich nanoclusters can play a role in crystal growth, attaching and spreading across the crystal surface acting as reservoir of growth units, thus providing an alternative to the classical approach of molecule-by-molecule attachment (18).

2.4.4 Assessment of nucleation kinetics

There has been a number of methodologies presented in literature for the interpretation and assessment of nucleation kinetics of solution crystallisation. These methodologies can be broadly separated into isothermal and polythermal methodologies. Isothermal methodologies use relationships between the induction time and the supersaturation to determine kinetic nucleation parameters such as the interfacial tension. Polythermal

methodologies relate the metastable zone width to the rate at which supersaturation was generated, typically by adjusting the cooling rate.

These methodologies are often used with high throughput techniques to gather large datasets for nucleation, which are needed due to the stochastic nature of nucleation. These techniques often take the form of multiple reactor systems with small solution volumes with the presence of crystalline material detected by solution turbidity measurements (7, 19, 20). More recent developments for studying nucleation make use of microfluidics to create monodispersed droplets of solution that act as individual reactors. The microfluidics chips can hold thousands of dispersed droplets in well controlled conditions whilst the presence of crystalline material can be detected by optical microscopy and image analysis software (21, 22). These microfluidic chips have also been coupled with techniques such as small-angle x-ray scattering for instance with protein crystallisation (23).

Polythermal techniques typically collect crystallisation and dissolution temperatures as a function of concentration and cooling/heating rate by carrying out a number of heating/cooling cycles for a range of concentrations and fixed heating/cooling rates. By collecting data at a number of heating/cooling rates, the crystallisation and dissolution temperatures can be extrapolated back to a zero cooling rate to give equilibrium values and to also enable construction of a supersolubility diagram. Isothermal methodologies collect the induction time as a function of the supersaturation by taking a saturated or undersaturated solution (to ensure complete dissolution of solute) and rapidly cooling to a temperature below the saturation temperature (to generate a desired supersaturation) and holding at the specified temperature until crystallisation is detected. Due to equipment detection limits the measured detection time is not the exact time required for formation of a stable nucleus as some crystal growth is required to enable detection. This means that the measured induction time, τ, can be expressed as eqn. (2.13) where t_r is the relaxation time needed for the solution to distribute clusters formed by the supersaturation, t_n is the time required to form a stable nucleus, and t_g is the time required for the nuclei to grow to a detectable size (19).

$$\tau = t_r + t_n + t_g \qquad \textbf{(2.13)}$$

2.4.4.1 Isothermal methodologies

Classical nucleation theory enables the derivation of an expression that relates the induction time, τ, to the supersaturation in terms of the difference in chemical potential between the solute molecules in the solution and in the

crystal. This difference in chemical potential can be related to the supersaturation ratio, S, allowing the derivation of a relationship between the induction time and the supersaturation (7). This relationship allows the effective interfacial tension, γ_{eff}, to be determined, which can then be used to calculate the radius of a critically sized nucleus and the number of molecules within.

The stochastic nature of nucleation has been used by a number of workers to evaluate nucleation parameters (19, 20). Based on a Poisson distribution of induction times, it can be shown that the probability, P, that at least 1 nucleus has been formed at time, t, is given by eqn. (2.14) where: V is solution volume, J is the nucleation rate, and t_g is the time delay between the nuclei forming and its growth to a detectable size (19).

$$P(t) = 1 - e^{(-JV(t-t_g))} \quad \textbf{(2.14)}$$

By building cumulative probability distributions of induction times for a supersaturation, the nucleation rate and the time delay can be determined by fitting to the experimental data. If this is repeated for a number of supersaturations, a plot of nucleation rate vs supersaturation can be used to determine the interfacial tension by fitting eqn. (2.12) to the data.

2.4.4.2 Polythermal methodologies

Polythermal methodologies are extensively used to establish the metastable zone width for a system and to determine nucleation kinetics. The most straightforward analysis is that of Nyvlt's classical approach that expresses the nucleation rate as a power-law function, eqn. (2.15), in terms of a nucleation order, m_o, and mass rate constant, k_m, and the supersaturation, ΔC_{max} (concentration difference between the actual concentration and the equilibrium concentration for the given temperature) (24, 25). By measuring the metastable zone width as a function of cooling rate the apparent nucleation order and the mass nucleation rate constant can be determined (26). Although Nyvlt's approach has been widely used, it is limited in that the physical significance of the nucleation constant and rate order are unknown.

$$J = k_m {\Delta C_{max}}^{m_o} \quad \textbf{(2.15)}$$

Similar to Nyvlt's approach, Kubota's approach used a power-law relationship for the nucleation rate with a nucleation order and rate constant but also accounted for the detection technique used to observe nucleation and provided a relation between the MSZW and the induction time (26, 27). Sangwal also developed a Nyvlt-type equation that provided physical insight

into the nucleation parameters (28). In addition, Sangwal developed an equation based on classical nucleation theory to describe the nucleation rate rather than using empirical relationships (29, 30).

A more recent approach for polythermal data is the KBHR approach, a first principles approach that doesn't contain empirical parameters or assume a linear relationship between the cooling rate and the MSZW. A key feature of the KBHR approach is its use of two models for the dependence of the relative critical undercooling, u_c defined as $u_c = (T_c - T_e)/T_e$, on the cooling rate – one model for instantaneous nucleation (IN) (31), and another for progressive nucleation (PN) (32). These models allow the KBHR approach to determine whether nucleation is occurring via progressive or instantaneous nucleation (7). Instantaneous nucleation is where all nuclei are formed simultaneously, meaning that under the assumption all nuclei grow at the same rate the solution will contain a fixed number of crystals of the same size. Instantaneous nucleation is typically associated with heterogeneous nucleation where there are strong nucleation sites. For the case of progressive nucleation, nuclei form over a period of time and nucleation and growth occur simultaneously leading to a range of crystal sizes in the solution. Homogeneous, secondary, and heterogeneous (on weak nucleation sites) nucleation can all proceed by progressive nucleation (7). For the case of progressive nucleation, the KBHR approach can determine the effective interfacial tension allowing the radius of a critical nucleus and the number of molecules within such a nucleus to be calculated.

2.5 Crystal growth

After formation of stable nuclei, the next stage in the crystallisation process is crystal growth in which solute molecules are transferred from the bulk solution and incorporated into the crystal structure. The crystal growth process is dependent on a number of external and internal factors such as environmental conditions (e.g. temperature, supersaturation, solvent, impurities) or the crystal structure (e.g. crystal defects, specific surface interactions) (33). The growth process can be broken down into the following major stages:

1) Transport of growth units through the bulk to the boundary layer around the crystal and diffusion through the boundary layer
2) Adsorption of the growth units onto the crystal surface and diffusion to energetically favourable attachment sites
3) Attachment and incorporation into the attachment sites

Depending on the rate determining step, the growth process is either diffusion (step 1) or surface integration (steps 2 or 3) controlled (1). The growth process was initially assumed to be a diffusional process, the reverse of dissolution, and that the rate of growth was proportional to the concentration difference between the bulk solution and the crystal surface (34). This theory was later modified to account for the assumption that there would be a stagnant layer around the crystal surface, through which the growth unit would have to diffuse. However, experimental measurements of the thickness of the stagnant layer around stationary crystals found that with agitation the layer thickness dropped to almost zero – therefore suggesting an almost infinite growth rate in agitated systems according to the theory. Further modifications were made to the theory which split the process into two steps: diffusion from the bulk to the solid surface and incorporation into the crystal.

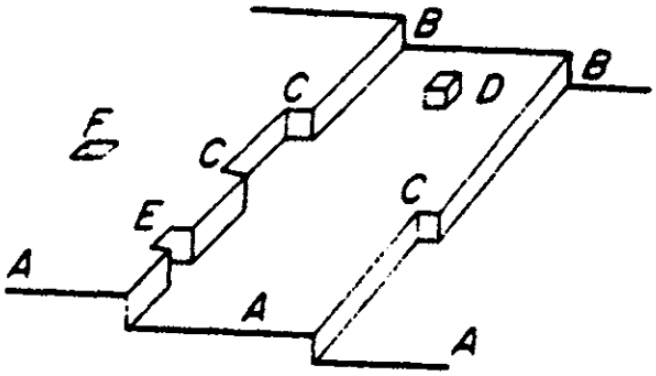

Figure 2.4: The Kossel model of a growing crystal surface (5).

The Kossel model of a growing crystal surface, shown in Figure 2.4, describes the surface as a series of moving steps that can provide three different types of attachment site: surface, step, and kink sites (5). Each attachment site provides different bonding environments for the growth unit, with the kink site being most favourable and the surface site being least favourable. The simplest representation is if the growth unit is represented by a cube where each face represents a bond; a surface site will have 1 bond whilst a step and a kink site will have 2 and 3 bonds respectively. The result of this is that due to their more favourable bonding arrangements, faces with more step and kink sites will often grow quicker than faces with less. The difference in growth rates of different crystal faces has an impact on the crystal morphology as the slowest growing faces determine the overall morphology as the faster growing faces “grow out” of the morphology (35). The availability of kink sites is a major factor affecting the growth rate of crystals (36).

There are three well-established growth mechanisms for integration of molecular units into the surface of a crystal: Screw dislocation mechanism

(BCF model), 2D nucleation, and continuous growth (also known as adhesive or rough interfacial growth (RIG)). Figure 2.5 highlights the relationship between the three crystal growth mechanisms and the supersaturation and the growth rate. The dependence of the crystal growth rate, R_{hkl}, on the supersaturation, σ, for spiral growth, 2D nucleation, and continuous growth are given by eqns. (2.16) *a, b, c* respectively, where A_i and B are growth rate constants (37).

$$a)\ R_{hkl} = A_1\sigma^2 \tanh\left(\frac{B}{\sigma}\right) \quad b)\ R_{hkl} = A_2\sigma^{\frac{5}{6}} \exp\left(\frac{A_3}{\sigma}\right) \quad c)\ R_{hkl} = A_4\sigma \qquad \textbf{(2.16)}$$

The growth mechanism is also dependent on the surface chemistry of the crystal surface, which can mean that the different crystal faces of a crystal can have different growth mechanisms depending on the exposed synthons. The individual faces can also have different growth rate dependencies on the supersaturation.

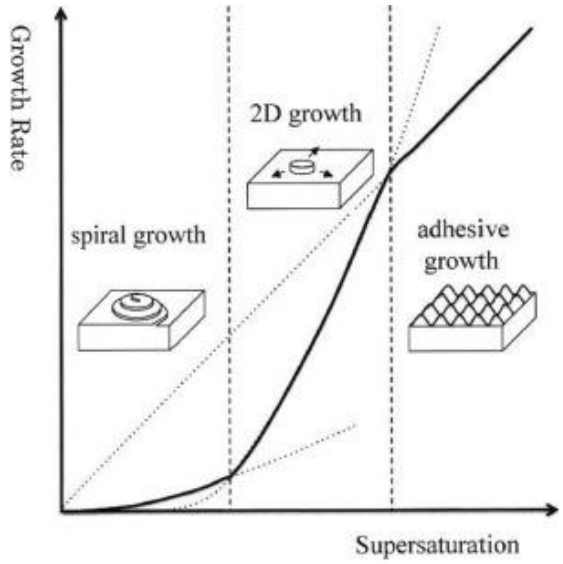

Figure 2.5: The relationship between the supersaturation and the growth rate and growth mechanisms (38).

The Burton-Cabrera-Frank model was proposed to explain crystal growth rates at low supersaturations as the 2D nucleation mechanism predicted far lower growth rates than those observed experimentally (39). The basis of the BCF model is that a screw dislocation acts as a source of new steps on the crystal surface, eliminating the need for 2D nucleation by providing favourable attachment sites. As the crystal surface grows, the layers form in a similar fashion to a spiral staircase with the screw dislocation continuously providing steps for growth units to attach to as shown in Figure 2.6. This results in distinctive growth spirals that can be observed in-situ on the crystal surface (38).

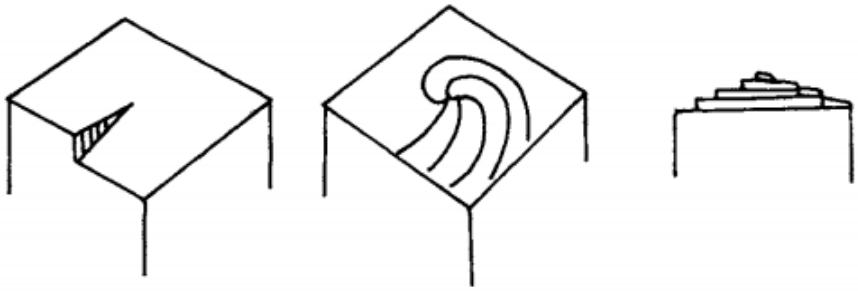

Figure 2.6: Spiral growth from a screw dislocation (5).

The 2D nucleation mechanism occurs at higher supersaturations than the screw dislocation mechanism. Similar to 3D nucleation, 2D nucleation involves the formation of a critically sized nucleus that then grows across the surface by absorption and integration of additional growth units into the monolayer. Once the monolayer covers the complete surface, further 2D nucleation events cans occur on the new surface to continue crystal growth. At very high supersaturations, the growth surface undergoes surface roughening in which the surface becomes molecularly rough. This results in a far greater number of strong integration sites such as step and kink sites that allows for a much higher rate of growth when compared to 2D nucleation or screw dislocation mechanisms.

2.6 Summary

This chapter has presented an overview of the fundamentals of the crystallisation process, from the generation of a supersaturated state to nucleation and crystal growth. These fundamentals of crystallisation provide insight into the crystallisation stability problems faced by liquid cleaning product formulations and their stability testing processes.

In liquid cleaning products crystallisation occurs due to the generation of supersaturation, most likely through a change in temperature due to the varying ambient conditions it is exposed to during manufacture, transportation, and storage. Alternatively, supersaturation could be generated by an increase concentration through solvent loss, such as the product being exposed to differing humidity levels. However, solvent loss is likely to be minimal in a well-sealed product container. Following the generation of supersaturation, the nucleation process in liquid cleaning products can be assumed to be by heterogeneous nucleation rather than homogeneous nucleation as it is unlikely foreign particles such as dust can be completely eliminated and thus crystallisation will proceed via the lower energy barrier route (5). Another factor to consider is agitation; whilst cleaning products may be relatively static

during storage, they are subjected to significant agitation during transportation and loading/unloading activities. This influences the mass transfer within the product, which has an impact on the formation of nuclei and their subsequent growth. The long time-scale over which the crystallisation process occurs in liquid cleaning products also needs to be considered with respect to Ostwald's rule of stages; the crystals that are eventually formed are likely to be the most stable form and thus the least soluble form. Therefore, it could be that crystallisation occurs due to a polymorph change, with the material initially being a less stable (or metastable) form that converts very slowly to a more stable (and less soluble) form that crystallises out. This conversion would present a significant problem for stability testing methodologies unless a method could be identified and developed to accelerate the rate of conversion e.g by seeding with pre-prepared crystals of the most stable form, though this requires a thorough understanding of the crystallisation behaviour of the material.

Current stability testing methodologies effectively replicate the temperatures that product formulations are subjected to; a sample is cycled between a cold temperature-controlled room and ambient conditions or alternatively held at a specific temperatures (typically between -3 °C and 50 °C) for a prolonged period (40). These testing methodologies are essentially isothermal approaches; a supersaturation is generated by cooling to a fixed temperature and the time until crystallisation, the induction time, is monitored. The issue with these isothermal approaches is due to the stochastic nature of nucleation, as demonstrated by ter Horst's work (19); for a given set of conditions there can be a wide distribution of induction times, raising the question of how many samples of each formulation need to be tested to ensure the mean induction time is accurate. In addition, the induction time can be relatively long which results in long testing timeframes, up to 28 days, making testing relatively resource intensive (40). In current stability testing methodologies, the product samples are not subjected to significant agitation, which means secondary nucleation due to breakage or attrition of crystals that nucleate will not occur, therefore slowing the nucleation process.

By considering the fundamentals of crystallisation, possible routes to improving the stability and stability testing of liquid cleaning products can be identified. For example, determining the solubility and MSZW of common components, in particular the least soluble components, can help with formulating products that are stable across a wider range of conditions. Similarly, by considering the nucleation process, testing could be accelerated

by agitating the liquid cleaning products or by seeding the formulations with crystalline material.

The overall effectiveness of these approaches are dependent on the kinetics and thermodynamics of the specific systems and thus a review of literature regarding the behaviour of the least soluble components in a typical liquid cleaning product is carried out within the following chapter.

2.7 References

1. MYERSON, A.S. *Handbook of Industrial Crystallization.* Oxford: Butterworth-Heinemann, 2001.
2. GROTHE, E., H. MEEKES, E. VLIEG, J.H. TER HORST and R. DE GELDER. Solvates, Salts, and Cocrystals: A Proposal for a Feasible Classification System. *Crystal Growth & Design*, 2016, **16**(6), pp.3237-3243.
3. DUGGIRALA, N.K., M.L. PERRY, O. ALMARSSON and M.J. ZAWOROTKO. Pharmaceutical cocrystals: along the path to improved medicines. *Chem Commun (Camb)*, 2016, **52**(4), pp.640-55.
4. AITIPAMULA, S., P.S. CHOW and R.B.H. TAN. Polymorphism in cocrystals: a review and assessment of its significance. *CrystEngComm*, 2014, **16**(17), p.3451.
5. MULLIN, J.W. *Crystallization (Fourth Edition).* Oxford: Butterworth-Heinemann, 2001.
6. KASHCHIEV, D. *Nucleation: Basic Theory with Applications.* Butterworth-Heinemann, 2000.
7. CAMACHO CORZO, D.M., A. BORISSOVA, R.B. HAMMOND, D. KASHCHIEV, K.J. ROBERTS, K. LEWTAS and I. MORE. Nucleation mechanism and kinetics from the analysis of polythermal crystallisation data: methyl stearate from kerosene solutions. *CrystEngComm*, 2014, **16**(6), p.974.
8. ERDEMIR, D., A.Y. LEE and A.S. MYERSON. Nucleation of crystals from solution: classical and two-step models. *Acc Chem Res*, 2009, **42**(5), pp.621-9.
9. KARTHIKA, S., T.K. RADHAKRISHNAN and P. KALAICHELVI. A Review of Classical and Nonclassical Nucleation Theories. *Crystal Growth & Design*, 2016, **16**(11), pp.6663-6681.
10. AGRAWAL, S.G. and A.H.J. PATERSON. Secondary Nucleation: Mechanisms and Models. *Chemical Engineering Communications*, 2015, **202**(5), pp.698-706.
11. VEKILOV, P.G. The two-step mechanism of nucleation of crystals in solution. *Nanoscale*, 2010, **2**(11), pp.2346-57.
12. GEBAUER, D., M. KELLERMEIER, J.D. GALE, L. BERGSTROM and H. COLFEN. Pre-nucleation clusters as solute precursors in crystallisation. *Chem Soc Rev*, 2014, **43**(7), pp.2348-71.
13. WOLDE, P.R.T. and D. FRENKEL. Enhancement of Protein Crystal Nucleation by Critical Density Fluctuations. *Science*, 1997, **277**(5334), pp.1975-1978.
14. VEKILOV, P.G. Nucleation. *Cryst Growth Des*, 2010, **10**(12), pp.5007-5019.
15. MYERSON, A.S. and B.L. TROUT. Chemistry. Nucleation from solution. *Science*, 2013, **341**(6148), pp.855-6.
16. JAWOR-BACZYNSKA, A., J. SEFCIK and B.D. MOORE. 250 nm Glycine-Rich Nanodroplets Are Formed on Dissolution of Glycine Crystals But Are Too Small To Provide Productive Nucleation Sites. *Crystal Growth & Design*, 2013, **13**(2), pp.470-478.
17. JAWOR-BACZYNSKA, A., B.D. MOORE and J. SEFCIK. Effect of mixing, concentration and temperature on the formation of

mesostructured solutions and their role in the nucleation of DL-valine crystals. *Faraday Discuss*, 2015, **179**, pp.141-54.

18. JIANG, Y., M. KELLERMEIER, D. GEBAUE, Z. LU, R. ROSENBERG, A. MOISE, M. PRZYBYLSKI and H. COLFEN. Growth of organic crystals via attachment and transformation of nanoscopic precursors. *Nat Commun*, 2017, **8**, p.15933.
19. TER HORST, J.H. and S. JIANG. Crystal Nucleation Rates from Probability Distributions of Induction Times. *Crystal Growth and Design*, 2011, **11**, pp.256-261.
20. MAGGIONI, G.M., L. BEZINGE and M. MAZZOTTI. Stochastic Nucleation of Polymorphs: Experimental Evidence and Mathematical Modeling. *Crystal Growth & Design*, 2017, **17**(12), pp.6703-6711.
21. TEYCHENÉ, S. and B. BISCANS. Crystal nucleation in a droplet based microfluidic crystallizer. *Chemical Engineering Science*, 2012, **77**, pp.242-248.
22. SELZER, D., B. SPIEGEL and M. KIND. A Generic Polycarbonate Based Microfluidic Tool to Study Crystal Nucleation in Microdroplets. *Journal of Crystallization Process and Technology*, 2018, **08**(01), pp.1-17.
23. PHAM, N., D. RADAJEWSKI, A. ROUND, M. BRENNICH, P. PERNOT, B. BISCANS, F. BONNETE and S. TEYCHENE. Coupling High Throughput Microfluidics and Small-Angle X-ray Scattering to Study Protein Crystallization from Solution. *Anal Chem*, 2017, **89**(4), pp.2282-2287.
24. NÝVLT, J. Kinetics of nucleation in solutions. *J Cryst Growth*, 1968, **3-4**, pp.377-383.
25. NÝVLT, J., R. RYCHLÝ, J. GOTTFRIED and J. WURZELOVÁ. Metastable zone-width of some aqueous solutions. *J Cryst Growth*, 1970, **6**(2), pp.151-162.
26. MITCHELL, N.A. and P.J. FRAWLEY. Nucleation kinetics of paracetamol–ethanol solutions from metastable zone widths. *J Cryst Growth*, 2010, **312**(19), pp.2740-2746.
27. KUBOTA, N. A new interpretation of metastable zone widths measured for unseeded solutions. *J Cryst Growth*, 2008, **310**(3), pp.629-634.
28. SANGWAL, K. A novel self-consistent Nývlt-like equation for metastable zone width determined by the polythermal method. *Crystal Research and Technology*, 2009, **44**(3), pp.231-247.
29. SANGWAL, K. and K. WÓJCIK. Investigation of metastable zone width of ammonium oxalate aqueous solutions. *Crystal Research and Technology*, 2009, **44**(4), pp.363-372.
30. SANGWAL, K. Novel Approach to Analyze Metastable Zone Width Determined by the Polythermal Method: Physical Interpretation of Various Parameters. *Crystal Growth & Design*, 2009, **9**(2), pp.942-950.
31. KASHCHIEV, D., A. BORISSOVA, R.B. HAMMOND and K.J. ROBERTS. Dependence of the critical undercooling for crystallization on the cooling rate. *J Phys Chem B*, 2010, **114**(16), pp.5441-6.
32. ---. Effect of cooling rate on the critical undercooling for crystallization. *J Cryst Growth*, 2010, **312**(5), pp.698-704.
33. SANGWAL, K. Growth kinetics and surface morphology of crystals grown from solutions: Recent observations and their interpretations.

Progress in Crystal Growth and Characterization of Materials, 1998, **36**(3), pp.163-248.

34. NOYES, A.A. and W.R. WHITNEY. Rate of solution of solid substances in their own solution. *Journal of the American Chemical Society*, 1897, (19), pp.930-934.
35. VLIEG, E. The role of surface and interface structure in crystal growth. *Progress in Crystal Growth and Characterization of Materials*, 2016, **62**(2), pp.203-211.
36. VEKILOV, P.G. What Determines the Rate of Growth of Crystals from Solution? *Crystal Growth & Design*, 2007, **7**(12), pp.2796-2810.
37. NGUYEN, T.T.H., R.B. HAMMOND, K.J. ROBERTS, I. MARZIANO and G. NICHOLS. Precision measurement of the growth rate and mechanism of ibuprofen {001} and {011} as a function of crystallization environment. *CrystEngComm*, 2014, **16**(21), p.4568.
38. TSUKAMOTO, K. In - situ observation of crystal growth and the mechanism. *Progress in Crystal Growth and Characterization of Materials*, 2016, **62**(2), pp.111-125.
39. BURTON, W.K., N. CABRERA and F.C. FRANK. The Growth of Crystals and the Equilibrium Structure of their Surfaces. Philosophical Transactions of the Royal Society A: Mathematical, Physical and Engineering Sciences, 1951, 243(866), pp.299-358.
40. SUMMERTON, E., BETTIOL, J., JONES, C., BRITTON, M. M. & BAKALIS, S. 2018. Understanding the Crystallization Process in Detergent Formulations in the Absence and Presence of Agitation. *Industrial & Engineering Chemistry Research*, 57, pp.16162-16171

Chapter 3 Surfactants, monoethanolammonium carboxylates, and related compounds

A review of the literature regarding the phase and crystallisation behaviour of sodium carboxylates and MEA carboxylates

3.1 Introduction

Surfactants are compounds that exhibit surface active behaviour, strongly absorbing at the interfaces between phases. This behaviour originates from surfactant molecules containing chemical groups that have opposite behaviours, the most commonly encountered pairing being hydrophobic and hydrophilic; this behaviour gives rise to complex phase behaviour. Surfactants are found throughout a range of cleaning products, one of the most commonly encountered surfactants being soap – the salt of long-chain fatty acids. The phase behaviour and properties of soap depend on a number of factors such as the counter-ion, the chain length of the carboxylate and whether there is unsaturation within the alkyl chain. This chapter briefly reviews the typical phase behaviours of surfactants before focusing on the study of soaps. The review of literature on soaps begins with sodium soaps, otherwise known as sodium carboxylates, as they have been extensively studied with regard to their phase behaviour and crystallisation behaviour. The chapter closes with a review of monoethanolammonium carboxylates and some related compounds – amine soaps as they are more commonly known – that are the core focus of the research within this thesis.

3.2 Surfactants

Surfactants are found in a wide range of products and applications from the food industry (1), oil and mineral recovery (2-4), pharmaceuticals (5), and cleaning products (6, 7). The surface active behaviour of surfactants arises from their chemical structure; they contain separate functional groups that are solvent-loving and solvent-hating.

3.2.1 Structure and properties

As the hydrophobic groups of surfactants tend to be chemically quite similar, typically based on hydrocarbon chains, surfactants are categorised by the chemical structure of their headgroup. This classification leads to four classes of surfactants; cationic, anionic, non-ionic, and amphoteric (6).

Anionic surfactants typically contain anionic functional groups, such as carboxylates or alkyl sulfates with small counterions such as sodium or potassium ions (6). Cationic surfactants have cationic functional groups such as tetraalkylammonium, with small counter ions including chloride or sulphate (8). Amphoteric surfactants, such as betaine, contain zwitterionic head groups whose charge depends on the solution pH. Non-ionic surfactants are neutrally

charged and have functional groups that do not dissociate in solution such as polyalkyloxylated alcohols (9).

The hydrophobic groups of surfactants show less variation in their chemical composition than their hydrophilic groups. Typically, the hydrophobic group is a long chain hydrocarbon but it can also contain other derivatives and components. The structure of the hydrophobic group can show significant variation in structure however, such as straight or branched chains, or alkylbenzene or fluoroalkyl chains (9). The structure of the chain can have a significant effect on the properties and phase behaviour of the surfactant with chain length, branching, and unsaturation all having various effects. For example, increasing the alkyl chain length decreases the aqueous solubility, but often lowers the critical micelle concentration (cmc) (10). Chain branching, in contrast, improves the surfactant solubility and inhibits liquid crystal formation as the branching affects the ability for the molecules to pack together. Branching can also introduce positional isomerism, where the position of the hydrophilic group can have a significant effect i.e if it attaches at the 2nd carbon on a 14 carbon chain it'll behave similar to a single chain surfactant whilst if it attaches at the 5th carbon it'll behave as a two-tailed surfactant (11). Introducing or increasing the level of unsaturation in a hydrocarbon chain can have a significant effect on a surfactants behaviour, as exemplified by the difference in behaviour of sodium stearate (C18:0) and sodium oleate (C18:1); 5 %wt sodium oleate dissolves at 27 °C whilst 5 %wt sodium stearate dissolves at 72 °C (12, 13).

3.2.2 Phase behaviour

Surfactants have complex aqueous phase behaviour as their chemical structure causes them to aggregate in solution to form self-assembled structures. These structures include micelles, vesicles, and liquid crystals, and their formation is driven by the hydrophobic effect that arises when the hydrophobic groups of a surfactant are solvated. When these groups are solvated, there is a decrease in entropy as the water molecules become highly ordered in the vicinity of the hydrophobic groups. If these groups were to move out of the aqueous solution, the water molecules would become less ordered and the system entropy would increase; this is known as the hydrophobic effect (14).

Surfactants aggregate in solution once their solution concentration increases above a minimum concentration known as the critical micelle concentration (cmc). Below the cmc, surfactants are present as individual molecules and absorb at interfaces between two phases, such as oil-water or air-water

interfaces. At these low concentrations, aggregated structures do not form as the formation of aggregates increases ordering of the system, decreasing the system entropy and creates a driving force for dissociation of aggregates. This driving force increases with decreasing free surfactant concentration and therefore with decreasing total surfactant concentration (15). The net result of the entropy effects is that at concentrations below the cmc, the driving force for dissociation is too large and prevent self-assembly. At concentrations above the cmc, the entropy gain on moving the surfactant tails out of solution and into aggregates is greater and drives formation of aggregates such as micelles. The micellisation process has a negative free energy change, meaning the process is favoured and spontaneous and it has been found that at room temperature, entropy is the dominant driving force for micellisation (due to the release of water molecules bound in hydration shells), whilst at higher temperatures enthalpy contributions dominate (16).

The concentration of surfactant monomers does not increase far above the cmc once micelles have formed, but the concentration of micelles does increase as the total surfactant concentration increases. The cmc of a surfactant depends on its chemical structure, with the hydrophobic groups having a significant effect as an increase in chain length can result in a decrease in the cmc (14). The type of aggregate formed by a surfactant can be predicted by the critical packing parameter, P, which is defined by eqn. (3.1) where v is the hydrocarbon chain volume, l_c is the length of hydrocarbon chain, and a_o is the area per molecule (17).

$$P = \frac{v}{a_o l_c} \qquad \textbf{(3.1)}$$

Where

For packing parameters $P < 1/3$ spherical micelles are expected to form, whilst for $1/3 < P < 1/2$ cylindrical or wormlike micelles are expected. At $1/2 < P < 1$ flexible bilayers or vesicles are expected, whereas at $P = 1$ lamellar bilayers are likely to form. Inverted micelles are expected at $P > 1$ (17).

3.2.2.1 Micelles

The first aggregates that surfactants tend to form above the cmc are micelles. In a micelle, surfactant molecules aggregate together and arrange themselves to move their hydrophobic groups out of aqueous solution, shielding them within the core of the micelle with the hydrophilic headgroups facing out into solution. Inverted micelles can form in organic solvents or water-poor mixtures of organic solvent and water, where the water and hydrophilic groups are

within the core of the micelle and the hydrophobic chains extend out into the solution (18). Micelles can form in a number of shapes including globular/spherical, rod-like or worm-like, branched, and disk-like. The morphology of micelles can change with increasing surfactant concentration and the ionic strength of solution as it affects the screening of electrostatic repulsion between headgroups. Above certain concentrations, micelles can grow into elongated, polymer like micelles, known as wormlike micelles (WLM) which above a certain concentration can entangle into a dynamic network similar to polymer solutions (19).

Micellar solutions are isotropic and are composed of micelles in equilibrium with surfactant monomers in solution. As such, surfactant molecules are exchanged between the solution and the micelles and the number of monomers with a micelle fluctuates around a mean value – the aggregation number. The aggregation number depends on the chemical structure of the surfactant; non-ionic surfactants typically are 100-1000 molecules, whilst ionic surfactants are often below 100 due to the electrostatic repulsion between headgroups (9). The formation of micelles from individual surfactant monomers has been studied, with several mechanisms proposed; the Aniansson-Wall mechanism proposed a step-wise incorporation of monomers into a micelle, but other mechanisms included the fission and fusion of pre-micellar aggregates (20). Synchrotron SAXS studies have shown that micelle formation follows a nucleation and growth type process that follows the Aniansson-Wall mechanism of single insertion events of monomers into micelles (21, 22). Fusion and fission of micelles has been observed by SAXS during micellar transitions and has been observed at equilibrium through simulations (23-25). The transition from micelles to vesicles has also been well studied (26-30).

3.2.2.2 Vesicles

Vesicles are spherical surfactant aggregates consisting of a spherical shell made up of a bilayer of surfactant molecules, with the interior of the vesicle containing the solution (31). Vesicles can range in size from a few nanometres to several micrometres and can be unilamellar, consisting of a single bilayer, or multilamellar, consisting of several bilayers forming the shell. In addition, vesicles can also be multivesicular, where vesicles are contained with a vesicle (32).

3.2.2.3 Liquid crystals

At higher surfactant concentrations, surfactants can form more ordered aggregates known as liquid crystals. There are three main types of lamellar crystals encountered; cubic, hexagonal, and lamellar (33).

There are two types of cubic crystals that can form; bicontinuous and discontinuous. Discontinuous cubic liquid crystals are formed from spherical or short cylindrical micelles that arrange in a cubic packing system (34). In contrast, bicontinuous cubic liquid crystals are formed from a surfactant bilayer that divides the solution into a connected network of solution-filled channels (35). Cubic liquid crystals both form isotropic solutions, in contrast to hexagonal and lamellar liquid crystals that are anisotropic.

Hexagonal liquid crystals consist of cylindrical micelles that are arranged in a hexagonal array surrounded by a monomer solution. If the surfactant is in a hydrophobic or water-poor solvent, inverse hexagonal liquid crystals can form (36). Lamellar liquid crystals are comprised of bilayers of surfactant molecules separated by layers of solution, where the layers of solution can be of a much greater thickness than the surfactant bilayers. In the bilayers the surfactant chains are typically tilted away from vertical, making their approximate length slightly less than double the surfactant chain length. Lamellar liquid crystals are similar in structure to lamellar gel networks and the crystal structures of surfactants such as sodium carboxylates with the key difference being the state of surfactant chain. In a lamellar liquid crystal the chains are in a dynamic and disordered state whilst in a lamellar crystal the chains hexagonally packed and fixed in position. A lamellar get network lies between these two states with the surfactant chains able to rotate around the long axis of the molecule (36).

3.3 Sodium Carboxylates

The phase behaviour of sodium carboxylates have been extensively studied in literature for aqueous systems and some organic solvents (13, 39-45, 49-54). Studies have typically focussed on the behaviour of a single chain length of soap in aqueous solution, although there have been several studies on the behaviour of mixtures of chain lengths (39, 40, 46-48). The behaviour of sodium soaps in organic solvents has been far less comprehensively studied, with limited information available for only several long chain lengths such as palmitate, stearate, oleate, albeit for a range of organic solvents (49-54).

Whilst the crystallisation behaviour of sodium soaps has been studied by a number of techniques including turbidity, differential scanning calorimetry

(DSC), and small-angle x-ray scattering (SAXS), a complete understanding of the crystallisation process is still lacking (48). Studies of nucleation kinetics of micellar solutions of sodium laurate and myristate, and mixtures of the two have been studied using Nyvlt's approach to nucleation kinetics (48). However, the nucleation behaviour is still unclear as the observed behaviour may be a combination of the kinetics of micelle dissolution and crystal nucleation. If crystallisation occurs from the monomer phase, rather than in the micelles in a manner akin to two-step nucleation, there will be an equilibrium between the crystal and the monomer phase and an equilibrium between the monomer and micellar phase at the point of crystallisation (37).

The crystal growth of sodium soaps has seen very little work, although this could be down to sodium soaps tendency to form coagels – heterogeneous mixtures in which soap crystal fibres enmesh water – rather than as discrete crystals (48). For example an aqueous 10% wt sodium myristate on cooling from an isotropic micellar solution will form a coagel, as shown in Figure 3.1. The structure and morphology of sodium soaps has been reasonably well studied by electron microscopy and x-ray diffraction, although research has mainly focused on soaps from aqueous solution. There has been a study which found that changing the polarity of the solvent induced a change in morphology from fibres to plate-like crystals (38).

3.3.1 Phase behaviour

The aqueous phase behaviour of sodium soaps has been extensively studied in literature by many different workers (39). A typical phase diagram for aqueous sodium soaps is shown in Figure 3.2. The temperature boundary above which liquid crystals and micellar solutions form is often called the Krafft boundary (67). Above the Krafft boundary, there is an isotropic micellar solution at concentrations between the cmc and around 25 % wt soap, hexagonal liquid crystal phase forming between 25 % wt soap to 50 % wt soap, and lamellar liquid crystal forming above 50% wt soap. Beyond a certain temperature, the hexagonal and lamellar liquid crystal phases melt to become an isotropic micellar solution. Below the Krafft boundary, the system is a mixture of soap crystals and water.

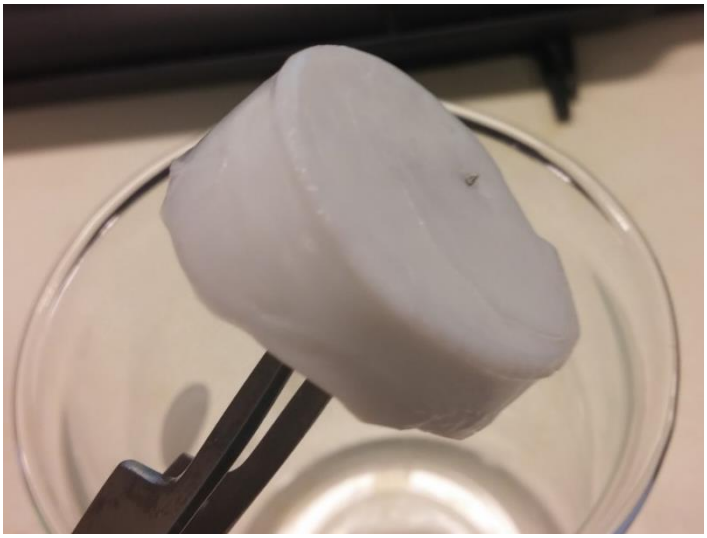

Figure 3.1: A crystallised 10%wt aqueous solution of sodium myristate.

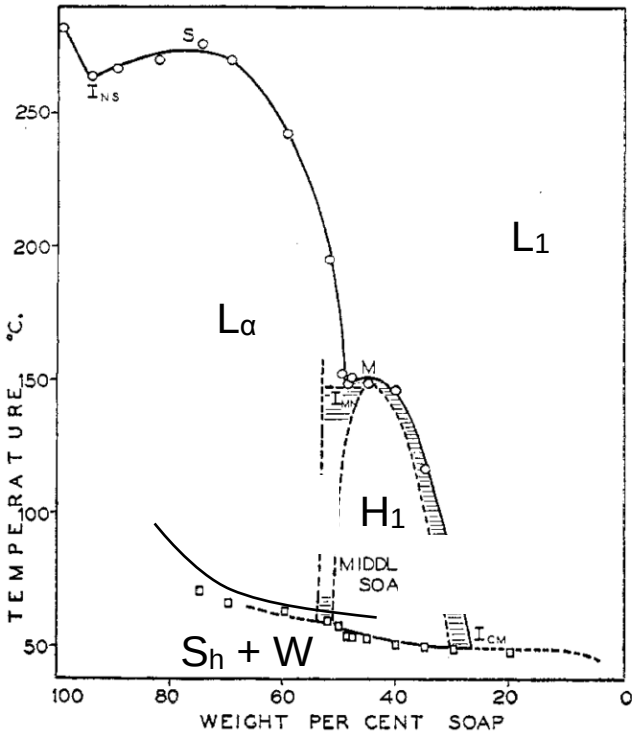

Figure 3.2: A typical sodium soap - water phase diagram, where L_1 is micellar solution, H_1 is hexagonal liquid crystal, L_α is lamellar liquid crystal, and S_h and W are hydrated surfactant crystals and water respectively. Modified from ref (40).

Comparing the aqueous phase diagrams of various sodium soaps of different chain lengths, from sodium laurate (C12:0) through to sodium stearate (C18:0), it is evident that the chain length has relatively little effect on the overall phase behaviour. As the chain length increases, the transition temperatures increase and the onset of liquid crystals occurs at lower soap concentration and the overall region of liquid crystals is larger (13, 39, 41, 42). From the phase diagrams of sodium stearate (C18:0) and sodium oleate

(C18:1), adding unsaturation into the carboxylate chain has a similar effect to decreasing chain length; there is little overall effect on the general features of the diagram, except that unsaturation drastically lowers the Krafft boundary compared to its saturated equivalent (12, 43-45).

The aqueous phase behaviour of various mixtures of sodium soaps have also been reported, including sodium oleate-palmitate/laurate/stearates mixtures (40), sodium laurate/palmitate mixtures (39), sodium laurate/oleate mixtures (46), and mixtures of sodium stearate/arachidate/behenate (47). For aqueous sodium soap mixtures, the general aqueous phase diagram for sodium soaps is still applicable as they exhibit the same general features. Studies on binary soap mixtures have shown that the behaviour is dependent on the relative amounts of each chain length. For binary mixtures with equal amounts of each soap, the phase behaviour is an average of the individual soap behaviours in both temperature and concentration boundaries (39). However, for mixtures with unequal quantities of the different soaps, the Krafft boundary can be at a lower temperature than any of the pure components and reaches a minimum for mixtures with a high mass fraction of the smallest chain length soap (47, 48).

In contrast to aqueous systems, the phase behaviour of sodium soaps in organic solvents has been studied in far less detail, with few complete phase diagrams. Although studies have tended to focus on a general description of the phases present for a limited temperature and concentration range, these studies were often carried out for a wide range of solvents.

The general behaviours of sodium oleate, palmitate, and stearate in 40 different organic solvents have been qualitatively described, though the temperatures and concentrations at which these phase transitions occurred were not well established (49). Solubility curves for sodium palmitate in a variety of organic solvents, both polar and non-polar, including glycerol, diethylene glycol, n-heptane, and isopropyl alcohol have been reported. The study found at higher concentrations of sodium palmitate, the equilibrium temperature is similar for both polar and non-polar solvents. However, at lower concentrations there is a more marked difference in the solubility curves as an increase in the polarity of the solvent increases solubility (50, 51). This is similar to what has been found for surfactant mixtures in organic solvents, with micelles forming in strongly polar solvents whilst in less polar solvents the surfactants remain as monomer solutions (52). Solubility curves have also been reported for sodium stearate in anhydrous hydrocarbons in which sodium stearate was equally soluble in each of the studied solvents (53).

Phase diagrams has been reported for sodium palmitate in glycerol (50) and sodium stearate in cetane, cyclohexane, and toluene (53, 54). The phase diagrams for sodium stearate were similar for the different hydrocarbon solvents, with five different general regions reported (53). The phase diagram of sodium palmitate in glycerol showed similar behaviour to sodium palmitate in water, with a qualitatively similar phase diagram showing a transition with increasing temperature to isotropic solution from a crystalline or wax-like phase at low concentration and a transition to liquid crystal phases at higher concentrations. Other polar organic solvents showed similar features, along with the presence of anisotropic gel phases (50).

3.3.2 Crystallisation behaviour

There have been a number of studies looking at the crystallisation behaviour of sodium soaps. However, the nucleation behaviour or crystal growth of soaps hasn't been particularly well studied.

The nucleation kinetics of aqueous solutions of sodium laurate and sodium myristate, along with mixtures of the two, have been studied by using a polythermal methodology and Nyvlt's approach to nucleation kinetics. It was reported that for solutions of a single soap the metastable zone width and the order of nucleation decrease as concentration and chain length increase. Solutions with a mixture of the two soaps exhibited higher metastable zone widths in mixtures where one component is dominant, whilst for 1:1 mixtures the metastable zone width was between that of the pure soaps (48). This is similar to what has been reported for the phase diagrams of sodium soap mixtures, with 1:1 mixtures behaving as an average of the soaps. It has also been suggested that a weak dependence of the metastable zone width on the cooling rate could mean that the overall crystallisation process from a micellar solution is more dependent on the exchange between micelles and the monomers (55).

Although single crystals have been grown of sodium stearate and sodium palmitate for analysis, there has been relatively little study on crystal growth of sodium soaps in literature (56). Anhydrous soaps exhibit complex melting behaviours and these transitions have been well studied in literature. As anhydrous sodium soaps are heated they transition through a number of liquid crystalline phases until they melt to form isotropic liquid (57). There has been a number of studies on the structure and morphology of sodium soap in literature, with the bulk of the studies focussing on sodium soap crystals from

aqueous solutions (58, 59). These crystals are often referred to as curd fibres or coagels, as when sodium soaps crystallise, they crystallise as long thin fibres which enmesh water (48, 58). These fibres have a lamellar bilayer structure as shown in Figure 3.3.

X-ray diffraction (XRD) experiments on sodium soaps, such as sodium palmitate and stearate have shown that there are a number of crystal phases (60-63). Originally it was proposed that there were four crystalline phases, but this was revised to eleven following XRD evidence for a further seven crystalline phases (64-66). However, further studies reduced this to seven phases as it was shown that three phases were members of one solid solution phase (62). The different crystalline soap phases are different phase compounds rather than polymorphs, due to them being compositionally different. The different phases have different crystal arrangements with different levels of hydration and can be linked to specific types of sodium soaps i.e by level of unsaturation or chain length (67).

The morphology and structure of sodium soap crystals depends on the soap chain length. Cryoelectron microscopy of sodium soaps from aqueous solution with chain lengths from C10:0 to C20:0 has shown that the C10:0 - C14:0 soaps have a different crystal packing compared to that of the C16:0 - C20:0 soaps. The shorter chains were found to have a structure where the normal of the bilayer is parallel with the fibre width, whilst for the longer chains the normal to the bilayer is perpendicular to the fibre width, as show in Figure 3.3 (68). For short chain lengths, the largest surface is made up of ionic head groups and relatively short hydrophobic tails. As the chain length increased, this surface would become increasingly apolar leading to unfavourable interaction between the surface and water. The change in morphology avoids this by having the largest surface made up of the ionic head groups, with the majority of the hydrophobic alkyl chain shielded from the water (68).

This crystal surface polarity effect also makes the soap morphology solvent dependent. In water-propylene glycol mixtures the morphology for short and long chain sodium soaps exhibits the opposite morphological behaviour to soaps in water, as shown by Figure 3.3. In the water-propylene glycol mixtures, the solubility of the ionic head group is limited, making large surfaces made up of ionic head groups unfavourable and there is also a reduction in hydrophobic interactions between the alkyl chains and the solvent (68). Similarly, studies on the morphology of sodium stearate in mixtures of water and propylene glycol have also found that increasing the proportion of propylene glycol in the mixture induced a morphology change from fibres to

plate-like crystals. It was also noted that sodium myristate had a different morphology to sodium stearate in these mixtures, again showing the morphology dependence on chain length (38).

The solid state structures of solid sodium soaps have been studied by a number of chemical and structural techniques including Fourier-Transform Infrared (FTIR) spectroscopy, DSC, 13C Nuclear Magnetic Resonance (NMR), and powder x-ray diffraction (PXRD) (69, 70). FTIR analysis indicated that the alkyl chains crystallise in an all-trans configuration whilst the metal-carboxylate bonding is via chelating with extensive head group interactions. The PXRD results indicate that the lamellar structure of sodium soaps has a spacing of approximately double the molecular length of the sodium soap regardless of the chain length. This indicates that the lamellar planes are bilayers where the alkyl chains are tilted at 27° relative to a normal of the metal plane (69). From the NMR it was reported that the metal-carboxylate bonding is mostly independent of chain length.

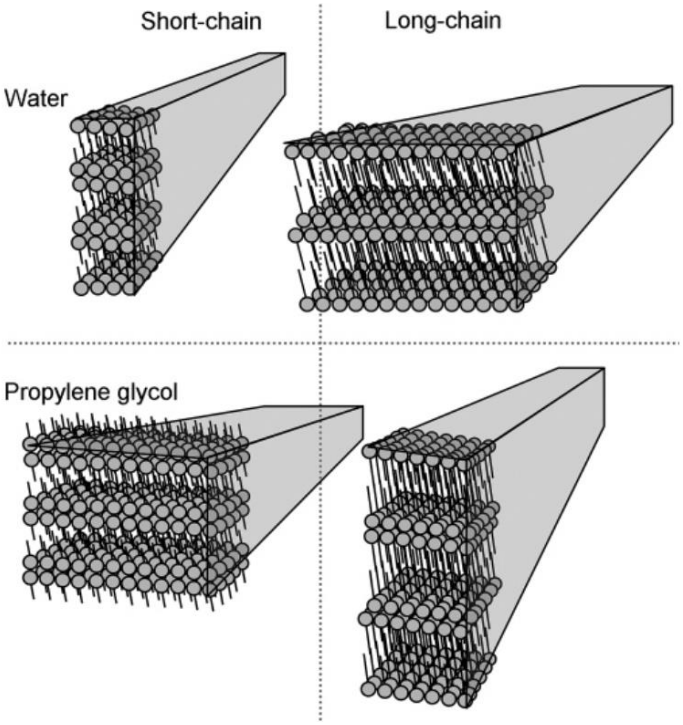

Figure 3.3: Morphology of short (C10-C14) and long (C16-20) chain sodium soaps in water and water-propylene glycol mixtures (1/3, w/w) (68).

3.3.3 Acid-soaps

Acid-soaps are cocrystals formed from a carboxylic acid and carboxylic acid salt. They contain the parent components in discrete stoichiometric ratios and retain characteristics of the parent fatty acid and soap as evidence by experimental data such as FTIR (71). Acid-soaps exist in discrete

stoichiometric ratios but for a given component pair several discrete acid-soaps are possible. For example, potassium laurate – lauric acid has been reported to form a 1:1 acid-soap, sodium palmitate – palmitic acid a 2:1, 1:1, 1:2 acid-soap, whilst for sodium myristate – myristic acid there have been numerous including 4:1, 3:2, and a 1:1 acid-soap (72-75).

Much of the study of acid-soaps in literature has focussed on acid-soaps of metal carboxylates such as sodium or potassium. Binary phase diagrams have been reported for several fatty acid – soap systems including potassium laurate – lauric acid, sodium palmitate – palmitic acid, and sodium oleate – oleic acid (73, 74, 76, 77). The phase diagram of sodium palmitate – palmitic acid is shown in Figure 3.4 and exhibits a number of phases, acid-soap stoichiometries, and acid-soap polymorphism. The low temperature regions are heterogeneous mixtures of crystals whose composition changes as the amount of sodium palmitate increases from palmitic acid and 2:1 acid-soap, to 2:1 and 1:1 acid-soap, 1:1 and 1:2 acid-soap, and 1:2 acid-soap and sodium palmitate. The progression of the composition indicates that the formation of acid-soap is favoured over the formation of palmitic acid.

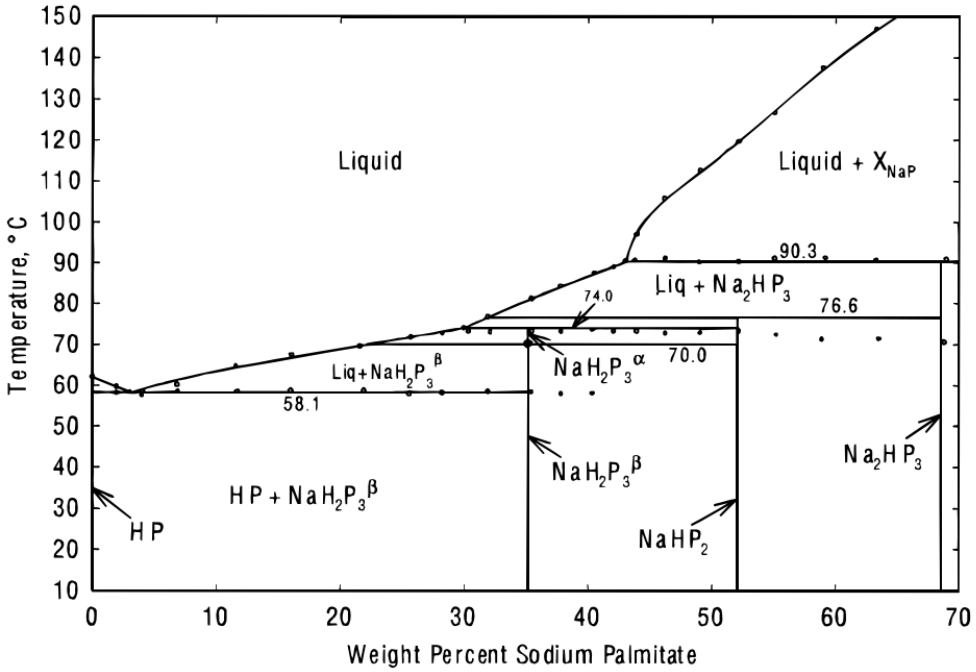

Figure 3.4: The sodium palmitate (NaP) - palmitic acid (HP) phase diagram. $NaHP_2$ – 1:1 acid-soap, NaH_2P_3 – 2:1 acid-soap α- and β-polymorphs, Na_2HP_3 – 1:2 acid-soap (73)

Studies of acid-soap have often studied the structural changes through FTIR studies due to sensitivity of IR to changes within the headgroup bonding i.e COO- and COOH groups and the alkyl chain conformation (73, 78-81). Analysis of the behaviour of the C=O absorption has suggested that 1:1 acid-

soaps of alkali metal carboxylates (Li, Na, K, Cs) form dimers between the acid and carboxylate with asymmetric hydrogen bonds (79). The headgroup region in IR, 1500-1800 cm^{-1}, is particularly informative for distinguishing between acid, acid-soap, and soaps due to the different characteristic peaks. Fatty acids exist as hydrogen bonded dimers in their crystal structure with a typical C=O stretch at around 1690-1700 cm^{-1}, whereas this peak is not evident in soaps and is shifted to higher values in the acid-soap e.g 1718 cm^{-1} for a 1:1 sodium oleate – oleic acid. The most prominent peak in this region for soaps is that of the asymmetric carboxylate stretch at approximately 1560 cm^{-1} (77).

Attempts have been made at growing single crystals of potassium myristate 1:1 acid-soaps for structural determination but growth of single crystals of soaps and acid-soaps is difficult with only crystals good enough for obtaining unit-cell dimensions (82). However, acid-soaps of sodium palmitate and palmitic acid have received considerable attention which has led to determination of the crystal structure of the 1:1 acid-soap (73, 79, 80). The 1:1 acid-soap of sodium palmitate – palmitic acid has a bilayer structure in which acid and carboxylate pairs couple perpendicular to the bilayer. The alkyl chain adopts an all-trans configuration with acid carboxylate pairs bonded via a short hydrogen bond and co-ordination to a sodium ion that is shared as part of a pseudo-six-member ring of carboxylate anions (80).

There has been some study of the behaviour of acid-soaps in aqueous solution as they can form spontaneously formation in aqueous soap solutions. Studies have focussed on sodium carboxylates such as sodium oleate and sodium myristate, but have also included potassium carboxylates (83, 84). The aqueous phase diagram of the 1:1 potassium oleate – oleic acid acid-soap has been reported and showed extensive liquid crystal formation across the entire water concentration range; at low water concentration inverse hexagonal liquid crystal phases are present whilst at higher water concentrations lamellar liquid crystal phases develop (84). Aqueous sodium myristate solutions have been used to study the effect of “hydrolysis” - the protonation of the soap carboxylate that can lead to fatty acid or acid-soap formation. Hydrolysis of sodium myristate in aqueous occurs to a limited extent, with approx. 1% becoming protonated, yet this has a strong effect on the solution behaviour effecting measurements of the cmc and solubility (81). The effects of hydrolysis and the resulting formation of fatty acid or acid-soap has led to the development of theory for the pH of carboxylate soap solutions with precipitates, enabling identification of different precipitates i.e fatty acid

or different acid-soap stoichiometries, through experimental pH vs total concentration isotherms (72). For the case of aqueous sodium laurate solutions and sodium myristate solutions the precipitate is dependent on the total concentration of the sodium soap with distinct regions corresponding to a certain precipitate as shown for sodium myristate at 25 °C in Figure 3.5.

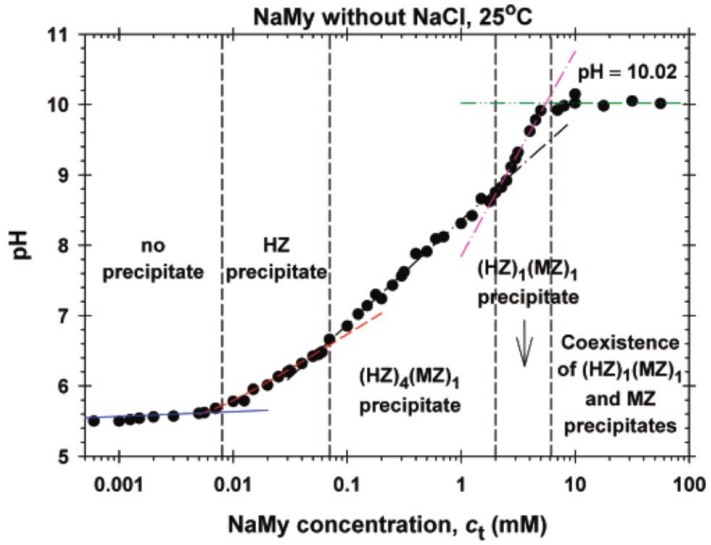

Figure 3.5: pH data for aqueous sodium myristate solutions at 25 °C, showing the fitted "characteristic functions" for the precipitated material. HZ – myristic acid, MZ – sodium myristate

3.4 Ethanolammonium carboxylates

Ethanolamines are a group of amino alcohols that include monoethanolamine (MEA), diethanolamine (DEA), and triethanolamine (TEA). They all are infinitely miscible with alcohols and water and are weak bases due to the amino group. For MEA and DEA, salt formation takes place in preference to ester formation during reaction with organic acids (85). By using ethanolamines to neutralise fatty acids alkanolammonium carboxylates, known as amine or ethanolamine soaps, can be produced.

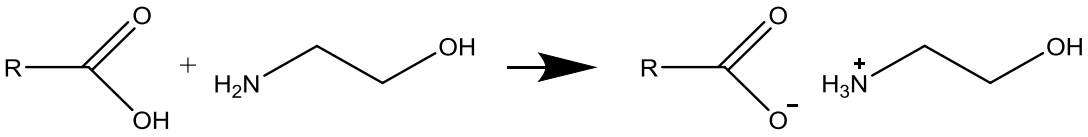

Figure 3.6: Formation of a MEA carboxylate by neutralisation of a fatty acid by MEA

Ethanolamine soaps were first reported in literature in the 1920s (86-88) but only became of more interest when ethanolamines became commercially available, permitting the preparation and study of their soaps (89, 90).

Although initial studies of these soaps were performed as early as the 1920s there is relatively little information available regarding their solution phase behaviour (87). The information in literature is limited to a partial phase diagrams of MEA or TEA soap in aqueous solution and the critical micelle concentrations for a selection of chain lengths. There is very little information on the phase behaviour of ethanolamine soaps in organic solvents.

There has been some solid-state characterisation of alkanolammonium carboxylates due to their ability to form ionic liquids or ionic greases (91-96). These characterisations have generally been used to confirm synthesis of the alkanolammonium carboxylates, with NMR, FTIR, and DSC being the most common techniques. These studies have covered a wide range of carboxylate chain lengths, from formate (C1) to stearate (C18), but they have provided little information about the crystallisation behaviour or crystal structure particularly for intermediate and longer chain lengths.

The partial aqueous phase diagrams for MEA and TEA soaps in literature are limited in that they do not show the Krafft boundary, as it appears to be below the lowest temperature studied (20 °C). There is also a region at low soap concentration which is described as “undetermined” where there are multiple phases present (97). The Krafft boundary is particularly important for crystallisation stability as it bounds the region where solid crystal soap would be expected and should show a dependence on soap chain length or headgroup e.g MEA or TEA.

There is more information available on the phase behaviour of TEA stearate than other ethanolamine soaps due to a series of papers looking at the acid-soap behaviour in TEA – stearic acid – water systems (87, 98, 99). Similarly, there have been solid-liquid equilibrium phase diagrams produced for systems of oleic or stearic acid in MEA or DEA (91).

3.4.1 Synthesis and solid state behaviour

The information on the solid-state behaviour of MEA or TEA soaps and their related compounds is quite limited, particularly for intermediate chain lengths e.g C12 - C16 as studies in literature have focussed on the behaviour of either short chains such as formate (C1:0) and acetate (C2:0) or longer chains, such as stearic (C18:0) or oleic (C18:1). For example, there are solid-liquid phase diagrams for stearic acid and MEA or DEA, yet none available for shorter chains lengths such as laurate (C12:0) (91). As ethanolamine soaps are not commercially available, they have been synthesised for study. There are a several synthesis methods that have been described in literature which can

be separated into two categories; direct mixing or solution synthesis. In the direct mixing technique, the fatty acid and the alkanolamine are simply mixed together in a vessel. For short acid chains lengths that are ambient at room temperature, the acid is added dropwise into the alkanolamine (94). For longer fatty acids, which are solid at ambient temperature, the acid is heated until molten and the neutralising base (MEA/DEA/TEA etc) is then added. The mixture is then heated until an isotropic liquid is formed and then allowed to cool. In the solution technique, the fatty acid and the neutralising base are mixed in a solvent, such as ethanol, and heated until an isotropic solution is formed.

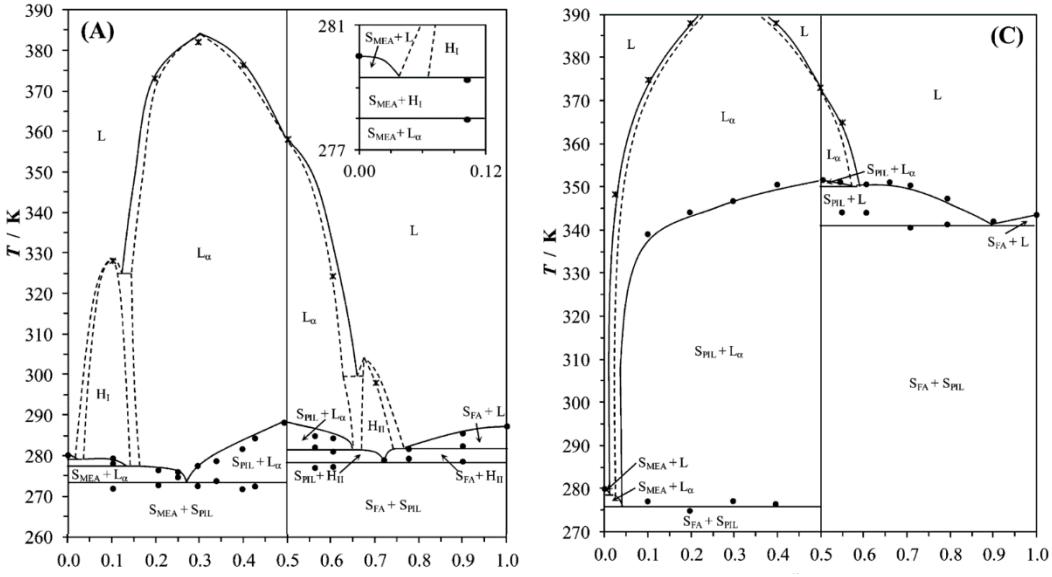

Figure 3.7: Solid-liquid phase diagrams for ethanolamine - oleic acid and ethanolamine - stearic acid, where: L – isotropic liquid, S_{PIL} – solid protic ionic liquid (MEA carboxylate), S_{FA} – solid fatty acid, S_{MEA} – solid ethanolamine, L_α – lamellar liquid crystal, H_I – hexagonal liquid crystal

The solid-liquid phase diagrams of MEA – stearic acid and MEA – oleic acid show that upon heating the MEA carboxylate (equimolar mix of MEA and fatty acid) transitions from a crystalline solid to a lamellar liquid crystal state before melting to an isotropic liquid (91). Similar behaviour is also observed for DEA carboxylates in the phase diagrams of DEA – stearic acid and DEA – oleic acid and for TEA carboxylates in the phase diagram of TEA stearate – stearic acid (87, 91, 99).

MEA stearate and DEA stearate have also been characterised by DSC, reporting their melting temperatures, and together with the data from the available phase diagrams the effect of counter-ion on the melting point of stearic and oleic acid based soaps is given by Figure 3.8 (87, 91, 92, 99, 100).

The literature data suggests that for stearate increasing the counter-ion size from MEA to TEA, decreases the temperature of transition to lamellar liquid crystal of the soap, likely due to the increased bulk of the counter-ion disrupting the packing of the crystal structure. The opposite trend is apparent for oleate, where the packing of the crystal is already disrupted due to the unsaturation in the alkyl chain. For both stearate and oleate, DEA offers the lowest transition temperature – a possible explanation for this is that whilst TEA is bulkier, there is some favourable inter-molecular interaction that is absent for DEA. The trends for melt of the liquid crystal phase to an isotropic liquid are almost a mirror image of the transition to liquid crystal trends. It appears that for the soap that is more stable in the crystal phase (higher melting point), the corresponding liquid crystal phase is less stable (lower melting point).

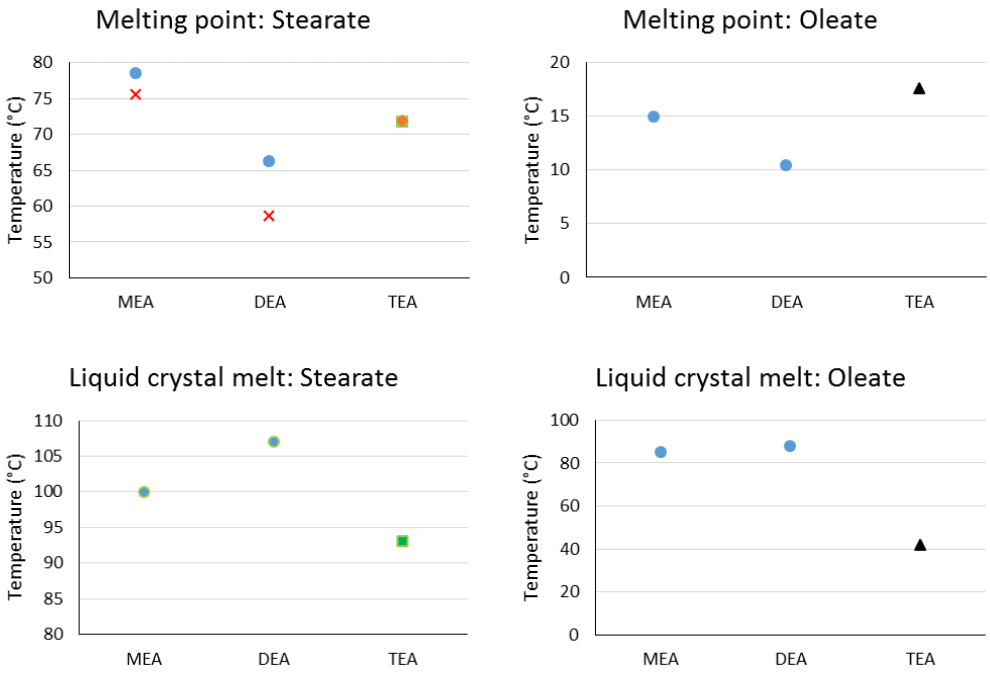

Figure 3.8: Melting points (transition to liquid crystal) and melt of the liquid crystal to isotropic melt for MEA/DEA/TEA stearate and oleate. Data from: ■ - ref. 87, ● - ref. 91, × - ref. 92, ◆ - ref. 99, ▲ - ref. 100. Note: For stearate melting point with TEA counterion, data points from ref. 87 and 99 are overlapped.

Whilst the phase diagrams of MEA and DEA stearic acid, shown in Figure 3.7, cover the full concentration range, there was limited or no attempt to determine the crystal structure and composition of the components that crystallised from the melt. This was due to the experimental techniques used to construct the phase diagram – DSC and polarised optical microscopy – which means that potentially acid-soap phases in the system have been

missed. This is not the case for the TEA – stearic acid system, which has been studied in more detail for the 0.5 – 1 mol fraction of stearic acid region – effectively the soap – acid system TEA stearate – stearic acid (87, 99). As Figure 3.9 shows, the same general features are present as in the equivalent region (0.5 – 1.0) in the MEA and DEA stearic acid phase diagrams. However, the use of FTIR and SAXS/WAXS in determining the diagram revealed the formation of acid-soap co-crystals rather than a mixture of soap and fatty acid as suggested by Figure 3.7 (87, 99).

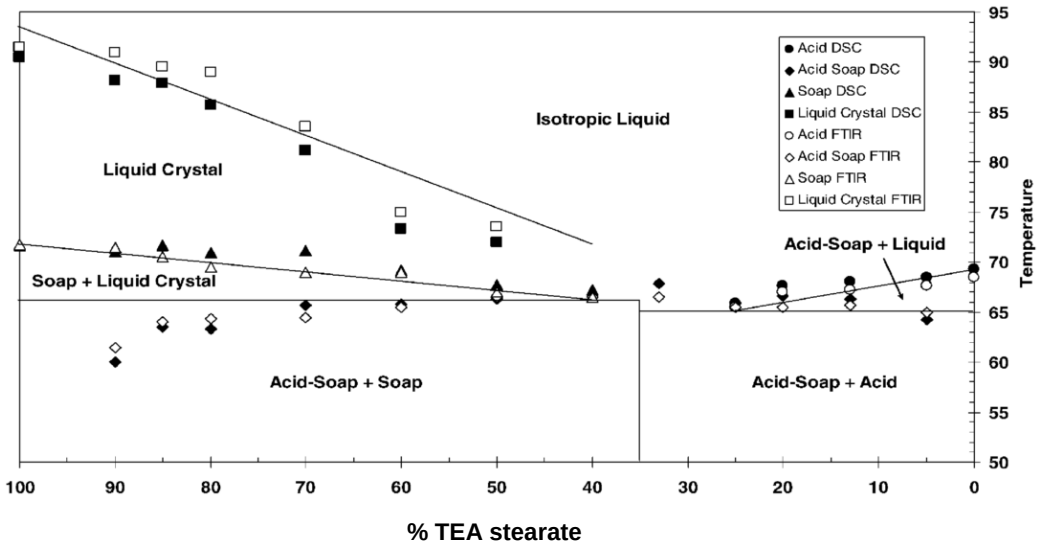

Figure 3.9: TEA stearate - stearic acid phase diagram (99)

Whilst TEA stearate has received a relatively detailed FTIR study, investigating the changes in spectra as stearic acid is neutralised by TEA with a comprehensive band assignment, the FTIR spectra of MEA stearate, DEA stearate, and several shorter chain DEA carboxylates have been reported with only limited band assignment (88, 92, 99, 101). The ^{1}H NMR for MEA stearate, DEA stearate, and for DEA acetate, propionate, and butyric have also been reported (92, 101). These FTIR and NMR measurements had an emphasis on proving synthesis rather than more detailed study about the structure.

Crystal structures have determined for a small number of alkanolammonium carboxylates, mainly with short chain carboxylates. There are some longer chain structures in literature, such as ethanandiamine or propanediamine salts of stearic acid (102). A number of the crystal structures determined have consisted of ethanolammonium with a similarly sized hydrogen bonding molecule such as succinate, acetate, or oxalate (103-105). Crystal structures of TEA salts of short chain dicarboxylic acids (oxalic, malonic, succinic) have also been reported (95). The crystal structure of ethanolammonium acetate has been determined alongside a number of closely related compounds such

as cholinium acetate, hydroxylammonium acete, and ethylammonium acetate where all structures formed were anhydrous 1:1 salts (103). The packing in ethanolammonium acetate is dominated by hydrogen bonding which leads to the formation of densely hydrogen bonded sheets. These sheets are linked through a single N-H group that is not involved in the interactions with the sheet. For the case of MEA with succinic acid, a co-crystal has been reported consisting of 2 monoethanolammonium cations, 1 succinate anion, and 1 succinic acid molecule. The succinate and succinic acid molecules form a chain linked through O-H…O hydrogen bonds with the MEA cations connected through O-H..O and N-H…O hydrogen bonds (105).

3.4.2 Solution phase behaviour

There is relatively little information in literature regarding the phase behaviour of ethanolamine soaps. For MEA soaps, partial phase diagrams for caprate (C8:0), laurate (C12:0), oleate (C18:1), and erucate (C22:1) in aqueous solution have been reported and are shown in Figure 3.10 (97, 106). They phase diagrams show that MEA soaps form micellar solutions (***L***) at low concentrations before forming liquid crystal phases such as hexagonal (***E***) or lamellar (***D***) phases. The phase behaviour of MEA soaps shows a strong dependence on the alkyl chain length, as increasing the chain length increases the extent of the liquid crystal regions and influences the type of liquid crystal phases present. This is in contrast to the phase behaviour of sodium soaps, which showed no significant change in aggregation behaviour with chain length. For sodium soaps, increasing chain length increased the concentration range for liquid crystals and increased the transition temperatures but still retained the general phase diagram features – a micellar solution at low concentrations followed by hexagonal and then lamellar liquid crystal phases as concentration increases.

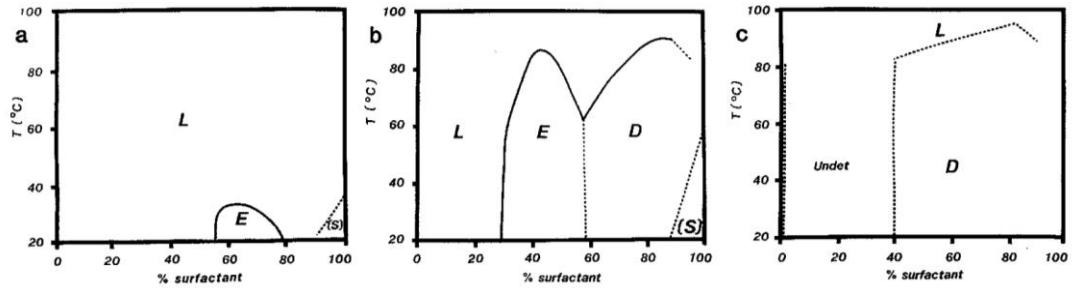

Figure 3.10: Partial phase diagrams for MEA soaps in water: a) MEA caprate, b) MEA laurate, c) MEA oleate. *L* – micellar solution, *E* – hexagonal liquid crystal, *D* – lamellar liquid crystal, *S* – solid MEA soap (106).

The critical micelle concentration of several MEA soaps in aqueous solution have been determined by a number of workers using techniques such as conductivity and surface tension measurements and are summarised in Table 3.1. The determined cmcs are much lower than those reported for sodium soaps due to the MEA ion being less hydrated that the sodium ion, leading to better shielding of the carboxylate charge. The electrostatic repulsion between the headgroups is therefore reduced, allowing aggregation into micelles (107). It should be noted that there is some variation in the reported values of the cmc for MEA soaps, but the discrepancy could be due to the weak minimum in the surface tension that was reported (106).

Table 3.1: The critical micelle concentrations for aqueous solution of MEA soaps and sodium soaps at 298 K. Multiple values of the cmc are reported from the same reference due to different experimental techniques being used e.g conductivity and surface tension.

Chain length	MEA soap	Ref.	Sodium soap	Ref.
C8	48.0, 46.0 80	(107) (106)	350	(97)
C10	26.4, 38.2	(107)		
C12	10.2, 11.5 8	(107) (106)	24.4	(106)
C14	1.8, 1.9	(107)	6.9	(108)
C16	0.6, 1.0	(107)	3.3	(108)
C18	0.16	(91)	1.8	(108)
C18:1	0.16	(91)	2.1	(108)

For TEA soaps in aqueous solution, partial phase diagrams are available for more alkyl chain lengths (97, 106, 109). The partial phase diagrams are present for TEA caprate (C8:0), laurate (C12:0), myristate (C14:0), palmitate (C16:0), stearate (C18:0), eicosanoate (C20:0), oleate (C18:1), and erucate (C22:1). Similar to MEA soap phase behaviour, TEA soaps shows a dependence on the alkyl chain length, with large qualitative differences between C8:0 and C12:0 chain. For C8:0 there are only micellar solutions and no liquid crystal phases (within the range studied) whilst for C12:0 there are micellar solutions at low concentration with hexagonal and lamellar liquid crystal at higher concentrations. The phase behaviour dependence on the alkyl chain is less strong as the chain length increases beyond C12:0, with only increased temperature stability and extent of liquid crystal regions for

longer chain lengths (97). However, adding unsaturation into the alkyl chain, still has a significant influence on the phase behaviour, behaving as if it were a shorter chain. As can be seen from Figure 3.10 and Figure 3.11 TEA inhibits liquid crystal formation compared to MEA, reducing the extent of liquid crystal regions, most likely due to the increase in counter-ion size.

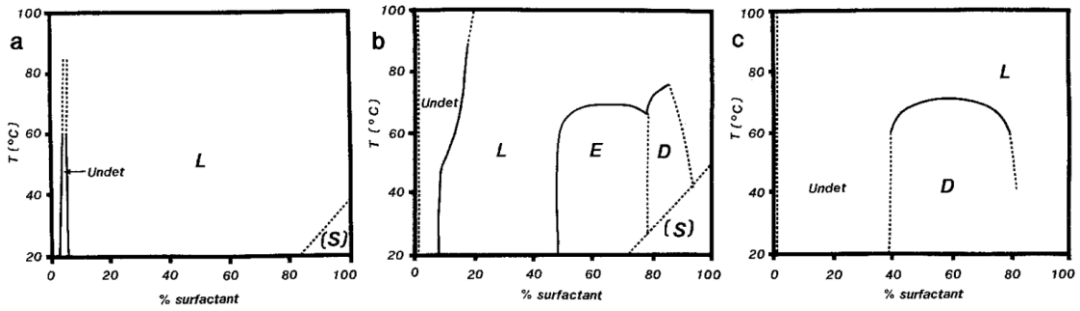

Figure 3.11: Partial phase diagrams for TEA soaps in water: a) TEA caprate (C8:0), b) TEA laurate (C12:0), c) TEA oleate (C18:1) (106).

The aqueous phase diagrams of MEA and TEA soaps feature regions that are multi-phase and have a miscibility gap (labelled ***Undet***). These behaviours are the result of incomplete neutralisation of the fatty acid resulting in free fatty acid in solution which can crystallise out due to the limited solubility of long chain fatty acids in water. Incomplete neutralisation of the acid occurs as ethanolamines are weak bases, with a pKa of 8 for TEA and 9.5 for MEA, whilst long chain fatty acids are weak acids that get weaker with increasing chain length. The net result is undissociated fatty acid and ethanolamine in the solutions, causing the miscibility gap (97). More recent research on TEA stearate is in agreement, suggesting the miscibility gap is due to the hydrolysis of the TEA soaps, the reverse of the neutralisation reaction, resulting in the formation of fatty acid crystals and TEA aqueous solution (98).

Outside of aqueous systems, there has been little study on the phase behaviour of MEA or TEA soaps. The phase behaviour of mixtures of different chain lengths of MEA or TEA soaps has not been studied in literature. However, the critical micelle concentration has been determined for various amine soaps of palm oil and coconut oil, including MEA, DEA, and TEA soaps (110, 111). There is a small amount in literature regarding the phase behaviour of TEA oleate in solvent systems such as *p*-xylene (112), and water/lipids and water/triglcyceride skin softener (113). TEA oleate has been reported to form a liquid crystal phase at room temperature by itself due to incomplete deprotonation of the oleic acid, resulting in a TEA oleate liquid crystal phase with oleic acid and triethanolamine acting as solvents (114).

There has also been a study on the aqueous phase behaviour MEA and TEA soap based anionic dimeric surfactants. The dimeric MEA soap and TEA soaps were found to have very low Krafft points, below 0 °C, and formed liquid crystals at lower soap concentrations compared to their monomeric equivalent soap, MEA and TEA laurate. Similar to the behaviour of single chain MEA and TEA soaps, dimeric TEA soaps require higher soap concentrations for liquid crystal formation than dimeric MEA soaps (115).

3.4.3 Related amine compounds

There has been some study in literature on soaps with similar organic counterions to ethanolamine.

There have been a number of papers on the phase behaviour of choline (trimethylethanolammonium) soaps (116-119). The phase diagrams for choline carboxylates (C12:0 – C18:0) have been reported and show similar behaviour to sodium carboxylates. However, the progression of liquid crystal phases are different, typically: micellar – discontinuous cubic (2 types) – hexagonal – bicontinuous cubic – lamellar. The phase diagrams for longer chain lengths showed increased dissolution temperature with decreasing concentration in the dilute region due to hydrolysis of the fatty acids, similar to that for some sodium soaps. The lowering of dissolution temperatures and change in liquid crystal formation/progression was stated to be due to the bulky, dissociated choline ion compared to a sodium ion (118). The reported cmc values for choline soaps are similar to their sodium soap equivalents, but the Krafft temperatures for choline soaps are much lower – the Krafft temperature of sodium palmitates is 60 °C whilst its choline equivalent is at 12 °C (116). A study into the effect of increasing the molar ratio of choline hydroxide to fatty acid on the dissolution temperature has also been reported, which indicated that an excess of choline hydroxide can result in a pronounced reduction in the dissolution temperature (117).

The addition of choline has been shown to promote micelle growth for sodium erucate solutions, promoting the formation of wormlike micelles. The mechanism for this was assigned to enhanced electrostatic effects as the –OH group can hydrogen bond to the carboxylate in addition to the electrostatic attraction of the ammonium group, resulting in compact contact and improved screening (120).

3.5 Summary

This chapter has reviewed the literature surrounding some of the least soluble components in a typical liquid cleaning product formulation – soaps, the salts of long chain fatty acids. As section 3.3 has shown, sodium soaps have received extensive attention over the last 80 years, covering both their aqueous and solid state phase behaviours. In addition, their crystallisation behaviour and their ability to form acid-soap co-crystals have been particularly well studied. The key drivers for their research has been their widespread use in both liquid formulations and solid soap bars, which has necessitated a more complete understanding of both solution and solid phase behaviours.

In contrast, MEA carboxylates have seen far less interest in literature despite their widespread use in liquid cleaning products. As sections 3.4.1 and 3.4.2 have shown, literature has tended to focus on aqueous phase behaviour with characterisation of their solid state limited to proof of synthesis (with the exception of TEA stearate). The lack of solid state characterisation or crystallisation behaviour can be explained based on the lack of industrial drive; MEA carboxylates are typically used in liquid formulations rather than in solid soap products, and thus the properties of interest were the solution phase behaviours. However, with recent industrial drives to increase the concentration of liquid cleaning detergents for sustainability reasons and to move towards ‘global’ formulations, the risk of crystallisation occurring after manufacture has increased. This now necessitates a better understanding of the crystallisation behaviour (and by extension the solid state) to enable improvements in product formulation and crystallisation stability testing. For example, determining the metastable zone width would give an indication of how easily the system would crystallise and would help assess formulation stabilities. Similarly, screening for polymorphism or co-crystal (acid-soap) formation would be useful as these may form after the initial dissolution of the input soap and re-crystallise out of solution due to their lower solubility. This would help assess the risk of more stable materials forming over the long time-scales that the liquid cleaning products are expected to be stable over.

This thesis aims to address this lack of understanding regarding the crystallisation behaviour of MEA soaps, through a range of *in-situ* and *ex-situ* characterisation techniques, including: characterisation of their solid state, their ability to form acid-soaps, and their crystallisation behaviour from aqueous solution. This research will enable improvements in product formulation and crystallisation stability testing methodologies.

3.6 References

1. SUMMERTON, E., G. ZIMBITAS, M. BRITTON and S. BAKALIS. Low temperature stability of surfactant systems. *Trends in Food Science & Technology*, 2017, **60**, pp.23-30.
2. ZHANG, N., A.V. NGUYEN and C. ZHOU. A review of the surface features and properties, surfactant adsorption and floatability of four key minerals of diasporic bauxite resources. *Adv Colloid Interface Sci*, 2018, **254**, pp.56-75.
3. RAFFA, P., A.A. BROEKHUIS and F. PICCHIONI. Polymeric surfactants for enhanced oil recovery: A review. *Journal of Petroleum Science and Engineering*, 2016, **145**, pp.723-733.
4. OLAJIRE, A.A. Review of ASP EOR (alkaline surfactant polymer enhanced oil recovery) technology in the petroleum industry: Prospects and challenges. *Energy*, 2014, **77**, pp.963-982.
5. WANG, G.D., F.P. MALLET, F. RICARD and J.Y.Y. HENG. Pharmaceutical nanocrystals. *Current Opinion in Chemical Engineering*, 2012, **1**(2), pp.102-107.
6. WOLF, R., D. WOLF, B. TÜZÜN and Y. TÜZÜN. Soaps, shampoos, and detergents. *Clinics in Dermatology*, 2001, **19**(4), pp.393-397.
7. CARROLL, B.J. Physical aspects of detergency. *Colloids and Surfaces A: Physicochemical and Engineering Aspects*, 1993, **74**(2-3), pp.131-167.
8. DI MICHELE, A., L. BRINCHI, P. DI PROFIO, R. GERMANI, G. SAVELLI and G. ONORI. Effect of head group size, temperature and counterion specificity on cationic micelles. *J Colloid Interface Sci*, 2011, **358**(1), pp.160-6.
9. KOSSWIG, K. Surfactants. *In: Ullmann's Encyclopedia of Industrial Chemistry*. Wiley, 2000.
10. ROSEN, M.J. and J.T. KUNJAPPU. *Surfactants and Interfacial Phenomena.* 4th ed. John Wiley & Sons, 2012.
11. MA, J.G., B.J. BOYD and C.J. DRUMMOND. Positional isomers of linear sodium dodecyl benzene sulfonate: solubility, self-assembly, and air/water interfacial activity. *Langmuir*, 2006, **22**(21), pp.8646-54.
12. ANTUNES, F.E., L. COPPOLA, D. GAUDIO, I. NICOTERA and C. OLIVIERO. Shear rheology and phase behaviour of sodium oleate/water mixtures. *Colloids and Surfaces A: Physicochemical and Engineering Aspects*, 2007, **297**(1-3), pp.95-104.
13. MCBAIN, J.W., R.D. VOLD and M. FRICK. A phase rule study of the system sodium stearate-water. *Journal of Physical Chemistry*, 1940, **44**(9), pp.1013-1024.
14. BERGSTROM, M.L. Thermodynamics of Self-Assembly. *In:* M. TADASHI, ed. *Application of Thermodynamics to Biological and Materials Science*. InTech, 2011.
15. BERGSTROM, L.M. Explaining the growth behavior of surfactant micelles. *J Colloid Interface Sci*, 2015, **440**, pp.109-18.
16. PAULA, S., W. SUES, J. TUCHTENHAGEN and A. BLUME. Thermodynamics of Micelle Formation as a Function of Temperature: A High Sensitivity Titration Calorimetry Study. *The Journal of Physical Chemistry*, 1995, **99**(30), pp.11742-11751.

17. ISRAELACHVILI, J.N., D.J. MITCHELL and B.W. NINHAM. Theory of self-assembly of hydrocarbon amphiphiles into micelles and bilayers. *Journal of the Chemical Society, Faraday Transactions 2*, 1976, **72**, p.1525.
18. ANACHKOV, S.E., P.A. KRALCHEVSKY, K.D. DANOV, G.S. GEORGIEVA and K.P. ANANTHAPADMANABHAN. Disclike vs. cylindrical micelles: generalized model of micelle growth and data interpretation. *J Colloid Interface Sci*, 2014, **416**, pp.258-73.
19. DREISS, C.C.A. Wormlike micelles: where do we stand? Recent developments, linear rheology and scattering techniques. *Soft Matter*, 2007, **3**(8), p.956.
20. ANIANSSON, E.A.G. and S.N. WALL. Kinetics of step-wise micelle association. *The Journal of Physical Chemistry*, 1974, **78**(10), pp.1024-1030.
21. LUND, R., L. WILLNER, M. MONKENBUSCH, P. PANINE, T. NARAYANAN, J. COLMENERO and D. RICHTER. Structural Observation and Kinetic Pathway in the Formation of Polymeric Micelles. *Physical Review Letters*, 2009, **102**(18).
22. JENSEN, G.V., R. LUND, J. GUMMEL, M. MONKENBUSCH, T. NARAYANAN and J.S. PEDERSEN. Direct observation of the formation of surfactant micelles under nonisothermal conditions by synchrotron SAXS. *Journal of the American Chemical Society*, 2013, **135**(19), pp.7214-22.
23. JENSEN, G.V., R. LUND, T. NARAYANAN and J.S. PEDERSEN. Transformation from Globular to Cylindrical Mixed Micelles through Molecular Exchange that Induces Micelle Fusion. *J Phys Chem Lett*, 2016, **7**(11), pp.2039-43.
24. RHARBI, Y., M. KARROUCH and P. RICHARDSON. Fusion and fission inhibited by the same mechanism in electrostatically charged surfactant micelles. *Langmuir*, 2014, **30**(27), pp.7947-52.
25. NARAYANAN, T., H. WACKLIN, O. KONOVALOV and R. LUND. Recent applications of synchrotron radiation and neutrons in the study of soft matter. *Crystallography Reviews*, 2017, **23**(3), pp.160-226.
26. SALKAR, R.A., D. MUKESH, S.D. SAMANT and C. MANOHAR. Mechanism of Micelle to Vesicle Transition in Cationic−Anionic Surfactant Mixtures. *Langmuir*, 1998, **14**(14), pp.3778-3782.
27. ZACKRISSON OSKOLKOVA, M., E. NORRMAN and U. OLSSON. Study of the micelle-to-vesicle transition and smallest possible vesicle size by temperature-jumps. *J Colloid Interface Sci*, 2013, **396**, pp.173-7.
28. FARQUHAR, K.D., M. MISRAN, B.H. ROBINSON, D.C. STEYTLER, P. MORINI, P.R. GARRETT and J.F. HOLZWARTH. The kinetics and mechanism of micelle-vesicle transitions in aqueous solution. *Journal of Physics: Condensed Matter*, 1996, **8**(47), pp.9397-9404.
29. BRINKMANN, U., E. NEUMANN and B.H. ROBINSON. Thermodynamics and kinetics of vesicle↔mixed micelle transitions of sodium tridecyl-6-benzene sulfonate/sodium dodecyl sulfate surfactant systems. *Journal of the Chemical Society, Faraday Transactions*, 1998, **94**(9), pp.1281-1285.

30. GRADZIELSKI, M. Kinetics of morphological changes in surfactant systems. *Current Opinion in Colloid & Interface Science*, 2003, **8**(4-5), pp.337-345.
31. SEGOTA, S. and D. TEZAK. Spontaneous formation of vesicles. *Adv Colloid Interface Sci*, 2006, **121**(1-3), pp.51-75.
32. GUIDA, V. Thermodynamics and kinetics of vesicles formation processes. *Adv Colloid Interface Sci*, 2010, **161**(1-2), pp.77-88.
33. TSCHIERSKE, C. Molecular self-organization of amphotropic liquid crystals. *Progress in Polymer Science*, 1996, **21**(5), pp.775-852.
34. BLUNK, D., P. BIERGANNS, N. BONGARTZ, R. TESSENDORF and C. STUBENRAUCH. New speciality surfactants with natural structural motifs. *New Journal of Chemistry*, 2006, **30**(12), p.1705.
35. LATYPOVA, L., W.T. GOZDZ and P. PIERANSKI. Facets of lyotropic liquid crystals. *Langmuir*, 2014, **30**(2), pp.488-95.
36. TIDDY, G. Surfactant-water liquid crystal phases. *Physics Reports*, 1980, **57**(1), pp.1-46.
37. SCAMEHORN, J.F. Precipitation of Mixtures of Anionic Surfactants. *In:* P.M. HOLLAND and D.N. RUBINGH, eds. *Mixed Surfactant Systems*. 1992, pp.392-401.
38. LIANG, J.M., Y. MA, Y. ZHENG, H.T. DAVIS, H.T. CHANG, D. BINDER, S. ABBAS and F.L. HSU. Solvent-induced crystal morphology transformation in a ternary soap system: Sodium stearate crystalline fibers and platelets. *Langmuir*, 2001, **17**(21), pp.6447-6454.
39. MCBAIN, J.W. and S.A. JOHNSTON. A Note on the Phase Rule Diagram for a Mixture of Sodium Palmitate and Sodium Laurate with Water. *Journal of the American Chemical Society*, 1941, **63**(3), pp.875-875.
40. MCBAIN, J.W., M.J. VOLD and J.L. PORTER. A phase study of commercial soap and water. *Industrial and Engineering Chemistry*, 1941, **33**, pp.1049-1055.
41. MADELMONT, C. and K. PERRON. Study of the influence of the chain length on some aspects of soap/water diagrams. *Colloid and Polymer Science*, 1976, **254**(6), pp.581-595.
42. VOLD, R.D., R. REIVERE and J.W. MCBAIN. A Phase Rule Study of the System Sodium Myristate-Water. *Journal of the American Chemical Society*, 1941, **63**(5), pp.1293-1296.
43. VOLD, R.D. The phase rule behavior of concentrated aqueous systems of a typical colloidal electrolyte. Sodium oleate. *Journal of Physical Chemistry*, 1939, **43**(9), pp.1213-1231.
44. VOLD, R.D. Phase Boundaries in Concentrated Systems of Sodium Oleate and Water. *J Phys Colloid Chem*, 1947, **51**(3), pp.797-816.
45. FLOCKHART, B.D. and H. GRAHAM. Study of dilute aqueous solutions of sodium oleate. *Journal of Colloid Science*, 1953, **8**(1), pp.105-115.
46. MONGONDRY, P., C.W. MACOSKO and T. MOADDEL. Rheology of highly concentrated anionic surfactants. *Rheologica Acta*, 2006, **45**(6), pp.891-898.
47. DE MUL, M.N.G., H.T. DAVIS, D.F. EVANS, A.V. BHAVE and J.R. WAGNER. Solution Phase Behavior and Solid Phase Structure of Long-Chain Sodium Soap Mixtures. *Langmuir*, 2000, **16**(22), pp.8276-8284.

48. VAN GELDER, R.N.M.R., K.J. ROBERTS, J. CHAMBERS and T. INSTONE. Nucleation of single and mixed straight chain surfactants from dilute aqueous solutions. *J Cryst Growth*, 1996, **166**(1-4), pp.189-194.
49. PRASAD, M., G.S. HATTIANGDI and B.K. WAGLE. Behavior of some alkali soap systems in organic solvents. *Journal of Colloid Science*, 1947, **2**(5), pp.467-477.
50. VOLD, R.D., C.W. LEGGETT and J.W. MCBAIN. Systems of Sodium Palmitate in Organic Liquids. *The Journal of Physical Chemistry*, 1940, **44**(9), pp.1058-1071.
51. LEGGETT, C.W., R.D. VOID and J.W. MCBAIN. The Solubility of Sodium Palmitate in Organic Liquids. *The Journal of Physical Chemistry*, 1942, **46**(3), pp.429-440.
52. STUART, M.C.A., J.C. VAN DE PAS and J.B.F.N. ENGBERTS. Phase behavior of laundry surfactants in polar solvents. *Journal of Surfactants and Detergents*, 2006, **9**(2), pp.153-160.
53. SMITH, G.H. and J.W. MCBAIN. The phase behavior of sodium stearate in anhydrous organic solvents. *J Phys Colloid Chem*, 1947, **51**(5), pp.1189-1204.
54. VOLD, R.D. and J.M. PHILIPSON. The Behavior of Sodium Stearate with Cetane and Water. *The Journal of Physical Chemistry*, 1946, **50**(1), pp.39-53.
55. SMITH, L.A., A. DUNCAN, G.B. THOMSON, K.J. ROBERTS, D. MACHIN and G. MCLEOD. Crystallisation of sodium dodecyl sulphate from aqueous solution: phase identification, crystal morphology, surface chemistry and kinetic interface roughening. *J Cryst Growth*, 2004, **263**(1-4), pp.480-490.
56. DE BRETTEVILLE, A. and F.V. RYER. A Method of Growing Single Crystals of Sodium Stearate and Sodium Palmitate. *The Journal of Physical Chemistry*, 1944, **48**(3), pp.154-158.
57. BINNEMANS, K. Ionic liquid crystals. *Chem Rev*, 2005, **105**(11), pp.4148-204.
58. MARTON, L., J.W. MCBAIN and R.D. VOLD. An Electron Microscope Study of Curd Fibers of Sodium Laurate. *Journal of the American Chemical Society*, 1941, **63**(7), pp.1990-1993.
59. RAPISARD, A.A. and J.E. BUJAKE. Electron Microscopy of Some Sodium Soaps. *J Colloid Interface Sci*, 1968, **27**(2), pp.239-246.
60. MCBAIN, J.W., A. DE BRETTEVILLE and S. ROSS. Diffraction of X-Rays by Sodium Stearate at Room Temperature. *The Journal of Chemical Physics*, 1943, **11**(4), p.179.
61. MCBAIN, J.W., O.E.A. BOLDUAN and S. ROSS. X-Ray Diffraction of Sodium Laurate, Palmitate and Stearate at Room Temperature. *Journal of the American Chemical Society*, 1943, **65**(10), pp.1873-1876.
62. FERGUSON, R.H., F.B. ROSEVEAR and H. NORDSIECK. The Phase Nature of Beta Sodium Palmitate. *Journal of the American Chemical Society*, 1947, **69**(1), pp.141-146.
63. BOLDUAN, O.E.A., J.W. MCBAIN and S. ROSS. Diffraction of X-rays by Sodium Laurate and Sodium Palmitate at Higher Temperatures. *The Journal of Physical Chemistry*, 1943, **47**(7), pp.528-535.

64. FERGUSON, R.H., F.B. ROSEVEAR and R.C. STILLMAN. Solid Soap Phases. *Industrial and Engineering Chemistry*, 1943, **35**, pp.1005-1012.
65. FERGUSON, R.H. The four known crystalline forms of soap. *Oil & Soap*, 1944, **21**(1), pp.6-9.
66. BUERGER, M.J., L.B. SMITH, F.V. RYER and J.E. SPIKE. The Crystalline Phases of Soap. *Proc Natl Acad Sci U S A*, 1945, **31**(8), pp.226-33.
67. ZHU, S., J.G. CHAMBERS and V. NAIK. Soap. *In: Kirk-Othmer Encyclopedia of Chemical Technology*. John Wiley & Sons, 2006.
68. STUART, M.C., J. VAN ESCH, J.C. VAN DE PAS and J.B. ENGBERTS. Chain-length and solvent dependent morphological changes in sodium soap fibers. *Langmuir*, 2007, **23**(12), pp.6494-7.
69. NELSON, P.N., H.A. ELLIS and N.A. WHITE. Solid state (1)(3)C-NMR, infrared, X-ray powder diffraction and differential thermal studies of the homologous series of some mono-valent metal (Li, Na, K, Ag) n-alkanoates: a comparative study. *Spectrochim Acta A Mol Biomol Spectrosc*, 2015, **145**, pp.440-53.
70. NELSON, P.N. and R.A. TAYLOR. Powder X-ray diffraction, infrared and (13)C NMR spectroscopic studies of the homologous series of some solid-state zinc(II) and sodium(I) n-alkanoates. *Spectrochim Acta A Mol Biomol Spectrosc*, 2015, **138**, pp.800-6.
71. LYNCH, M.L. Acid-soaps. *Current Opinion in Colloid & Interface Science*, 1997, **2**(5), pp.495-500.
72. KRALCHEVSKY, P.A., K.D. DANOV, C.I. PISHMANOVA, S.D. KRALCHEVSKA, N.C. CHRISTOV, K.P. ANANTHAPADMANABHAN and A. LIPS. Effect of the precipitation of neutral-soap, acid-soap, and alkanoic acid crystallites on the bulk pH and surface tension of soap solutions. *Langmuir*, 2007, **23**(7), pp.3538-53.
73. LYNCH, M.L., Y. PAN and R.G. LAUGHLIN. Spectroscopic and thermal characterization of 1:2 sodium soap fatty acid acid-soap crystals. *Journal of Physical Chemistry*, 1996, **100**(1), pp.357-361.
74. MCBAIN, J.W. and M.C. FIELD. Phase Rule Equilibria of Acid Soaps. I. Anhydrous Acid Potassium Laurate. *The Journal of Physical Chemistry*, 1932, **37**(6), pp.675-684.
75. GODDARD, E.D., S. GOLDWASSER, G. GOLIKERI and H.C. KUNG. Molecular Association in Fatty Acid-Potassium Soap Systems. 1968, **84**, pp.67-77.
76. MCBAIN, J.W. and M.C. FIELD. 216. Phase-rule equilibria of acid soaps. Part II. Anhydrous acid sodium palmitates. *Journal of the Chemical Society (Resumed)*, 1933, p.920.
77. TANDON, P., S. RAUDENKOLB, R.H. NEUBERT, W. RETTIG and S. WARTEWIG. X-ray diffraction and spectroscopic studies of oleic acid-sodium oleate. *Chem Phys Lipids*, 2001, **109**(1), pp.37-45.
78. MANTSCH, H.H., S.F. WENG, P.W. YANG and H.H. EYSEL. Structure and thermotropic phase behavior of sodium and potassium carboxylate ionomers. *Journal of Molecular Structure*, 1994, **324**(1-2), pp.133-141.
79. HADŽI, D., J. GRDADOLNIK and A. MEDEN. Infrared spectra of, and hydrogen bonding in acid palmitates. *Journal of Molecular Structure*, 1996, **381**(1-3), pp.9-14.

80. LYNCH, M.L., F. WIREKO, M. TAREK and M. KLEIN. Intermolecular Interactions and the Structure of Fatty Acid−Soap Crystals. *The Journal of Physical Chemistry B*, 2001, **105**(2), pp.552-561.
81. WEN, X. and E.I. FRANSES. Effect of Protonation on the Solution and Phase Behavior of Aqueous Sodium Myristate. *J Colloid Interface Sci*, 2000, **231**(1), pp.42-51.
82. DUMBLETON, J.H. The unit-cell dimensions of potassium myristate and 1:1 acid potassium myristate. *Acta Crystallographica*, 1965, **19**(2), pp.279-280.
83. ANANTHAPADMANABHAN, K.P. and P. SOMASUNDARAN. Acid-Soap Formation in Aqueous Oleate Solutions. *J Colloid Interface Sci*, 1988, **122**(1), pp.104-109.
84. CISTOLA, D.P., D. ATKINSON, J.A. HAMILTON and D.M. SMALL. Phase behavior and bilayer properties of fatty acids: hydrated 1:1 acid-soaps. *Biochemistry*, 1986, **25**(10), pp.2804-2812.
85. FRAUENKRON, M., J.-P. MELDER, G. RUIDER, R. ROSSBACHER and H. HÖKE. Ethanolamines and Propanolamines. *In: Ullmann's Encylcopedia of Industrial Chemistry*. Wiley, 2001.
86. KOGANEI, R. On fatty acids obtained from cephalin. Compounds of β-aminoethyl alcohol with saturated and unsaturated fatty acids. *Journal of Biochemistry*, 1923.
87. ZHU, S., M. HEPPENSTALL-BUTLER, M.F. BUTLER, P.D. PUDNEY, D. FERDINANDO and K.J. MUTCH. Acid soap and phase behavior of stearic acid and triethanolamine stearate. *J Phys Chem B*, 2005, **109**(23), pp.11753-61.
88. ÁLVAREZ, V.H., S. MATTEDI, M. MARTIN-PASTOR, M. AZNAR and M. IGLESIAS. Synthesis and thermophysical properties of two new protic long-chain ionic liquids with the oleate anion. *Fluid Phase Equilibria*, 2010, **299**(1), pp.42-50.
89. TRUSLER, R.B. Ethanolamine Soaps. *Industrial & Engineering Chemistry*, 1929, **21**(7), pp.685-687.
90. TRUSLER, R.B. Soaps from organic bases. *Oil & Fat Industries*, 1928, **5**(12), pp.338-347.
91. MAXIMO, G.J., R.J.B.N. SANTOS, J.A. LOPES-DA-SILVA, M.C. COSTA, A.J.A. MEIRELLES and J.A.P. COUTINHO. Lipidic Protic Ionic Liquid Crystals. *ACS Sustainable Chemistry & Engineering*, 2014, **2**(4), pp.672-682.
92. SANTOS, D., F. COSTA, E. FRANCESCHI, A. SANTOS, C. DARIVA and S. MATTEDI. Synthesis and physico-chemical properties of two protic ionic liquids based on stearate anion. *Fluid Phase Equilibria*, 2014, **376**, pp.132-140.
93. TOLEDO HIJO, A.A.C., G.J. MAXIMO, M.C. COSTA, E.A.C. BATISTA and A.J.A. MEIRELLES. Applications of Ionic Liquids in the Food and Bioproducts Industries. *ACS Sustainable Chemistry & Engineering*, 2016, **4**(10), pp.5347-5369.
94. PINKERT, A., K.N. MARSH and S. PANG. Reflections on the Solubility of Cellulose. *Industrial & Engineering Chemistry Research*, 2010, **49**(22), pp.11121-11130.
95. FUNDAMENSKY, V.S., T.A. KOCHINA, Y.A. KONDRATENKO, A.A. ZOLOTAREV, Y.G. VLASOV and I.S. IGNATYEV. Ionic liquids based on Triethanolammonium Salts of Dicarboxylic Acids (oxalic, malonic,

succinic). Crystal structure and cation-anion interaction. *Journal of Molecular Liquids*, 2017.

96. GREAVES, T.L. and C.J. DRUMMOND. Protic Ionic Liquids: Evolving Structure-Property Relationships and Expanding Applications. *Chem Rev*, 2015, **115**(20), pp.11379-448.
97. WÄRNHEIM, T. and A. JÖNSSON. Phase behavior of alkanolammonium carboxylates. 1992, **88**, pp.18-22.
98. ZHU, S., P.D. PUDNEY, M. HEPPENSTALL-BUTLER, M.F. BUTLER, D. FERDINANDO and M. KIRKLAND. Interaction of the acid soap of triethanolamine stearate and stearic acid with water. *J Phys Chem B*, 2007, **111**(5), pp.1016-24.
99. PUDNEY, P.D., K.J. MUTCH and S. ZHU. Characterising the phase behaviour of stearic acid and its triethanolamine soap and acid-soap by infrared spectroscopy. *Phys Chem Chem Phys*, 2009, **11**(25), pp.5010-8.
100. MU, L., Y. SHI, T. JI, L. CHEN, R. YUAN, H. WANG and J. ZHU. Ionic Grease Lubricants: Protic [Triethanolamine][Oleic Acid] and Aprotic [Choline][Oleic Acid]. *ACS Appl Mater Interfaces*, 2016, **8**(7), pp.4977-84.
101. SANTOS, D., É. LOURENÇO, M.F.C. SANTOS, E. FRANCESCHI, C. DARIVA, A. BARISON, A. ZUBER, M. CASTIER and S. MATTEDI. Volumetric properties of binary aqueous solutions of protic ionic liquids based on bis (2-hydroxyethyl) ammonium. *Journal of Molecular Liquids*, 2016, **222**, pp.867-872.
102. BASIT, H., A. PAL, S. SEN and S. BHATTACHARYA. Two-component hydrogels comprising fatty acids and amines: structure, properties, and application as a template for the synthesis of metal nanoparticles. *Chemistry*, 2008, **14**(21), pp.6534-45.
103. PEREIRA, J.F.B., P.S. BARBER, S.P. KELLEY, P. BERTON and R.D. ROGERS. Double salt ionic liquids based on 1-ethyl-3-methylimidazolium acetate and hydroxyl-functionalized ammonium acetates: strong effects of weak interactions. *Phys Chem Chem Phys*, 2017, **19**(39), pp.26934-26943.
104. JORDANOVSKA, V., P. NAUMOV, M.-J. KIM, H.-J. LEE and S.W. NG. Bis(2-hydroxyethylammonium) oxalate. *Acta Crystallographica Section E Structure Reports Online*, 2000, **57**(1), pp.o45-o47.
105. ZHANG, M., C. WANG and Z. FAN. Bis(ethano-laminium) succinate-succinic acid (1/1). *Acta Crystallogr Sect E Struct Rep Online*, 2011, **67**(Pt 9), p.o2504.
106. WARNHEIM, T. and A. JONSSON. Surfactant Aggregation in Systems Containing Alkanolamines and Fatty-Acids. *J Colloid Interface Sci*, 1990, **138**(2), pp.314-323.
107. BRAVO, B., G. CHAVEZ, C. GAMARRO, A. MORENO, N. MARQUEZ, N. DELGAO, A. CACERES, M. LUZARDO and I. PARRA. Physico-chemical characterisation of new amphiphilic ion pairs based on alkylcarboxyilic acids. *Biointerfce Res. Appl. Chem.*, 2015, **5**(1).
108. MUKERJEE, P. and K.J. MYSELS. *NSRDS-NBS 36: Critical Micelle Concentrations of Aqueous Surfactant Systems.* National Bureau of Standards (US), 1971.
109. JÖNSSON, A., J. BOKSTRÖM, A.-C. MALMVIK and T. WÄRNHEIM. Preparation and characterization of surface active erucic acid

derivatives. *Journal of the American Oil Chemists' Society*, 1990, **67**(11), pp.733-738.

110. RAHIMOV, R.A. and Z.H. ASADOV. Ammonium Salts of Palm Oil Fatty Acids. *Journal of Oil Palm Research*, 2013, **25**(3), pp.336-342.
111. RAHIMOV, R.A. and Z.H. ASADOV. Coconut oil fatty acid ammonium-type salts. *Journal of Molecular Liquids*, 2013, **182**, pp.70-75.
112. FRIBERG, S.E., W. CHANG SUP, B. GREENE and R. VAN GILDER. A nonaqueous foam with excellent stability. *J Colloid Interface Sci*, 1984, **101**(2), pp.593-595.
113. FRIBERG, S.E. and D.W. OSBORNE. Interaction of a model skin surface lipid with a modified triglyceride. *Journal of the American Oil Chemists' Society*, 1986, **63**(1), pp.123-126.
114. FRIBERG, S.E., P. LIANG, F.E. LOCKWOOD and M. TADROS. Single compound forming a lyotropic liquid crystal at room temperature. *The Journal of Physical Chemistry*, 1984, **88**(5), pp.1045-1046.
115. RODRIGUEZ-ABREU, C., E. RODRIGUEZ and C. SOLANS. Monomeric and dimeric anionic surfactants: A comparative study of self-aggregation and mineralization. *J Colloid Interface Sci*, 2009, **340**(2), pp.254-60.
116. KLEIN, R., D. TOURAUD and W. KUNZ. Choline carboxylate surfactants: biocompatible and highly soluble in water. *Green Chemistry*, 2008, **10**(4), p.433.
117. KLEIN, R., M. KELLERMEIER, M. DRECHSLER, D. TOURAUD and W. KUNZ. Solubilisation of stearic acid by the organic base choline hydroxide. *Colloids and Surfaces A: Physicochemical and Engineering Aspects*, 2009, **338**(1-3), pp.129-134.
118. KLEIN, R., G.J.T. TIDDY, E. MAURER, D. TOURAUD, J. ESQUENA, O. TACHE and W. KUNZ. Aqueous phase behaviour of choline carboxylate surfactants—exceptional variety and extent of cubic phases. *Soft Matter*, 2011, **7**(15), p.6973.
119. ARNOULD, A., A.A. PEREZ, C. GAILLARD, J.P. DOULIEZ, F. COUSIN, L.G. SANTIAGO, T. ZEMB, M. ANTON and A.L. FAMEAU. Self-assembly of myristic acid in the presence of choline hydroxide: effect of molar ratio and temperature. *J Colloid Interface Sci*, 2015, **445**, pp.285-93.
120. HAN, Y., Z. CHU, H. SUN, Z. LI and Y. FENG. "Green" anionic wormlike micelles induced by choline. *RSC Advances*, 2012, **2**(8), p.3396.

Chapter 4 Crystallisation characterisation techniques

The core concepts of crystal characterisation techniques

4.1 Introduction

This chapter reviews the fundamentals of the main characterisation techniques used within the experimental work of this thesis. This chapter beings with infrared and Raman spectroscopy, highlighting the different advantages of each, before moving onto differential scanning calorimetry. The chapter ends with a discussion of the theory of x-ray diffraction and small angle x-ray scattering.

4.2 Infrared spectroscopy

Infrared spectroscopy is based on the absorption of infrared radiation (IR) where the absorption of the photon of the molecule results in a transition between molecular energy levels. The absorption of IR by molecules is therefore a resonance condition where the IR radiation frequency matches the natural frequency of a mode of vibration of the molecule. In addition, IR is selective as for energy to be transferred from the photon to the molecule, the vibration must change the dipole moment of the molecule (1). IR spectroscopy is best for asymmetric, out-of-phase, and polar molecular vibrations. Modern IR spectrometers are Fourier-transform infrared spectrometers (FTIR) as they have significant advantages over dispersive instruments. In dispersive instruments energy from the IR source follows a reference and a sample path before entering a monochromator, which spatially separates the wavelengths. The radiation is directed through a slit that controls the range of frequencies reaching the detector and the spectrum is collected progressively.

In contrast, Fourier-transform infrared spectrometers make use of an interferometer and Fast Fourier Transform to collect the whole spectrum in microseconds. The interferometer consists of a beamsplitter that splits the source radiation in approximately equal intensity transmitted and reflected beams. These beams are both directed to mirrors, one fixed, one moving at a constant speed, and are reflected back to the beamsplitter where they recombine. Depending on the position of the moving mirror, the recombination will be constructive if the path difference is an integer value of the wavelength and destructive if an non-integer value. Following recombination at the beamsplitter and generating an interference pattern, the beam passes through the sample, which absorbs and transmits some of the beam, before reaching the detector (2). The detector records the total intensity, giving an interferogram which contains information about all the wavelengths being transmitted at once. The detector output is digitized and a Fast Fourier

Transform is used to process the data to give a “single beam” spectrum. A background spectrum is typically recorded and subtracted from the collected sample spectrum to give only the sample spectrum.

Whilst there are number of different techniques available for carrying out FTIR measurements, one of the most versatile and commonly used techniques is Attenuated Total Reflectance (ATR). In the ATR technique, the recombined infrared beam from the beamsplitter passes into a high refractive index crystalline material (common materials include ZnSe and diamond) where the beam is totally internally reflected. This internal reflectance creates an evanescent wave that extends to a small degree beyond the ATR crystal surface. This means that if a sample is placed in contact with the ATR crystal, the evanescent wave will penetrate the sample surface, thus obtaining an FTIR spectrum of the sample. The ATR technique can be used for both ex-situ and in-situ for a vast range of samples types (depending to a degree on the ATR crystal used) (1).

4.3 Raman spectroscopy

Raman spectroscopy is based on inelastic light scattering. When light photons are incident on a molecule, the photons are momentarily absorbed and the molecule increases in energy level from a ground state to a higher ‘virtual state’. A new photon is then created and scattered by the molecule dropping down from the higher energy ‘virtual state’. This can occur either by elastic scattering, which is most probable, or by inelastic scattering. In elastic scattering (Rayleigh scattering) the molecule drops from the ‘virtual state’ back to the original ‘ground state’ and therefore there is no energy change and thus the incident and scattered photon have the same wavelength. In contrast, in inelastic Raman scattering, the molecule drops from the ‘virtual state’ to an energy level different from its original state. As the molecule is at a different energy state to its original state, this results in the scattered photon having a different energy to that of the incident photon and thus a change in wavelength. Raman scattering can be categorised as either Stokes or anti-Stokes. Stokes scattering corresponds to molecules that begin in their ground state and end in an excited state, whilst anti-Stokes scattering is where molecules begin at an excited state and end at their ground state. At ambient temperature, most molecules are in their ground state and thus Stokes scattering is significantly more intense than anti-Stokes scattering (1). Raman spectroscopy is best for vibrations that are symmetric, in-phase, and non-polar. Raman is also better suited for aqueous samples compared to IR as the

water spectrum of Raman is far less intrusive and complicated compared to its IR spectrum.

Raman spectrometers are either interferometer-based or dispersive instruments with multi-channel detectors. The main challenge with Raman is being able to analyse the weak Raman scattering whilst reducing/eliminating the stronger Rayleigh scattered radiation. A typical Raman system consists of: a laser source and delivery optics, collection optics, a monochromator or interferometer, and a detector. There are two typical arrangements used for the collection optics, either 90° or 180° backscattering geometries using refractive and reflective optics respectively. The 180° backscattering geometry is frequently found in in-situ process probes and in Raman microscopes (1). As Raman spectroscopy only needs to be able to illuminate the sample and collected the scattered radiation, standard optical windows can be used and therefore a minimum of sample preparation is needed.

In dispersive instruments, the radiation scattered by the sample is collected and passes through a Rayleigh filter, to reduce the Rayleigh scattering reaching the detector, before entering a monochromator. The monochromator spatially separates the radiation before directing it to an array detector, such as a photodiode array or a CCD (charge coupled device) detector. In an array detector each pixel records a different band on the spectrum, although the number of pixels or elements is usually much less than the entire spectral range to be covered. This means either low resolution full spectrum measurements or a high resolution spectrum produced by scanning the spectral range in segments and combining the spectra together (1). Interferometer-based Raman spectrometers are very similar in construction to FTIR spectrometers, with only a few changes in optical components. FT-Raman spectrometers typically feature notch filters before the entrance to the interferometer to reduce the amount of Rayleigh scattering light reaching the detector. The operating principles of FT-Raman spectrometers are essentially the same as those for FTIR spectrometers except the radiation source is the radiation scattered from the sample (1).

4.4 Differential scanning calorimetry

Differential scanning calorimetry (DSC) is a common experimental technique which is used to measure the heat flows and temperatures of transitions. There are two main types of DSC instruments; power compensation and heat-flux.

In power compensation DSC, the temperature of a sample and an inert reference are kept equal as they undergo a specified temperature program or cycle. The sample and reference are heated by separate heating units and the difference in power required to maintain equal temperatures of sample and reference is measured. If thermal events occur in the sample the amount of power required by the heater to maintain the sample temperature will vary (3). For example, if an exothermic event such as crystallisation occurs, the heater will require less power to maintain the temperature whilst if an endothermic event such as dissolution occurs, the heater will require more power. In heat-flux DSC, the temperature difference between the sample and reference across a defined thermal path is used to determine the heat flows of the sample. A common type of heat-flux DSC is the disk-type DSC. Disk type DSCs are where the flow of heat from the heater in the furnace flows to the sample pans via a disk of good thermal conductivity on which the sample and reference pans are placed. As the furnace is heated, heat flows through the disk and into the pans. If there is a thermal transition in the sample, the sample and reference pans will have a temperature differential which is proportional to the difference in heat flows (4).

4.5 X-ray diffraction

A crystal structure can be represented as a series of evenly spaced layers by a distance *d* – the interplanar spacing. If an x-ray beam of wavelength, *λ,* was incident to the crystal planes at an angle of *θ* and the x-rays are diffracted by the planes of atoms, the scattered x-rays will be in phase if the difference in their path length is zero or a whole number of wavelengths. This leads to the Bragg equation, given by equation (4.1), where *n* is the order of diffraction.

$$n\lambda = 2d \sin\theta \qquad \textbf{(4.1)}$$

Powder x-ray diffraction (PXRD) is a commonly used crystallographic technique used to study the atomic arrangements within a material and to identify crystalline phases. In PXRD, the sample is a powder of the material, which is essentially a large number of microscopic crystals that are randomly orientated. The random orientation and large number of crystals result in all orientations of the reflection planes being aligned to the x-ray beam, resulting in a cone of diffracted radiation that appears as diffraction rings on 2D detectors (5).

4.6 Small angle x-ray scattering (SAXS)

In SAXS, x-rays are scattered due to the electron density of the scatterer and as in XRD (or any other scattering phenomena), the scattered x-rays must be in phase for constructive interference resulting in a scattering pattern. Unlike XRD, SAXS relies on contrast between the scatterer and the bulk solvent, which is given by the difference in electron density (6).

The experimental procedure of a SAXS experiment is straightforward; it requires a sample, x-ray source (and monochromator), and a detector. The collimated monochromatic x-ray beam illuminates the sample and the intensity of scattered radiation is recorded by the detector (7). A background pattern of the pure solvent is typically collected and subtracted from the sample pattern to give a pattern that is only from the particles of interest. In the sample solution, the particles are randomly orientated which results in an isotropic scattering pattern and thus most SAXS setups use two-dimensional detectors. Using a 2D detector allows for the pattern to be radially integrated which results in a one-dimensional scattering curve *I(q)* where *q* is a measure of the momentum transfer of scattered x-ray photon given by eqn. (4.2) where 2θ is the scattering angle and λ is the wavelength of the incident x-ray. Peaks in the scattering curve, together with the slope of the curve give information about the structure of the sample (8).

$$q = \frac{4\pi \sin(\theta)}{\lambda} \qquad \textbf{(4.2)}$$

4.7 References

1. LARKIN, P. *Infrared and Raman Spectroscopy.* Boston: Elsevier, 2011.
2. THOMPSON, J.M. *Infrared Spectroscopy.* 1st ed. New York: Pan Stanford, 2018.
3. CHIAVARO, E. *Differential Scanning Calorimetry: Applications in Fat and Oil Technology.* Boca Raton: CRC Press, 2014.
4. HOHNE, G., W. HEMMINGER and H.J. FLAMMERSHEIM. *Differential Scanning Calorimetry.* London: Springer, 2003.
5. SEECK, O.H. and B. MURPHY. *X-ray Diffraction Modern Experimental Techniques.* New York: Pan Stanford, 2014.
6. PUTNAM, C.D., M. HAMMEL, G.L. HURA and J.A. TAINER. X-ray solution scattering (SAXS) combined with crystallography and computation: defining accurate macromolecular structures, conformations and assemblies in solution. *Q Rev Biophys*, 2007, **40**(3), pp.191-285.
7. PAUW, B.R. Everything SAXS: small-angle scattering pattern collection and correction. *J Phys Condens Matter*, 2013, **25**(38), p.383201.
8. KIKHNEY, A.G. and D.I. SVERGUN. A practical guide to small angle X-ray scattering (SAXS) of flexible and intrinsically disordered proteins. *FEBS Lett*, 2015, **589**(19 Pt A), pp.2570-7.

Chapter 5 Materials and Methods

Materials used in this research, presented alongside a description of the experimental methodologies employed

5.1 Introduction

This chapter describes the materials used in the experimental work and the experimental methodologies and techniques used to obtain the data required to meet the overall project objectives. The chapter starts with an overview of the chemicals and solvents used throughout the work before moving on to describing sample preparation methodologies and various characterisation techniques. These include chemical analysis techniques such as Fourier Transform Infrared and Raman spectroscopy and structural techniques such as differential scanning calorimetry and powder x-ray diffraction. Finally the instrumentation and methodologies used to carry out simultaneous small- and wide- angle x-ray scattering at synchrotrons are described.

5.2 Materials

The main chemicals used throughout the experimental work are monoethanolamine and fatty acids. Monoethanolamine (ACS reagent, 99%) was purchased from Sigma-Aldrich. The fatty acids used in the studies were: Lauric acid (99%), Palmitic acid (98%), Stearic acid (97%) purchased from Fisher Scientific, and Myristic acid (98%) purchased from Sigma-Aldrich. Absolute Ethanol (99.9%) was purchased from VWR whilst deionised water was prepared by the department laboratory. All the chemicals and solvents used in this thesis were used as supplied.

5.3 Methods

5.3.1 Preparation of MEA carboxylates and their acid-soaps

Samples of pure MEA carboxylates and were prepared in ethanol by neutralising fatty acid with monoethanolamine (MEA) using an AutoMATE reactor system from HEL Ltd. The AutoMATE system from HEL Ltd. is a parallel reactor system with four independent 100 ml glass jacketed reactors each with overhead stirring, temperature and turbidity probes. Temperature control in each reactor is provided by the oil jacket and an electric card heater beneath each reactor vessel.

The solutions were prepared at an approximately 80 ml scale. The MEA carboxylates were prepared at a concentration of 10% wt MEA carboxylate with a 5% molar excess of MEA to ensure complete neutralisation (1). MEA carboxylate acid-soaps were prepared at a 10%wt scale by neutralising 55%(molar basis) of the fatty acid. The aim of this was to ensure that there

was no free fatty acid; only the 1:1 acid-soap and a small quantity of soap. If there was still free fatty acid in solution, this would likely crystallise out before the acid-soap resulting in a mixed precipitate. However, by running a small excess of MEA over the required neutralisation level of 50% to form a 1:1 acid-soap, there would be a small quantity of the more soluble soap present instead of the acid. Thus enabling the use of cooling crystallisation to isolate the acid-soap.

The solutions of MEA carboxylates and MEA carboxylate acid-soaps were heated and agitated until a clear isotropic solution was obtained. The solutions were then slowly cooled at a rate of 0.1 °C/min (the slowest possible rate for the reactor system) until the solutions crystallised. The crystals were filtered out by vacuum filtration and left to air dry at ambient temperature until constant weight.

The slowest cooling rate was used to keep to relatively low supersaturations, to ensure good-quality and stable crystal forms were obtained rather than driving the system too quickly and obtaining crystals with impurities or metastable forms. In addition, using the slowest cooling rate mirrors the slow crystallisation conditions that can occur within product formulations over long time-spans.

5.3.2 Preparation of partially neutralised fatty acid crystal samples

A series of samples of fatty acids partially neutralised by MEA were prepared for analysis. Fatty acids were neutralised to various degrees in ethanol by MEA on a 10 – 90 %molar basis (i.e at 10% neutralisation, the ratio of soap to acid is 1:9) in 10% increments in an AutoMATE reactor system from HEL Ltd. The solutions were prepared at an approximately 60 g ethanol scale and a 10 %wt total concentration of acid and MEA. The MEA and fatty acid were added to ethanol in their required ratio and mixed in the reactors and heated to 60 °C at a rate of 1 °C/min to obtain clear isotropic solutions. The solutions were then transferred to 100 ml glass evaporating basins and the ethanol allowed to evaporate off at ambient temperature in a fume hood until sample weight became constant. The resulting crystals were then lightly ground to create a homogeneous powder for analysis.

5.3.3 Powder X-ray Diffraction measurements

Powder x-ray diffraction (PXRD) measurements were carried out on powdered crystal samples for fatty acids, MEA carboxylates, and partially neutralised fatty acids. PXRD was performed using a Bruker D8 Advance using Cu Kα

radiation in Bragg-Brentano reflection geometry. The step size over a 2θ range of 5-55 2θ was 0.033 2θ with a step time of 0.25 s/step. For low angles, with a 2θ range of 1.5-10 2θ, the step size was 0.033 2θ with a step time of 0.25 s/step. The detector used was a Vantec-1 position sensitive detector.

5.3.4 Differential Scanning Calorimetry measurements

Differential scanning calorimetry (DSC) measurements on powder samples were carried out using a Mettler-Toledo DSC 1 Star system. Approximately 5-10 mg of each powdered sample was sealed in 40 µl aluminium pans. The samples were subjected to heating ramps to determine the melting temperature and other thermal transitions. These ramps were carried out at 1 °C/min after an initial equilibration at 25 °C for 10 minutes.

The ramp rate of 1 °C/min was used throughout to allow fair comparison between different samples. The ramp rate was a compromise between resolution, sensitivity, and instrument time-constraints. The ramp rate in a typical DSC experiment is often 10 °C/min, which wouldn't have been suitable for temperature cycling as this rapid rate of cooling is far greater than the typical of temperature changes that MEA carboxylates are exposed to in 'real world' conditions (2). DSC experiments in literature on TEA stearate have used ramp rates of 10 °C/min, 1 °C/min, and 0.1 °C/min, with the slowest rate providing increased temperature resolution with better separation of close thermal events (3). However, the issue with 0.1 °C/min was instrument time-constraints as a single 25-100 °C ramp would take 12.5 hours and thus a single cycle would take *ca*. 26 hours. Therefore a ramp speed of 1 °C/min was selected as a compromise.

5.3.5 Fourier Transform Infrared Spectroscopy

Fourier transform infrared spectroscopy measurements were carried out either using a Thermo-Nicolet iS10 Infrared Spectrometer with a diamond ATR attachment or a Thermo-Nicolet Nexus 670 Infrared Spectrometer with a zinc selenide, ZnSe, ATR attachment. Spectra were recorded using the Omnic software at a resolution of 4 cm^1 for 32 scans with a background scan taken before each sample.

5.3.6 Raman Spectroscopy measurements

5.3.6.1 Measurements of crystal samples

Raman spectroscopy measurements were carried out using a Kaiser Optical Systems RamanRXN1 system with a 785 nm laser on crystal samples placed on a glass slide in an enclosed sample compartment. Spectra were created

from a 3-position average of the crystal sample, with spectra recorded at each position consisted of 3 accumulations of 5 seconds.

5.3.6.2 In-situ solution measurements

Process Raman measurements were carried out on aqueous solutions in a 0.5 L Simular reactor system from HEL Ltd. using a Kaiser Optical Systems RXN1 system with a dip-in probe. Spectra were recorded every 30 seconds, with each spectra consisting of three 5-second accumulations.

Aqueous MEA myristate solutions were prepared at 2.5, 5, 10, 15 g soap/100 g deionised water concentrations at a 0.5 L scale to enable comparisons with the Crystal16 turbidity data. The solutions underwent temperature cycles as used in the turbidity measurements in Crystal16 with high and low hold temperatures of 60 °C and 10 °C respectively with a heating/cooling rate set to 1 °C/min. The cooling/heating rate of 1 °C/min rate was used as multiple events were observed in the turbidity data collected in section 5.3.8 and the Raman data should have been able to help identify the transitions. For each concentration three heating/cooling cycles were used.

Figure 5.1: Simular 0.5 L reactor from HEL Ltd with RamanRXN1 system from Kaiser Optical systems used for in-situ measurements

5.3.7 Multivariate Curve Resolution of FTIR and Raman data

Multivariate curve resolution (MCR) using an Alternating Least Squares (ALS) algorithm was used to analyse the FTIR and Raman spectra of crystal samples produced by variable neutralisation of fatty acids with MEA. The analysis was carried out using MCR-ALS GUI 2.0 with Matlab R2014a (4, 5).

The number of components was determined using the Singular Value Decomposition (SVD) algorithm and considering the number of largest singular values combined with prior knowledge from the PXRD, DSC, and FTIR spectra analysis. An initial estimate of the component spectra was determined by the purest variable detection method (6). The constraints selected for the ALS optimisation were non-negativity using the *fnnls* algorithm (7). The optimisation was carried out until the convergence criteria was met or for 50 iterations.

5.3.8 Polythermal data collection

5.3.8.1 Equipment

Turbidity measurements were carried out using an Avantium Crystal16 system, in which the solutions underwent heating and cooling cycles at different heating/cooling rates. The Crystal16 system is a multi-reactor system which consists of four independent temperature-controlled blocks each containing four 1.8 ml reactors each with magnetic stirring. Each reactor has turbidity measurement to detect crystallisation and dissolution temperatures.

5.3.8.2 Aqueous sample preparation

Aqueous solutions of MEA carboxylates were prepared by mixing equimolar amounts of monoethanolamine and the appropriate fatty acid in deionised water and heating to above the acid melting point and mixing until the solution became isotropic. The solutions were then transferred to the 1.8 ml glass vials by micropipette with pre-heated tips and sealed with a screw top lid. Aqueous solutions of MEA carboxylates with a 10%molar excess of MEA were prepared in a similar manner as described above, with the exception of the excess amine.

Solutions of MEA carboxylates in ethanol were prepared in a similar manner as above, except they were heated to a lower temperature (40-50 °C depending on chain length) due to the higher solubility in ethanol. MEA carboxylates in MEA were also prepared in a similar manner with fatty acid mixed in the appropriate ratio in ethanolamine to give the desired MEA carboxylate concentration.

5.3.8.3 Methodology

Heating/cooling rates of 0.1, 0.25, 0.5, 0.75, and 1 °C/min were used and five cycles were carried out for each combination of cooling rate and concentration to obtain representative transition temperatures. For MEA myristate a cycle consisted of holding the sample at 40 °C for 30 minutes to ensure complete

dissolution, followed by cooling at a constant rate to 5 °C and holding for 30 minutes before reheating at a constant rate to 40 °C. For MEA laurate, the high hold temperature was 40 °C and the low hold temperature was -5 °C. All solutions were magnetically agitated at a rate of 700 rpm. The turbidity transitions were sharp and crystallisation was judged to have occurred when the transmittance of light fell below 50 % and dissolution was defined as occurring when the transmittance increased above 50 %.

5.3.9 In-situ optical microscopy

Optical microscopy was carried out on aqueous MEA myristate solutions using an Avantium Crystalline Particle Viewer system. The Crystalline system works in a similar manner to the Crystal16 system previous described; it consists of 8 temperature-controlled blocks which hold an 8 ml glass vial. Each vial has overhead stirring, together with turbidity measurement. Four of the reactors have particle viewers with various magnifications for observing and capturing images of the solution (and crystals) within the vial.

Aqueous MEA myristate solutions were prepared by mixing equimolar amounts of MEA and myristic acid in deionised water at a 10 ml scale in 20 ml glass vials. The vials were magnetically agitated and heated to above the fatty acid melting temperature on a hot plate. Aqueous MEA myristate solutions with an excess of MEA were prepared in a similar manner. On obtained an isotropic solution, 5 ml of solution was transferred into 8 ml glass vials by pipette. The vials had overhead hook impellers for agitation. The solutions were subjected to heating/cooling cycles and images of the solution in the vial captured at regular time intervals; every 10 seconds during heating/cooling ramps and every 30 seconds during the high and low temperature holds.

5.3.10 Preparation of crystal samples from aqueous MEA carboxylate solutions

Crystal samples from aqueous MEA laurate and MEA myristate solutions were produced by preparing isotropic solutions at an 80 ml scale in an AutoMATE system from HEL Ltd. The solution concentrations used were 2.5, 5, 10, and 15 g soap/100 g deionised water. The isotropic solutions were cooled to 5 °C at a rate of 1 °C/min. Once the solutions had crystallised, they were vacuum filtered and left to air dry until the sample weight became constant. The crystals were then lightly ground using a pestle and mortar to ensure a homogenous sample for analysis.

The concentrations used were to allow correlation of obtained crystals with the turbidity data collected in section 5.3.8. The turbidity data collected using the Crystal16 as detailed in section 5.3.8 also showed multiple turbidity events at higher ramp rates, which could have been due to multiple components. A cooling rate of 1 °C/min was therefore chosen to try replicate this in order to determine if multiple components were present.

5.3.11 Dynamic Light Scattering measurements

Dynamic light scattering (DLS) measurements were performed using a Malvern Zetasizer Nano on aqueous solutions of MEA carboxylates to inform the size range required for SAXS experiments. Aqueous solutions of MEA laurate, MEA myristate, and MEA stearate were prepared at low concentrations (<1 g soap/100 g deionised water) and transferred to disposable polystyrene sizing cuvettes for analysis. Measurement times were automatically determined and three measurements were carried out per run with a measurement angle of 173˚ backscatter.

Measurements on the solution state of aqueous MEA laurate, MEA myristate, and MEA stearate samples with concentrations of 1 g soap/100 g deionised water were carried out for temperatures of 25 °C, 40 °C, and 60 °C respectively. The measurement temperatures for MEA laurate (25 °C) and MEA myristate (40 °C) were selected based on the turbidity data collected in section 5.3.8, which indicated that the solutions should be clear, isotropic solutions. The measurement temperature for MEA stearate (60 °C) was determined based on the temperature required to produce an isotropic solution during sample preparation. A total of six measurements were carried out after temperature equilibration.

Aqueous samples of MEA myristate with concentrations of 0.5 and 0.75 g soap/100 g deionised water were analysed at temperatures of 25 - 50 °C in 5 °C increments. An equilibration period of 3 minutes between temperature changes was used and two runs were carried out per temperature giving 6 measurements per temperature.

5.3.12 Simultaneous Small and Wide Angle X-ray Scattering; I22 Diamond

5.3.12.1 Instrumentation

Simultaneous SAXS/WAXS measurements were carried out at the I22 beamline at the Diamond Light Source in Oxfordshire, UK. The primary beam was set at an energy of 12.4 keV, giving a wavelength of 1 Å. The sample to SAXS detector distance was 1.956 m and sample to WAXS detector distance

was 0.164 m, both these distances and the detectors were in vacuum to avoid unwanted air scatter. The SAXS detector was a Pilatus P3-2M with 1475 x 1679 (W x H) pixels with a pixel size of 172 x 172 µm. The WAXS detector was a Pilatus P3-2M-DLS-L, the same as the SAXS detector except with 3 modules removed (494 x 636 pixels, W x H) to allow the SAXS beam to pass through, giving the detector an L-shape active area.

The sample environment used was an in-house built capillary flow cell system. The flow cell system consisted of a 100 ml jacketed reactor with magnetic stirrer agitation (120 rpm to minimise bubble formation) coupled to a capillary flow cell with jacketed transfer lines. Temperature control for the cell and reactor was provided by a Lauda Proline RP 855 circulating bath with Pt100 temperature monitoring of the reactor contents. The reactor contents were also monitored by turbidity using an in-house built turbidity probe and signal amplifier and a LabView program. The contents on the reactor were circulated through the jacketed transfer lines to the capillary cell by a Watson Marlow peristaltic pump with four roller head to reduce pulsation through the lines. Also, the pump was used to draw the sample through the cell rather than “pushing” to avoid putting excess pressure on the capillary.

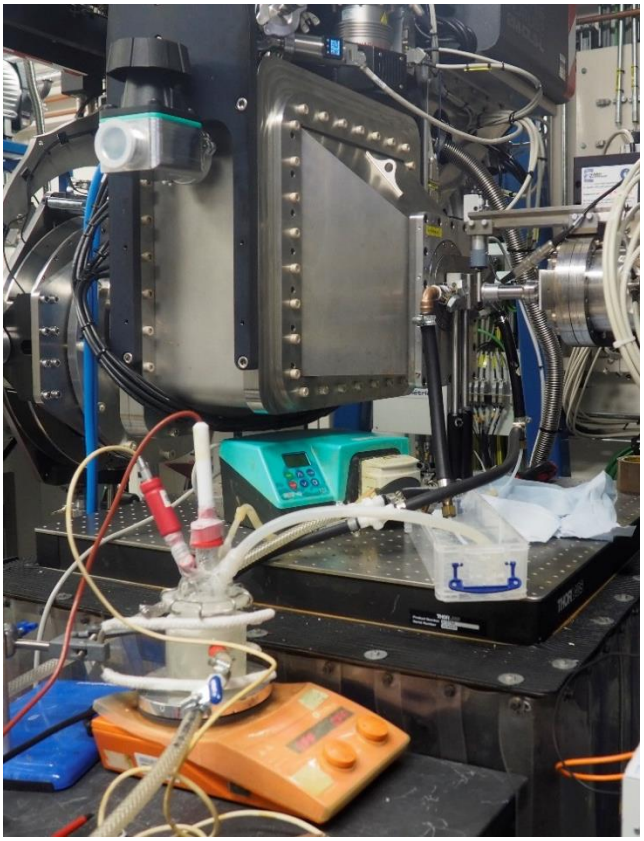

Figure 5.2: The capillary flow cell setup used at I22 at Diamond

The capillary cell had a 1.5 mm outside diameter borosilicate glass capillary tube, with a wall thickness of 10 µm as window for the x-ray beam to impinge on the sample. The cell was temperature controlled by the same Lauda bath, connected via jacketed transfer lines.

5.3.12.2 Sample preparation

Aqueous solutions of MEA myristate were prepared at a range of concentrations: 0.5, 1, 2.5, 5, 10, 15 g MEA myristate/100 g deionised water. These concentrations allowed for comparison with the previously collected data from section 5.3.8 and section 5.3.6. These were prepared by mixing equimolar amounts of MEA and myristic in deionised water in a sealed screw-top laboratory bottle and heating to 55 °C in a water bath to obtain a clear isotropic solution. The samples were then poured into the pre-heated reactor before each run.

During each run the samples were held at 55 °C for 20 minutes to equilibrate before being cooled at a fixed rate to 5 °C. The samples were cooled at either 0.25 or 1 °C /min. The higher cooling/heating rate was use to try study the two-step dissolution behaviour observed in the turbidity data collected in section 5.3.8. A slow cooling rate was used as a contrast to the higher rate and to study the effect of kinetics on the process. Whilst a rate of 0.1 °C/min would have been preferred, due to time constraints a 0.25 °C/min rate was used.

They were held at 5 °C for 20 minutes before being reheated to 55 °C at the same fixed heating rate as during the cooling ramp. Data collection started as soon as the equilibration had begun.

5.3.12.3 Data collection and analysis

Data was collected in multi-frame files of 10 frames with 2 second frame collection times with 20 seconds waiting time between sets of frames. Frames were collected from the start of the solution equilibration and ended once the temperature cycle had finished.

The scattering patterns were integrated, corrected for primary beam intensity variation, transmission, and a background was subtracted using DAWN (8). The background subtraction consisted of two parts; the empty capillary cell, and deionised water scaled to account for the solution concentration. The deionised water background was processed first by subtracting the empty capillary cell.

5.3.13 Simultaneous Small and Wide Angle X-ray Scattering; BM28 ESRF

5.3.13.1 Instrumentation

Simultaneous SAXS/WAXS measurements were performed on the BM28 beamline at the European Synchrotron Radiation Facility, ESRF, in Grenoble, France. The primary beam was set to an energy of 12.4 keV giving a wavelength of 1 Å. The sample to SAXS detector distance was 1.630 m and the sample to WAXS detector distance was 0.504 m. The SAXS detector was a MAR165 CCD (charge coupled device) detector with 165 mm diameter active area with a pixel size of 80 x 80 µm. The WAXS detector was a Pilatus 300K-W with 1475 x 195 pixels with a pixel size of 172 x 172 µm. The distance between the sample and the SAXS detector was not under vacuum but was covered by a beam tube that was purged with helium to reduce unwanted scattering. The short distance between the sample and the WAXS detector was an air gap. The SAXS detector was calibrated using silver behenate calibration standard powder in a 1 mm quartz capillary tube with a wall thickness of 10 µm. The WAXS detector was calibrated using alpha – Al_2O_3 powder in a 1 mm quartz capillary tube with a wall thickness of 10 µm.

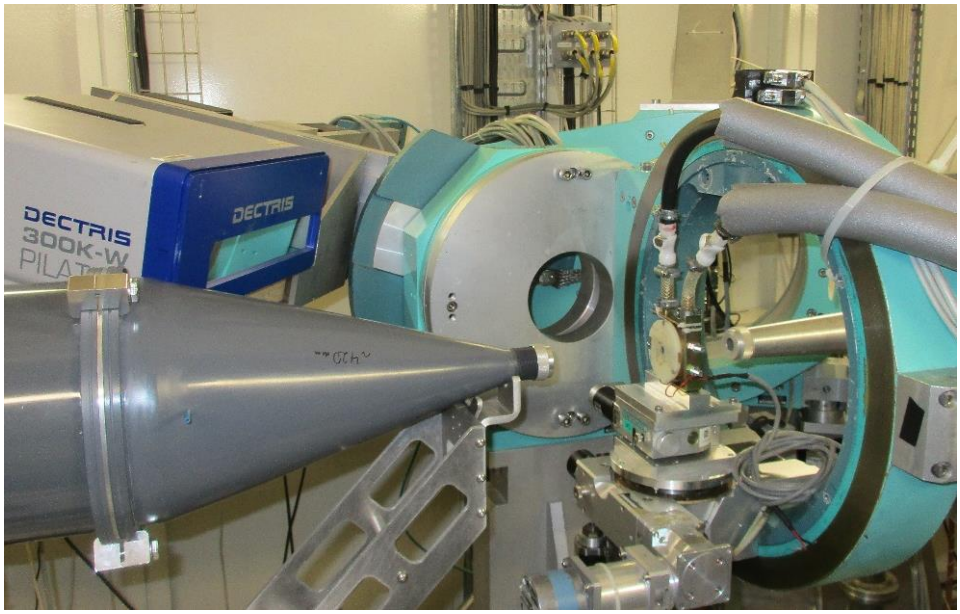

Figure 5.3: The capillary stage used at BM28 at ESRF

An in-house built temperature-controlled brass capillary sample stage was used. Temperature control was provided by a programmable Huber Ministat 125 with insulated hoses, with the temperature of the outside of the capillary in the holder also monitored via a thermocouple and an in-house built temperature recorder and LabView program. The samples were contained in 1 mm outside diameter quartz capillary tubes with a wall thickness of 10 µm.

5.3.13.2 Sample preparation

Aqueous solutions of MEA carboxylates were prepared at a 10 ml scale for MEA laurate, MEA myristate, and MEA palmitate solutions at concentrations ranging from 0.5 – 15 g MEA carboxylate per 100 g deionised water. These concentration ranges were used to allow comparison with the data collected by other techniques. Samples were prepared by mixing equi-molar amounts of MEA and fatty acid in deionised water and heating to above the fatty acid melting point to obtain an isotropic solution. Samples were transferred via a pre-heated pipette to pre-heated quartz capillary tube (1 mm outside diameter, 10 µm wall thickness) to prevent unwanted crystallisation. The capillary tubes were then sealed using an epoxy.

Measurements were taken on samples at constant temperature and on samples subjected to a cooling/heating cycle. Due to time constraints, measurements of MEA laurate and MEA stearate samples were only carried out on the solution state at a single temperature. Measurements were taken on MEA myristate and MEA palmitate samples during heating/cooling cycles. The heating/cooling cycles used a set rate of 1 °C/min as it allowed for comparison with data collected via other techniques and to allow for a higher-throughput of samples during the limited time available. The temperature cycles programmed into the Huber Ministat consisted of a 20 minute high-temperature hold to allow for equilibration before cooling at a set rate of 1 °C/min to a set temperature. This lower temperature was held for 20 minutes before reheating at 1 °C/min to the starting temperature. For the myristate samples the high and low temperatures were set to 60 °C and -15 °C, whilst for the palmitate samples the high and low temperatures were set to 75 °C and 5 °C respectively. Samples were also tapped during the low hold if they had not already crystallised in an attempt to trigger crystallisation in the sample.

5.3.13.3 Data collection and analysis

Data was collected in continuous 10 second exposures, with an approximate. 5 second delay between each frame due to the MAR165 CCD detector read out time. Data collection began during temperature equilibration and finished once the temperature cycle had finished.

The scattering patterns were integrated and background subtracted using DAWN (8).

5.4 References

1. WÄRNHEIM, T. & JÖNSSON, A. 1992. Phase behavior of alkanolammonium carboxylates. 88, 18-22.
2. SUMMERTON, E., BETTIOL, J., JONES, C., BRITTON, M. M. & BAKALIS, S. 2018. Understanding the Crystallization Process in Detergent Formulations in the Absence and Presence of Agitation. Industrial & Engineering Chemistry Research, 57, 16162-16171
3. ZHU, S., HEPPENSTALL-BUTLER, M., BUTLER, M. F., PUDNEY, P. D., FERDINANDO, D. & MUTCH, K. J. 2005. Acid soap and phase behavior of stearic acid and triethanolamine stearate. J Phys Chem B, 109, 11753-61.
4. JAUMOT, J., A. DE JUAN and R. TAULER. MCR-ALS GUI 2.0: New features and applications. *Chemometrics and Intelligent Laboratory Systems*, 2015, **140**, pp.1-12.
5. *Matlab R2014a* [CD-ROM]. Natick, MA.: The Mathworks, Inc., 2014.
6. WINDIG, W. and D.A. STEPHENSON. Self-modeling mixture analysis of second-derivative near-infrared spectral data using the SIMPLISMA approach. *Analytical Chemistry*, 1992, **64**(22), pp.2735-2742.
7. BRO, R. and S. DE JONG. A fast non-negativity-constrained least squares algorithm. *Journal of Chemometrics*, 1997, **11**(5), pp.393-401.
8. BASHAM, M., J. FILIK, M.T. WHARMBY, P.C. CHANG, B. EL KASSABY, M. GERRING, J. AISHIMA, K. LEVIK, B.C. PULFORD, I. SIKHARULIDZE, D. SNEDDON, M. WEBBER, S.S. DHESI, F. MACCHEROZZI, O. SVENSSON, S. BROCKHAUSER, G. NARAY and A.W. ASHTON. Data Analysis WorkbeNch (DAWN). *J Synchrotron Radiat*, 2015, **22**(3), pp.853-8.

Chapter 6 Synthesis and characterisation of MEA carboxylates and acid-soap complexes

Characterisation of monoethanolammonium carboxylates and their acid-soaps through a variety of chemical and structural analysis techniques

6.1 Introduction

Monoethanolammonium carboxylates have received relatively little attention in literature compared to their sodium carboxylate equivalents and as such there is a lack of fundamental characterisation data. There is a small amount of characterisation data for solid MEA carboxylates (1) and there have been some studies on similar carboxylate-based species such as triethanolammonium carboxylates and choline carboxylates (2, 3). This chapter aims to address this by characterising the solid state of four common long chain MEA carboxylates; laurate, myristate, palmitate, and stearate. These four components cover the chain length range of C12:0 to C18:0 and represent the bulk of most naturally occurring fatty acid sources such as coconut, tallow, and palm kernel oil. This is of industrial interest as fatty acids used in consumer goods are usually derived from these natural sources.

In addition to the lack of basic characterisation data for MEA carboxylates, there is little information on their ability to form acid-soap cocrystals. Soaps are known to form acid-soap cocrystals and the acid-soaps of sodium and potassium soaps have been well studied (4-11). There has also been some investigation of the acid-soaps of triethanolammonium stearate and stearic acid (12-14). Phase diagrams of the MEA – stearic acid and MEA – oleic acid systems are reported in literature but don't feature acid-soaps as no characterisation techniques were used in the study that could reliably differentiate acid-soap from its respective MEA carboxylate (15). The acid-soap complexes of MEA carboxylates have not been studied and as formation of fatty acid in MEA carboxylate – water systems is thought to occur, acid-soap cocrystals will likely play a role in the crystallisation process and phase behaviour of MEA carboxylates. Acid soaps have been reported to form in a number of acid:soap ratios, depending on the system. For example, TEA stearate – stearic acid has been reported to form a 2:1 acid-soap, whilst for sodium palmitate – palmitic acid a 1:1, 2:1, 3:2 acid-soap have been reported (6, 13). By characterising the crystals formed from fatty acids neutralised to various extents by MEA, a soap – acid phase diagram can be built and the structure and solid state properties of the MEA carboxylates and acid-soap cocrystals can be determined.

These characterisation studies enable the identification of these compounds in later chapters when dealing with in-situ measurements such as Raman or XRD/SAXS/WAXS and for confirmation of composition in off-line characterisation of crystallised material.

6.2 Characterisation of fatty acids: C12:0 – C18:0

Fatty acids are a core component of MEA carboxylates and their acid-soaps, representing up to approx. 80 %wt of the MEA carboxylates and more for the acid-soaps. Due to its size, the fatty acid molecule will have a leading role in determining the overall properties of the soap or acid-soap. Therefore, characterisation of the fatty acids used throughout these studies is required to allow for identification of the MEA carboxylates and their acid-soaps. Characterisation will include structural characterisation such as by PXRD and DSC and spectroscopic techniques such as FTIR and Raman to identify chemical changes.

6.2.1 PXRD and DSC

The PXRD measurements of lauric, myristic, palmitic, and stearic acid are shown in Figure 6.1. The PXRD pattern for lauric acid conforms to the pattern generated from the crystal structures of the C form deposited in the CCDC (16-20). The d_{001} – the long spacing – of 27.5 Å is consistent with that reported for the C form (21). Similarly, myristic acid is found to be of the C form, matching the PXRD pattern generated from the structures deposited with the CCDC, whilst the palmitic acid and stearic acid patterns also agree with those of the C form reported in literature (16, 17, 22-27). However, the experimental pattern for palmitic acid shows an additional peak at 2.89 °2θ and shoulders on some of the peaks at low angle. Similarly, the stearic acid sample showed an additional peak – 2.49 °2θ. This peak does not correspond to the reported long-spacing of either the A or B form of stearic acid (28). The peak could be explained by a raw material impurity e.g isostearic acid impurity (the isostearic acid (001) peak is close at 2.6 °2θ) (29). However, it is more likely that these additional peaks are due to the sample preparation issue as there is no other evidence in the patterns for iso-fatty acids.

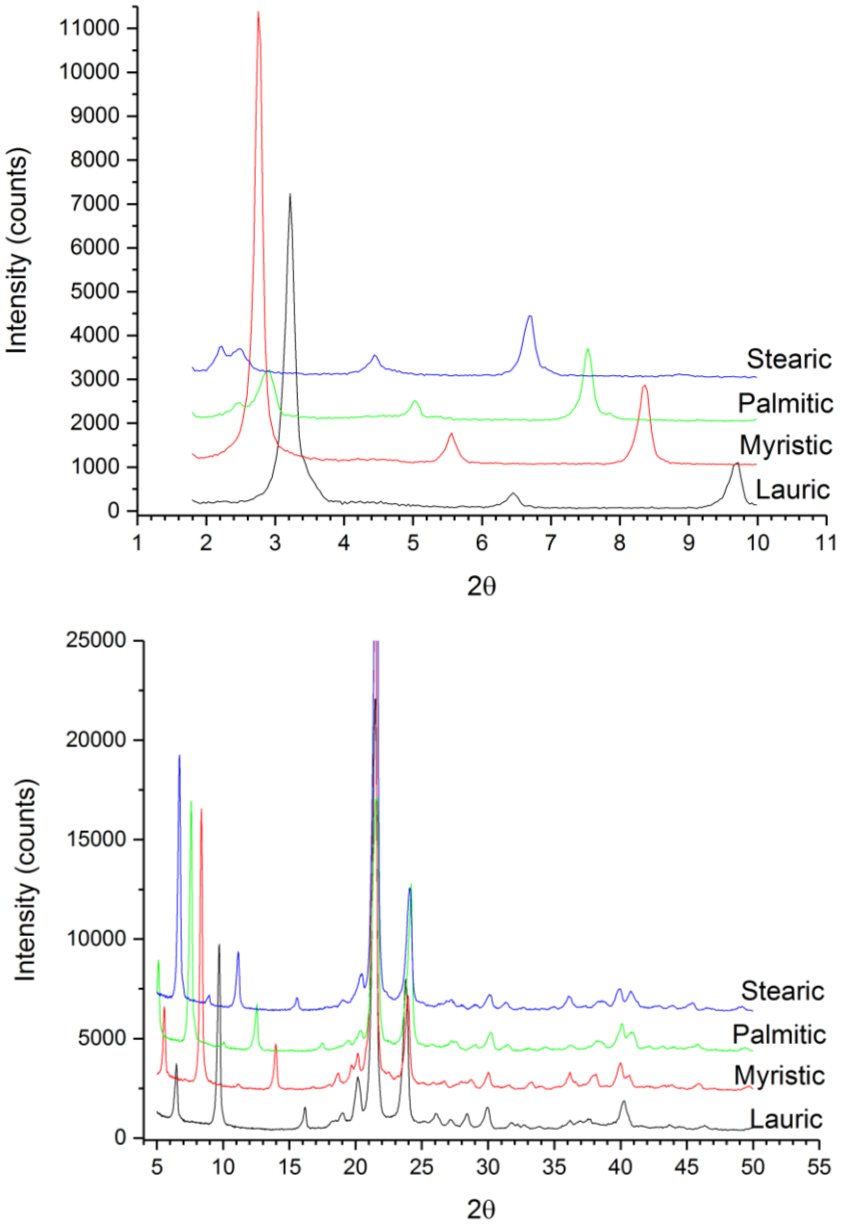

Figure 6.1: Low and wide angle PXRD of the raw fatty acids. Note: Peak at approx. 1.5 °2θ is the beam stop.

The melting points and enthalpies of fusion of the fatty acids determined by DSC are in agreement with those reported in literature (17, 30, 31). For each fatty acid there was only one endothermic peak in the temperature range covered, further suggesting that the unexpected low angle peaks are due to a sample preparation issue rather than an impurity such as isopalmitic or isostearic acid. According to literature the iso-fatty acids have melting points just below that of their respective straight chain fatty acids, 61.5 °C and 68.2 °C respectively for isopalmitic and isostearic acid (29, 32). These temperatures are close to the experimental melting peaks observed for the raw material, but if these iso-fatty acids were present they should exhibit a distinct melting peak or a shoulder. The crystallisation onset temperatures are

also in agreement with those reported in literature and the enthalpies of melting and crystallisation are generally in agreement with literature too (31).

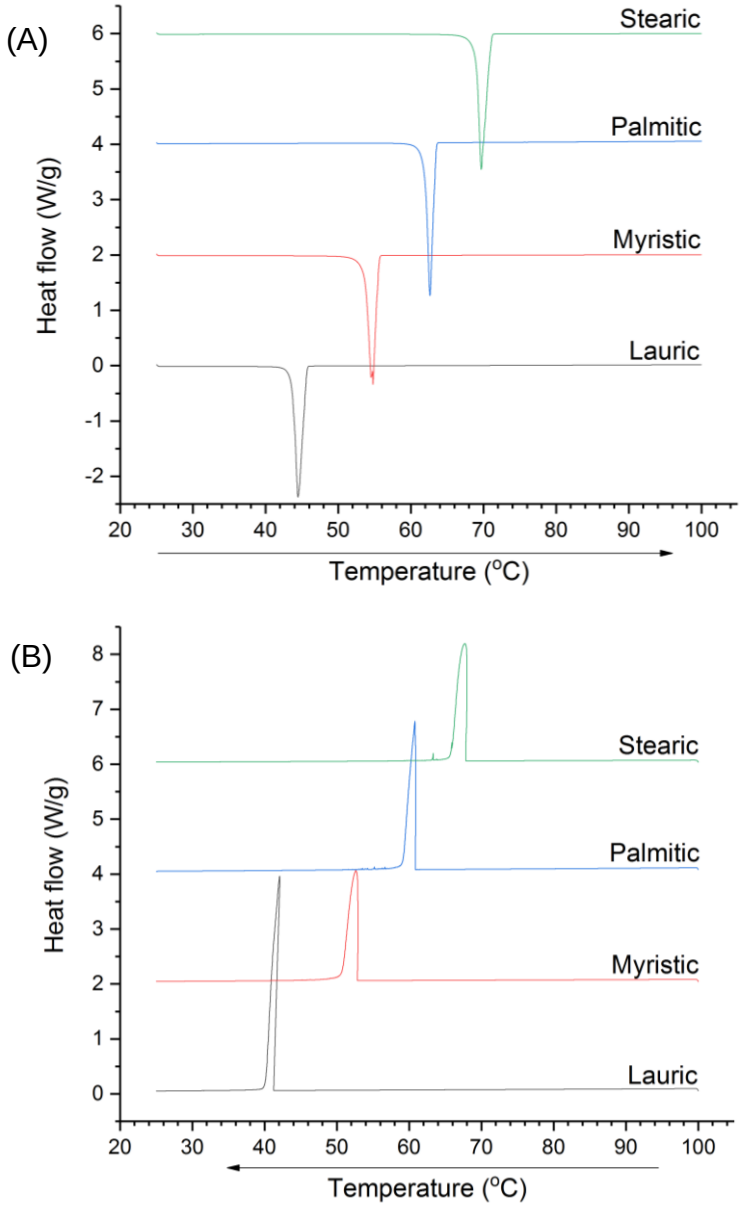

Figure 6.2: Melting/Crystallisation peaks in DSC traces of fatty acids (C12:0-C18:0) during heating (A) and cooling (B) temperature cycle

Table 6:1: Summary of fatty acid melting and crystallisation temperatures and their associated enthalpies as determined by DSC measurements

	Melting point		Crystallisation	
	Onset (°C)	Enthalpy (J/g)	Onset (°C)	Enthalpy (J/g)
Lauric (C12:0)	43.64	-173.67	41.28	173.78
Myristic (C14:0)	54.04	-175.19	52.84	175.77
Palmitic (C16:0)	61.86	-166.53	60.86	165.70
Stearic (C18:0)	68.87	-187.69	67.82	189.50

6.2.2 FTIR and Raman spectroscopy

The FTIR spectra of the fatty acids are in agreement with the typical spectra of fatty acids reported in literature and there are little differences between the chain lengths. The chain lengths are distinguishable however by the CH_2 wagging progression, where the number of peaks is dependent on the alkyl chain length. Table 6:2 summarises some of the key IR absorption bands in the spectra of fatty acids as shown in Figure 6.3 for myristic acid. The key feature of the spectra for this study was the carbonyl peak around 1694 cm^{-1} as it is characteristic of a fatty acid dimer in which hydrogen bonds between the COOH groups link the two acid molecules.

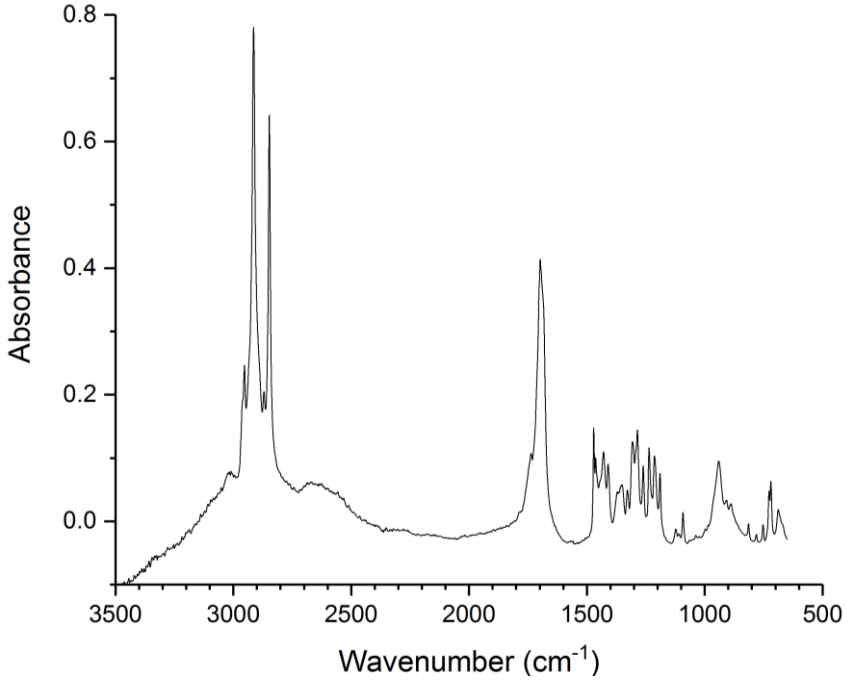

Figure 6.3 Infrared spectrum of myristic acid at room temperature

Similar to the infrared spectra the Raman spectra agree with those reported in literature and show no significant differences between the chain lengths (aside from the differences in CH2 wag vibrations). Table 6:3 summarises the key Raman bands shown in the fatty acid spectra (myristic acid is shown in Figure 6.4). The low wavenumber peaks are due to vibrations associated with the bonding of the fatty acid dimer (33). As Raman is less sensitive to polar, asymmetric stretches it is less useful in distinguishing between acid, acid-soap, and soap. However, the sensitivity of Raman to changes in the alkyl chains and its insensitivity to water (unlike IR) means it is useful in studying the structure of the acid/acid-soap/crystals as well as their crystallisation behaviour in solution.

Table 6:2: Summary of key IR bands in the spectra of long-chain fatty acids

Wavenumber (cm^{-1})	**Band**	**Ref.**
2953	CH3 antisymmetric stretch	(12, 34-36)
2926	CH2 asymmetric stretch	(12, 34, 36)
2870	CH3 symmetric stretch	(12, 34, 36)
2854	CH2 symmetric stretch	(12, 34-37)
1694	C=O asymmetric stretch	(5, 6, 12)
1465	CH2 scissor	(5, 35)
1410	CH3 bending	(34)
1180-1330	CH2 wagging	(5, 34, 35)
720	CH2 rocking	(5, 12, 34)

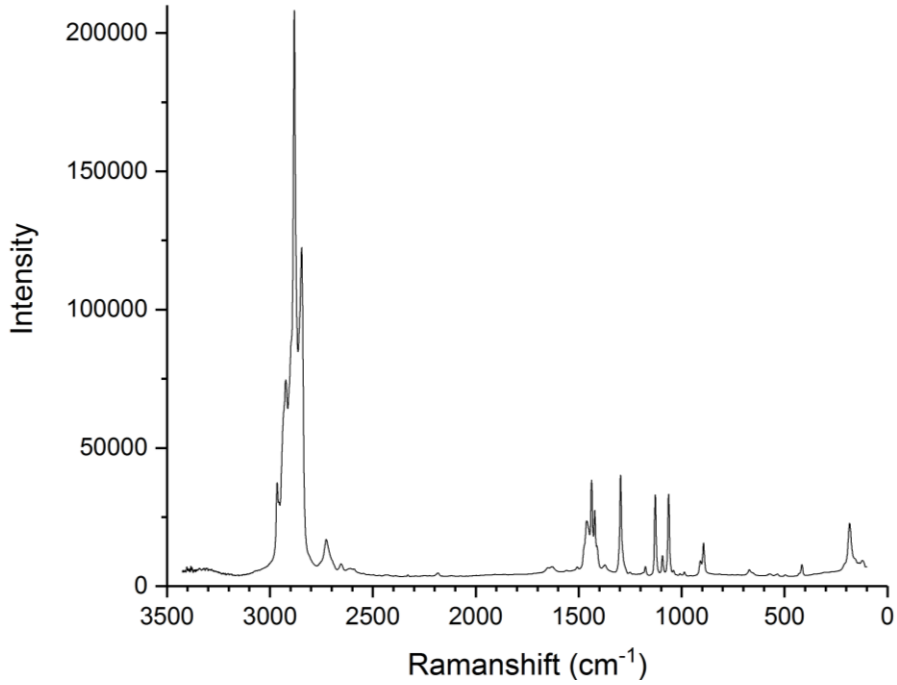

Figure 6.4: Raman spectra of myristic acid at room temperature

Table 6:3 Summary of Raman bands of long-chain fatty acids

Wavenumber (cm^{-1})	**Band**	**Ref.**
2940-2970	CH3 o. ph. str.	(36, 38-40)
2909-2930	CH3 i. ph. str.	(40)
2930	CH str.	(36, 38, 39, 41, 42)
2922	CH2 str.	(36, 38)
2870-2880	CH2 o. ph. str.	(36, 38-42)
2830-2850	CH2 i. ph. str.	(36, 38-42)
1633	C=O i. ph. str. (dimer)	(35, 36, 38)
1440-1460	CH2 bending	(36, 41, 42)
1430-1445	CH2/CH3 scissoring	(40)
1297	CH2 twisting	(36, 41)
1128	C-C-C i. ph. str. (trans)	(36)
1063	C-C-C o. ph. str. (trans)	(36)
1050-1150	C-C str.	(35, 38, 40-42)
891, 908	CH2 rocking	(40, 43)

6.3 Characterisation of MEA carboxylates

Monoethanolammonium carboxylates have received little attention in literature and their characterisation has often been limited to confirming their synthesis. In this section, MEA carboxylates produced in ethanol and purified by cooling crystallisation will be characterised in terms of structure, by PXRD and DSC, and chemically, by FTIR and Raman spectroscopy.

6.3.1 PXRD of MEA carboxylates

PXRD measurements of the MEA carboxylates, shown in Figure 6.5 for the low angle scans and Figure 6.6 for the wider angle scans, showed a series of evenly spaced sharp peaks, most obviously between 1.5 – 20 2θ. The d-spacing ratios of these first five peaks are in the ratio of 1: 1/2 : 1/3 : 1/4: 1/5, which is characteristic of a lamellar structure. The wider angle peaks are also sharp, indicating that the MEA carboxylates are crystalline.

From the low angle peaks, the long spacing of the lamellar structure can be determined by from fitting the d-spacing of the peaks to the characteristic d-spacing ratios. This ensures that the long-spacing of the lamellar structure is correctly determined, even if the first Bragg peak is larger than the d-spacing range covered. However, the lamellar series of peaks for the MEA carboxylates indicated that the first peak observed in each low angle scan was the n = 1 peak in the series and the corresponding long-spacing of the structure are summarised in Table 6:4. The d-spacing for the MEA carboxylates is smaller than that of the corresponding fatty acid and sodium soap and only slightly larger than the approximate length of the alkyl chain (44). An explanation for this short d-spacing could be that the alkyl chains adopt an interdigitated structure or a small tilt angle, similar to that proposed for TEA stearate which also has an usually small long-spacing given its chain length (13).

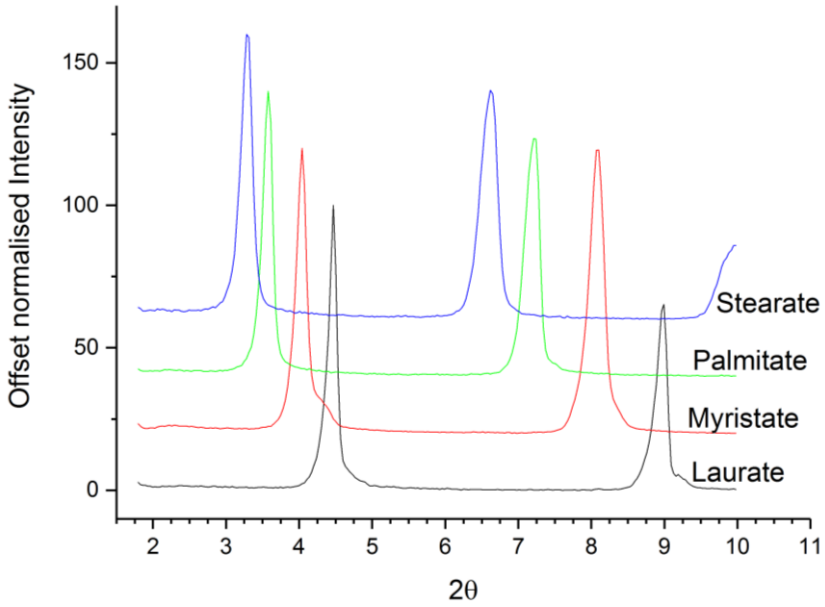

Figure 6.5: Low angle (1.5-10 °2θ) XRD scan of MEA carboxylates showing the first two peaks of the lamellar series.

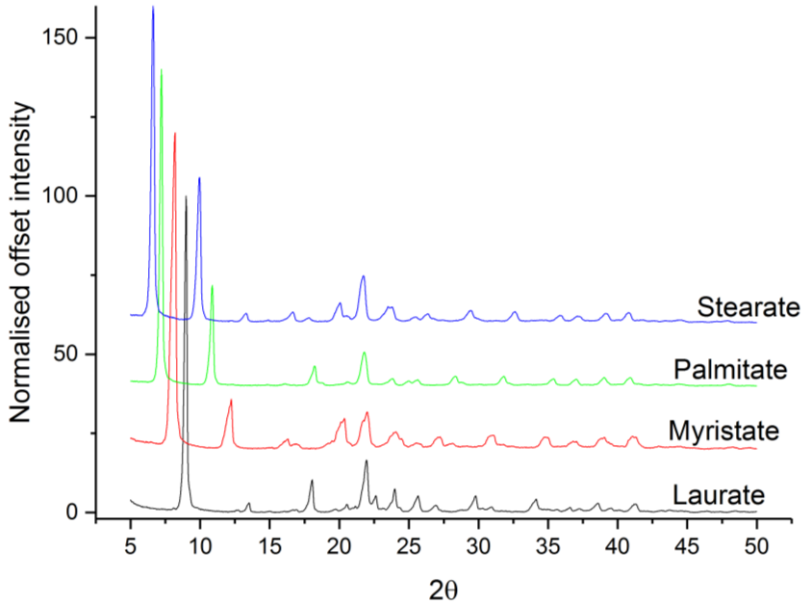

Figure 6.6: Wider angle (5-50 °2θ) XRD scan of MEA carboxylates

Table 6:4: Long spacings for MEA carboxylates as determined by PXRD and their fatty acid and sodium soap equivalents for comparison

Chain length	Fatty acid (Å)	Sodium carboxylate (Å)	MEA carboxylate (Å)
C12:0	27.5	31.6	19.8
C14:0	32.1	36.5	22.2
C16:0	35.7	41.8	24.7
C18:0	40.1	45.6	26.8

From the variation of long-spacing with chain length, the tilt angle of the alkyl chains can be approximated (assuming there is no significant changes in the crystal structure with chain length) for a single-layer or a double-layer type structure. From the PXRD data and the little variation between chain lengths, it can be assumed there is no significant change in structure with chain length. The long-spacing of MEA carboxylates increases by 2.38 Å per 2 extra CH_2 groups whilst the corresponding increase in tail length is approximately 2.53 Å. As Figure 6.7 shows, this enables the angle of tilt from the d_{001} plane to be calculated through trigonometry using the changes in d-spacing and chain length, resulting in a tilt angle of 70° for a single layer structure and 28° for a double layer structure. For comparison, long-chain saturated fatty acids have tilt angles of 60° (45).

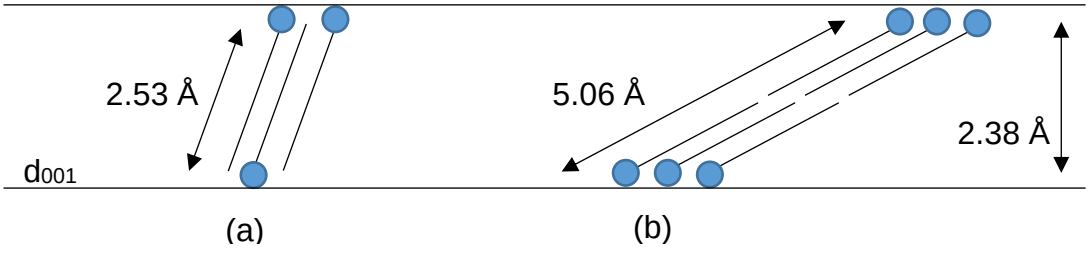

Figure 6.7: Calculation of tilt angle for MEA carboxylates assuming: (a) single layer structure and (b) double layer structure

The adoption of a single or interdigitated layer can be explained by considering the size and shape of the MEA ion compared to that of sodium or ammonium. Sodium soaps form double layers with the carboxylates coordinating around the sodium ions, which are effectively spherical and isotropic. A similar case can be made for ammonium carboxylates which exhibit a zig-zag pattern with 4 hydrocarbon chains that leads to larger long-spacings e.g 60.8 Å for ammonium myristate (46). MEA and TEA however are less isotropic and are bulkier which could make an interdigitated type structure more favourable as it could allow more room for MEA/TEA ion.

6.3.2 DSC of MEA carboxylates

The DSC traces for the MEA carboxylates all show consistent endothermic thermal events during heating of the sample across the three cycles – apart from the third cycle of MEA stearate, which showed additional thermal events. There are multiple exothermic events during the cooling of the MEA carboxylate samples, which shift to lower temperatures as the samples are cycled. This behaviour may be due to loss of monoethanolamine at the higher temperatures, shifting the composition of sample towards an excess of the respective fatty acid. However, the change in behaviour with cycling could be

the result of poor mixing in the melt phase causing acid-rich or MEA-rich regions to develop. These regions would then exhibit different crystallisation behaviours and thus different thermal events.

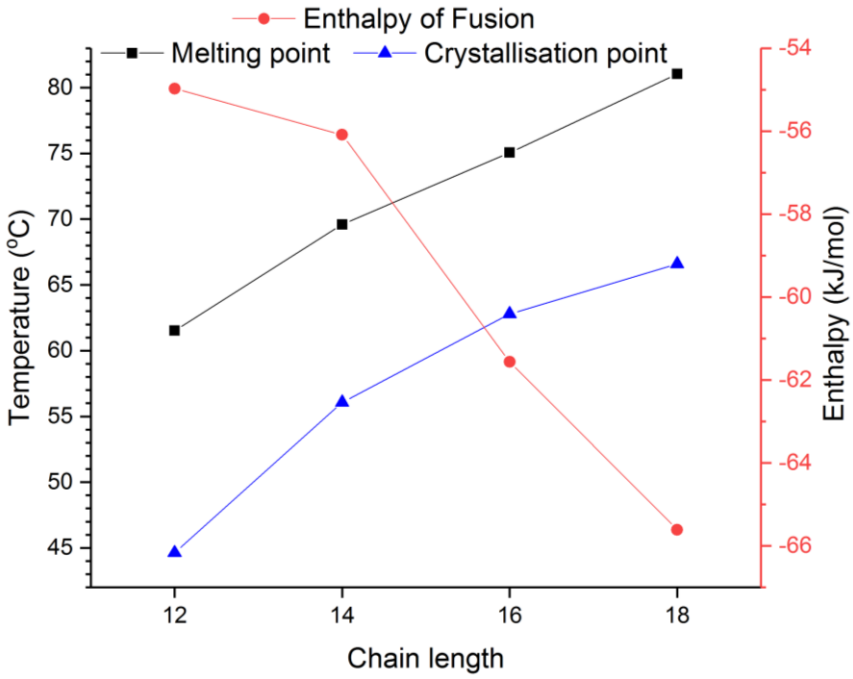

Figure 6.8: Average endothermic (melting) and exothermic (crystallisation) thermal transition onsets for MEA carboxylates together with their average enthalpy of fusions.

The endothermic events for all (apart from in the 3rd cycle of the MEA stearate) are the transition from the crystalline state to lamellar liquid crystal. The transition temperatures determined by DSC for MEA stearate are similar to reported literature values of 78.5 °C and 75.6 °C (1, 15).

The exothermic peaks during crystallisation of the samples are due to a number of phase changes occurring over a relatively small temperature range. The multiple peaks suggests that it is not recrystallisation of just the MEA carboxylate but that other components such as acid-soap or fatty acid may be forming too. The formation of these components could occur due to loss of MEA or poor mixing in the melt phase. For MEA stearate, there are three main exothermic peaks which can be identified as the following transitions (ordered from higher temperature to lower) according to ref. (15):

- Lamellar liquid crystal phase --> solid MEA stearate + lamellar liquid crystal
- Solid MEA stearate + lamellar liquid crystal --> solid MEA stearate + liquid
- Solid MEA stearate + liquid --> solid MEA stearate + solid fatty acid

The shift to lower temperatures and the change in enthalpy of the peaks are consistent with the sample shifting towards the fatty acid rich side of the monoethanolamine-stearic acid phase diagram in ref. (15). This is particularly evidenced by the heating ramp of the third temperature cycle, where there is an additional endothermic and exothermic peak before the endothermic peak seen in the previous cycles. This additional endothermic peak is at a temperature corresponding to the transition from the solid stearic acid and solid MEA stearate to solid MEA stearate and liquid.

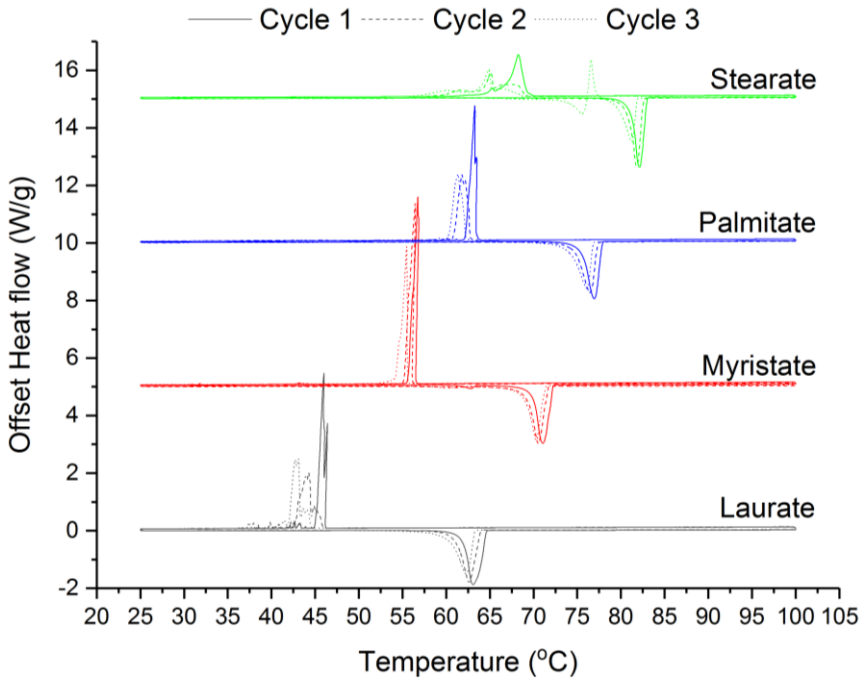

Figure 6.9: DSC traces of the MEA carboxylates during heating/cooling cycles showing the effect of thermal cycling. Endothermic - negative, exothermic – positive.

6.3.3 FTIR and Raman spectroscopy

The FTIR and Raman spectra collected for MEA carboxylates were consistent with the expected structures. In the FTIR spectra, no acid carbonyl peaks (COOH) and only carboxylate stretches (COO-) were observed, consistent with that reported for sodium soaps and other carboxylate-based soaps (6, 12).

The FTIR spectra collected for the MEA carboxylates showed no significant differences between the spectra collected for the different chain lengths. The exception to this was the CH2 wagging progression, between 1150 – 1380 cm^{-1}, as the number of peaks in the progression is chain-length dependent. The observed number of peaks are consistent with that expected from literature for the given chain length (half the number of CH2 groups) (12, 34, 47). The in-phase CH2 rock showed splitting at 718 and 728 cm^{-1} which

indicated that the MEA carboxylate samples are crystalline with an orthorhombic sublattice (12).

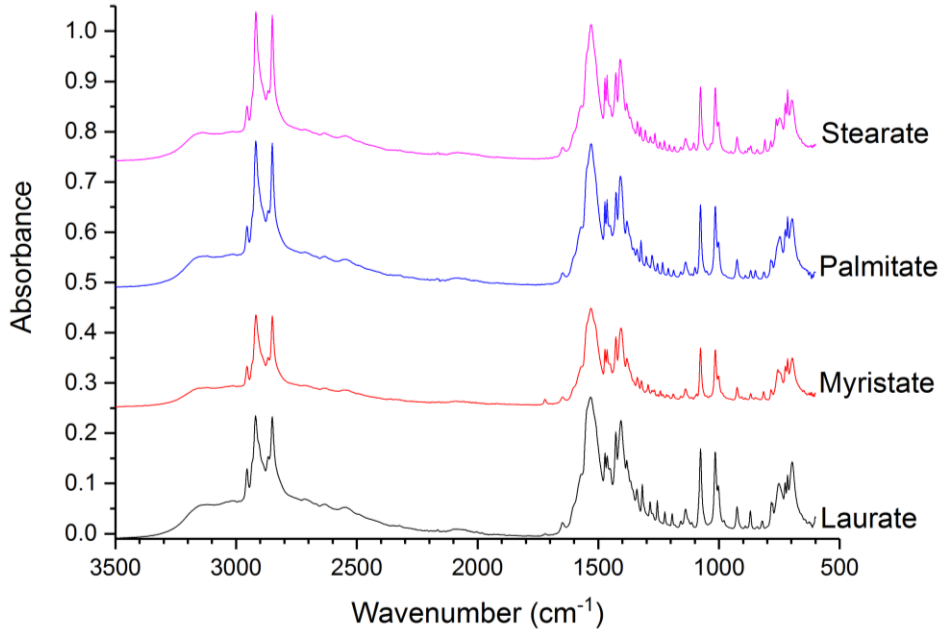

Figure 6.10: FTIR spectra of MEA carboxylates

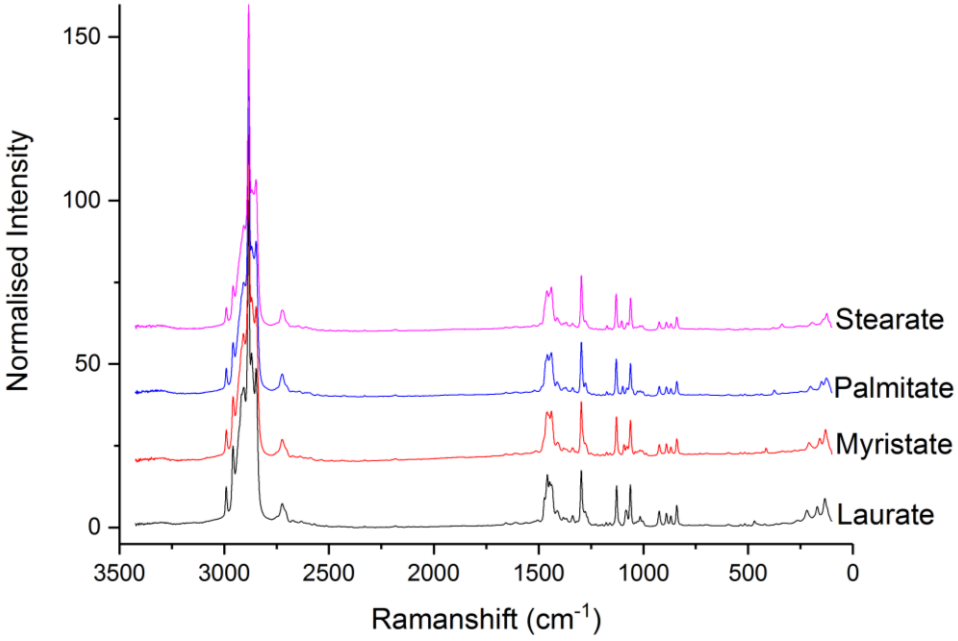

Figure 6.11: Raman spectra of MEA carboxylates

Table 6:5: Band assignment for the FTIR spectra of MEA carboxylates

Band (cm^{-1})	**Assignment**	**Ref.**
3500-2200	OH str	(6)
2955	CH3 antisymmetric str	(12, 47, 48)
2918	CH2 antisymmetric str	(12, 47, 48)
2868	CH3 symmetric str	(12, 47, 48)
2850	CH2 symmetric str	(12, 47, 48)
1721*	C=O antisymmetric str	(5, 6, 12, 47)
1648	N-H def	(6, 8)
1570	COO antisymmetric str	(5, 12, 47)
1548	COO-	(5, 6)
1531	COO antisymmetric str	(5, 12, 47)
1472	CH2 scissor	(5, 8, 12, 48)
1464		
1427	C-O stretch	(12)
1406	αCH2 bend	(8, 12)
1382	CH3 umbrella deformation	(12, 48)
1367	CH3 symmetric deformation	(12)
1338-1185	CH2 wag progression	(5, 12)
1076	CH2 antisymmetric rock	(12)
1015	CH2 rock	(12)
890	CH3 rock	(12)
718	CH2 in phase rock	(12)
728		

* only present in MEA myristate spectra due to small amount of myristic acid impurity.

Table 6:6: Summary of MEA carboxylates Raman bands

Band (cm^{-1})	Assignment	Ref.
2958	CH3 o. ph. str.	(36)
2906	NH3+ str.	(36)
2884	CH2 o. ph. str.	(36)
2848	CH2 i. ph. str.	(36)
1461	CH2/CH3 bend	(36)
1440	CH2/CH3 bend	(36)
1297	CH2 chain twist	(36)
1131	C-C-C i. ph. str.	(36)
1062	C-C-C o. ph. Str.	(36)

6.4 Neutralisation of fatty acids by MEA

As TEA stearate can form acid-soaps with stearic acid, it is probable that MEA carboxylates will also form acid-soaps. These acid-soaps can be screened for by neutralising fatty acids to various degrees to cover the a range of acid:soap ratios and characterising the resulting crystals both structurally through PXRD and DSC and chemically via FTIR and Raman spectroscopy. These resulting data can be used to establish the stoichiometry of any acid-soaps and build MEA carboxylate – fatty acid phase diagrams.

6.4.1 Lauric Acid

The PXRD patterns of the crystal samples formed from lauric acid neutralised by ethanolamine showed that the samples consisted of mixtures of several structures. The PXRD patterns also showed that they are lamellar structures due to the characteristic d-spacing ratios of the observed peaks. Characterising the structures by the distance between the layers, the ‘long spacing’, there were 5 structures having long spacings of approx.: 19.5, 27.2, and 35.6 Å. The long spacings of 19.5 and 27.2 Å are characteristic of MEA laurate and lauric acid (C form) respectively, as previously determined in sections 6.2 and 6.3. There was a low angle peak at 31.8 Å that matches that of the A-super form of lauric acid but no higher order peaks for the A-super were observed (19). This leaves the 35.6 Å structure as potentially an acid-soap complex or other polymorph of MEA laurate or lauric acid.

Lauric acid (C-form) peaks could be observed between 0-40 % neutralisation, whilst the single peak of the A-super form could be observed with increasing

intensity between 10-30 % neutralisation. The structure with a spacing of 35.6 Å was observed from 20-90 % neutralisation and the wide range of neutralisation suggests that it is an acid-soap; a polymorph of MEA laurate would be unlikely to have strong peaks at low levels of neutralisation and similarly a polymorph of lauric acid would not be likely at 80-90 % neutralisation. From the series of PXRD patterns it was possible to crudely approximate the composition of the acid-soap; insufficient neutralisation will show acid peaks as well as those for the acid-soap, whilst excess neutralisation will show soap peaks and those for acid-soap. This therefore gives a rough approximation as to the acid-soap composition. The PXRD patterns for 40 % neutralisation showed lauric acid (C-form) peaks whilst 60 % neutralisation showed MEA laurate peaks. The 50 % neutralisation pattern has a shoulder on the first peak which corresponds to lauric acid (A-super) however, it shows no other strong peaks of lauric acid or MEA laurate. This suggests that the 35.6 Å lamellar structure is approximately a 1:1 lauric acid – MEA laurate acid-soap.

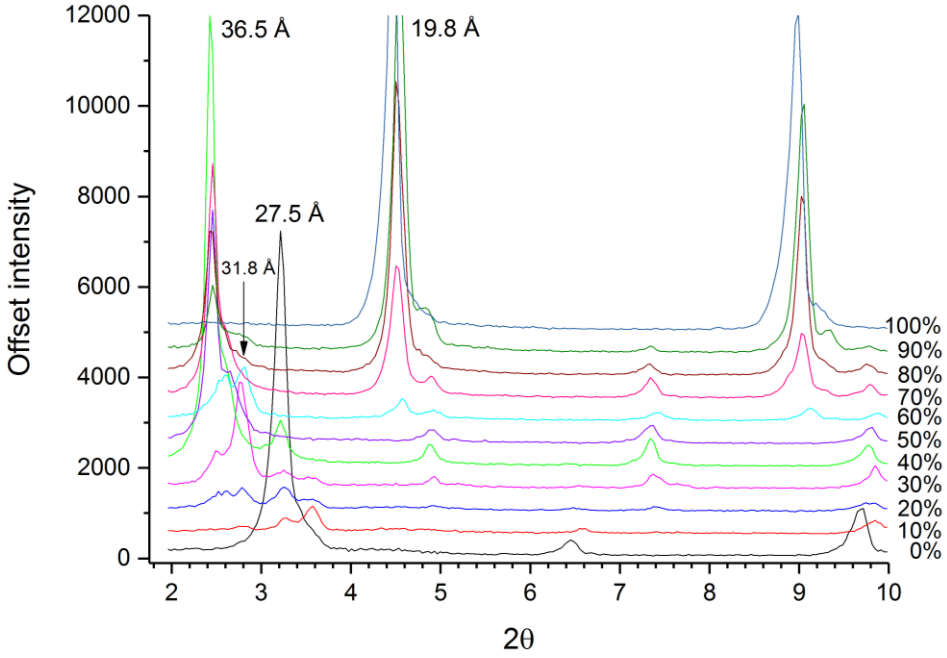

Figure 6.12: Low angle PXRD of lauric acid neutralised to different degrees by ethanolamine showing three sets of lamellar peaks corresponding to structures of d-spacing; 36.5, 27.5, 19.8 Å

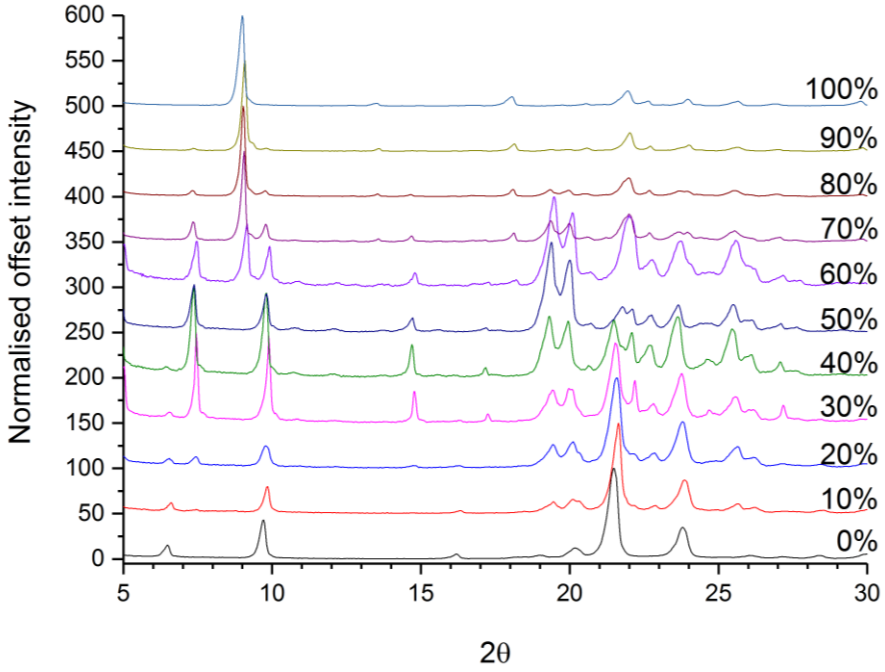

Figure 6.13: PXRD scan of lauric acid neutralised to different degrees by ethanolamine, highlighting the different structures formed both in terms of their lamellar spacing at lower angle (5-15 °2θ) and their packing within the layers (20-30 °2θ)

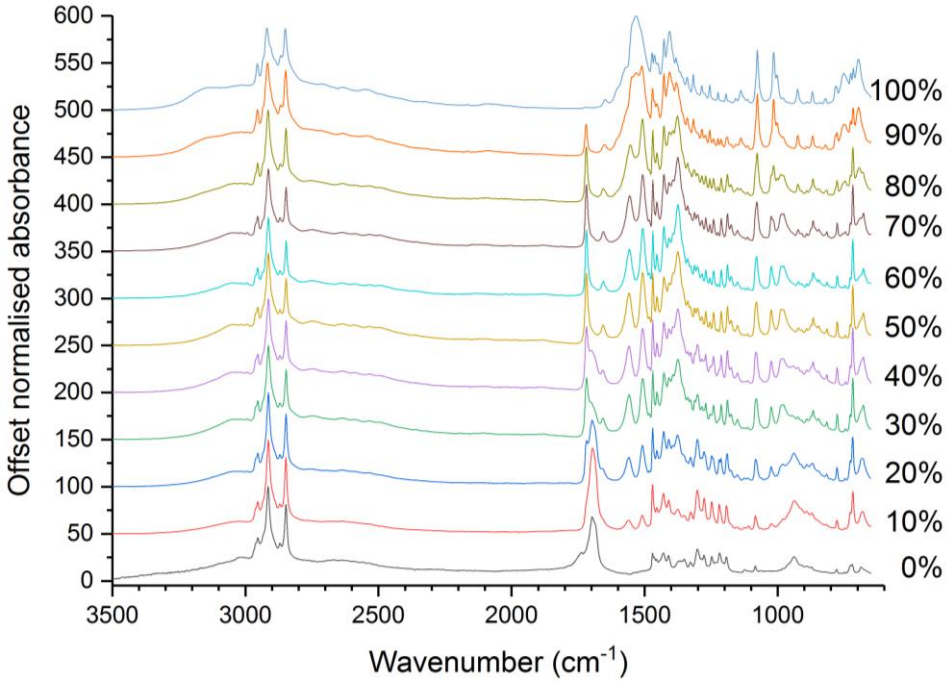

Figure 6.14: Overview of the IR spectra of lauric acid neutralised to various degrees by MEA in 10% increments from lauric acid (0%) to MEA laurate (100%)

The IR spectra collected for the partially neutralised samples of lauric acid are consistent with the observations in the PXRD data, showing a gradual progression from fatty acid to acid-soap to MEA laurate. This progression is

best observed by following the carbonyl asymmetric stretch. In lauric acid, the carbonyl stretch is 1695 cm^{-1}, typical for a fatty acid dimer (5, 6, 12). As the percentage neutralisation increases from 10% - 40%, the intensity of the fatty acid carbonyl peak decreases until it is no longer present and a new peak at 1719 cm^{-1} forms, initially as a shoulder. The peak at 1719 cm^{-1} is a carboxylic carbonyl peak that is either not or much less hydrogen bonded compared to in a fatty acid dimer (49). The intensity of the peak at 1719 cm^{-1} increases up to 50% neutralisation before decreasing and not being present in the fully neutralised MEA laurate spectra. The carbonyl peak behaviour is consistent with the suggestion from the PXRD pattern that the MEA laurate acid-soap has a stoichiometric ratio of 1:1. Similarly, the carboxylate stretching region between 1500-1600 cm^{-1} also shows significant changes as a function of neutralisation. As the degree of neutralisation increases, peaks at 1540 and 1510 cm^{-1} appear and increase in intensity up to 50% neutralisation. These peaks are likely a doublet for the antisymmetric COO- stretch as has been observed for metal carboxylates (47). As neutralisation increases further, these peaks fall in intensity and a peak centred at 1530 cm^{-1} begins to appear at 60% before merging with the doublet at 90% neutralisation.

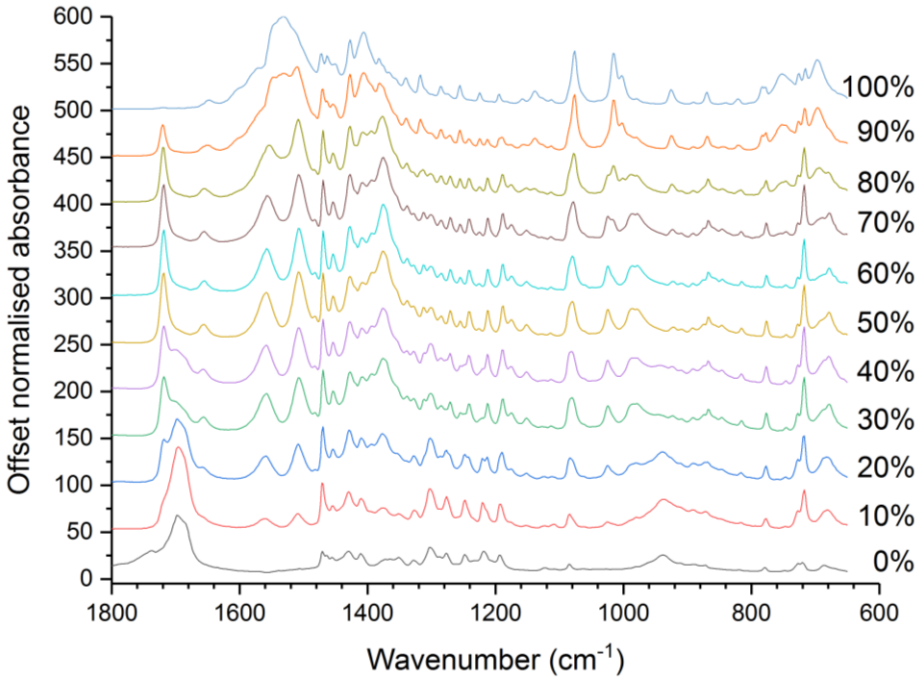

Figure 6.15: IR spectra of partially neutralised lauric acid samples, focussing on the more diagnostic lower wavenumber region

Differences in the IR spectra can also be observed in the CH2 wagging region between 1380-1150 cm^{-1}. There are three distinct set of wagging progression peaks that can be assigned: lauric acid (0%), MEA laurate (100%), and the acid-soap (50%). As the degree of neutralisation is increased peaks belonging

to lauric acid decrease in intensity whilst those belonging to the acid-soap increase in intensity. After 50% neutralisation, the peaks belonging to the acid-soap decrease in intensity until they are no longer visible in the completely neutralised spectra. In the 50% neutralised sample, the acid-soap, there are two sets of regularly-spaced CH2 wagging vibrations. One of these sets closely correspond to that of MEA laurate, which suggests that the other set are due to the acid molecule.

As Raman spectroscopy is less sensitive to polar, asymmetric stretches than FTIR, such as carbonyl/carboxylate groups, the differences between the recorded spectra at various neutralisations are more subtle due to the smaller changes in the alkyl chains. The Raman spectra can be split into two regions; 3200-2500 cm^{-1} and 1800-800 cm^{-1}.

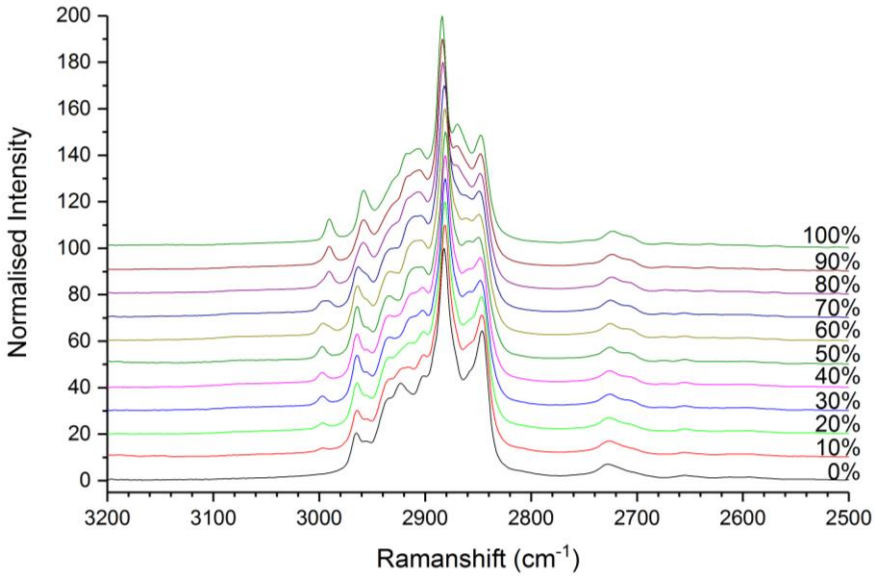

Figure 6.16: 3200-2500 cm region of the Raman spectra of lauric acid neutralised to different degrees by MEA in 10% increments

The 3200-2500 cm^{-1} region shows subtle changes as the degree of neutralisation changes. From 10% onwards, a peak emerges at 2997 cm^{-1} and increases with intensity as the degree of neutralisation increases up to 50%. From 60% upwards, it decreases in intensity whilst a peak at 2990 cm^{-1} appears and increases in intensity. The behaviour of these peaks can be linked to the acid-soap and soap respectively as the behaviours match those of the expected composition changes; the acid-soap concentration will increase up to a maximum at 50%, whilst the soap concentration will obviously be a maximum at 100%. The peak at 2965 cm^{-1} for the 0-50% samples shifts to 2958 cm^{-1} for the 60-100% samples. There are other slight changes in peak position between the acid, acid-soap, and soap but these are minor and of the scale of a 2-3 cm^{-1} shift.

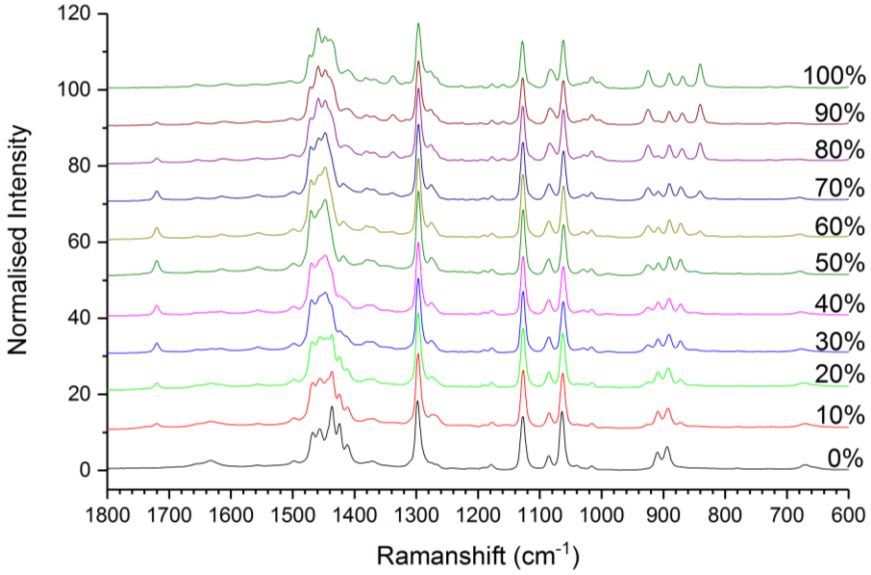

Figure 6.17: 1800-800 cm^{-1} region of the Raman spectra of powder samples of the partially neutralised lauric acid samples neutralised by MEA in 10% increments

The 1800-800 cm^{-1} region displays the largest differences between the various crystal samples. For all of the partially neutralised samples. (10-90% neutralisation), there is a carbonyl stretch peak at 1720 cm^{-1}. The carbonyl stretch is not usually Raman active, such as in the lauric acid dimer, but can become Raman active due to symmetry reasons. The presence of the carbonyl stretch at 1720 cm^{-1} suggests that fatty acid molecules that are part of the acid-soap structure are not strongly hydrogen bonded (50). The peak increases in intensity up to 50% neutralisation, before decreasing with increasing neutralisation. This carbonyl peak can therefore be assigned to the acid-soap, which would be in agreement with the FTIR and PXRD results. Similarly, differences in the CH2 rocking vibrations can be used to distinguish the components in the samples. In lauric acid, the 0% sample, the CH2 rocking vibrations are at 894 and 909 cm^{-1} whilst in the partially neutralised samples, up to 50 %, these peaks shift to 890 and 907 cm^{-1}, with additional peaks at 872 and 924 cm^{-1}. Above 50% neutralisation, the peak at 907 cm^{-1} decreases in intensity until it is no longer present at 100% neutralisation whilst a new peak at 840 cm^{-1} appears and increases in intensity (43). These CH2 rocking peaks can therefore be used to distinguish between the acid-soap, soap, and acid. The CH3 and CH2 deformation region, 1400-1500 cm^{-1}, also shows differences with the acid-soap, soap, and acid having distinct series of peaks within this region that can be used to distinguish between the components. The C-C stretching vibrations (1127, 1085, 1062 cm^{-1}) show more subtle changes with neutralisation, shifting from 1064 cm^{-1} in the acid to 1062 and 1063 cm^{-1} for the acid-soap and soap respectively. The 1085 cm^{-1} peak shifts

slightly lower for the 100% neutralised sample whilst the peak at 1127 cm^{-1} didn't shift with changing neutralisation. The CH2 twist vibration at 1296 cm^{-1} also didn't shift with degree of neutralisation (43).

Multivariate curve resolution was performed on the IR and Raman spectra of the series of partially neutralised lauric acid samples. The purest variable detection method was used to obtain an initial estimate of the spectra and for both sets of data the samples selected three components; 0%, 50%, and 100% neutralised samples. The 0% and 100% samples are pure lauric acid and MEA laurate respectively and the 50% is potentially pure 1:1 MEA laurate – lauric acid acid-soap. The determined concentration profiles that were averaged and are shown in Figure 6.18, were consistent with the results from analysis of the PXRD patterns and the FTIR and Raman spectra; lauric acid concentration rapidly falls to a low value by 30% neutralisation, acid-soap concentration peaks at 50% neutralisation, and MEA laurate concentration steadily increases from 50% neutralisation.

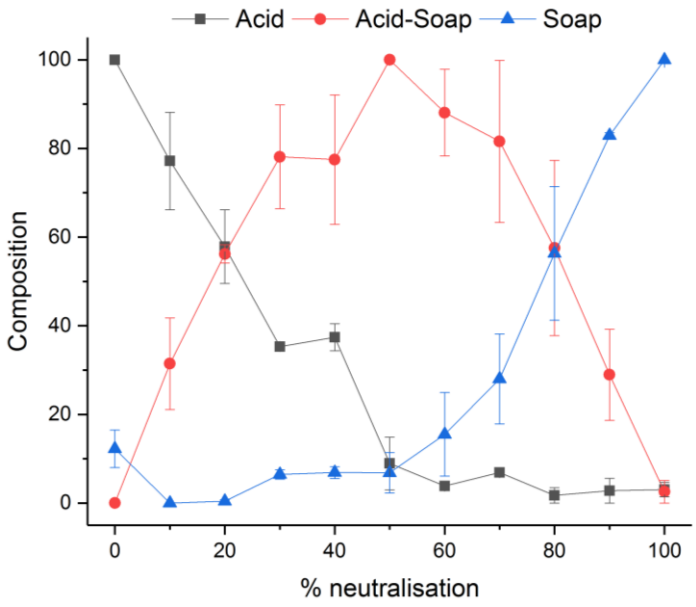

Figure 6.18: Average MCR-ALS analysis concentration profiles showing the evolution of the relative concentrations of lauric acid, acid-soap, and MEA laurate with the increase in degree of neutralisation

The determined spectra are consistent with lauric acid, MEA laurate, and the 50% neutralised sample (acid-soap). The percentage of variance explained by the determined concentration profile and determined Raman spectra were 99.89 %, whilst for the IR spectra it was 99.32 %. The determined concentration profiles are consistent with 1:1 acid-soap formation being preferred over either MEA laurate or lauric acid. However, this could be due to the crystallisation conditions during the sample preparation and it could be a kinetics effect – if the crystallisation occurred at relatively high

supersaturation conditions, the acid-soap may form preferably if the kinetics of its formation are much quicker/easier versus the formation of pure MEA laurate and lauric acid.

DSC heating curves of the lauric samples are consistent with the other experimental data with the 0%, 50%, and 100% samples each showing a single sharp melting peak, providing further evidence for a 1:1 acid-soap complex. The DSC data revealed that the acid-soap has a melting point of 55 °C, between that of the lauric acid and MEA laurate, and a melting enthalpy, in terms of kJ per mole per alkyl chain (to account for there being two in the acid-soap), that is only slightly lower than that of MEA laurate.

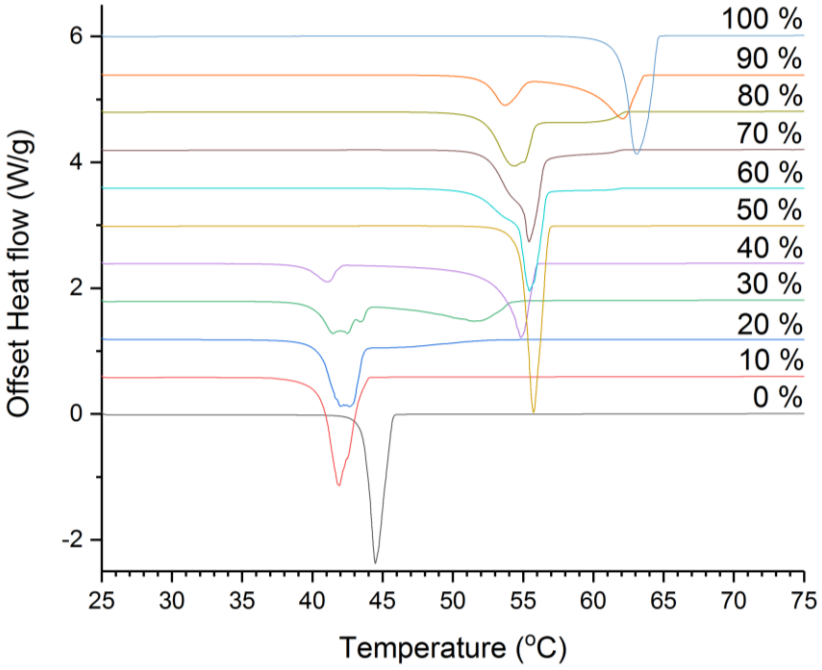

Figure 6.19: DSC curves of lauric samples during heating with the three pure components highlighted

By assuming that the three transitions observed in the DSC traces correspond to three individual components, the relative amounts of each component can be compared through integrating the peak areas of the heat flow (normalised to the sample weight). The energy associated with each transition will be proportional to the amount of that component within the sample. The resulting trend for each of the melting transitions (fatty acid, acid-soap, and soap) with degree of neutralisation were in agreement with those found in FTIR and Raman data using MCR-ALS.

6.4.2 Myristic Acid

The PXRD patterns of the partially neutralised myristic acid samples showed similar trends to those observed in the lauric acid samples. At low angle, sets

of regularly spaced peaks exhibiting the characteristic d-spacing ratios of lamellar structures were observed with long-spacings of: 22.1, 33.3, 37.6, 42.2 Å. The long-spacing of 22.1 Å was observed from 60% neutralisation upward and corresponded to that previously determined for MEA myristate. The spacings of 33.3 and 37.6 Å occurred below 30% neutralisation and correspond to that of myristic acid C-form and A-super respectively (21, 51, 52). The formation of multiple polymorphs from solution crystallisation of myristic acid has previously reported, with the C-form being the dominant polymorph (16). The long-spacing 42.2 Å was dominant between 30-70 % and was present up to 90 % neutralisation. At 50 % neutralisation, the 42.2 Å structure was the only set of peaks observed at low angle suggesting that the sample was of a pure component – a 1:1 acid-soap similar to that observed in the lauric samples.

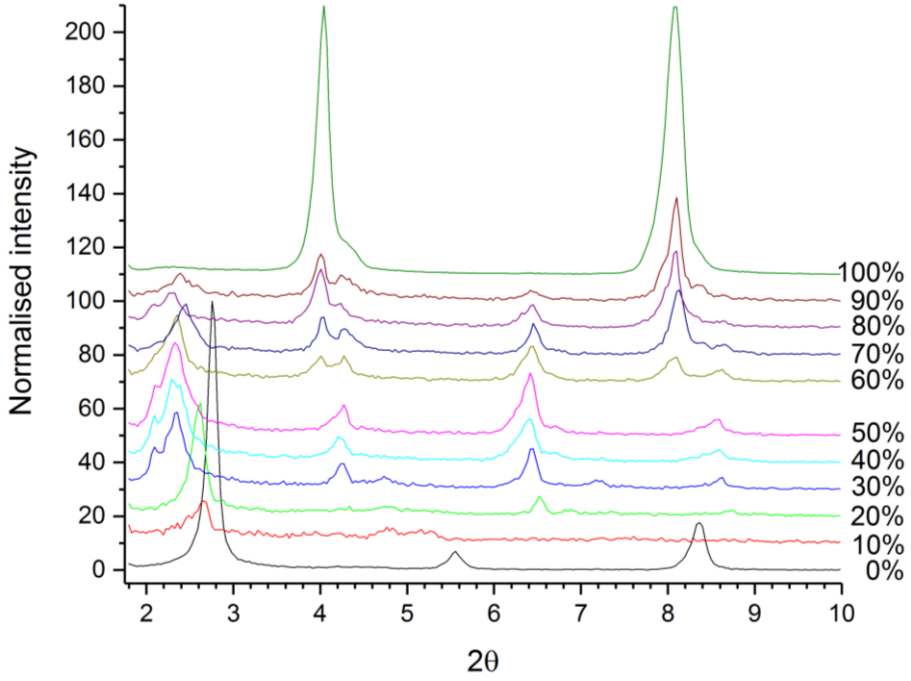

Figure 6.20: Low angle PXRD patterns of myristic acid samples neutralised to varying degrees.

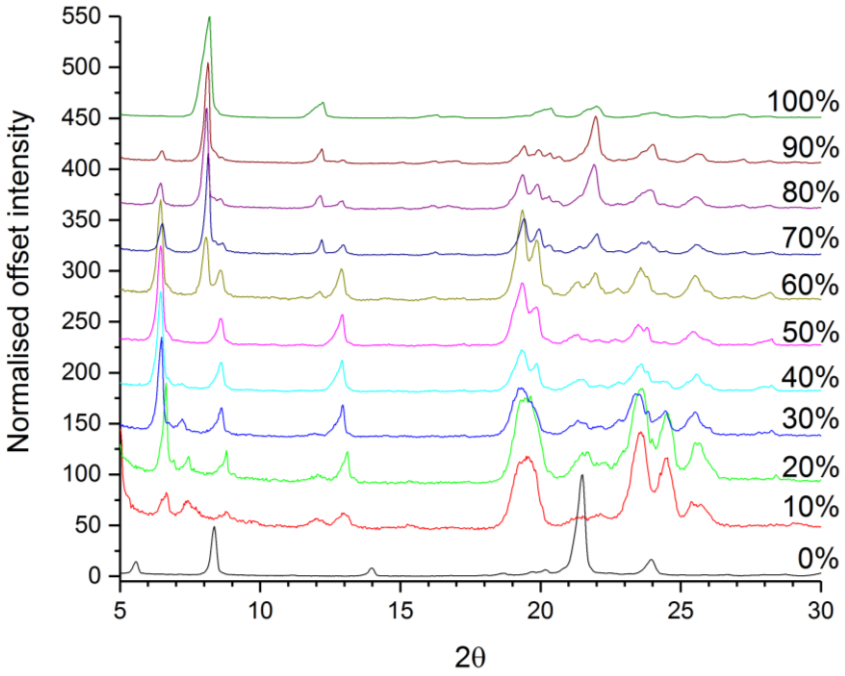

Figure 6.21: Wide-angle PXRD of partially neutralised myristic acid samples

The FTIR data for the myristic samples showed similar trends to those found for the lauric acid samples, therefore only the major peaks and differences between chain lengths will be discussed for myristic acid and the longer acids.

An acid carbonyl at 1696 cm^{-1} is observed up to 30% neutralisation, whilst at 10% a new carbonyl peak at 1719 cm^{-1} appears and increases in intensity up to 50% and is present up to 90% neutralisation. As in the lauric acid samples, the carbonyl peak at 1719 cm^{-1} is assigned to the 1:1 acid-soap and arises from the acid-component of the co-crystal. The carboxylate peak positions are shifted compared to the lauric acid samples however, appearing at 1510 and 1559 cm^{-1}.

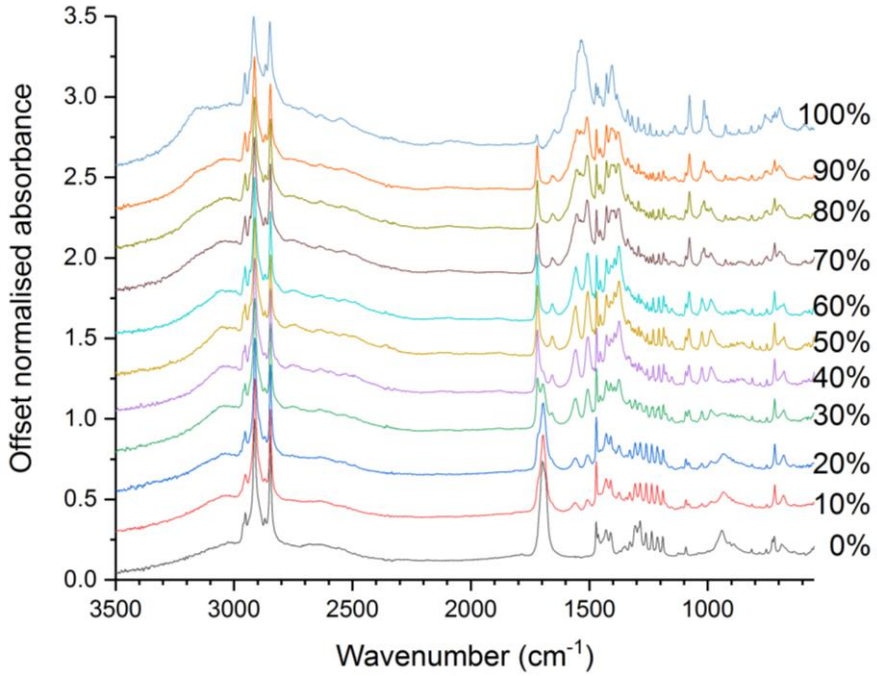

Figure 6.22: FTIR spectra of myristic acid samples neutralised to various degrees by MEA

The CH2 wagging vibrations also show similar trends to the lauric acid samples, with the acid and the MEA soap showing distinct sets of wagging progressions and the acid-soap appearing to have two sets of CH2 wagging progressions, one acid-like and the other soap-like.

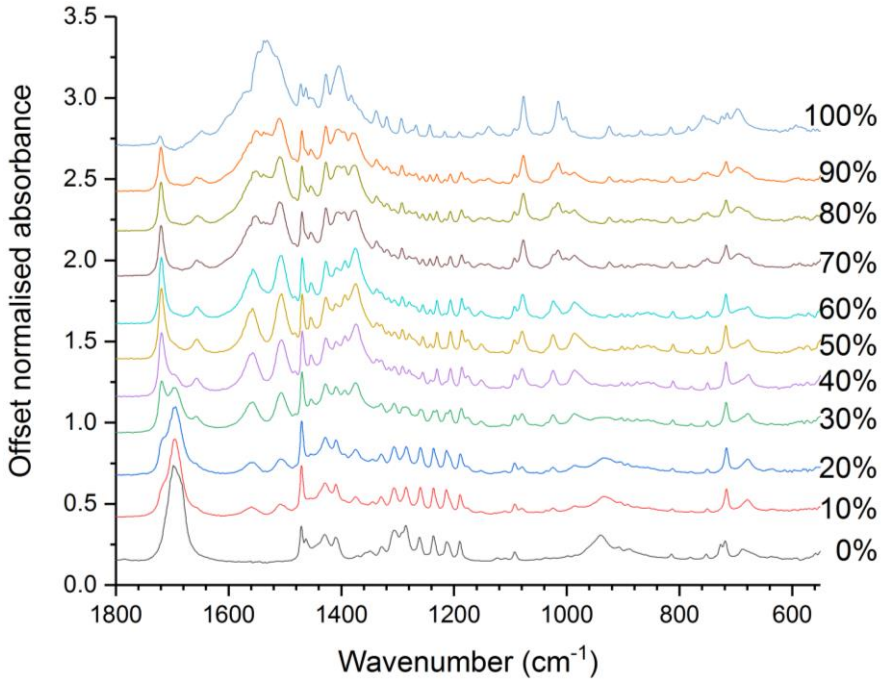

Figure 6.23: FTIR spectra of the headgroup region (1800 – 1500 cm^{-1}) and CH2 wagging region (1350-1150 cm^{-1}) of partially neutralised myristic acid samples

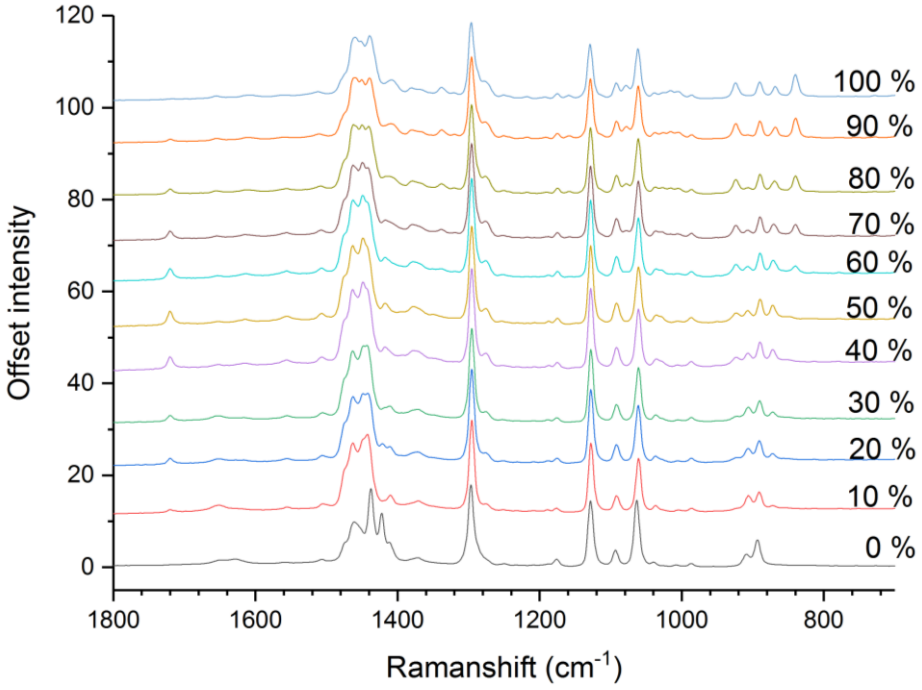

Figure 6.24: Raman spectra of powder samples of myristic acid neutralised to various degrees

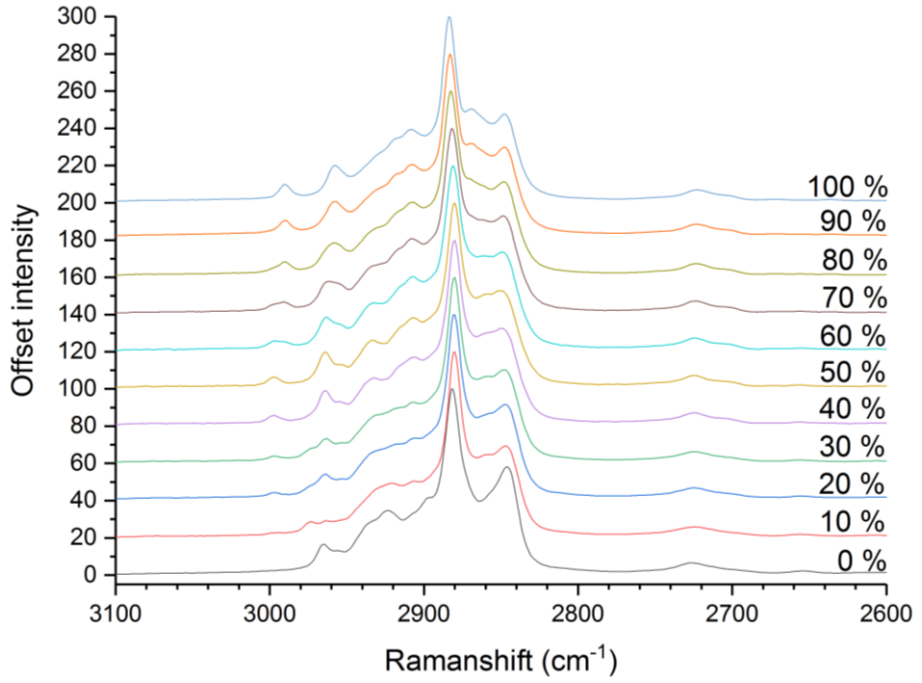

Figure 6.25: Raman spectra of powder samples of partially neutralised myristic acid, focussing on the CH2 and CH3 stretching region

The Raman spectra of the myristic acid samples show similar trends to those identified for the lauric acid samples. In the 1800-800 cm^{-1} range, Figure 6.24, the carbonyl peak at 1719 cm^{-1} is present for all the partially neutralised samples (10-90%), the CH2 twist at 1296 cm^{-1} is consistent for all samples, the C-C stretch vibration at 1063 cm^{-1} in the acid slightly shifts with increasing

neutralisation to 1061 cm^{-1} whilst the C-C stretches at 1092 and 1128 cm^{-1} do not shift. There are distinct changes in the CH3 and CH2 deformation region, 1500-1400 cm^{-1}, as the acid becomes neutralised, first into acid-soap and then soap. The CH2 rocking vibrations were at 894 and 908 cm^{-1} in the acid, shifting to 890 and 906 cm^{-1} in the partially neutralised samples, with the peak at 906 cm^{-1} decreasing in intensity after 50% neutralisation until no longer present in the 100% sample (43).

MCR-ALS analysis of the FTIR and Raman data for the myristic samples identified 3 components and their relative concentrations as a function of neutralisation. Two of the component spectra were consistent with the spectra previously recorded for myristic acid and MEA myristate, whilst the third matched that recorded for a 50% neutralised sample. The third component was therefore assigned to a 1:1 acid-soap and was consistent with the expected structure, including the position of the carbonyl peak at 1719 cm^{-1} in the IR/Raman spectra, and the spectra assigned to the acid-soap by MCR-ALS analysis of the lauric samples. The determined concentration profiles were consistent with that found for the lauric samples and were in agreement with the PXRD of the myristic samples with respect to the observed trend of the lamellar structures. However, there were larger differences in composition trends identified by MCR analysis of the Raman and IR data as shown by the error bars in Figure 6.26, though the overall general trend is still consistent with that identified for the lauric acid samples. The profiles further support the hypothesis that a 1:1 acid-soap forms and that its formation is preferred over that of either myristic acid or MEA myristate.

The DSC heating ramps for the myristate samples in Figure 6.27 show similar trends to those for the laurate samples but shifted to higher temperatures. The 50% sample shows a single sharp transition which is consistent with the melting peak of a pure component at 64.2 °C – the 1:1 acid-soap. The melting enthalpy, in terms of kJ/mol/chain, of the 50% sample is very close to that determined for 100% sample, the pure soap, with values of 56.08 and 56.09 kJ/mol/chain respectively. The melting enthalpy for myristic acid, the 0% sample, was determined to be much lower at 39.9 kJ/mol/chain.

Analysis of the three transition enthalpies as a function of neutralisation showed similar trends to those determined by MCR-ALS from the FTIR and Raman data. There are slight differences however as the trends from the DSC data showing steeper changes in neutralisation and that myristic acid is still present in the 50% sample. The overall shapes of the trends are consistent and these minor differences are due to slight differences in composition

between the individual DSC and FTIR samples and the different sensitivities of each technique.

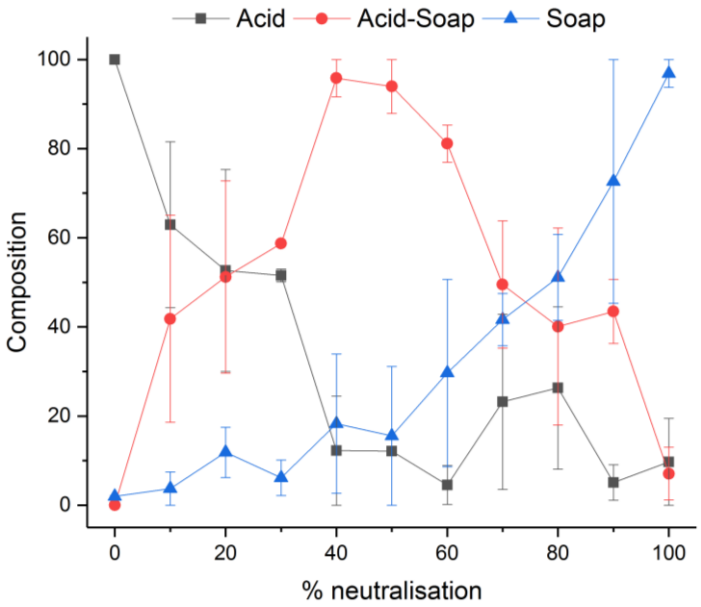

Figure 6.26: Average concentration profiles as a function of degree of neutralisation for MEA myristate, myristic acid, and their 1:1 acid-soap as determined by MCR-ALS using FTIR and Raman data

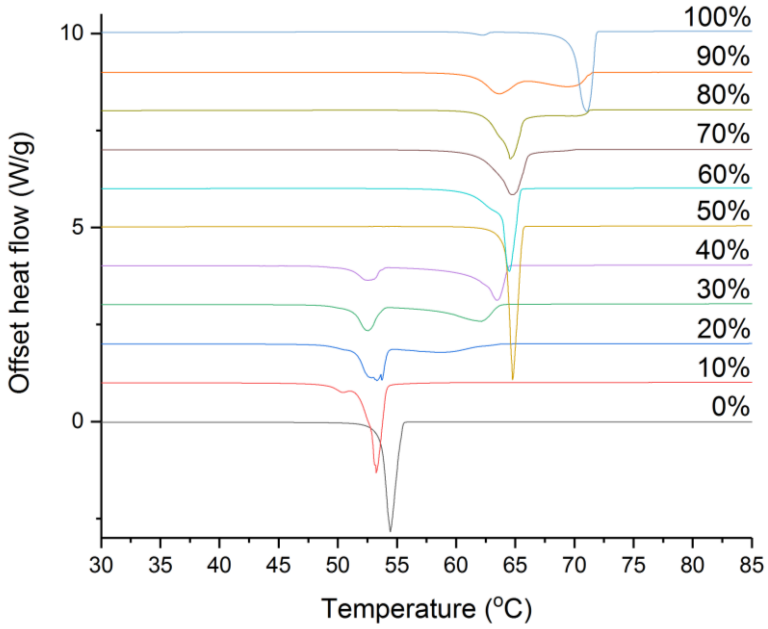

Figure 6.27: DSC curves of heating ramps of partially neutralised myristic acid samples with the three pure components highlight: myristic acid, MEA myristate, and their 1:1 acid-soap

6.4.3 Palmitic Acid

The low angle PXRD patterns for the palmitic acid samples partially neutralised by MEA indicated that a single acid-soap formed. At low degrees of neutralisation (0-20%), the pattern is dominated by that of palmitic acid C-

form, with some evidence of the E form being present. Between 30-60% neutralisation, the pattern shows a series of evenly spaced peaks, corresponding to a lamellar structure, most likely the acid-soap. Due to a change in the XRD equipment configuration, the pattern below approx. 2 2θ in Figure 6.28 is not due to the sample. This resulted in the 1st peak in the lamellar series of the acid-soap being cut-off, as evidenced by the peak shape and the expected peak position based on the higher order lamellar peaks. The expected peak position was calculated from the characteristic lamellar d-spacing ratios and lamellar peaks n = 2, 3, 4 and was found to be at 1.98 2θ, just below the signal cut off and explaining the apparent peak at approx. 2.1 2θ. The d-spacing of the lamellar structure of the acid-soap was therefore determined to be 44.7 Å. At neutralisations from 60% to 100%, a lamellar series of peaks with a d-spacing of 24.7 Å appeared. These peaks correspond to those determined for MEA palmitate. The PXRD patterns therefore show similar trends to those for the other chain lengths; mixtures of acid-soap and acid below 50%, and mixtures of acid-soap and soap above 50%.

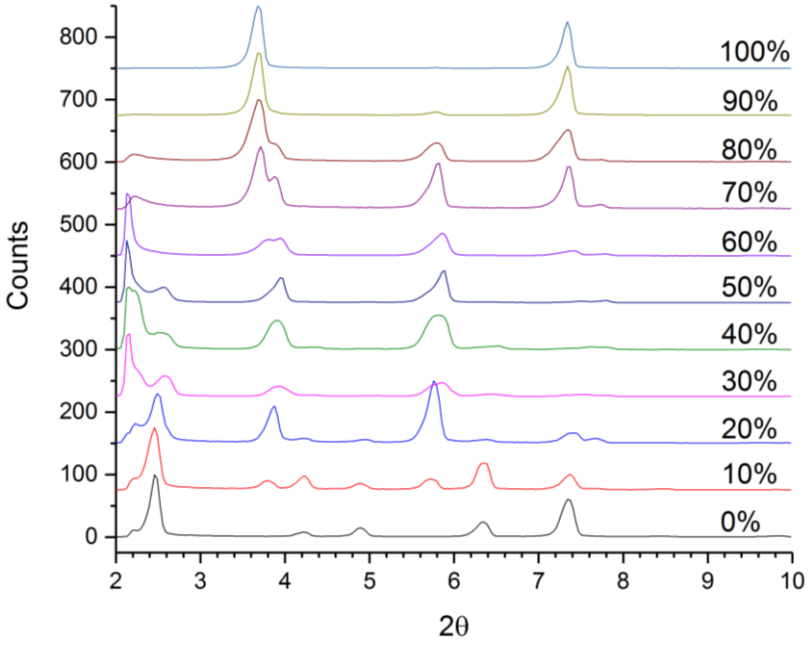

Figure 6.28: Low angle PXRD scan of partially neutralised samples of palmitic acid

The FTIR spectra of partially neutralised palmitic acid samples in Figure 6.29 exhibit similar trends to those observed for lauric and myristic acids. In the headgroup region, 1800-1500 cm^{-1}, a broad acid dimer carbonyl peak was present at 1698 cm^{-1} for 0-40 neutralisation, whilst at 50% neutralisation it may have been present as a shoulder. The acid-soap carbonyl peak at 1720 cm^{-1} was present from 10-90% neutralisation. The carboxylate peak positions were similar to those for the myristic samples, appearing at 1559 and 1508 cm^{-1}.

The CH2 wagging region between 1350 – 1180 cm^{-1} showed a transition from the regularly ordered wagging progression of palmitic acid C form to a set of peaks at 50% neutralisation that were not as well ordered that appeared to have 14 peaks which would correspond to two different sets of wagging progression – one acid-like and one soap-like. As the degree of neutralisation increased further and up to 100%, the soap-like CH2 wagging peaks shifted to their position in the pure soap whilst the acid-like CH2 peaks disappeared. The 90% neutralised sample showed an unexpected feature in its spectra – a broad peak at 1740 cm^{-1}. This peak was not observed for any of the other palmitic acid samples or in any of the other chain lengths. The peak was likely a carbonyl peak, shifted

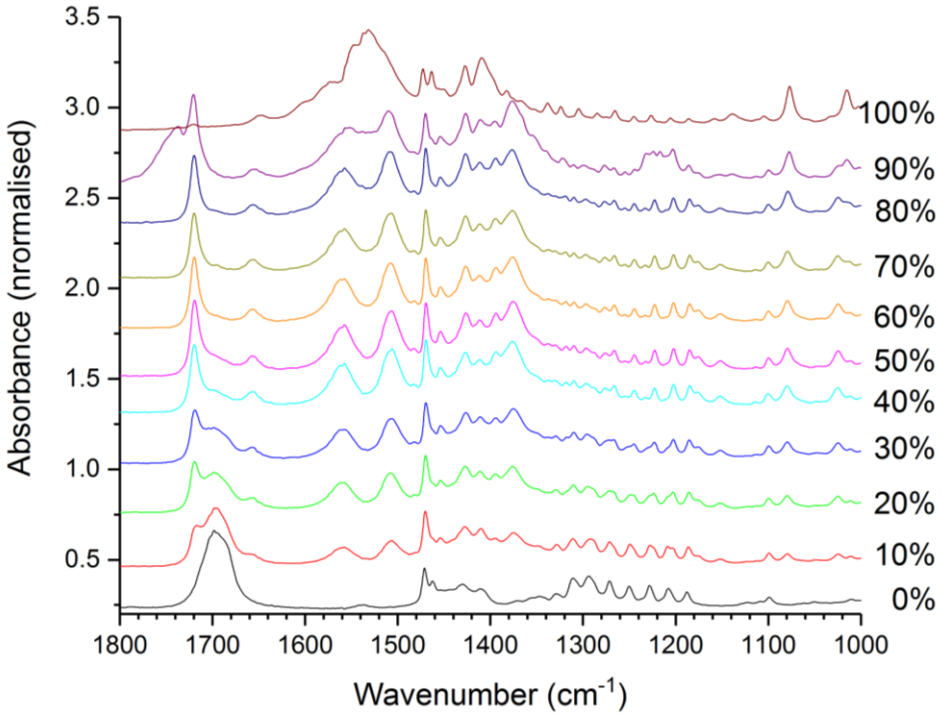

Figure 6.29: FTIR spectra of partially neutralised palmitic acid

The variation in Raman spectra with degree of neutralisation for the palmitic acid sample followed the trends established by the other chain lengths. In the 1800 – 1000 cm^{-1} region, the weak peak at 1719 cm^{-1} assigned to a carbonyl stretch was present for the 10-90% neutralised samples, with maximum intensity in 40-70% samples. The CH2 twist at 1296 cm^{-1} was consistent for all the samples as the CH2 twisting vibration is unlikely to change due to the similarity between the alkyl chain environments in the acid, acid-soap, and soap. Similarly, the C-C stretching vibrations at 1129 and 1099 cm^{-1} are consistent. However, the C-C stretch at 1062 cm^{-1} in the acid shifted to 1060 cm^{-1} at 50% neutralisation before shifting to 1061 cm^{-1} in the soap. The CH3 and CH2 deformation region at 1400-1500 cm^{-1} showed distinct changes on

increasing neutralisation. The deformation peaks can be observed to shift from being pure acid peaks to a combination of acid peaks and another set of peaks – the acid-soap – at neutralisations from 10-50%. The same can be said of those belonging to MEA palmitate as the neutralisation decreases; the deformation region is a combination of MEA palmitate and the acid-soap deformation peaks, though the difference is less pronounced. The CH2 rocking vibrations also showed the ability to differentiate between the different components with the samples, changing from 893 and 908 cm^{-1} in the acid to 890 and 907 cm^{-1} in the partially neutralised samples up to 50%, after which the 907 cm^{-1} peak decreases in intensity.

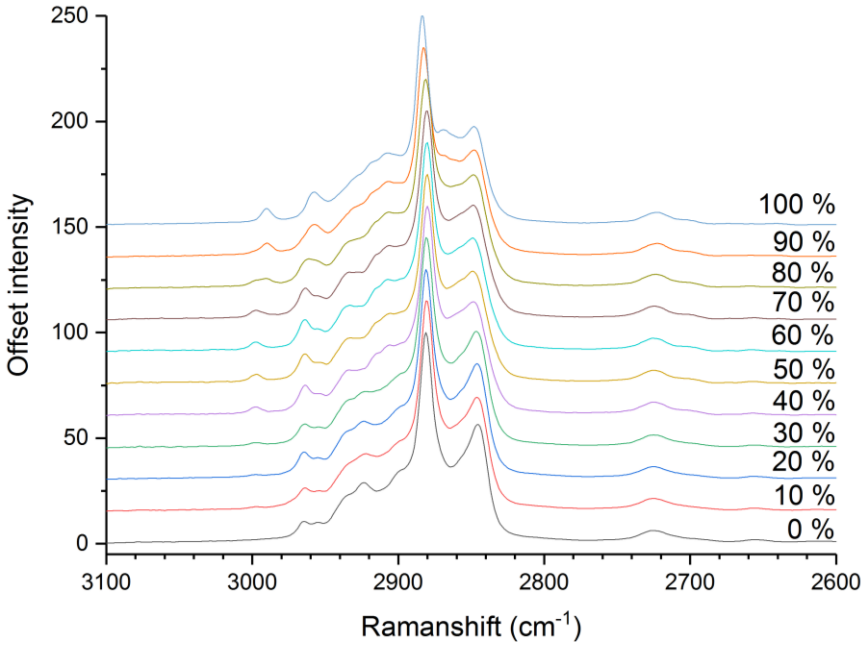

Figure 6.30: Raman spectra of partially neutralised samples of palmitic acid, focussing on the CH2 and CH3 stretching region

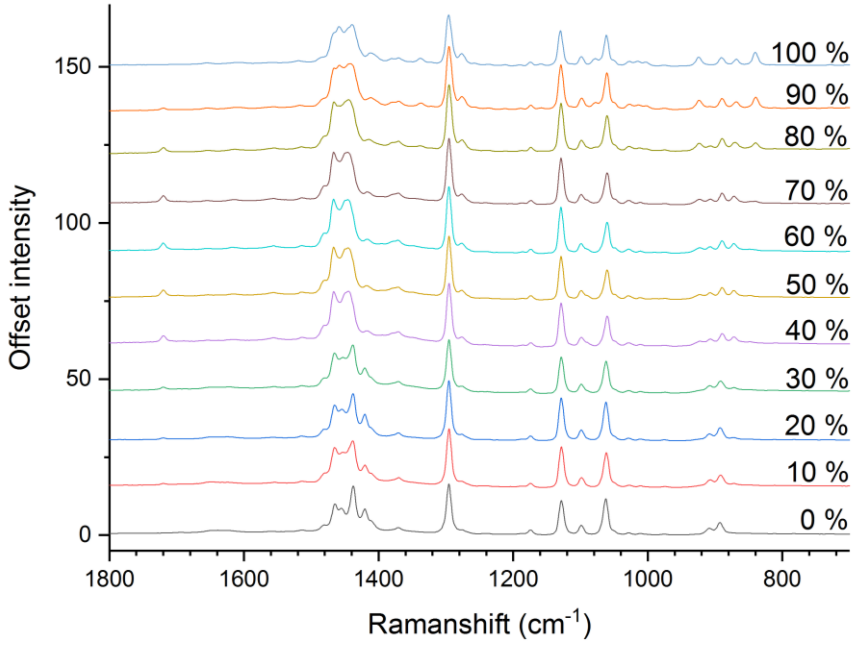

Figure 6.31: Raman spectra of partially neutralised samples of palmitic acid, focussing on the 1800-800 cm^{-1} region

The results of the MCR-ALS analysis of the FTIR and Raman data showed similar results to those obtained for the other chain lengths. The three spectra determined for the individual components were consistent with the 0%, 50%, and 100% neutralised samples and were therefore assigned to palmitic acid, MEA palmitate – palmitic acid acid-soap, and MEA palmitate. The Raman spectra determined captured the majority of the features of the three components but there were subtle differences that were enough to affect the concentration profile determined, hence the larger differences identified by Raman and IR. The concentration profiles followed similar general trends to those already established for the lauric and myristic samples, with the exception of the trend for acid-soap. The trend determined for the Raman and the IR data were similar, but the key difference was that the amount of acid-soap increased in the Raman trend up to 80% neutralisation before decreasing. In contrast, the trend from the IR data plateaued between 40-90% neutralisation and thus averaging resulted in a peak at 80% neutralisation. The concentration profiles showed that below 50% the samples were composed of palmitic acid and acid-soap, whilst above 50% the samples were acid-soap and MEA palmitate.

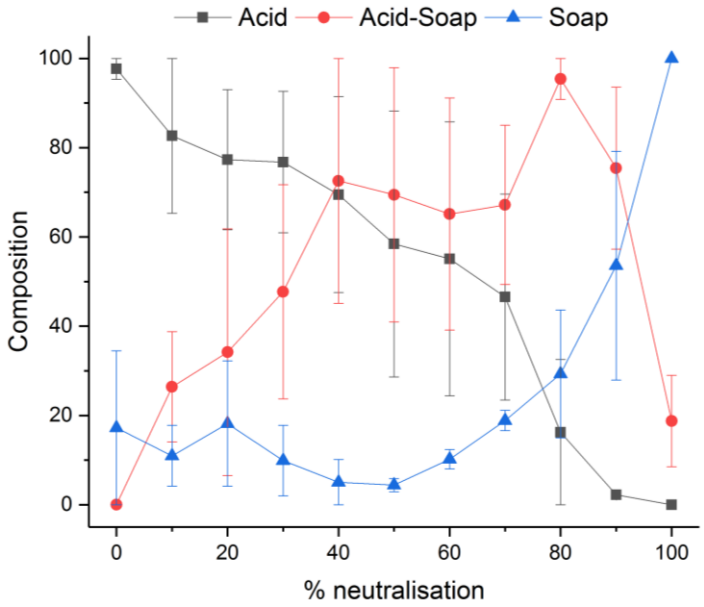

Figure 6.32: Average concentration profiles of MEA palmitate, palmitic acid, and their acid-soap as determined by MCR-ALS using FTIR and Raman data for the partially neutralised palmitic acid samples.

The DSC heating curves of the partially neutralised palmitic acid samples showed similar general trends to those observed for the shorter chain lengths. Between concentrations of 0 - 50% neutralisation, the first thermal transition is observed at approx. 61 °C and corresponds to the melting of palmitic acid. The energy absorbed during this transition decreases as the degree of neutralisation increases until the transition was no longer visible at 60% neutralisation, meaning that palmitic acid was no longer present in the sample. From 30% neutralisation, a second transition was observed at approx. 71 °C which corresponded to melting of the acid-soap. This transition increased in sharpness, reaching a maximum in the 60% sample before broadening and decreasing in magnitude from 70%. The transition was still visible in the 100% sample trace which indicated that there was still a small quantity of acid-soap produced in the 100% neutralised sample. It was only at 90% neutralisation at which the melting transition of MEA palmitate was observed as a broad peak at approx. 75 °C.

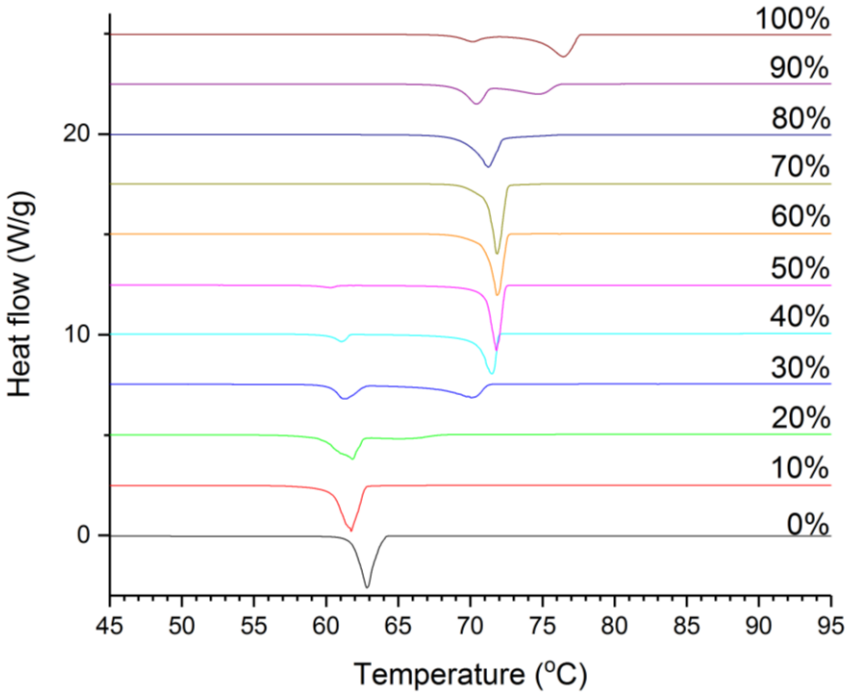

Figure 6.33: DSC traces during heating ramps at 1 °C/min of samples of palmitic acid neutralised to various degrees by MEA

6.4.4 Stearic Acid

The PXRD patterns of the partially neutralised samples showed a number of different components formed as the degree of neutralisation increased.

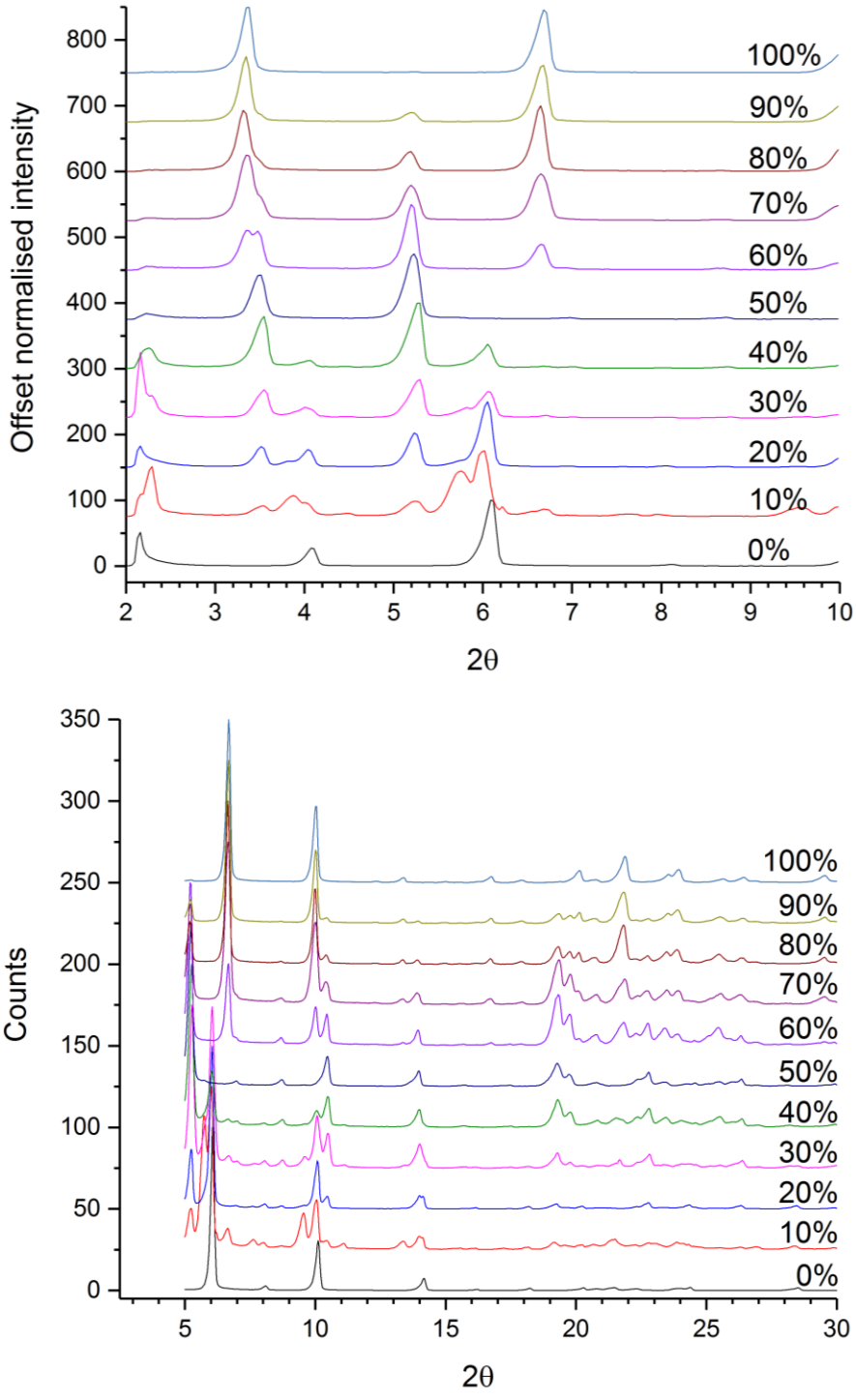

Figure 6.34: Low-angle XRD patterns of stearic acid to various degrees by MEA

The 0% sample pattern was consistent with that of the B or E form of stearic acid, whose similar structures and resulting patterns make positive determination difficult (24, 25). The 10% neutralised sample pattern shows a

mixture of components with peaks consistent with the C form and B/E forms of stearic acid, with low angle measurements suggesting two other lamellar structures are present with long-spacings of approx. 49.6 and 45.3 Å whose n = 1 peaks were not observed but calculated from the other peaks in the series (16). The d-spacing of 45.3 Å is close to the reported long-spacing of the A form of stearic acid; 46.6 Å (51, 53). The formation of the A, C, and E polymorphs of stearic acid has been reported for stearic acid partially neutralised by triethanolamine in aqueous solution (14). From 20% neutralisation upwards, the dominant form of stearic acid observed in the PXRD was the C form. Peaks belonging to stearic acid polymorphs could be observed up to 40% neutralisation. The lamellar structure with a long spacing of approx. 49.6 Å (estimated from higher order peaks) was observed from 10% neutralisation to 90% neutralisation, with the 2nd peak of the series at 3.52 2θ becoming a shoulder from 70% neutralisation upwards whilst the 3rd peak at 5.18 2θ remains clearly visible. The pattern for the 50% neutralised sample appears to consist of only the 50 Å structure peaks. From 60% neutralisation, a new lamellar series of peaks appeared with a spacing of 26.3 Å, corresponding to those determined for MEA stearate in section 6.3.

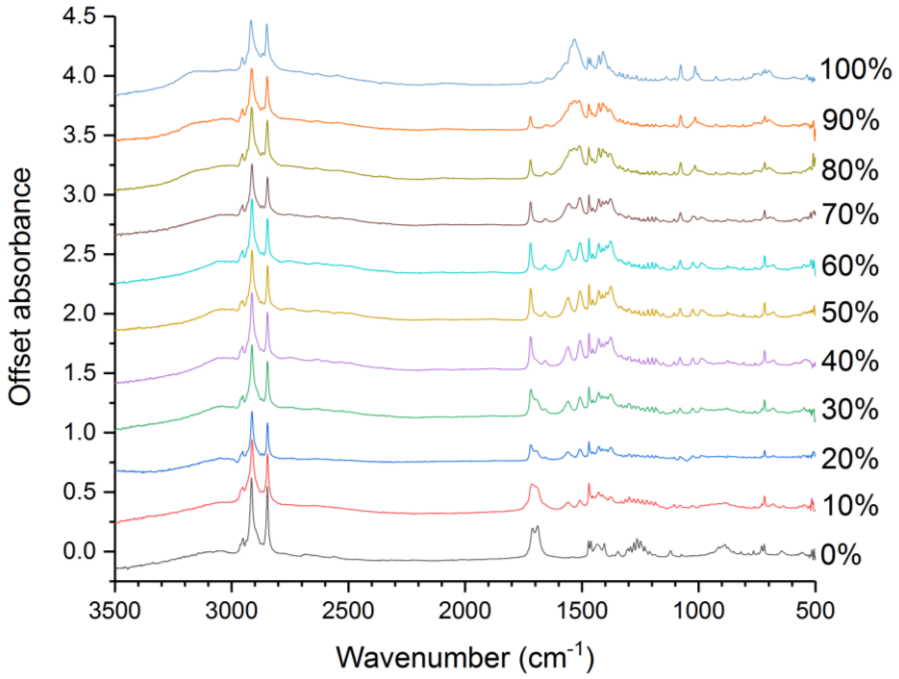

Figure 6.35: FTIR spectra of stearic acid neutralised to different degrees by MEA

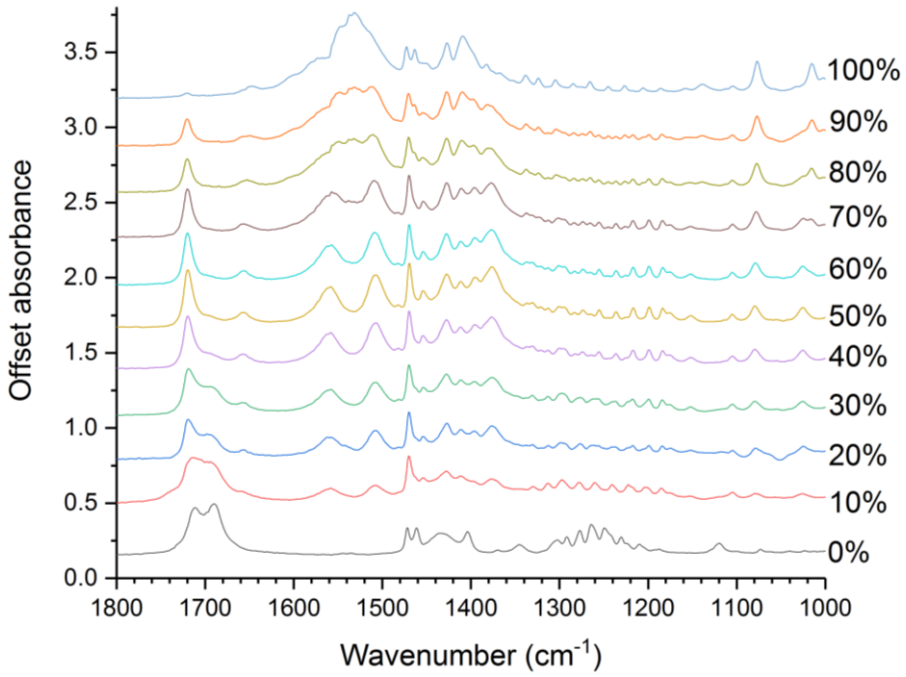

Figure 6.36: FTIR of the partially neutralised stearic acid samples showing the headgroup (COOH and COO^-) stretching region and the CH2 wagging region

The FTIR spectra of partially neutralised stearic acid samples show the same general features observed for the other chain lengths. At 0% neutralisation, stearic acid polymorphs are observed with the dominant polymorph being B based on the splitting of the carbonyl peak at 1689 cm^{-1} and 1712 cm^{-1}, the irregular CH2 wag vibrations between 1320 – 1180 cm^{-1} (54). The presence of a shoulder at 1698 cm^{-1} suggests that the C form of stearic acid is also present. The occurrence of the B and C forms from a slow crystallisation with B being dominant has been previously reported (54). There appears to be a change of stearic acid polymorph from 10% neutralisation and upward from the B form to the A form based on the CH2 wagging region showing regularly spaced peaks and the O-C=O in phase stretch shifted to a double band at 683 cm^{-1} and 638 cm^{-1}. The change in polymorph could be due to addition of MEA but it has also been reported to form in slow crystallisations. Stearic acid carbonyl peaks are visible up to 40% neutralisation. From 20% neutralisation upwards, there is a carbonyl peak present at 1720 cm^{-1} which is assigned to the 1:1 acid-soap, as observed in the other chain lengths. The acid-soap carbonyl peak, which should be absent in pure MEA stearate, is still present in the 100% neutralised sample indicating that acid-soap still formed in the 1:1 molar mixture of stearic acid and MEA. The peak has a low intensity however and the rest of the spectra conforms to that obtained for MEA stearate produced by the slow cooling crystallisation with an excess of MEA. The formation of acid-soap could occur due to measurement error meaning that

there was a slight excess of stearic acid. If this was the case, then this further supports the proposal that acid-soap formation is preferred over both acid and soap formation. Aside from the stearic acid polymorph changes between the 0% and 10% samples, the CH2 wagging region shows similar trends to that observed for the other chain lengths – a shift from the stearic acid wagging progression to a set at 50% neutralisation, the 1:1 acid-soap, which appears to have two sets of wagging progression peaks, and finally to a distinct set at 100% neutralisation that belong to MEA stearate.

The changes in Raman spectra for the partially neutralised stearic acid samples follow the trends observed for the shorter chain lengths. The 10-90% neutralised samples showed the characteristic carbonyl peak at 1719 cm^{-1}. The CH2 and CH3 deformation peaks at 1500-1400 cm^{-1} showed a distinct change between the 0% and 10% samples due to the change in stearic acid polymorphs already identified through IR. Aside from these partially neutralised samples, the trends in CH2 and CH3 deformation followed those established for the other chain lengths.

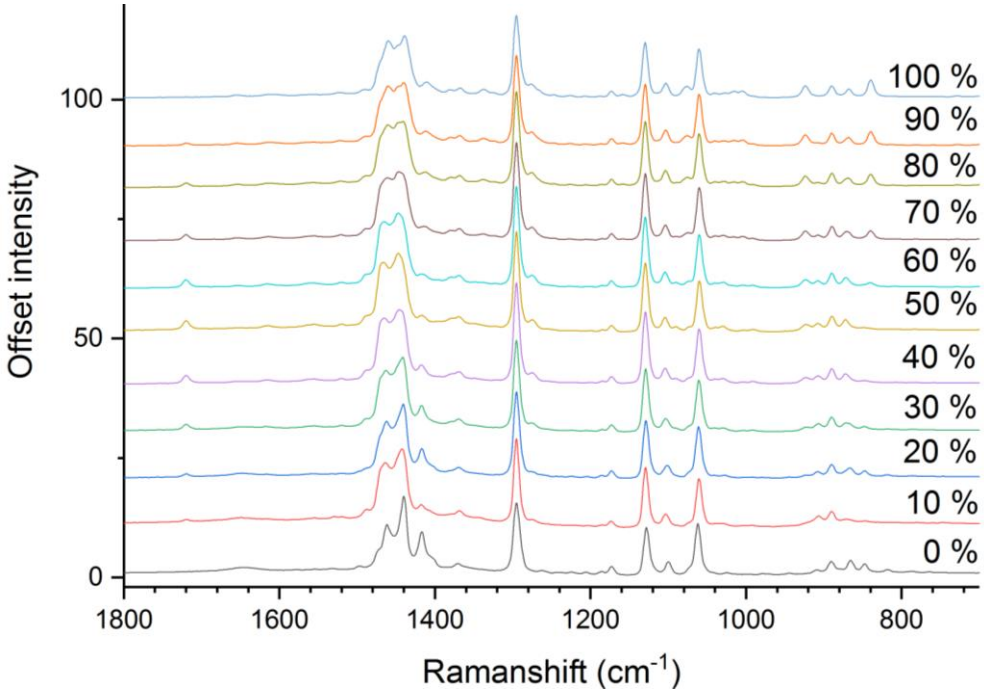

Figure 6.37: Raman spectra of partially neutralised stearic acid samples, focussing on the 1800-800 cm^{-1} region

The CH2 rocking peaks at 950-800 cm^{-1} followed the trends established by the IR and PXRD data and are consistent with those observed for the shorter chain lengths (with the exception of 0% and 10% due to the differing stearic acid polymorphs). From 0% to 50%, the rocking peaks transition from those of stearic acid to those of the acid-soap and from 60% to 100% the peaks of MEA stearate emerge and increase in intensity.

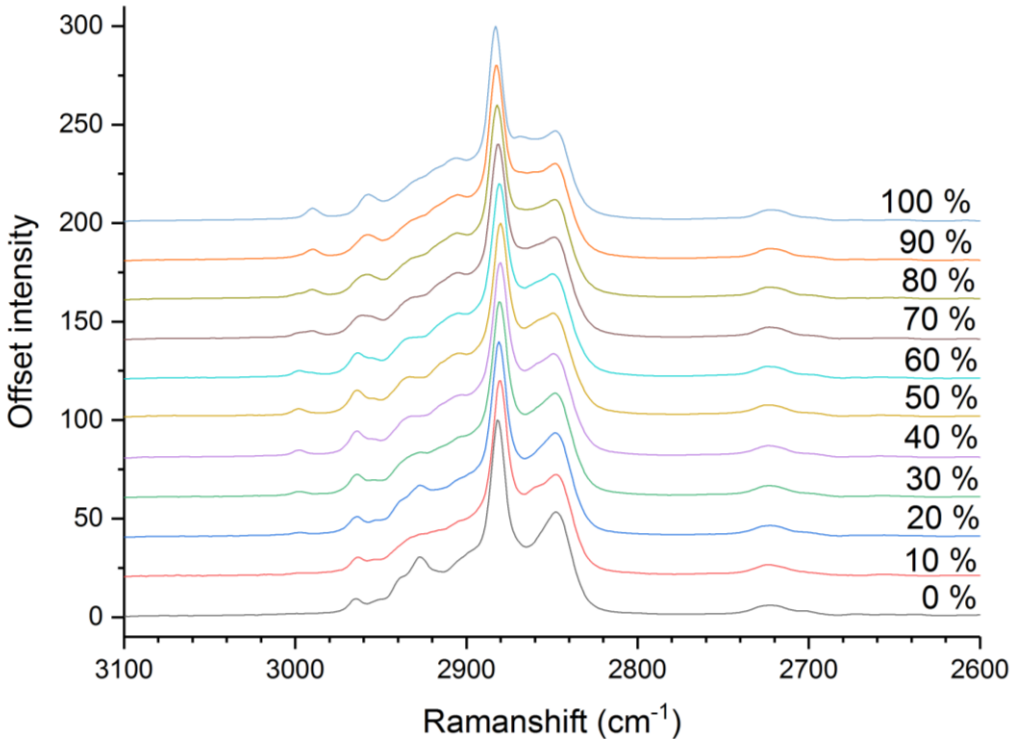

Figure 6.38: Raman spectra of partially neutralised stearic acid samples, focussing on the CH2 and CH3 stretching region

The MCR-ALS analysis for the FTIR was more complicated than for the other chain lengths due to the presence of the different stearic acid polymorphs and their differing IR spectra.

Using 4 components with the MCR-ALS analysis gave mixed results. The analysis provided spectra for the acid-soap and the soap that were in close agreement with those reported and calculated for the other chain lengths with the main differences observed in the CH2 wagging progression (which was expected). However, the spectra for the stearic acid C form was incorrect as it included the carbonyl peak at 1719 cm^{-1}. This affected the determined concentration profiles giving trends that were not in keeping with the experimental data; the concentration profiles appeared to suggest that the 20% neutralised sample was overwhelmingly stearic acid C-form whilst experimental data showed it was a mixture of stearic acid and the acid-soap. They also suggested that stearic acid C-form was present up to 90% neutralisation which did not agree with the other experimental data. The determined concentration profile for the soap was consistent with the other chain lengths and the profile for the acid-soap was consistent bar for the 20% sample.

Running the MCR-ALS analysis with 3 pure components (stearic acid B form, MEA stearate, and acid-soap) gave results that agreed with the trends

observed for the other chain lengths in terms of their spectra and concentration profiles. Three pure component spectra were obtained which corresponded to the 0%, 50%, and 100% samples which corresponded to stearic acid B form, the 1:1 acid-soap, and MEA stearate respectively. The obtained concentration trends are in agreement with those observed for the other chain lengths, with rapid decreases in stearic acid concentration as neutralisation increases, a maximum concentration of acid-soap at 50% neutralisation, and a rapid increase in the concentration of soap as neutralisation increases past 80%.

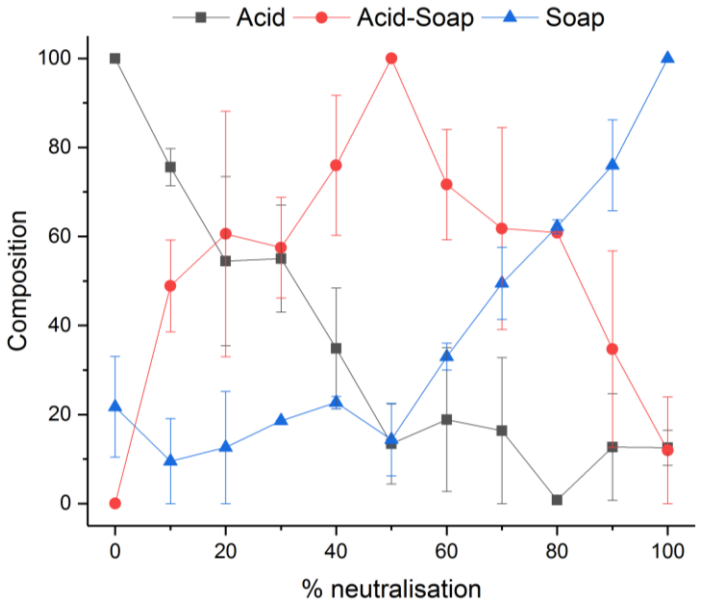

Figure 6.39: Average concentration profiles of MEA stearate, stearic acid, and their acid-soap determined by MCR-ALS using FTIR and Raman data of the partially neutralised stearic acid samples.

The DSC traces of the partially neutralised stearic acid samples followed the overall trends observed for the other chain lengths. For the 0-40% samples, the first endothermic transition observed corresponded to the melting of stearic acid at 68 °C. From 30% to 90% an endothermic transition was observed at approx. 76 °C, which was the only transition observed for the 50%-80% samples. The sharpness of the transition for the 50% and 60% sample suggested it was a melting peak of a pure component, most likely an acid-soap cocrystal. At 90% and 100% neutralisation an endothermic transition was observed at 80.5 °C which corresponded to that of the melt of MEA stearate.

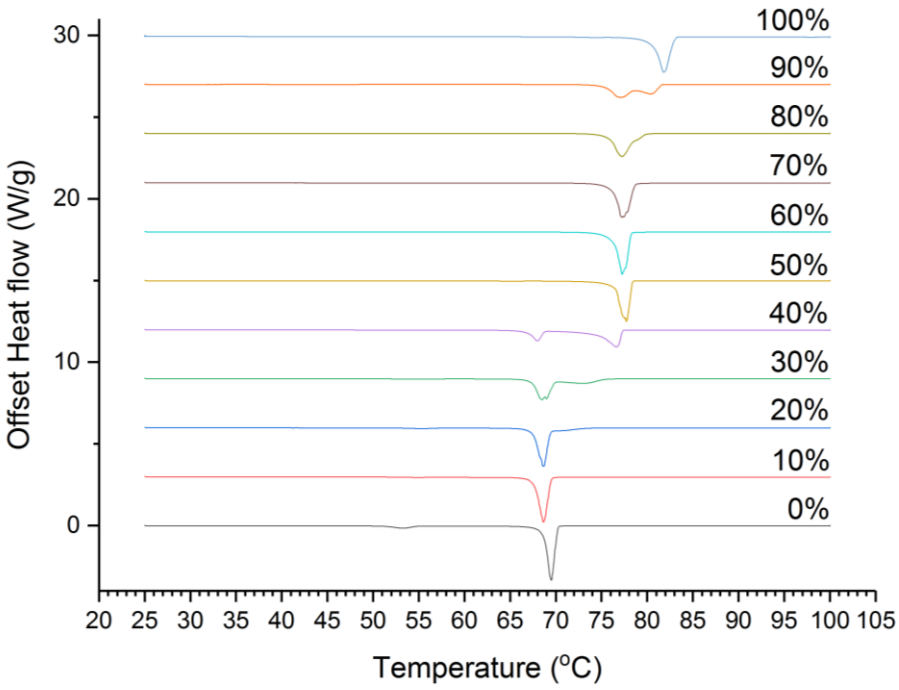

Figure 6.40: DSC traces of partially neutralised stearic acid samples during a heating ramp at 1 °C/min shown endothermic (melting) peaks

6.4.5 Summary

The series of even saturated fatty acids from C12:0 to C18:0 neutralised to various degrees by ethanolamine shared common trends. Analysis by PXRD and DSC indicated that there were three separate crystalline components present in the crystal samples and that two of these components could be assigned to the respective fatty acid and the MEA carboxylate. The third component could therefore be an acid-soap or a polymorph of the MEA carboxylate. A polymorph of the MEA carboxylate could be ruled out however as for a partially neutralised sample there should also be fatty acid in the sample and this was not observed. FTIR and Raman showed similar trends with the behaviour of the carbonyl stretch in the IR spectra proving particularly diagnostic. Multivariate curve resolution (MCR) was used with the FTIR and Raman data to provide further insight into the composition of the samples. Due to the similarity of the spectra for the MEA carboxylates, fatty acids, and acid-soaps the IR and Raman data showed significant differences in the approximate compositions, hence the relatively large error, yet the general trends identified in both data sets by the MCR analysis were consistent. Therefore the results of the MCR analysis should be treated as qualitative rather quantitative and must be considered alongside the other experimental data, such as XRPD and DSC. The general trend showed that below 50%

neutralisation the samples were mixtures of the fatty acid and the unknown third component, whilst above 50% samples were mixtures of the third component and the MEA carboxylate. Taking the characterisation data and composition trends as whole, the unknown component can be identified as an MEA carboxylate acid-soap with a 1:1 stoichiometry.

6.5 Characterisation of MEA carboxylate acid-soaps

From the data in the previous section, acid-soaps were found to form for each of the chain lengths with a potential 1:1 acid-soap stoichiometry. Samples of the acid-soap were therefore prepared in ethanol by cooling crystallisation and characterised to confirm their stoichiometry, chemistry, and structure.

6.5.1 PXRD

The low angle PXRD patterns of the acid-soaps of the four chain lengths each showed evenly spaced peaks, corresponding to lamellar crystal structures. The first peak in the series are not fully visible for the palmitate and stearate patterns due to the signal cut-off truncating the peaks, with only the tail end of the peak being observed. The first peak position can be calculated however from the other peaks observed in the lamellar series. The lamellar d-spacings for the laurate, myristate, palmitate, and stearate acid-soaps were 34.9, 39.7, 45.3, 49.6 Å respectively. These spacings are almost twice the approximate length of alkyl chain, suggesting a single-layered structure where MEA molecules are at the centre of the layer with the carboxylate and carboxylic acid chains extended in opposite directions. The long-spacing of the acid-soaps as a function of the number of carbons in the chain, showed a strong linear correlation and that the change in the long-spacing for an increase of two carbons was 5.08 Å (as determined by a linear fit). The corresponding approximate combined change in chain length of the carboxylate and carboxylic acid was 5.06 Å. This further suggests that the alkyl chains are extended in the direction of the long-spacing of the acid-soap.

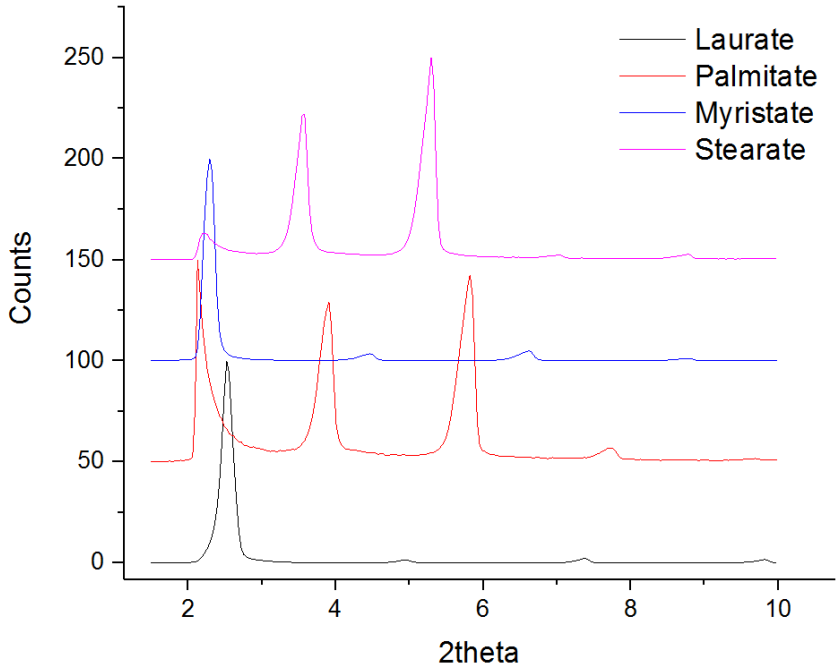

Figure 6.41: Low angle PXRD patterns of the acid-soaps of MEA carboxylates of different chain lengths

However, an alternative arrangement could be a double layer of acid-soap "molecules" within the lamellae, such as a zig-zag arrangement. The alkyl chains would be tilted in a configuration such as this and this tilt angle could be approximated by assuming a certain number of alkyl chains per layer and that the alky chains are equally tilted. For instance, in a double-layer structure such as zig-zag, the overall change in chain length for an increase of two carbons per chain is approx. 10.1 Å, resulting in an average tilt angle of 59.9° from the vertical.

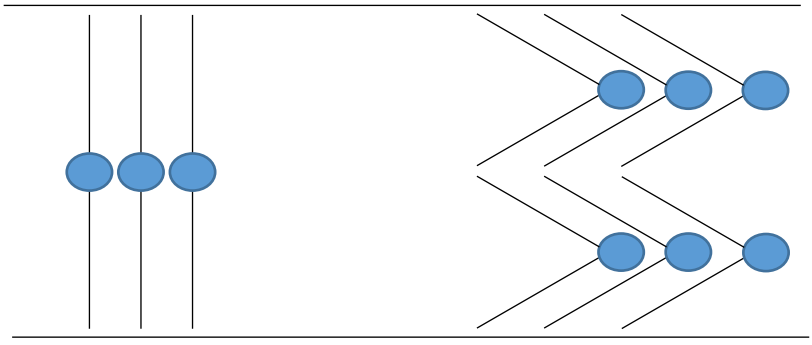

Figure 6.42: Possible structural arrangements in 1:1 MEA carboxylate acid-soaps assuming: a) single layer structure b) double-layer type structure with tilted chains. Note: carboxylic and carboxylate chains are not differentiated in the diagram

6.5.2 DSC

The DSC traces of heating ramps of the acid-soaps each showed a single, sharp, endothermic peak, consistent with that of a melting transition. The

temperatures of this transition showed a clear linear trend with the melting point increasing as the chain length increases. The melting points observed are consistent with the transitions assigned to the acid-soap in the partially neutralised samples in the previous section, indicating the same structure had formed through the two crystallisation routes: cooling and evaporation. The enthalpy of the melting transition also showed a linear relationship with the chain length, increasing in magnitude as the chain length increased

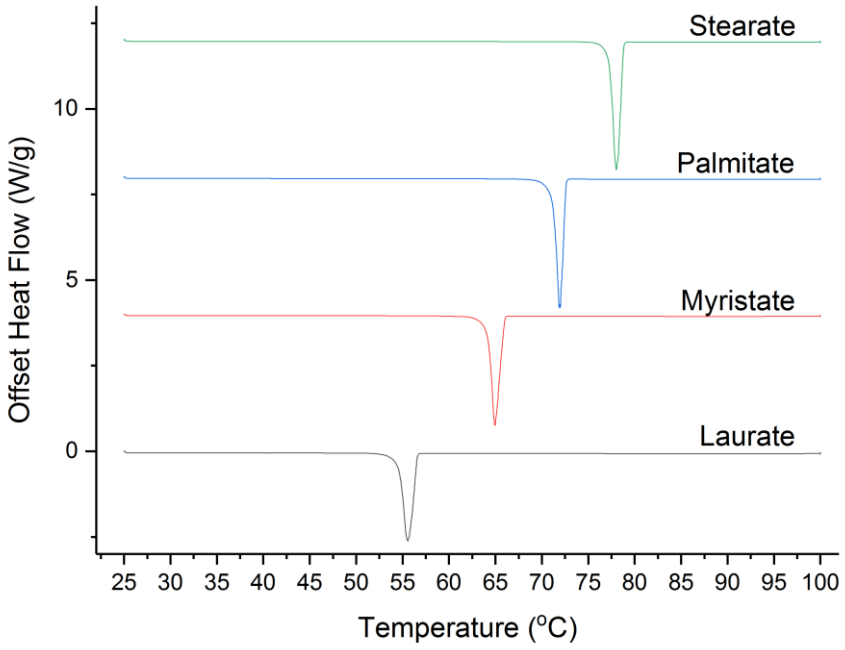

Figure 6.43: DSC traces of MEA carboxylate acid-soaps during a heating ramp at 1 °C/min

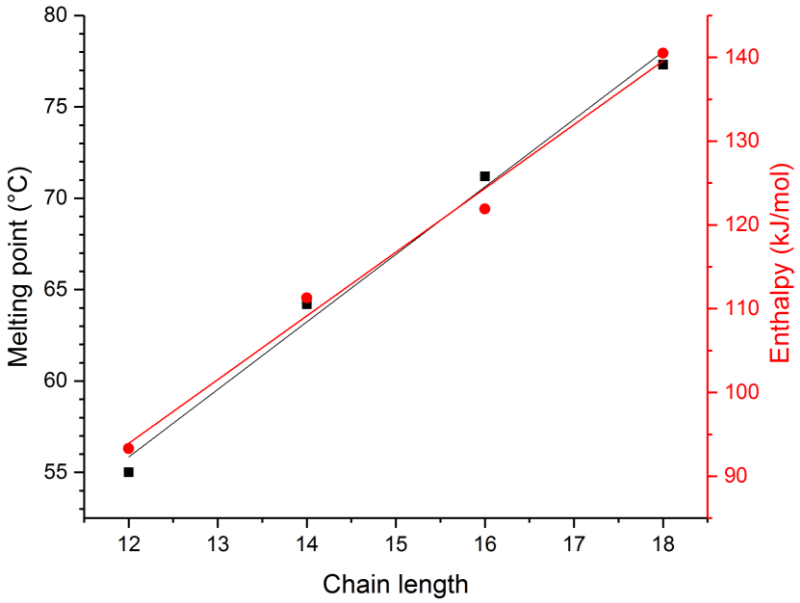

Figure 6.44: Melting point and enthalpies for a series of MEA carboxylate acid-soaps, with linear fits.

6.5.3 FTIR and Raman

The FTIR spectra of the 1:1 acid-soaps did not show a strong chain length dependence with the main differences restricted to the CH2 wagging progression, in which the number of peaks is chain length dependent. The main characteristic feature of the FTIR spectra of the acid-soap compared to the acid or MEA carboxylate is the position of the carbonyl peak at 1719 cm^{-1}.

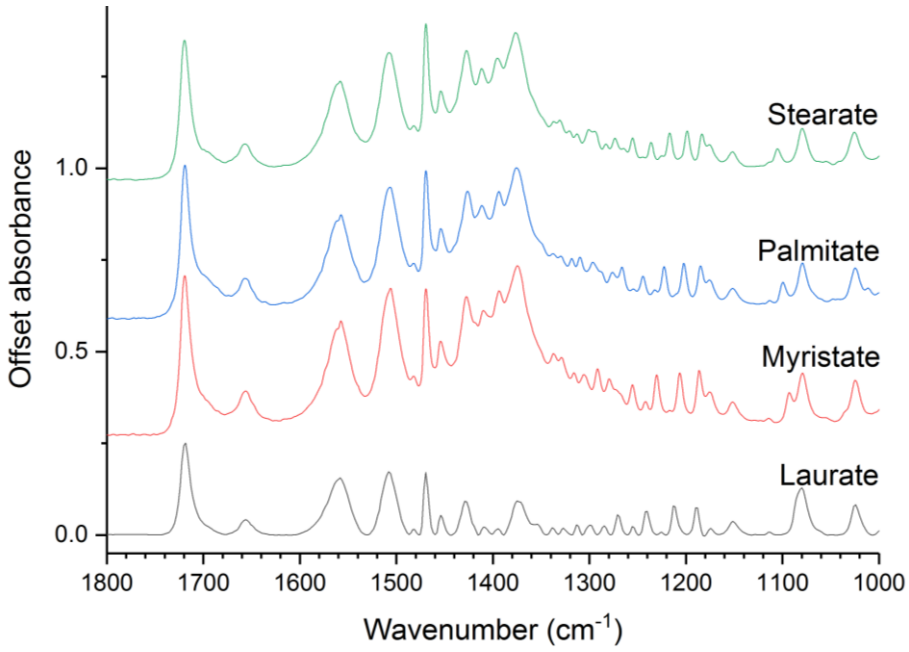

Figure 6.45: FTIR spectra of 1:1 MEA carboxylate acid soaps

The Raman spectra of the 1:1 acid-soaps indicated that there was little difference in the crystal structure across the chain lengths studied. The CH2 and CH3 stretching region, between 3000-2600 cm^{-1} showed no significant differences between the different chain lengths whilst there was only minor differences in the CH2 and CH3 deformation region at 1500-1400 cm^{-1}. All the chain lengths studied showed the characteristic peak at 1719 cm^{-1} that was assigned to a carbonyl stretch. The C-C stretch peaks allowed differentiation of the chain lengths with the peak between 1080 and 1110 cm^{-1} appearing to be dependent on chain length.

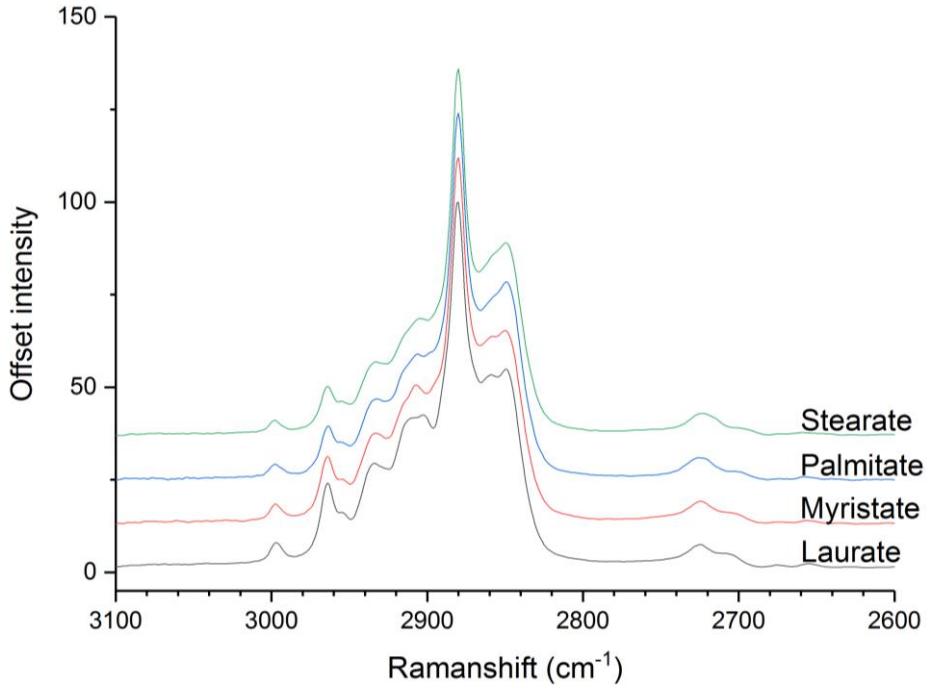

Figure 6.46: Raman spectra of MEA carboxylate acid-soaps focussing on the CH2 and CH3 stretching region

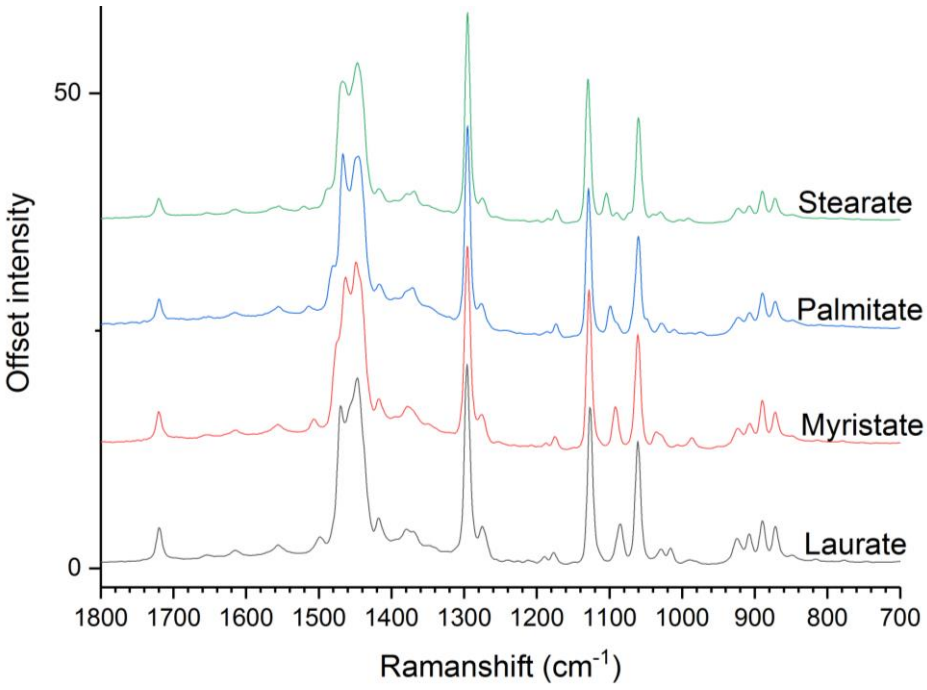

Figure 6.47: Raman spectra of MEA carboxylate acid-soaps

6.6 MEA carboxylate – fatty acid phase diagrams

From the experimental data collected for MEA carboxylates, their acid-soaps, and the partially neutralised acid samples phase diagrams of the MEA carboxylate – fatty acid systems can be constructed and are shown in Figure 6.48. The phase diagrams show the same general trends as the acid-rich side

of the phase diagram reported in literature for MEA – Stearic acid (15). However, the phase diagrams presented here improve on the diagram in literature by using techniques that can distinguish between fatty acid, acid-soap, and MEA carboxylate. The phase diagrams in this work reveal two regions of crystals at lower temperatures; one a mixture of fatty acid and acid-soap, and the other a mixture of acid-soap and soap.

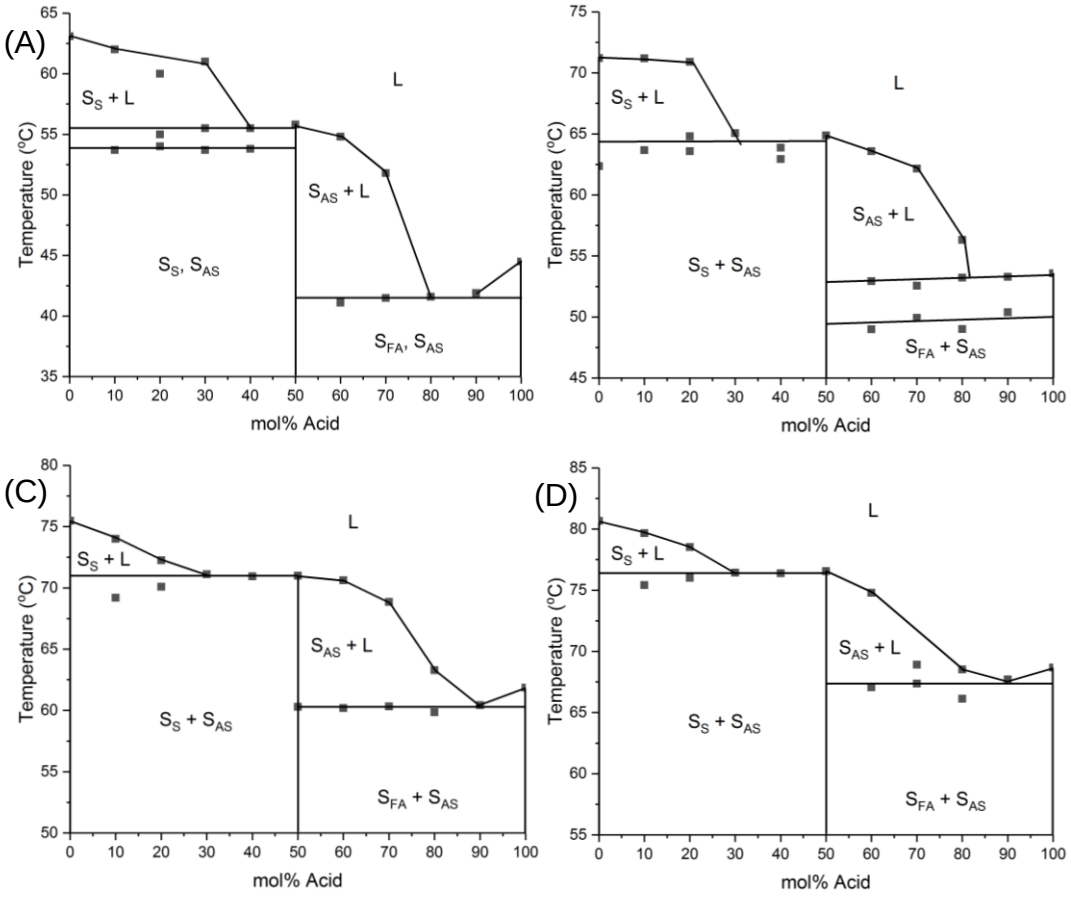

Figure 6.48: Binary phase diagrams of A) MEA Laurate – Lauric acid, B) MEA Myristate – myristic acid, C) MEA Palmitate – palmitic acid, D) MEA Stearate – stearic acid, where: S_s – solid MEA carboxylate, S_{AS} – solid 1:1 acid-soap, L – isotropic liquid

The phase diagrams show similar behaviours across the range of chain lengths studied with the trends shifting to higher temperatures with increasing chain length. There are narrow regions in the MEA laurate – lauric acid and MEA myristate – myristic acid diagrams that were not present in any of the other phase diagrams. By comparison with the MEA – oleic acid diagrams in literature, these are likely to be inverse hexagonal liquid crystal phases where the solvent is liquid fatty acid in the case of the myristic acid diagram and liquid acid-soap for the lauric acid diagram.

6.7 Conclusions

MEA carboxylates and their acid-soaps both have lamellar crystal structures in which their long-spacings are linearly dependent on the chain length. Whilst the MEA carboxylates have long-spacings close to their approximate extended alkyl chain lengths, the acid-soap long-spacings are almost double their chain length. This suggests that the MEA carboxylates either adopt a single layer interdigitated structure or a highly tilted double layer structure, whilst the acid-soaps adopt a bilayer structure. A bilayer structure for the acid-soap is not unexpected due to the need for the fatty acid molecule to orientate itself such it can interact with the carboxylate and/or MEA groups, most likely through hydrogen bonding, whilst its alkyl chain is fully extended in an all-trans configuration as suggested by the CH2 wagging behaviour observed by FTIR.

Table 6:7: Comparison of long-spacings determined by PXRD for MEA carboxylates and their 1:1 acid-soaps

Chain length	Approximate alkyl chain length (Å)	MEA carboxylate (Å)	1:1 Acid-soap (Å)
Laurate: C12	16.7	19.8	34.9
Myristate: C14	19.2	22.2	39.7
Palmitate: C16	21.7	24.7	45.3*
Stearate: C18	24.3	26.8	49.6*

* estimated from higher order peaks

The FTIR data shows that for the chain lengths covered for the MEA carboxylates, the main difference in spectra was within the CH2 wagging progression due to differing chain length. The other bond absorptions were identical, suggesting that they are isostructural due to similar nature of the interactions between molecules. Similarly, the spectra for the 1:1 acid-soaps were consistent across the range of chain lengths with the exception of the CH2 wagging region where the number of peaks is proportional to the chain length. The position of the carbonyl peak in the acid-soap spectra indicates the COOH group is involved in hydrogen bonding, but to a much lesser extent than in a COOH dimer.

The melting point data for the various chain lengths of fatty acid, acid-soap, and MEA soap showed that they have a strong linear dependence on the chain length. This dependence was not unexpected as the increased alkyl chain length increases the number of Van der Waals interactions between the packed alkyl chains, increasing the energy required to separate the

molecules. The increased chain length does not have a major influence on the crystal structure as it will not affect the headgroup interactions and would merely increase the height of the layers in the lamellar structure.

Comparing the difference in melting point between the soaps and the fatty acids, the increase in melting point by becoming a soap shows a chain length dependence; MEA laurate melts 17.9 °C higher than lauric acid, whilst MEA stearate melts 12.1 °C higher than stearic acid. The trend showed that melting point elevation decreased with increasing chain length. This could be due to the alkyl chain becoming increasingly dominant in terms of the interaction between molecules in the crystal structure, with the headgroup becoming less important i.e switching from a COOH dimer to COO^- +MEA had less of an effect.

Table 6:8: Comparison of the melting points and melting enthalpy (in terms of per alkyl chain) for the fatty acids (FA), MEA soaps (S), and their acid-soaps (AS) for various chain lengths

	Melting point (°C)			Enthalpy (kJ/mol/chain)		
Chain length	FA	AS	S	FA	AS	S
C12:0	43.6	55.0	61.5	34.8	46.7	55.0
C14:0	54.0	64.2	69.6	39.9	55.7	56.1
C16:0	61.9	71.4	75.1	42.6	61.0	61.6
C18:0	68.9	77.3	81.0	53.2	70.2	65.6

Comparison of the spectra determined by MCR-ALS for the acid-soap with the recorded spectra of the actual acid-soap samples showed no significant differences in terms of spectral features. Re-analysis of the variable neutralisation data by MCR-ALS using the spectra collected for the raw fatty acids, and the MEA carboxylate and acid-soaps prepared by cooling crystallisation showed no significant differences in terms of the determined composition trends.

From the observed composition trends in the partially neutralised samples, it appeared that the formation of the acid-soap was favoured as its formation provided a lower overall system energy than the formation of fatty acid and soap. This explains why for neutralisations below 50% only acid-soap and fatty acid is observed; the amount of fatty acid is in excess of the MEA carboxylate formed and thus the system maximises acid-soap formation, resulting in only acid-soap and fatty acid. Above 50% neutralisation, the MEA carboxylate is in excess of the fatty acid, resulting in formation of acid-soap and MEA carboxylate.

6.8 References

1. SANTOS, D., F. COSTA, E. FRANCESCHI, A. SANTOS, C. DARIVA and S. MATTEDI. Synthesis and physico-chemical properties of two protic ionic liquids based on stearate anion. *Fluid Phase Equilibria*, 2014, **376**, pp.132-140.
2. MU, L., Y. SHI, T. JI, L. CHEN, R. YUAN, H. WANG and J. ZHU. Ionic Grease Lubricants: Protic [Triethanolamine][Oleic Acid] and Aprotic [Choline][Oleic Acid]. *ACS Appl Mater Interfaces*, 2016, **8**(7), pp.4977-84.
3. ARNOULD, A., A.A. PEREZ, C. GAILLARD, J.P. DOULIEZ, F. COUSIN, L.G. SANTIAGO, T. ZEMB, M. ANTON and A.L. FAMEAU. Self-assembly of myristic acid in the presence of choline hydroxide: effect of molar ratio and temperature. *J Colloid Interface Sci*, 2015, **445**, pp.285-93.
4. LYNCH, M.L. Acid-soaps. *Current Opinion in Colloid & Interface Science*, 1997, **2**(5), pp.495-500.
5. LYNCH, M.L., Y. PAN and R.G. LAUGHLIN. Spectroscopic and thermal characterization of 1:2 sodium soap fatty acid acid-soap crystals. *Journal of Physical Chemistry*, 1996, **100**(1), pp.357-361.
6. LYNCH, M.L., F. WIREKO, M. TAREK and M. KLEIN. Intermolecular Interactions and the Structure of Fatty Acid−Soap Crystals. *The Journal of Physical Chemistry B*, 2001, **105**(2), pp.552-561.
7. ANANTHAPADMANABHAN, K.P. and P. SOMASUNDARAN. Acid-Soap Formation in Aqueous Oleate Solutions. *J Colloid Interface Sci*, 1988, **122**(1), pp.104-109.
8. HADŽI, D., J. GRDADOLNIK and A. MEDEN. Infrared spectra of, and hydrogen bonding in acid palmitates. *Journal of Molecular Structure*, 1996, **381**(1-3), pp.9-14.
9. MCBAIN, J.W. and M.C. FIELD. Phase Rule Equilibria of Acid Soaps. I. Anhydrous Acid Potassium Laurate. *The Journal of Physical Chemistry*, 1932, **37**(6), pp.675-684.
10. ---. 216. Phase-rule equilibria of acid soaps. Part II. Anhydrous acid sodium palmitates. *Journal of the Chemical Society (Resumed)*, 1933, p.920.
11. TANDON, P., S. RAUDENKOLB, R.H. NEUBERT, W. RETTIG and S. WARTEWIG. X-ray diffraction and spectroscopic studies of oleic acid-sodium oleate. *Chem Phys Lipids*, 2001, **109**(1), pp.37-45.
12. PUDNEY, P.D., K.J. MUTCH and S. ZHU. Characterising the phase behaviour of stearic acid and its triethanolamine soap and acid-soap by infrared spectroscopy. *Phys Chem Chem Phys*, 2009, **11**(25), pp.5010-8.
13. ZHU, S., M. HEPPENSTALL-BUTLER, M.F. BUTLER, P.D. PUDNEY, D. FERDINANDO and K.J. MUTCH. Acid soap and phase behavior of stearic acid and triethanolamine stearate. *J Phys Chem B*, 2005, **109**(23), pp.11753-61.
14. ZHU, S., P.D. PUDNEY, M. HEPPENSTALL-BUTLER, M.F. BUTLER, D. FERDINANDO and M. KIRKLAND. Interaction of the acid soap of triethanolamine stearate and stearic acid with water. *J Phys Chem B*, 2007, **111**(5), pp.1016-24.

15. MAXIMO, G.J., R.J.B.N. SANTOS, J.A. LOPES-DA-SILVA, M.C. COSTA, A.J.A. MEIRELLES and J.A.P. COUTINHO. Lipidic Protic Ionic Liquid Crystals. *ACS Sustainable Chemistry & Engineering*, 2014, **2**(4), pp.672-682.
16. MORENO-CALVO, E., G. GBABODE, R. CORDOBILLA, T. CALVET, M.A. CUEVAS-DIARTE, P. NEGRIER and D. MONDIEIG. Competing intermolecular interactions in the high-temperature solid phases of even saturated carboxylic acids (C10H19O2H to C20H39O2H). *Chemistry*, 2009, **15**(47), pp.13141-9.
17. BOND, A.D. On the crystal structures and melting point alternation of the n-alkyl carboxylic acids. *New Journal of Chemistry*, 2004, **28**(1), p.104.
18. VON SYDOW, E. On the Structure of Crystal Form A of Lauric Acid. *Acta Chemica Scandinavica*, 1956, **10**, pp.1-8.
19. GOTO, M. and E. ASADA. The Crystal Structure of the A-super Form of Lauric Acid. *Bulletin of the Chemical Society of Japan*, 1978, **51**(1), pp.70-74.
20. LOMER, T.R. The crystal and molecular structure of lauric acid (form A). *Acta Crystallographica*, 1963, **16**(10), pp.984-988.
21. ABRAHAMSSON, S. and E. VON SYDOW. Variation of unit-cell dimensions of a crystal form of long normal chain carboxylic acids. *Acta Crystallographica*, 1954, **7**(8), pp.591-592.
22. MORENO, E., R. CORDOBILLA, T. CALVET, F.J. LAHOZ and A.I. BALANA. The C form of n-hexadecanoic acid. *Acta Crystallogr C*, 2006, **62**(Pt 3), pp.o129-31.
23. MALTA, V., G. CELOTTI, R. ZANNETTI and A.F. MARTELLI. Crystal structure of the C form of stearic acid. *Journal of the Chemical Society B: Physical Organic*, 1971, p.548.
24. LARSSON, K. and E. VON SYDOW. The Crystal Structure of the B-Form of Fatty Acids. *Acta Chemica Scandinavica*, 1966, **20**, pp.1203-1207.
25. GOTO, M. and E. ASADA. The Crystal Structure of the B-form of Stearic Acid. *Bulletin of the Chemical Society of Japan*, 1978, **51**(9), pp.2456-2459.
26. KANEKO, F., H. SAKASHITA, M. KOBAYASHI, Y. KITAGAWA, Y. MATSUURA and M. SUZUKI. Double-layered polytypic structure of the B form of octadecanoic acid, C18H36O2. *Acta Crystallographica Section C Crystal Structure Communications*, 1994, **50**(2), pp.245-247.
27. ---. Double-layered polytypic structure of the E form of octadecanoic acid, C18H36O2. *Acta Crystallographica Section C Crystal Structure Communications*, 1994, **50**(2), pp.247-250.
28. SATO, K. and M. OKADA. Growth of Large Single-Crystals of Stearic-Acid from Solution. *J Cryst Growth*, 1977, **42**(Dec), pp.259-263.
29. ABRAHAMSSON, S. and B.M. LUNDÉN. The crystal structure of isostearic acid. *Acta Crystallographica Section B Structural Crystallography and Crystal Chemistry*, 1972, **28**(8), pp.2562-2567.
30. JALAL, I.M., G. ZOGRAFI, A.K. RAKSHIT and F.D. GUNSTONE. Thermal Analysis of Fatty Acids. *Chem Phys Lipids*, 1982, **31**, pp.395-404.

31. YUAN, Y., N. ZHANG, W. TAO, X. CAO and Y. HE. Fatty acids as phase change materials: A review. *Renewable and Sustainable Energy Reviews*, 2014, **29**, pp.482-498.
32. STENHAGEN, E., V. VAND and A. SIM. The crystal structure of isopalmitic acid. *Acta Crystallographica*, 1952, **5**(5), pp.695-696.
33. VOGEL-WEILL, C. and J. CORSET. Spectres infrarouge et Raman de l'acide stéarique et d'une série d'acides gras forme C: modes de squelette, couplage des modes longitudinaux acoustiques (LAM1, LAM3) avec les modes dans le plan de la liaison hydrogène du dimère en dessous de 700 cm−1. *Spectrochimica Acta Part A: Molecular and Biomolecular Spectroscopy*, 1995, **51**(13), pp.2357-2377.
34. SINCLAIR, R.G., A.F. MCKAY and R.N. JONES. The Infrared Absorption Spectra of Saturated Fatty Acids and Esters. *Journal of the American Chemical Society*, 1952, **74**(10), pp.2570-2575.
35. OTERO, V., D. SANCHES, C. MONTAGNER, M. VILARIGUES, L. CARLYLE, J.A. LOPES and M.J. MELO. Characterisation of metal carboxylates by Raman and infrared spectroscopy in works of art. *Journal of Raman Spectroscopy*, 2014, **45**(11-12), pp.1197-1206.
36. LARKIN, P. *Infrared and Raman Spectroscopy.* Boston: Elsevier, 2011.
37. YU, F., Y. WANG, L. ZHANG and G. ZHU. Role of oleic acid ionic−molecular complexes in the flotation of spodumene. *Minerals Engineering*, 2015, **71**, pp.7-12.
38. DE SOUSA, F.F., P.T. FREIRE, A.S. DE MENEZES, G.S. PINHEIRO, L.P. CARDOSO, P. ALCANTARA, JR., S.G. MOREIRA, F.E. MELO, J. MENDES FILHO and G.D. SARAIVA. Low-temperature phase transformation studies in the stearic acid: C form. *Spectrochim Acta A Mol Biomol Spectrosc*, 2015, **148**, pp.280-8.
39. DE SOUSA, F.F., C.E. NOGUEIRA, P.T. FREIRE, S.G. MOREIRA, A.M. TEIXEIRA, A.S. DE MENEZES, J. MENDES FILHO and G.D. SARAIVA. Conformational change in the C form of palmitic acid investigated by Raman spectroscopy and X-ray diffraction. *Spectrochim Acta A Mol Biomol Spectrosc*, 2016, **161**, pp.162-9.
40. CZAMARA, K., K. MAJZNER, M.Z. PACIA, K. KOCHAN, A. KACZOR and M. BARANSKA. Raman spectroscopy of lipids: a review. *Journal of Raman Spectroscopy*, 2015, **46**(1), pp.4-20.
41. PICQUART, M. Vibrational model behavior of SDS aqueous solutions studied by Raman scattering. *The Journal of Physical Chemistry*, 1986, **90**(2), pp.243-250.
42. CAZZOLLI, G., S. CAPONI, A. DEFANT, C.M.C. GAMBI, S. MARCHETTI, M. MATTARELLI, M. MONTAGNA, B. ROSSI, F. ROSSI and G. VILIANI. Aggregation processes in micellar solutions: a Raman study. *Journal of Raman Spectroscopy*, 2012, **43**(12), pp.1877-1883.
43. DE GELDER, J., K. DE GUSSEM, P. VANDENABEELE and L. MOENS. Reference database of Raman spectra of biological molecules. *Journal of Raman Spectroscopy*, 2007, **38**(9), pp.1133-1147.
44. ESUMI, K. and M. UENO. *Structure-Performance Relationships in Surfactants.* Surfactant Science Series. 2nd ed. New York: Taylor & Francis Inc, 2003.

45. BAILEY, A.V., D. MITCHAM, A.D. FRENCH and G. SUMRELL. Unit cell dimensions of some long chain fatty acid polymorphs. *Journal of the American Oil Chemists' Society*, 1975, **52**(6), pp.196-197.
46. YU, G.-S., H.-W. LI, F. HOLLANDER, R.G. SNYDER and H.L. STRAUSS. Comparison of the Structures of Ammonium Myristate, Palmitate, and Stearate by X-ray Diffraction, Infrared Spectroscopy, and Infrared Hole Burning. *The Journal of Physical Chemistry B*, 1999, **103**(47), pp.10461-10468.
47. ROBINET, L. and M.C. CORBEIL. The characterization of metal soaps. *Studies in Conservation*, 2003, **48**(1), pp.23-40.
48. WEERS, J.G. and D.R. SCHEUING. Micellar Sphere to Rod Transitions. *In:* D.R. SCHEUING, ed. *Fourier Transform Infrared Spectroscopy in Colloid and Interface Science*. American Chemical Society, 1990, pp.87-122.
49. MANTSCH, H.H., S.F. WENG, P.W. YANG and H.H. EYSEL. Structure and thermotropic phase behavior of sodium and potassium carboxylate ionomers. *Journal of Molecular Structure*, 1994, **324**(1-2), pp.133-141.
50. EDSALL, J.T. Raman Spectra of Amino Acids and Related Compounds I. The Ionization of the Carboxyl Group. *The Journal of Chemical Physics*, 1936, **4**(1), pp.1-8.
51. BAILEY, A.V., G. SUMRELL, R.A. PITTMAN and D. MITCHAM. Fatty-Acid Polymorph Identification by Infrared. *Journal of the American Oil Chemists Society*, 1972, **49**(7), pp.419-&.
52. LOMER, T.R. Unit-Cell Dimensions of γ-Lauric and γ-Myristic Acids. *Nature*, 1955, **176**(4483), pp.653-654.
53. FRANCIS, F., S.H. PIPER and T. MALKIN. The n-Fatty Acids. *Proceedings of the Royal Society A: Mathematical, Physical and Engineering Sciences*, 1930, **128**(807), pp.214-252.
54. MORENO, E., R. CORDOBILLA, T. CALVET, M.A. CUEVAS-DIARTE, G. GBABODE, P. NEGRIER, D. MONDIEIG and H.A.J. OONK. Polymorphism of even saturated carboxylic acids from n-decanoic to n-eicosanoic acid. *New Journal of Chemistry*, 2007, **31**(6), p.947.

Chapter 7 Aqueous phase behaviour of MEA carboxylates

Characterisation of monoethanolammonium carboxylates and their acid-soaps through a variety of chemical and structural analysis techniques

7.1 Introduction

Anionic surfactants are common components of liquid detergents, particularly fabric detergents where they make up to 5 %wt of the formulation. Typically, these surfactants are soap mixtures – neutralised fatty acids from natural sources (e.g palm kernel, tallow, coconut) with a counter-ion such as Na+. The counter-ion used has a significant effect on the aqueous phase behaviour of the soaps, as exemplified by the differences between sodium and choline soaps (1).

Although alkanolammonium soaps are commonly used, the aqueous phase behaviour of these soaps have received far less attention in literature (2-5) than their sodium equivalents which have been extensively studied (6-10). The phase diagrams available for MEA and TEA carboxylates show similar phase behaviours to sodium soaps, progressing from micelles to hexagonal and then lamellar liquid crystals as the concentration of surfactant increases (2, 11). However, these phase diagrams do not show what occurs below typical room temperature. This lower temperature region is of interest from a product stability point of view for liquid cleaning products, as during a products lifespan it is likely to be exposed to temperatures lower than room temperature during storage or transportation. Knowledge of this low temperature region and the associated crystallisation behaviour would enable better formulation of the products, enhancing product stability or controlling the crystallisation process such that the performance of the product is not degraded.

In this chapter, the aqueous phase behaviour of MEA carboxylates will be studied from a crystallisation viewpoint, working in the micellar concentration regime. The classic starting point for a crystallisation study is the determination of solubility and supersolubility and hence the metastable zone width (MSZW). This chapter begins with establishing the solubility, supersolubility, and MSZW of aqueous MEA carboxylate solutions through a polythermal methodology using turbidity based techniques. It then moves onto offline crystal characterisation to identify the crystallising components in order to understand the non-typical crystallisation behaviours observed. In-situ Raman spectroscopy is employed to further characterise the crystallisation process and crystallised material. The chapter ends with a study on how an excess of MEA effects the MSZW.

7.2 Metastable zone width measurements of aqueous MEA carboxylate solutions

Crystallisation and dissolution temperatures were determined by turbidity changes by Crystal16 as a function of cooling rate and solution concentration. The transitions in turbidity due to crystallisation were relatively sharp, with the fall from 100% transmittance to 0% transmittance occurring within a short time-frame as demonstrated in Figure 7.1. The decreases in turbidity caused by dissolution were less sharp, which could be in part due to the magnetic stirrer bar being trapped by the crystallisation solution and needing to break free to begin agitating the solution. There were some MEA myristate solutions which showed two distinct increases in transmittance, as shown for 15 g/100g MEA myristate solution in Figure 7.1, which could correspond to two dissolution events. These events only occurred for higher concentrations (10 and 15 g /100g) and higher cooling rates (>0.5 °C/min). In this chapter, 'dissolution' refers to the event at which transmittance increases up to 100%, whilst 'dissolution b' refers to the first initial increase in transmittance for the case of a two-step dissolution profile, as in the 15 g/100g profile in Figure 7.1

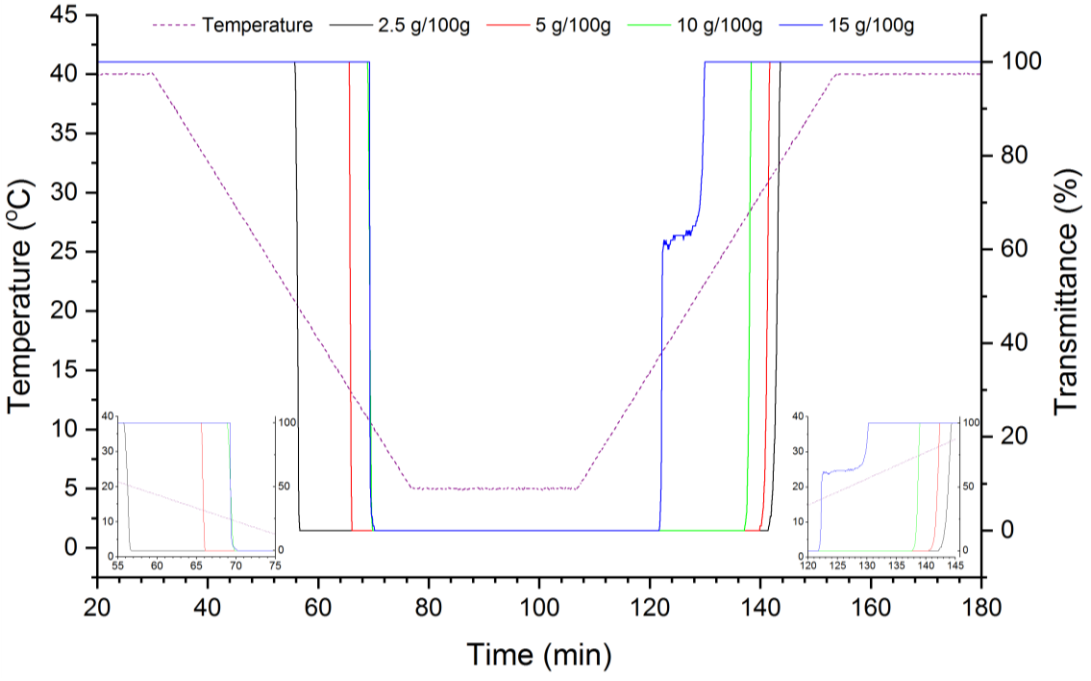

Figure 7.1: Turbidity data of MEA myristate solutions during a temperature cycle at 0.75 °C/min. Inset graphs show detail of crystallisation events (decreased in transmittance) and dissolution events (increase in transmittance).

MEA palmitate and MEA stearate solutions presented a problem however as they formed turbid solutions, which did not become clear even after heating well above the respective fatty acids melting point. For instance, a 1 g/100 g

water MEA stearate solution did not become clear at 100 °C, with the solution still remaining turbid at its boiling point, suggesting that the turbidity was due to the presence of an oil phase. The lack of clear solution meant that MEA palmitate and MEA stearate solutions were not suitable for study using a turbidity-based system such as the Crystal16.

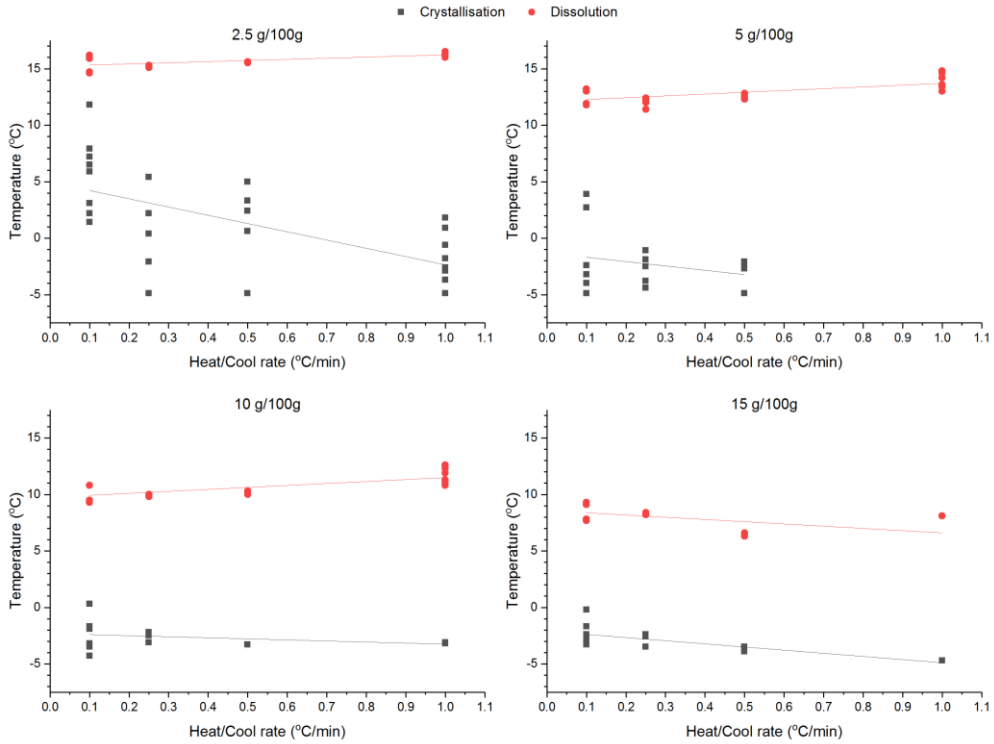

Figure 7.2: Crystallisation and dissolution temperatures of MEA laurate in water as a function of concentration and cooling rate

The crystallisation temperatures for MEA laurate and MEA myristate show significant variations in onset temperature. The low variance in the dissolution temperature (excluding the experiments which showed two dissolution events) rules out system errors i.e it is unlikely for the Crystal16 system to consistently have an issue when crystallisation occurs yet not when dissolution occurs. Condensation on the vials at low temperatures within the instrument can also be eliminated as the vials are in a 0% relative humidity environment due to the instruments dry gas purge stream (and also that variance was observed at temperatures where condensation wouldn't be an issue). Measurement error, such as crystals forming but not passing through the measurement zone of the vial, is unlikely due to the small scale of the experiments meaning that they will be well-mixed by the magnetic stirrers (which also tend to break crystals and thus trigger secondary nucleation events, generating more crystals). These variations can therefore be explained by the probabilistic nature of nucleation rather than variation within

the Crystal16 system or measurement error, which raises question for product stability testing in regards to how many samples need to be tested for each formulation to gain a representative distribution (26).

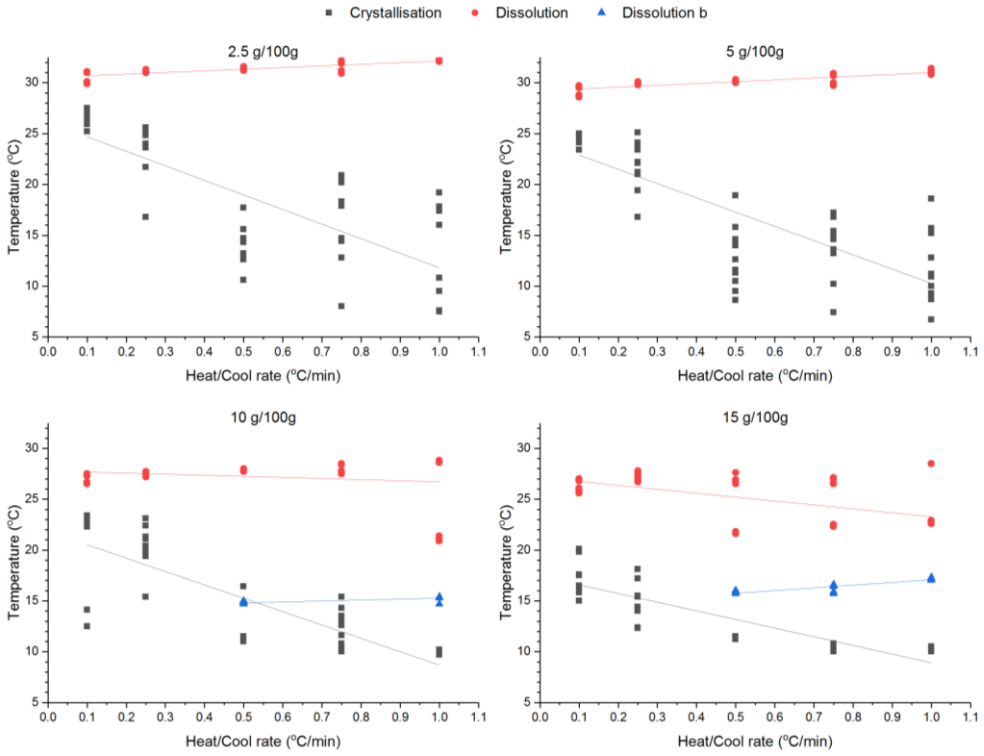

Figure 7.3: Crystallisation and dissolution temperatures as function of heating/cooling rate and concentration for aqueous MEA myristate solutions. Dissolution 'b' values represent the first decrease in transmittance for samples with two distinct steps.

The crystallisation data for MEA laurate solutions is more limited that its corresponding dissolution data, exemplified by the 5 g/100g concentration in Figure 7.2 where for 1 °C/min there is only dissolution data. This was due to crystallisation occurring whilst the sample was being held at the low hold temperature after the linear cooling had ended. This meant that rather than reaching the metastable zone width limit, crystallisation had begun due to exceeding the induction time. Whilst this meant that a crystallisation temperature wasn't recorded for that temperature cycle, the dissolution data was still captured. The issue is more prevalent at higher cooling rates due to the MSZW being wider and thus the crystallisation temperature lower.

Linear fits were applied to crystallisation and dissolution temperatures, as shown in Figure 7.2 and Figure 7.3 for MEA laurate and MEA myristate respectively. The intercepts of the linear fits indicated the equilibrium values - an infinitely slow heating/cooling rate - of crystallisation and dissolution. The slope of these linear fits gave an indication whether the process is more kinetically controlled (larger slope, greater dependence on cooling/heating

rate) or more dependent on thermodynamics (smaller slope, less dependent on cooling/heating rate).

The slopes of the linear fits for the dissolution data of MEA laurate increased with increasing concentration, with the exception of the 15 g/100g concentration which showed anomalous behaviour. The increase in slope indicates that the dissolution process becomes increasingly kinetically controlled as the concentration increases. The crystallisation data for MEA laurate shows the opposite behaviour, with the slope of the linear fits decreasing with increasing concentration and the crystallisation process becoming more thermodynamically controlled. The slopes for MEA myristate solutions suggest that the crystallisation process becomes less dependent on kinetics and more thermodynamically controlled as the solution concentration increases. The dissolution slopes appeared to be more dependent on thermodynamics than kinetics, which was also borne out by the small variation in the dissolution temperatures.

The linear fitting for the MEA myristate data also gave insight into the two-step dissolution behaviour observed at higher concentrations and cooling rates. The first step of the dissolution occurred around 15 °C and didn't show a particularly strong dependence on cooling rate or concentration, but a linear fit indicated there would be a crossover with the crystallisation curves. Additionally, the crystallisation temperatures for 0.5 – 1 °C/min rates in the 15 g/100g and possibly the 10 g/100g don't fit particularly well with the slower cooling rates in terms of their trend and also the variation for each point. This could suggest that there are different crystals forming at higher cooling rates compared to lower cooling rates for a given concentration. For the samples which showed the first dissolution event, the second dissolution event occurs at a slightly lower temperature than expected given the dissolution temperatures at slow heating rates and the trends observed for the lower concentration samples. This results in a poorer fit and results in a negative trend for the dissolution temperature with heating rate for the higher concentrations, which is unexpected.

A possible explanation for the two-step dissolution behaviour is that there are multiple components crystallising out or a solution-mediated transformation which results in two components that have different solubility. The MEA myristate data for individual concentrations, particularly 15 g/100g suggests a dependence on the heating/cooling rate as two steps are only observed at higher cooling/heating rates and some possible differences in crystallisation behaviour. The dependence on heating/cooling rate for a given concentration

could be explained by the kinetics of the transformation process; if the kinetics of the transformation are slow compared to the heating/cooling cycle, then the transition will have progressed to differing degrees resulting in changes in the relative proportions of the components and hence different dissolution temperatures. However, the heating/cooling rate dependence could be due to the differing kinetics of the crystallisation processes of two different components.

An explanation for the concentration dependence is that there are two components that can crystallise out: MEA myristate, its 1:1 acid-soap, or myristic acid. From the results in the previous experimental chapter, it appears likely that one of the components will be the 1:1 acid-soap as it formed across the range of MEA:acid ratios. Considering the low solubility of fatty acid in water, it would appear more likely that the second component was MEA myristate. Assuming the two components are MEA myristate and its 1:1 acid-soap, the acid-soap would form in solution due to weak base – weak acid equilibria resulting in incomplete neutralisation of myristic acid. The free myristic acid would then form the 1:1 acid-soap, whose formation appears to be favoured over the fatty acid as shown in the previous results chapter. The relative amounts of acid and soap would be dependent on the overall solution concentration and as the acid-soap would have a different solubility, likely lower than that of the MEA myristate, two dissolution events may be observed. However, from turbidity alone it is not possible to assign the dissolution events to their respective components as they will also be affected by the relative amounts of each component.

For each sample that showed a two-step decrease in turbidity during dissolution, only one increase in turbidity was observed during cooling. Unfortunately, this does not shed further light on what is causing the two-step dissolution. If there was a phase transformation taking place in solution, it occurred after crystallisation and therefore only one crystallisation event would be observed. If two components were crystallised out, the second crystallisation event could have been obscured if it represented a small proportion of the overall crystallised material or if it occurred once the solution was turbid.

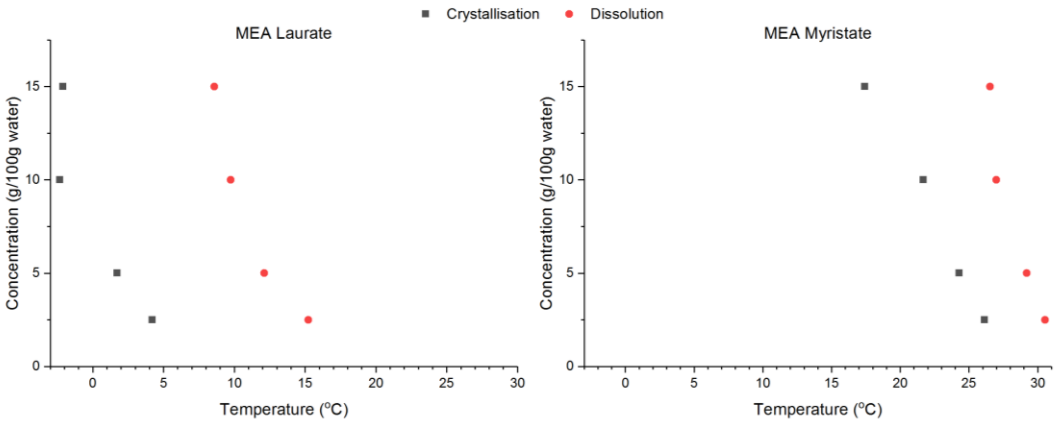

Figure 7.4: Equilibrium crystallisation and dissolution trends of MEA Laurate and MEA Myristate in deionised water obtained by turbidity measurements.

The extrapolated crystallisation and dissolution temperatures for MEA laurate and MEA myristate solutions are shown in Figure 7.4. The dissolution data used for the MEA myristate curve the higher temperature dissolution points shown in Figure 7.3.

The metastable zone width diagrams show unexpected trends as dissolution temperature decreased with increasing concentration yet crystallisation occurred by cooling – given the solubility curve, supersaturation (and thus crystallisation) should be generated for a given concentration by heating the solution. Similar behaviour has been reported for choline, potassium, sodium, and TEA carboxylates, where it was suggested free fatty acid was formed due to hydrolysis of the soap resulting in an apparent increase in dissolution temperature at low concentrations (1-3, 11, 12). It has also been reported that free fatty acid is present in alkanolamine carboxylate – water systems due to incomplete neutralisation (2, 11). These mechanisms are the same and they originate from alkanolamines being weak bases and fatty acids being weak acids (2, 13). It is therefore probable in the MEA carboxylate – water system that there is incomplete neutralisation resulting in the formation of free fatty acid and aqueous MEA solution. Depending on the extent of the neutralisation either the MEA carboxylate or fatty acid will be formed alongside their respective 1:1 acid-soap.

The type of precipitate formed from carboxylate soap solutions has been shown to be concentration dependent with fatty acid precipitate at low concentrations, acid-soap precipitated at intermediate concentrations, and soap at higher concentrations (14-16). The amount of free fatty acid will be concentration dependent as the solution pH increases with total MEA-carboxylate concentration, which favours dissociation of the fatty acid. The

presence of free fatty is therefore more prominent at lower total MEA-carboxylate concentrations (12). This behaviour can result in the increase of the dissolution temperature with decreasing total concentration as the proportion of the less soluble fatty acid (or acid-soap) is higher and would therefore require higher temperatures for complete dissolution. This concentration effect may be more pronounced as the amount of MEA carboxylate, which would help solubilise the fatty acid/acid-soap, would also be lowered by the formation of the acid-soap.

7.2.1 In-situ optical microscopy

In-situ optical microscopy using an Avantium Crystalline system was carried out on MEA myristate solutions in order to characterise the transitions observed by turbidity. For a 2.5 g/100g MEA myristate solution, the turbidity transitions were caused by the nucleation and growth, and subsequent dissolution during reheating, of high aspect ratio crystals that were ribbon or needle-like. These crystals were typically approx. 10 – 20 µm in width and depth but varied in length considerably with crystals observed over 500 µm in length.

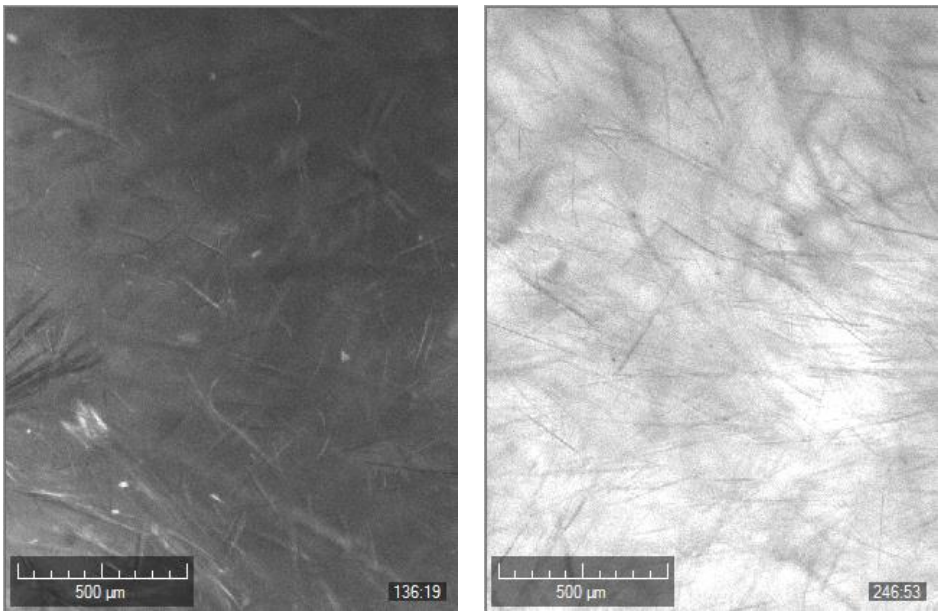

Figure 7.5: Crystals formed from a 2.5 g/100g solution on cooling at; onset of cooling (left) and during dissolution (right)

7.2.2 Dynamic Light Scattering

The solution state of MEA carboxylate solutions was probed by dynamic light scattering (DLS) to determine the size of micelles forming in solution. Aqueous solutions of MEA laurate and MEA stearate were initially used to provide upper and lower bounds to the micelle size. However, the solution concentrations that could be studied were limited to much lower concentrations than those

studied by turbidity; solution concentrations were limited to 1 g MEA carboxylate per 100g deionised water and lower. Concentrations such as those in the turbidity studies (2.5 g MEA carboxylate/100 g water and higher) were attempted, however the data quality was poor and did not meet the Malvern Zetasizer software's built-in quality criteria, which was used to determine if the collected data was of appropriate quality for use.

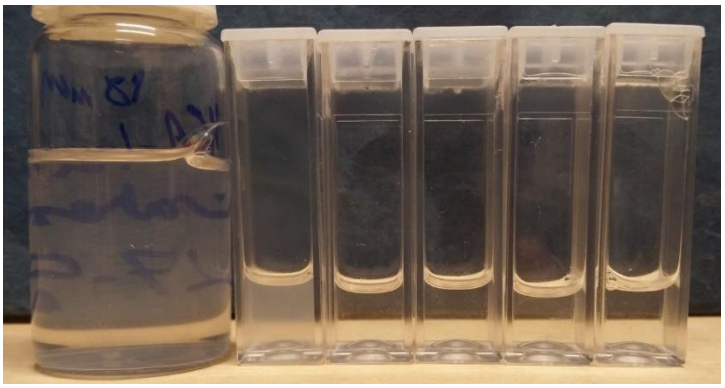

Figure 7.6: Aqueous MEA laurate samples prepared for DLS, increasing in concentration from left to right: 0.5, 1, 2.5, 5, 10, 15 g/100g.

The samples for MEA laurate are shown in Figure 7.6, increasing in concentration from left to right, at the same temperature – of note is that the lowest concentrations are turbid whilst the much higher concentrations are clear. An explanation for this is that hydrolysis is more prevalent at low solution concentrations meaning more fatty acid was in solution. Combining this with theory of carboxylate soap solutions as it was likely to be fatty acid rather than acid-soap precipitated at very low solution concentration (15). As the fatty acid is poorly soluble it would rapidly precipitate out, resulting in the turbid solutions.

The results of the 1 g/100g MEA laurate solutions (measured at 25 °C) indicated a bimodal size distribution; 103 nm and 886 nm by intensity, and 82 nm and 1116 nm by volume. The 1 g/100g MEA stearate solutions (measured at 60 °C) also indicated a bimodal size distribution; 171 nm and 1331 nm by intensity, and 164 nm and 1525 nm by volume. Both these solutions were slightly turbid at the measurement temperature – neither became clear on heating further. The larger sized peak in the distributions were therefore due to the precipitated material causing the turbidity whilst the small peak was the hydrodynamic radius of the MEA carboxylate micelle. The large size of the hydrodynamic radius for the micelle suggest that the micelles have already become elongated and wormlike.

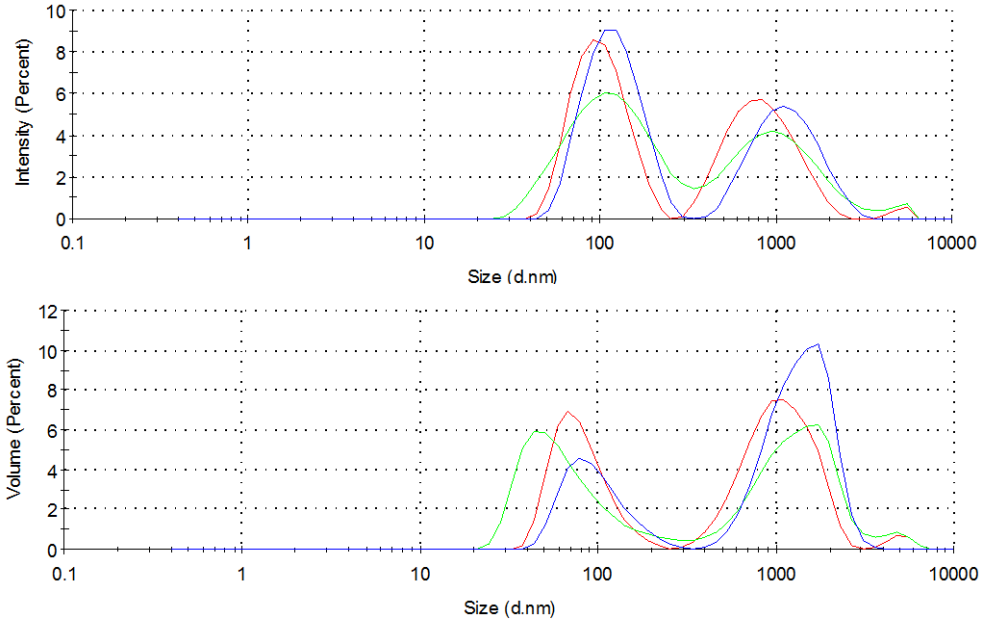

Figure 7.7 Size distribution by intensity (top) and by volume (bottom) of 1 g/100g MEA laurate solution from DLS measurements at 25 °C

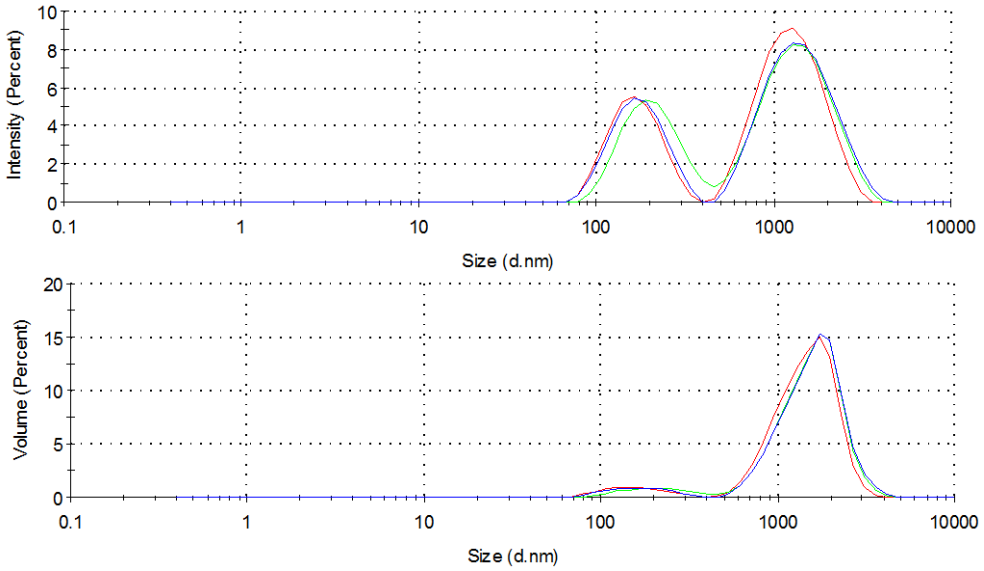

Figure 7.8 Size distribution by intensity (top) and by volume (bottom) of 1 g/100g MEA stearate solution from DLS measurements at 60 °C

Aqueous MEA myristate solutions were studied by DLS during a stepped temperature ramp, in 5 °C increments, from 25 °C to 50 °C in order to observe how the micelle size changed with temperature and also as a check on the measurements for the MEA laurate and MEA stearate solutions. At 30 °C and below, the correlograms were poor due to large crystals present in the solution as the solution was below the dissolution temperature. At 35 °C and above, the solution was in the micellar regime and as Figure 7.9 shows, the hydrodynamic diameters of the micelles increased in size with increasing solution temperature. The mean micelle hydrodynamic diameter varied

linearly with temperature from 86 nm (by intensity) and 67 nm (by volume) at 35 °C to 123 nm (by intensity) and 92 nm (by volume) at 50 °C. The larger sized particles didn't show a clear trend with temperature. Comparing the 1 g/100g solutions of MEA stearate at 60 °C, MEA myristate at 50 °C, and MEA laurate at 25 °C, the mean micelle hydrodynamic diameter varied linearly with chain length, as shown by Figure 7.10.

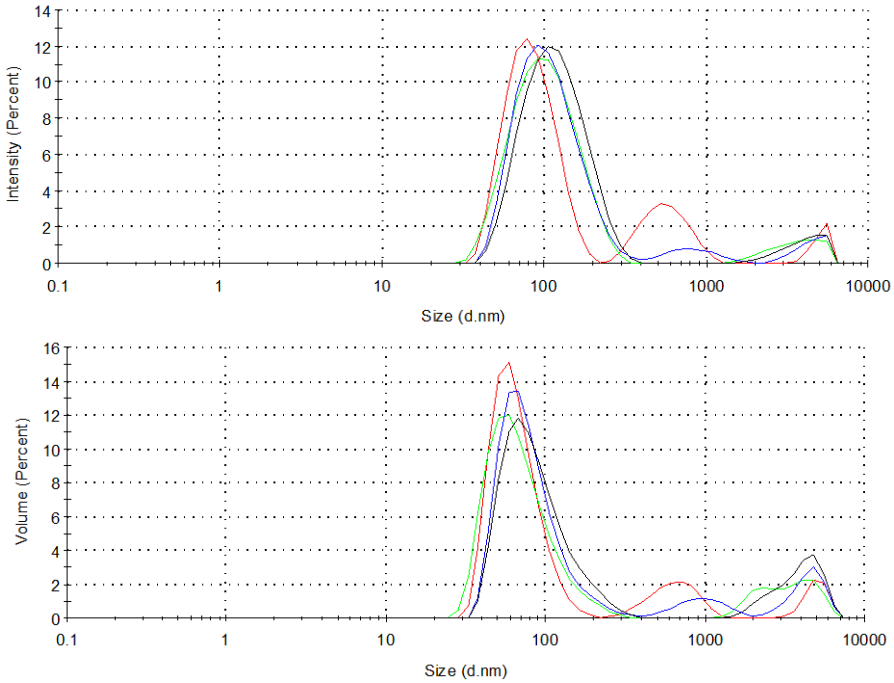

Figure 7.9: Size distributions by intensity (top) and by volume (bottom) by DLS of 0.5 g/100g MEA myristate solution, during a stepped heating profile: red 35 °C, green 40 °C, blue 45 °C, and black 50 °C.

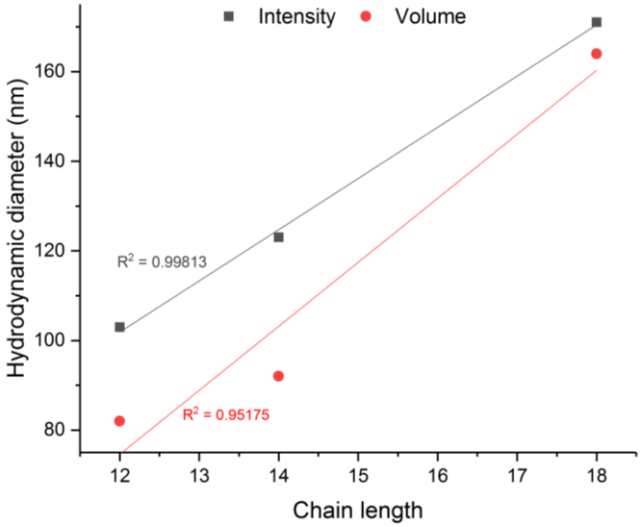

Figure 7.10: Variation of mean micelle hydrodynamic diameter (by intensity and volume) of MEA carboxylates in water with chain length, with linear fits.

7.3 Offline characterisation of crystallised material from aqueous MEA carboxylate solutions

Samples of crystallised material from aqueous MEA carboxylate solutions were taken to further study the crystallisation process and to shed light onto the unexpected crystallisation and dissolution temperature trends. Crystals generated by cooling crystallisation were filtered and air-dried before being characterised by a number of structural and chemical analysis techniques.

The FTIR spectra of the filtered crystals from aqueous MEA laurate and MEA myristate solutions, shown in Figure 7.11 and Figure 7.12, showed acid-soap was present in the samples from MEA laurate and MEA myristate solutions across the concentration range studied. This is due to the carbonyl peak at approx. 1720 cm^{-1} which is characteristic of the 1:1 acid-soap as identified previously; in a pure soap the carbonyl peak isn't present and in a fatty acid the peak is closer to 1700 cm^{-1} (4, 17-19). A similar position of the carbonyl peak has been reported for palmitic acid sodium palmitate acid-soap (19). The carboxylate peak positions at 1510 cm^{-1} and 1550 cm^{-1} are also in agreement with those previously determined for the acid-soap.

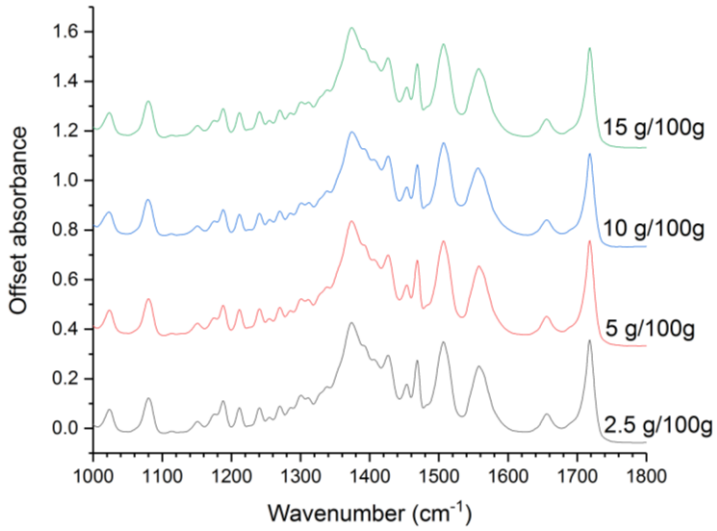

Figure 7.11: ATR-FTIR spectra of precipitate from MEA laurate solutions of differing concentration

The FTIR spectra of the crystal samples from the MEA laurate solutions are shown in Figure 7.11. The FTIR spectra of the crystals was consistent across the concentration range studied. By comparison with the spectra of partially neutralised lauric acid samples in the previous chapter, the sample spectra were consistent with that of a 50% neutralised sample.

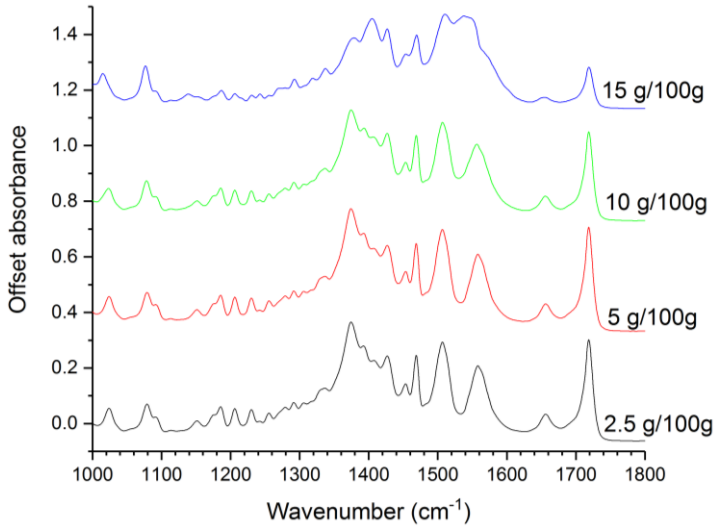

Figure 7.12: ATR-FTIR spectra of precipitate from MEA myristate solutions of differing concentration

Comparison of the FTIR spectra shown for the crystal samples from MEA myristate with those recorded for partially neutralised samples in the previous chapter indicated that the samples from each concentration were a mixture of MEA myristate and its 1:1 acid-soap. The 2.5, 5, 10 g/100g samples were consistent with neutralised samples between 50%-70%, whilst the 15 g/100g sample was consistent with the 80% and 90% samples.

The low-angle PXRD results further confirmed the presence of the 1:1 acid-soap by their expected lamellar crystal structures with long-spacings of 36 Å and 41 Å for the laurate and myristate acid-soaps respectively. The samples from higher concentrations of MEA laurate and MEA myristate also contained the respective MEA carboxylate. For the 10 g/100g concentration and above for both samples, the lamellar peaks of MEA laurate (20 Å) and MEA myristate (22 Å) were observed in their respective samples. There was no evidence in the low-angle PXRD patterns of fatty acid within any of the samples (20-23). The patterns for the MEA myristate solution samples showed a stronger concentration dependence than for the MEA laurate solutions. By visual comparison with the partially neutralised myristic acid samples in the previous results chapter, the closest matches for the wider angle PXRD scans are; the 15 g/100g to the 90% neutralised sample, 10 g/100g to the 60% neutralised sample, and the 2.5 g/100g and 5 g/100g to the 40% or 50% neutralised samples. Comparison of the wider angle PXRD scans for the samples from the MEA laurate solutions showed a lower concentration dependence with; 2.5 g/100g sample closest to the 50% neutralised sample, the other concentrations were between the 50% - 60% neutralised samples.

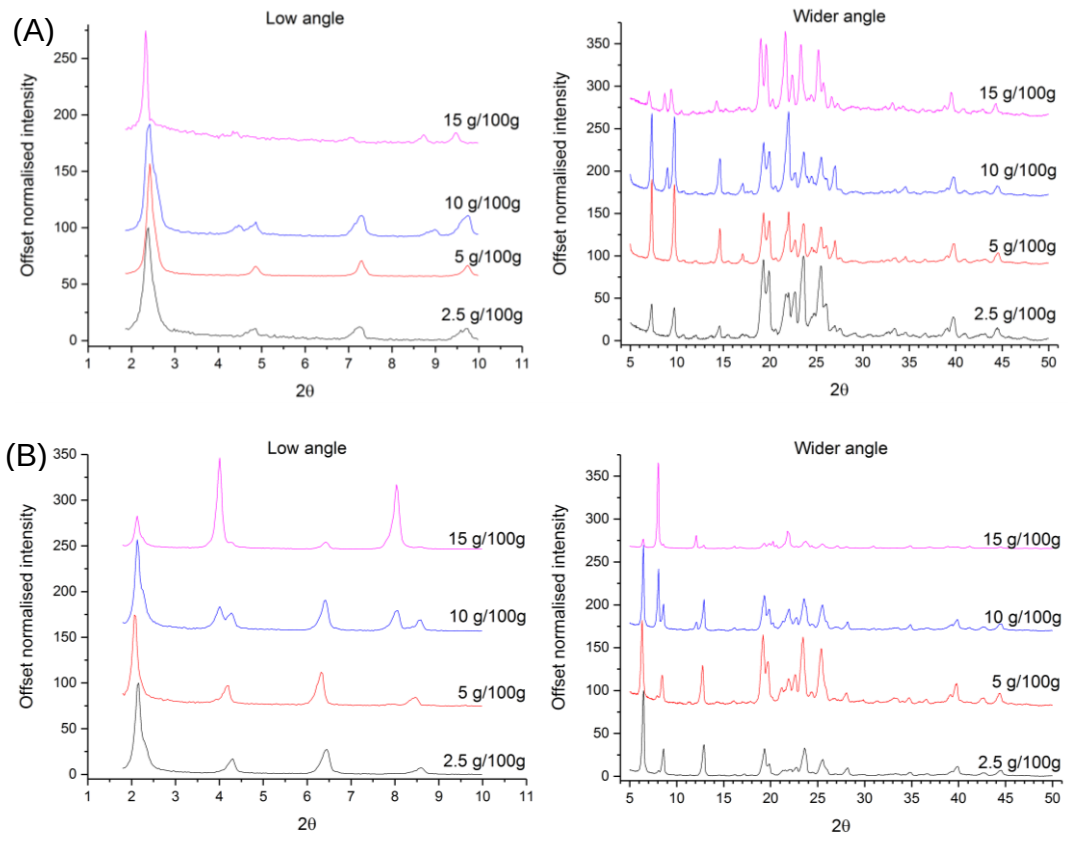

Figure 7.13: PXRD patterns of crystal samples from various concentrations of (A) MEA laurate and (B) MEA myristate solutions compared to their respective fatty acid and pure soap.

Differential scanning calorimetry measurements were carried out on the samples from each concentration with the traces further confirming that the bulk of the crystal samples from both the MEA laurate and MEA myristate solutions were the 1:1 acid-soap. For the MEA laurate samples, the heating ramp traces showed only one endothermic melting peak, the temperature of which was consistent with that determined previously for the 1:1 acid-soap. The 10 g/100g and 15 g/100g samples showed a shoulder on the main peak, which was consistent with the behaviour of the DSC heating ramps of 60% and 70% partially neutralised lauric acid samples.

For the MEA myristic samples, all except for the 15 g/100g sample contained a main endothermic melting peak consistent with that of the 1:1 acid-soap. The 10 g/100g trace showed a shoulder on the peak, consistent with the behaviour of the 60% and 70% partially neutralised samples. The 15 g/100g sample contained two peaks, similar to the 90% partially neutralised sample; an acid-soap melting peak and a peak consistent with that for MEA myristate.

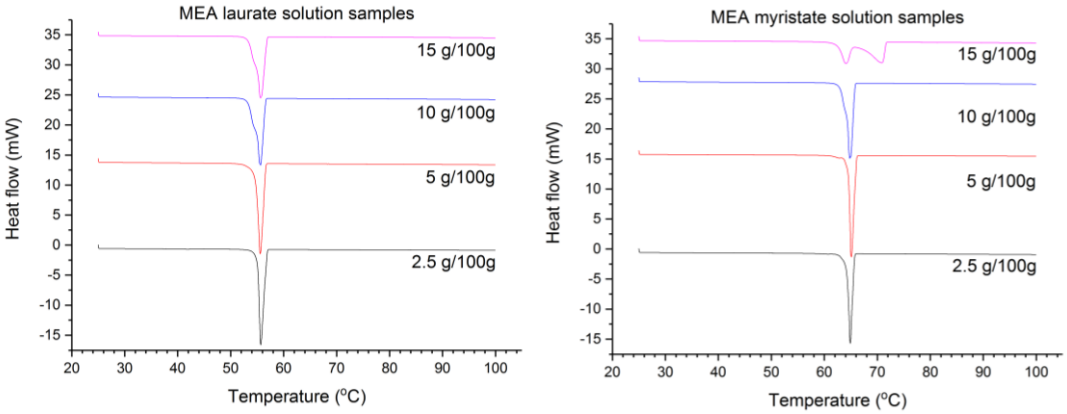

Figure 7.14: DSC traces of crystal samples from aqueous MEA carboxylate solutions during a heating ramp

The PXRD, FTIR, and DSC data displayed consistent trends for the samples from MEA laurate and MEA myristate solutions. The MEA laurate samples were more consistent in composition for the solution concentrations studied, predominantly the 1:1 MEA laurate – lauric acid acid-soap. The samples contained increasing amounts of MEA laurate as the concentration increased, with 10 g/100g and 15 g/100g samples showing clear evidence of this. The MEA myristate samples showed similar trends, but more pronounced; at low concentrations the sample was mainly the 1:1 acid-soap but on increasing concentration the precipitate consisted of more MEA myristate. Approximate compositions can be determined through comparison with the partially neutralised acid data from the previous chapter; the MEA laurate samples were equivalent to 50% to 70% neutralised whilst the MEA myristate samples ranged from 50% to 90% neutralised. From these estimations, the ratio of MEA:acid in the crystal sample is known and as the total amount of acid in the solution is known, it allows calculation of the MEA in the crystal sample and thus the amount of carboxylate (as the MEA will be bound to the carboxylate) and acid. Assuming the formation of acid-soap is preferred, the amount of soap and acid-soap can then be calculated.

The approximate compositions for the crystal samples from aqueous MEA laurate and MEA myristate solutions are summarised in Table 7:1. The approximate compositions of the crystal samples help explain the trends in crystallisation and dissolution temperatures shown in Figure 7.4. The overall observed trend is that as the starting concentration of the MEA carboxylate solution increases, the crystals formed are increasingly the MEA carboxylate rather than its acid-soap, reflecting a change in speciation in the solution. The decrease in dissolution temperature with increasing concentration is therefore likely due to the MEA carboxylate helping to solubilise the less soluble acid-soap.

Table 7:1: Approximate compositions in terms of MEA carboxylate (soap) and their 1:1 acid-soap (AS) of crystal samples from aqueous MEA laurate and MEA myristate solutions. The used degree of neutralisation was used in the composition calculations and was determine by evaluating the characterisation data.

		Approx. neutralisations				Composition	
Chain length	Conc. (g/100g)	IR	PXRD	DSC	Used	Soap %wt	AS %wt
C12:0	2.5	50	50	50	50	0	100
	5	50	50-60	50	55	11	89
	10	50	50-60	60-70	60	22	78
	15	50	50-60	60-70	70	43	57
C14:0	2.5	50-70	50	50	50	0	100
	5	50-70	50	50	50	0	100
	10	50-70	60	60-70	70	43	57
	15	80-90	90	90	90	82	18

The change in composition of the crystallised material for the MEA carboxylate solutions also influenced the observed metastable zone width. The MEA laurate solutions showed a consistent MSZW across the concentration range studied. The approximate compositions determined indicated that the acid-soap was the dominant component across the range studied. The MSZW of the MEA myristate solutions increased as the concentration increased, with a prominent increase in the 15 g/100g sample. This can be explained by the changing composition of the crystal samples; the 15 g/100g sample was predominantly MEA myristate whilst the other samples were mainly its acid-soap.

The approximate compositions for the MEA laurate samples showed a more steady change in composition than the MEA myristate samples. However, this is mainly due to the estimation of the degree of neutralisation for the 5 g/100g MEA myristate sample as if it was 5% higher for example, it would give a composition of 11% MEA carboxylate which would represent less of a step change in composition. The differences in estimation could be down to sampling issues e.g the portion of sample used for a characterisation wasn't representative of the rest of the sample, though the use of multiple techniques should have helped to mitigate this risk.

7.4 Process Raman measurements of aqueous MEA myristate solutions

Process Raman measurements were carried out on aqueous MEA carboxylation solutions in order to establish if the turbidity transitions attributed to crystallisation and dissolution were correctly attributed and to further characterise the crystallisation behaviour. The crystallisation and dissolution events were followed via tracking the state of the carboxylate alkyl chain as in a micelle the chain will be disordered and liquid-like whereas in the crystal, the chain will be well-structured and ordered. The changes in alkyl chain order were followed by using two intensity ratios (eqn. 7.1 and 7.2) that have been reported to be sensitive to the state of the alkyl chain (24, 25). In addition, the relative intensities of the CH2 asymmetric and symmetric stretches are inverted in the case of micelles as opposed to the crystalline state.

$$\frac{CH_2\ symmetric, 2850\ cm^{-1}}{CH\ stretch, 2930\ cm^{-1}} : lateral\ order\ and\ chain\ packing \quad \textbf{7.1}$$

$$\frac{CH_2\ asymmetric, 2880\ cm^{-1}}{CH_2\ symmetric, 2850\ cm^{-1}} : confirmational\ disorder \quad \textbf{7.2}$$

The spectra of the crystallised solutions were averaged using the spectra collected during the low hold at constant temperature to improve the signal-to-noise ratio and identify any weak peaks from the background noise. Similarly, the spectra of the solution state were averaged at constant temperature during the high temperature hold.

7.4.1 Transition temperatures

The intensity ratios as a function of reactor temperature are shown in Figure 7.16 for the MEA myristate solutions. On cooling there was no change in the 2880/2850 intensity ratio until the point of crystallisation where there was a sharp increase in the intensity ratio, signifying an increase in ordering of the alkyl chains due to the formation of crystalline structures. The 2850/2930 intensity ratio increased linearly during cooling until the point of crystallisation when there was a sharp increase in the intensity ratio. This suggests that lateral order and chain packing increased during cooling, but the alkyl chains still have conformational disorder until they crystallised.

On reheating the decrease in the intensity ratio is caused by the alkyl chains becoming more disordered due to the dissolution of the crystals and the formation of a micellar solution. The 2880/2850 ratios showed a sharp initial decrease followed by a more gradual decrease to its value before crystallisation. The 2850/2930 ratio showed similar behaviour – a sharp initial

decrease followed by a gradual decrease – during dissolution, but also showed a linear decrease as the solution temperature further increased. This was the reverse of its behaviour observed on cooling and thus represents a decrease in chain packing and lateral order with increasing solution temperature.

The reactor temperature profiles in Figure 7.15 for the cooling ramps for the 2.5, 5, and 10 g/100g concentrations showed a linear decrease in temperature, followed by a slight increase in reactor temperature at the point of crystallisation due to the heat of crystallisation. The 15 g/100g sample showed different behaviour however as a deviation from linear cooling was observed at 24 °C, where there was a change in solution properties which slowed the rate of reactor cooling. However, there was no change observed in the monitored intensity ratios at this temperature or the recorded spectra. There was no clear increase in temperature observed for the 15 g/100g solution from the heat of crystallisation as the circulator had already further decreased in temperature due to the change in solution properties.

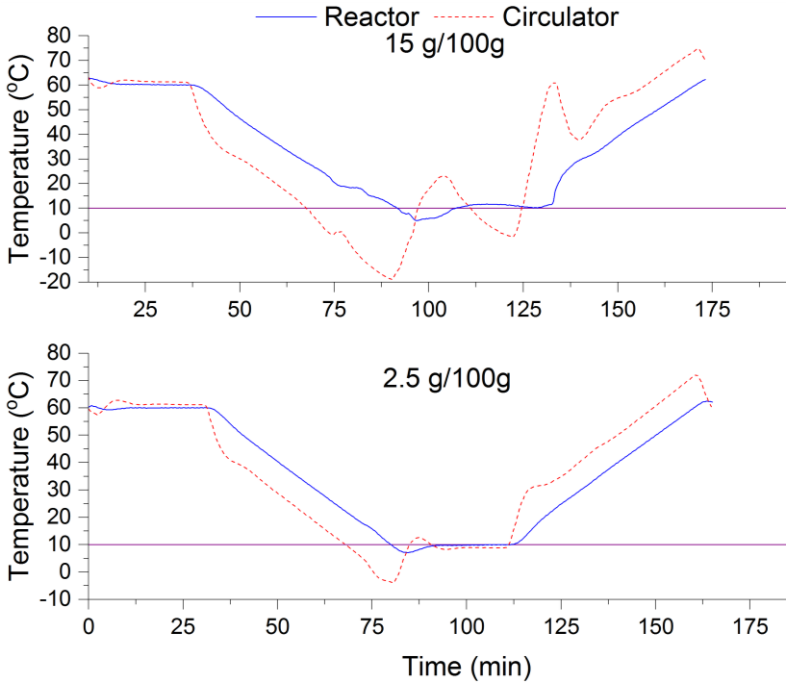

Figure 7.15: 0.5 L reactor and circulator temperature profiles during a 60-10 °C cycle at 1 °C/min of aqueous MEA myristate solutions

During the heating ramps the temperature difference between the onset (initial decrease in the ratios) and endset (ratios return to values before crystallisation) of dissolution can be significant – over 5 °C difference. The difference may be the result of slow dissolution kinetics combined with the relatively fast heating rate. The overall dissolution kinetics were likely to be slow, particularly for the more concentrated solutions, due to the soaps

crystallising as long crystalline fibres that enmesh the water. This would have hampered mass and heat transfer as mixing would have been localised to near the impeller whilst heat transfer was concentrated around the reactor walls, meaning a degree of dissolution would be required before good mixing was achieved. This, combined with the endothermic dissolution process, resulted in a slow increase in reactor temperature that caused the circulator to rapidly increase in temperature, leading to a rapid reactor temperature increase once good mixing was achieved. This phenomenon was also observed at the 80 mL scale (in the HEL Ltd AutoMATE reactor system) but to a lesser extent, due to the better mixing afforded by the smaller scale. However, the two reactor scales are not directly comparable due to the different temperature control arrangements; the 0.5 L reactor used an oil jacket to control the reactor temperature, whilst the 80 mL reactors ran in power-compensation configuration with an oil jacket and electric heater. In power-compensation, the oil jacket was set 10 °C below the target temperature and an electric card heater underneath the reactor was used to raise the reactor contents to the desired temperature. This type of control afforded a faster response to changes in the reactor temperature compared to that used for the 0.5 L reactor.

The reactor scale effect has implications for stability testing within industry as the scale of the sample volume tested will influence how the formulation sample cools or heats in response to ambient temperature changes. In addition, it will affect the extent to which thermal gradients will develop within a sample, which could cause localised areas of supersaturation and affecting the crystallisation process. For example, small volume formulation samples will likely equilibrate to ambient temperature quicker and have lesser thermal gradients. However, as discussed in section 2.4, smaller solution volumes have lower rates of nucleation, and thus small volume samples may require longer testing times. The overall implication of the scale-effects is that formulations ideally need to be tested at a similar scale to their end-usage form if current testing methodologies are used i.e being placed into a isothermal temperature-controlled environment. However, different sample scales could be used, if the difference in thermal-response is accounted for, perhaps through the use of cooling profiles rather than pure iso-thermal conditions.

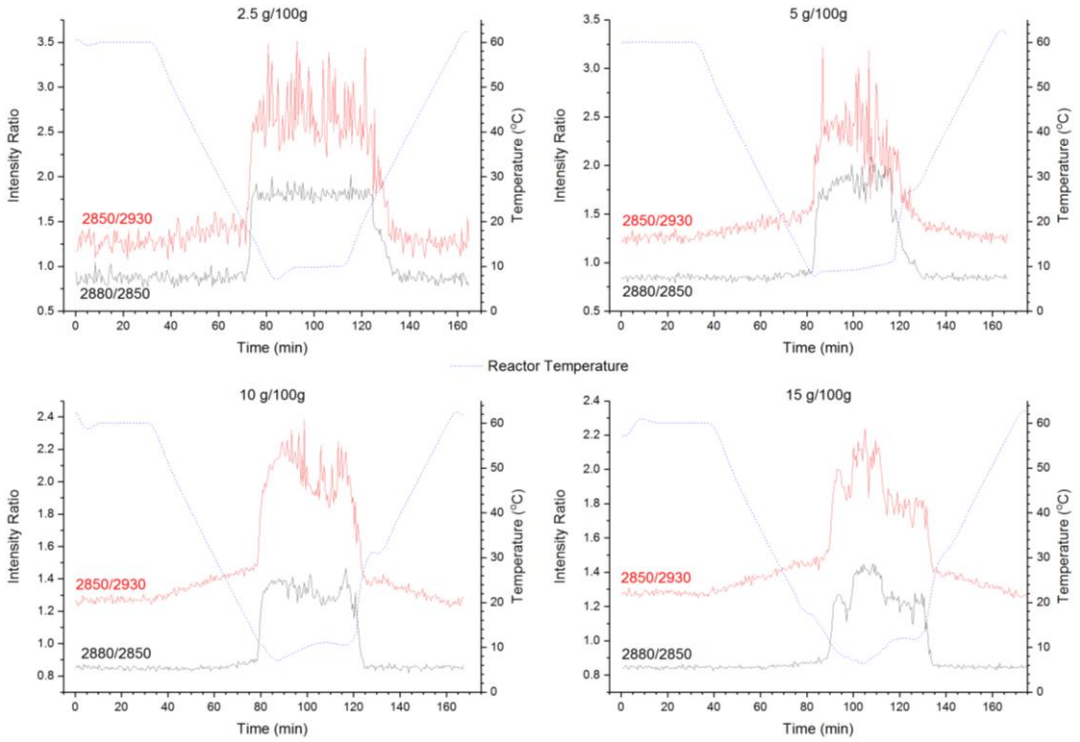

Figure 7.16: Intensity ratios during a temperature cycle of 2.5 g/100g aqueous solution of MEA myristate

For the MEA myristate solutions the crystallisation temperatures determined by the sharp changes in the intensity ratios were consistent (within 1-2 °C) with the average temperatures observed in the turbidity measurements in Crystal16 (section 7.2) and the samples crystallised in the HEL AutoMATE for the same cooling rate. The exception to this is the 2.5 g/100g MEA myristate sample which crystallised 5 °C higher in the Raman experiments than in the turbidity data, though they still fell within the temperature range observed in the Crystal16 data. The dissolution temperatures (temperature 2 in Table 7:2) observed in the Raman data had a trend consistent with the Crystal16 turbidity data but were slightly lower, though still within 4 °C of the turbidity results. These differences in crystallisation and dissolution temperatures are likely due to the different geometries and scales – Crystal16 uses 1 ml of solution and magnetic agitation whilst the Raman measurements used a 0.5 L reactor with overhead stirring and probes. The dissolution 1 temperatures could be related to the two-step dissolution profiles observed for the higher concentrations and the faster cooling rates in the Crystal16 data. However, it is hard to determine if this is the case from the Raman data due to the rapid increases in temperature during the onset of dissolution for the higher concentrations; the temperature ramp was set at 1 °C/min, but the initial temperature ramp during reheating was in excess of 2.5 °C/min for all but the 2.5 g/100g concentration.

Table 7:2: Crystallisation and dissolution temperatures determined via Raman for aqueous MEA myristate solutions. Dissolution temperature 1 represents the start of dissolution and temperature 2 the point when the intensity ratios level off.

Concentration (g/100g)	Crystallisation Temperature (°C)	Dissolution Temperature 1 (°C)	Dissolution Temperature 2 (°C)
2.5	17.1	24.1	33.4
	18.0	24.5	32.7
	18.7	25.9	34.0
5	13.8	20.8	28.4
	13.5	21.1	28.6
	8.3	23.3	27.8
10	11.1	19	26.1
	12.0	20	27.0
	11.2	20	27.1
15	12.2	19	24.4
	11.5	18	25.1
	10.7	-	24.6

7.4.2 Crystallised solution spectra – MEA myristate solutions

The most useful region for identifying the crystallised components of the MEA myristate solution was the 1800-800 cm^{-1} region. The spectra suggested an acid-soap had formed for all the concentrations studied due to the presence of a weak peak at 1718 cm^{-1}, which is characteristic of an MEA carboxylate acid-soap. The peak was weak and difficult to observe against the background noise in the individual spectra, but becomes clear on averaging the spectra. The intensity of the carbonyl peak showed a concentration dependence, with the peak becoming less intense as the solution concentration increased.

The CH2 rocking peaks, between 930-830 cm^{-1}, also indicated that an acid-soap had formed due to the presence of a peak associated with the acid-soap: 908 cm^{-1}. The intensity of the peak showed concentration dependence, decreasing in intensity with increasing concentration – similar to the carbonyl peak behaviour. The three other peaks in the region, 924, 908, 890, 872 cm^{-1}, are present in both the acid-soap and MEA myristate. However, the 10 and 15 g/100g concentrations also had an additional peak at 840 cm^{-1} that is associated with MEA myristate, suggesting that the soap had crystallised out alongside the acid-soap. This was further supported by the behaviour of the peak at 1078 cm^{-1} and the 1490-1400 cm^{-1} region. The peak at 1078 cm^{-1} was present in only the 10 and 15 g/100g and is associated with MEA myristate.

In the 1490 cm^{-1} region, there are clear differences between the 2.5 and 5 g/100g samples and the 10 and 15 g/100g samples. The two main peaks in the 2.5 and 5 g/100g samples are at 1464 and 1449 cm^{-1}, consistent with the previously determined acid-soap spectrum. In the 10 and 15 g/100g sample, the main peaks are at 1459 and 1439 cm^{-1}, consistent with MEA myristate.

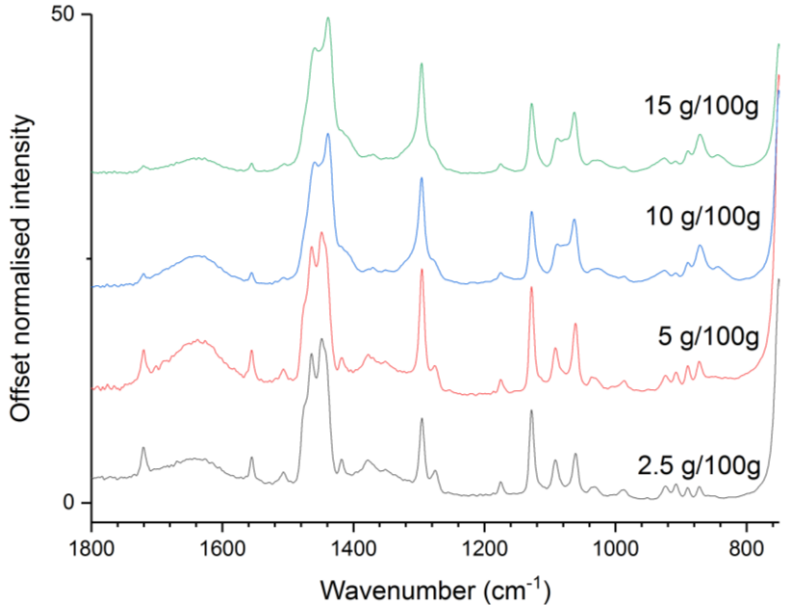

Figure 7.17: Raman spectra of crystallised aqueous MEA myristate solutions at 10 ºC

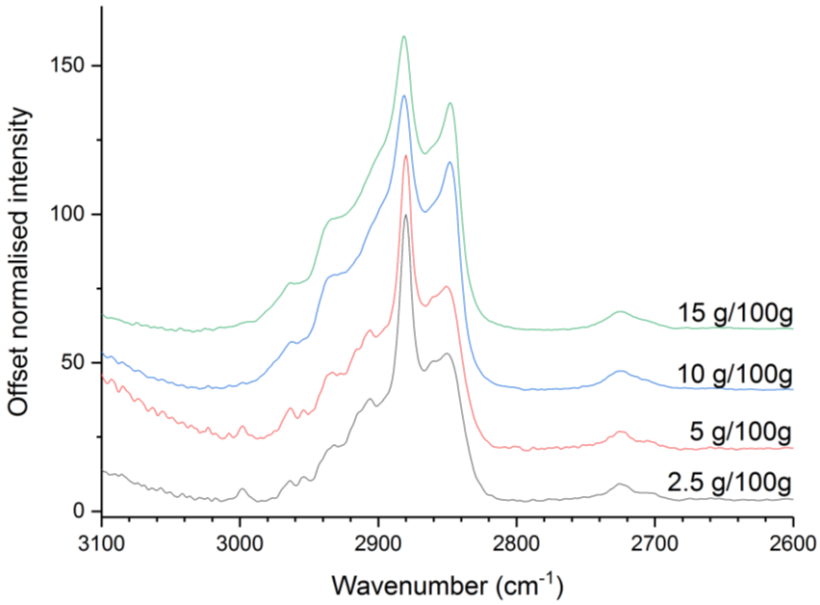

Figure 7.18: Raman spectra of crystallised aqueous MEA myristate solutions at 10 °C focussing on the CH2 and CH3 stretching bands

The 3100-2600 cm^{-1} region is less diagnostic for distinguishing between MEA myristate and its acid-soap, with more subtle differences between the components. The spectra for the 2.5 and 5 g/100g concentrations were more

consistent with that of the acid-soap than the soap due to characteristic peaks at 2936, 2964, and 2998 cm^{-1}. The position of the CH2 asymmetric peak at 2880 cm^{-1} was also consistent with the acid-soap spectrum. The 10 and 15 g/100g concentrations also showed peaks at 2936 and 2965 cm^{-1} indicating the presence of acid-soap, but the CH2 asymmetric peak broadened and shifted to 2881 cm^{-1} which is consistent with a mixture of soap and acid-soap.

The spectra of the crystallised MEA myristate solutions therefore suggest that the composition of the precipitated material has a concentration dependence, shifting with increasing concentration from acid-soap at lower concentrations to mixtures of acid-soap and soap, with the proportion of soap increasing as the concentration increases. This type of behaviour is similar to that predicted by theory of the pH of carboxylate soap solutions; for coexistence of a 1:1 acid-soap and a soap, increasing the total carboxylate concentration increases the amount of soap linearly whilst the amount of acid-soap remains constant (15).

7.4.3 Solution state spectra – MEA myristate

The Raman spectra of the solution state of the MEA myristate solutions showed small differences between the concentrations. The peak at 1555 cm^{-1} appears to decrease in intensity in Figure 7.19 as the solution concentration increased, but in the non-normalised data the peak was almost identical across the concentrations in terms of peak height and shape. The concentration dependence is therefore explained by the amount of fatty acid/acid-soap remaining constant whilst the amount of the soap increased. This explanation would agree with the crystallised solution spectra that suggested that acid-soap formed across the concentration range but the amount of MEA myristate formed increased with increasing total concentration.

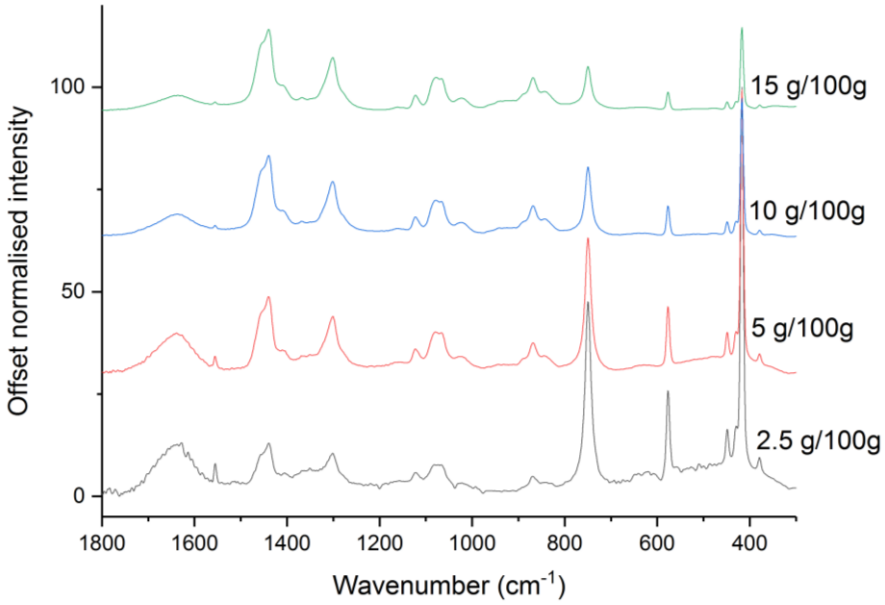

Figure 7.19: Raman spectra of aqueous MEA myristate solutions at 60 °C

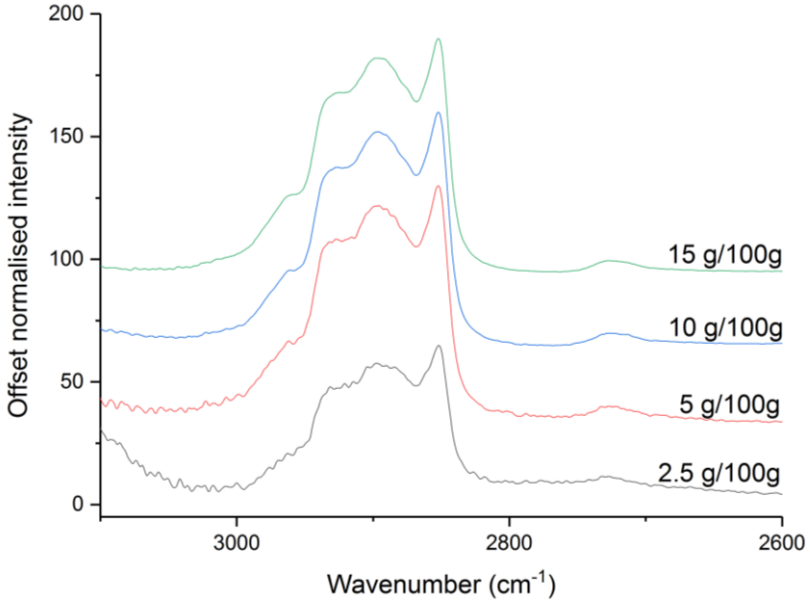

Figure 7.20: Raman spectra of aqueous MEA myristate solutions at 60 °C

7.5 MEA carboxylates with excess MEA in aqueous solution

The previous results showed that acid-soap was forming in aqueous MEA carboxylate solutions due to incomplete deprotonation of the fatty acid. Thus by adding an excess of MEA, the degree of deprotonation should be increased and therefore a lower amount of acid-soap should form. Turbidity measurements were carried out on aqueous MEA myristate solutions with

excess MEA to determine the effect on crystallisation and dissolution temperatures. Crystallisation and dissolution temperatures determined as a function of concentration and cooling rate are shown in Figure 7.21. Compared to the trends for the equi-molar mixtures of MEA and myristic acid, the samples with excess MEA showed smaller standard deviations in their transition temperatures. The samples with excess MEA also showed a weaker dependence on kinetics than the equi-molar samples and that the crystallisation process became more thermodynamically controlled as the total concentration is increased.

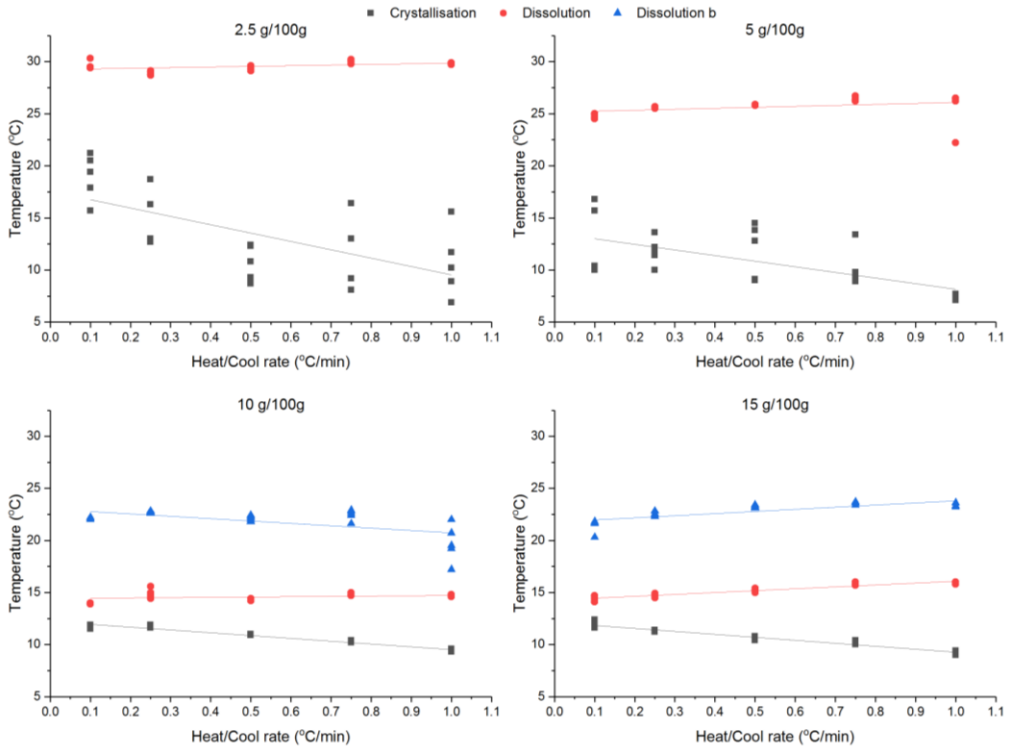

Figure 7.21: Crystallisation and dissolution temperatures as a function of cooling rate for aqueous MEA myristate samples with a 10% molar excess of MEA

The 10 g/100g and 15 g/100g concentrations showed a two-step decrease in turbidity on reheating that occurred for all the heating rates studied, compared to just the higher rates in the equi-molar MEA myristate solutions in section 7.2. The first decrease in turbidity did not appear to be affected by the addition of MEA as its onset temperature was very close to that in section 7.2. However, the second step of the dissolution process showed a decrease in onset temperature. This difference in behaviour gives insight into the mechanisms behind the two-step dissolution process as the main effect of a 10% molar excess of MEA is to adjust the pH and therefore the speciation in the solution rather than acting as a solvent. This suggests that the first step in

the two-step dissolution is MEA myristate as it is more likely to be insensitive to increasing the pH of the solution compared to the acid-soap.

The extrapolated equilibrium dissolution and crystallisation temperatures for MEA myristate with 10%molar excess MEA are shown in Figure 7.22. The addition of 10% excess MEA to aqueous MEA myristate samples lowers the dissolution temperature, with the greatest effect occurring at higher concentrations. The crystallisation temperatures also decreased with the addition of MEA, but the trend was reversed with the greatest effect seen at lower concentrations. The excess MEA had a more pronounced effect on the crystallisation temperatures than the dissolution temperatures, which resulted in a net increase in the MSZW with lower concentrations showing the largest increases.

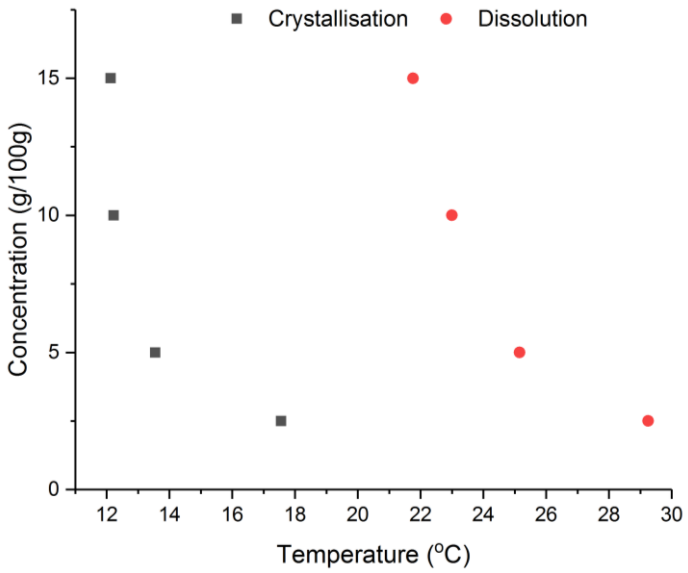

Figure 7.22: Metastable zone width diagram of aqueous MEA myristate with a 10% molar excess of MEA

These solutions were further characterised by in-situ optical microscopy using an Avantium Crystalline system. The images captured for MEA myristate solutions with a 10% excess of MEA showed a concentration dependence in that the lower two concentrations showed the presence of needle-like crystals whereas the higher concentrations did not show discrete crystals, only a turbid solution.

For the 2.5 g/100g solution, the decrease in light transmission was observed to be due to the nucleation and growth of needle-like crystals, as shown in Figure 7.23, whilst the increase in transmission during reheating was due to dissolution of these crystals. These needle-like crystals showed a very high aspect ratio with lengths over 250 µm yet widths and depths in the region of

10 – 20 µm. The 5 g/100g solution showed similar behaviours but the appearance of visible crystals in the solution was not always coincident with the increase in turbidity – the transmittance of light through the solution would decrease, yet crystals would only be observed in the “dark” solution after a period of time had elapsed.

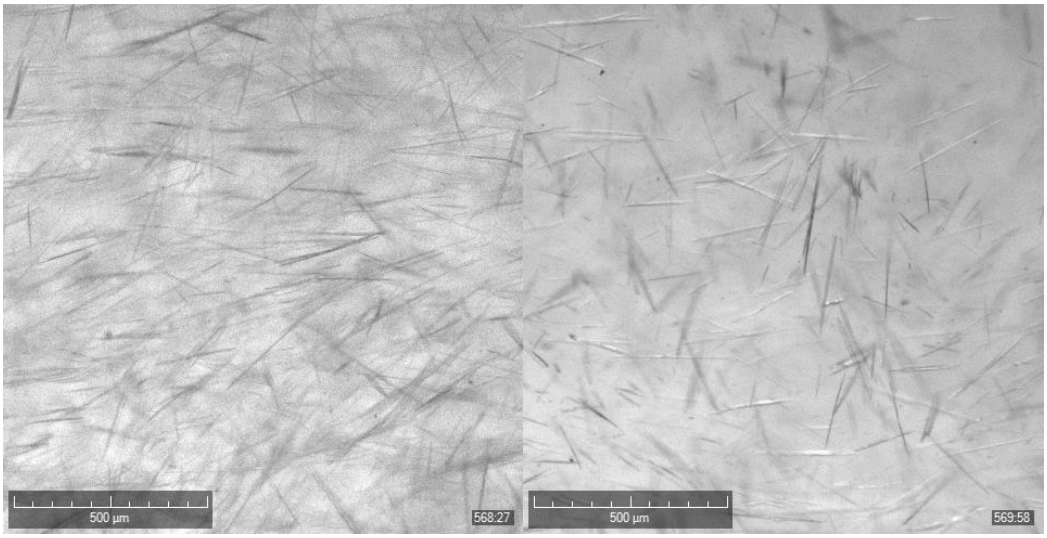

Figure 7.23: Needle-like crystals that formed during cooling of a 2.5 g/100g aqueous MEA myristate solution with a 10% excess of MEA

The 10 g/100g and 15 g/100g solutions showed different behaviours on cooling with no crystals observed, only a “textured” turbid solution observed throughout the temperature cycle. The changes in turbidity were still relatively sharp – similar to those expected for a crystallisation. In addition, there was no evidence of the two-step decrease in turbidity that was clearly and consistently observed in the equivalent Crystal16 data.

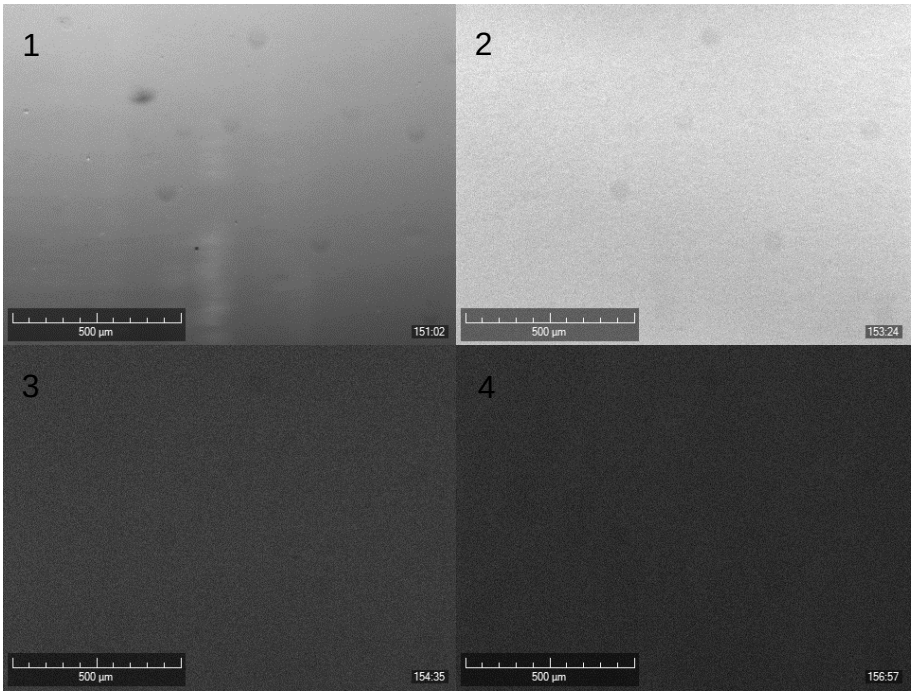

Figure 7.24: Images captured during the increase in turbidity of a 10 g/100g MEA myristate aqueous solution during cooling. 1) Initial solution state, 2) & 3) during the increase in turbidity, 4) Final solution state after maximum turbidity reached.

7.6 Conclusions

In this chapter the aqueous phase behaviour of MEA carboxylates has been studied, revealing unexpected behaviours; MEA laurate and MEA myristate solutions showed solubility profiles in which increasing concentration resulted in decreased dissolution temperature. In addition, crystallisation occurred on cooling of these solutions even though their solubility profiles indicated supersaturation would be generated by heating the solutions. Off-line characterisation of crystal samples from these solutions revealed that the 1:1 acid-soap of the MEA carboxylate and its respective fatty acid was forming in solution and crystallising out alongside the MEA carboxylate. This resulted in mixed crystal samples, which showed a concentration dependence as the proportion of the crystal sample that was MEA carboxylate compared to the 1:1 acid-soap increased with increasing solution concentration.

In-situ Raman was used to further study the crystallisation of MEA myristate from aqueous solution and found that the turbidity transitions observed in the Crystal16 data were mainly due to crystallisation and dissolution of the 1:1 acid-soap. The Raman data showed that the crystallised material was dependent on the solution concentration with lower concentrations yielding mainly the 1:1 acid-soap and higher concentrations yielding acid-soap and

MEA carboxylate mixtures. These results confirmed those of the off-line characterisation, reducing the possibility of transformation of the crystal samples during filtering and drying.

The crystallisation and dissolution temperatures observed in the turbidity data were therefore not for a binary system as the relative amounts of MEA carboxylate and its corresponding acid-soap would vary as the total solution concentration changed. Based on this, the unusual trends can then be explained on the assumption that the acid-soap will be less soluble than its corresponding MEA carboxylate. At low solution concentrations, the formation of the acid-soap appears to be favoured resulting in predominantly acid-soap crystallising out, leading to a high dissolution temperature. As the solution concentration is increased, more MEA carboxylate was present in the solution which helped to solubilise the acid-soap, thereby reducing the observed dissolution temperature. The two-steps in the turbidity data during dissolution observed for the higher concentrations of MEA myristate can therefore by assigned to the dissolution of MEA myristate and its acid-soap. The MEA carboxylate dissolution resulted in the first decrease in turbidity and its temperature showed a low concentration dependence due to the typical behaviour of surfactants – a rapid increase in solubility above the Krafft temperature. The second step in the dissolution profile was therefore dissolution of the acid-soap.

Crystallisation and dissolution behaviours of MEA myristate solutions with a small excess of MEA showed decreased dissolution temperatures and a wider metastable zone. They also showed a more pronounced two-step decrease in turbidity during dissolution, which when considered with the explanation for the two-step behaviour in the equimolar system, is to be expected; increased MEA should result in more MEA carboxylate forming at the expense of acid-soap and thus the dissolution of both components should become more distinct.

7.7 References

1. KLEIN, R., G.J.T. TIDDY, E. MAURER, D. TOURAUD, J. ESQUENA, O. TACHE and W. KUNZ. Aqueous phase behaviour of choline carboxylate surfactants—exceptional variety and extent of cubic phases. *Soft Matter*, 2011, **7**(15), p.6973.
2. WÄRNHEIM, T. and A. JÖNSSON. Phase behavior of alkanolammonium carboxylates. 1992, **88**, pp.18-22.
3. ZHU, S., P.D. PUDNEY, M. HEPPENSTALL-BUTLER, M.F. BUTLER, D. FERDINANDO and M. KIRKLAND. Interaction of the acid soap of triethanolamine stearate and stearic acid with water. *J Phys Chem B*, 2007, **111**(5), pp.1016-24.
4. PUDNEY, P.D., K.J. MUTCH and S. ZHU. Characterising the phase behaviour of stearic acid and its triethanolamine soap and acid-soap by infrared spectroscopy. *Phys Chem Chem Phys*, 2009, **11**(25), pp.5010-8.
5. ZHU, S., M. HEPPENSTALL-BUTLER, M.F. BUTLER, P.D. PUDNEY, D. FERDINANDO and K.J. MUTCH. Acid soap and phase behavior of stearic acid and triethanolamine stearate. *J Phys Chem B*, 2005, **109**(23), pp.11753-61.
6. MCBAIN, J.W., R.D. VOLD and M. FRICK. A phase rule study of the system sodium stearate-water. *Journal of Physical Chemistry*, 1940, **44**(9), pp.1013-1024.
7. MCBAIN, J.W., M.J. VOLD and J.L. PORTER. A phase study of commercial soap and water. *Industrial and Engineering Chemistry*, 1941, **33**, pp.1049-1055.
8. MCBAIN, J.W. and S.A. JOHNSTON. A Note on the Phase Rule Diagram for a Mixture of Sodium Palmitate and Sodium Laurate with Water. *Journal of the American Chemical Society*, 1941, **63**(3), pp.875-875.
9. VOLD, R.D. The phase rule behavior of concentrated aqueous systems of a typical colloidal electrolyte. Sodium oleate. *Journal of Physical Chemistry*, 1939, **43**(9), pp.1213-1231.
10. VOLD, R.D., R. REIVERE and J.W. MCBAIN. A Phase Rule Study of the System Sodium Myristate-Water. *Journal of the American Chemical Society*, 1941, **63**(5), pp.1293-1296.
11. WARNHEIM, T. and A. JONSSON. Surfactant Aggregation in Systems Containing Alkanolamines and Fatty-Acids. *J Colloid Interface Sci*, 1990, **138**(2), pp.314-323.
12. MCBAIN, J.W. and W.C. SIERICHS. The solubility of sodium and potassium soaps and the phase diagrams of aqueous potassium soaps. *Journal of the American Oil Chemists Society*, 1948, **25**(6), pp.221-225.
13. KANICKY, J.R. and D.O. SHAH. Effect of Degree, Type, and Position of Unsaturation on the pKa of Long-Chain Fatty Acids. *J Colloid Interface Sci*, 2002, **256**(1), pp.201-207.
14. LUCASSEN, J. Hydrolysis and Precipitates in Carboxylate Soap Solutions. *The Journal of Physical Chemistry*, 1966, **70**(6), pp.1824-1830.
15. KRALCHEVSKY, P.A., K.D. DANOV, C.I. PISHMANOVA, S.D. KRALCHEVSKA, N.C. CHRISTOV, K.P. ANANTHAPADMANABHAN

and A. LIPS. Effect of the precipitation of neutral-soap, acid-soap, and alkanoic acid crystallites on the bulk pH and surface tension of soap solutions. *Langmuir*, 2007, **23**(7), pp.3538-53.

16. BONEVA, M.P., K.D. DANOV, P.A. KRALCHEVSKY, S.D. KRALCHEVSKA, K.P. ANANTHAPADMANABHAN and A. LIPS. Coexistence of micelles and crystallites in solutions of potassium myristate: Soft matter vs. solid matter. *Colloids and Surfaces A: Physicochemical and Engineering Aspects*, 2010, **354**(1-3), pp.172-187.
17. LYNCH, M.L., Y. PAN and R.G. LAUGHLIN. Spectroscopic and thermal characterization of 1:2 sodium soap fatty acid acid-soap crystals. *Journal of Physical Chemistry*, 1996, **100**(1), pp.357-361.
18. WEN, X. and E.I. FRANSES. Effect of Protonation on the Solution and Phase Behavior of Aqueous Sodium Myristate. *J Colloid Interface Sci*, 2000, **231**(1), pp.42-51.
19. LYNCH, M.L., F. WIREKO, M. TAREK and M. KLEIN. Intermolecular Interactions and the Structure of Fatty Acid−Soap Crystals. *The Journal of Physical Chemistry B*, 2001, **105**(2), pp.552-561.
20. ABRAHAMSSON, S. and E. VON SYDOW. Variation of unit-cell dimensions of a crystal form of long normal chain carboxylic acids. *Acta Crystallographica*, 1954, **7**(8), pp.591-592.
21. LOMER, T.R. Unit-Cell Dimensions of γ-Lauric and γ-Myristic Acids. *Nature*, 1955, **176**(4483), pp.653-654.
22. BOND, A.D. On the crystal structures and melting point alternation of the n-alkyl carboxylic acids. *New Journal of Chemistry*, 2004, **28**(1), p.104.
23. MORENO-CALVO, E., G. GBABODE, R. CORDOBILLA, T. CALVET, M.A. CUEVAS-DIARTE, P. NEGRIER and D. MONDIEIG. Competing intermolecular interactions in the high-temperature solid phases of even saturated carboxylic acids (C10H19O2H to C20H39O2H). *Chemistry*, 2009, **15**(47), pp.13141-9.
24. PICQUART, M. Vibrational model behavior of SDS aqueous solutions studied by Raman scattering. *The Journal of Physical Chemistry*, 1986, **90**(2), pp.243-250.
25. CAZZOLLI, G., S. CAPONI, A. DEFANT, C.M.C. GAMBI, S. MARCHETTI, M. MATTARELLI, M. MONTAGNA, B. ROSSI, F. ROSSI and G. VILIANI. Aggregation processes in micellar solutions: a Raman study. *Journal of Raman Spectroscopy*, 2012, **43**(12), pp.1877-1883.
26. TER HORST, J.H. and S. JIANG. Crystal Nucleation Rates from Probability Distributions of Induction Times. *Crystal Growth and Design*, 2011, **11**, pp.256-261.

Chapter 8 In-situ SAXS/WAXS studies of crystallisation of MEA carboxylates from aqueous solutions

In-situ simultaneous small- and wide-angle synchrotron x-ray scattering studies carried out at Diamond and ESRF, probing the crystallisation process of MEA carboxylates from solution

8.1 Introduction

In-situ studies of the crystallisation process of MEA carboxylates in aqueous solution were carried out to better characterise and understand the overall process and to answer questions raised by work in the previous chapter. These studies also provided insight into the starting solution state and the effect of concentration and temperature on solution structure.

Synchrotron SAXS/WAXS studies were carried out as synchrotron radiation provided the necessary time-resolution to characterise the micelle-crystal transition and x-ray scattering would allow characterisation of both solution and crystal states. The SAXS/WAXS studies at I22 Diamond used agitated conditions through the use of a flow cell connected to a small stirred reactor to better replicate the conditions used in the previous chapter, enabling comparison. The studies at BM28 ESRF used static conditions, with solutions held in sealed capillaries. This was partly to enable a higher throughput to study a greater range of samples, but also to allow the comparison between agitated and static conditions. Static conditions are of industrial relevance as both crystallisation stability testing and the consumer products themselves are under mainly static conditions with little agitation.

This chapter begins with SAXS/WAXS studies carried out at Diamond, investigating the micellar solution structure, crystals formed in solution, and the transition from micelles to crystals. Crystallisation and dissolution temperatures are also determined by SAXS/WAXS and compared to the turbidity data presented in previous chapters. Following this, the data collected at ESRF is examined and the influence of agitation of the crystallisation process studied with respect to the solution state, crystallised state, and the transition between. In addition, the solution state structure is determined for additional MEA carboxylates.

8.2 SAXS/WAXS studies at I22, Diamond

Simultaneous SAXS/WAXS measurements were carried out on aqueous solutions of MEA myristate during temperature cycles using a capillary flow cell. The aim of these studies was to better characterise the crystallisation process of MEA carboxylates, using MEA myristate as an example, and to further investigate some of the features and trends observed via turbidity for MEA carboxylate solutions in the previous chapter.

There were some problems during the runs that affected a number of the measurements. The main issue was that the more concentrated solutions, 10 and 15 g MEA myristate/100 g water, blocked the inlet of the capillary cell shortly after crystallisation. As the peristaltic pump was set up to draw the solution through the capillary, the cell would empty after the inlet blocked and the SAXS/WAXS patterns would be of an empty capillary. During reheating and the onset of dissolution, the capillary inlet would unblock and the solution would flow through the cell again. This means that there were no patterns recorded for the time period between just after the onset of crystallisation and just after the onset of dissolution. A separate issue that the blocked capillary cell had was that bubbles could form and be pulled through the capillary if a small amount of the surfactant solution made it through the blockage. The bubbles would scatter very strongly and would trip the count limits on the detectors, causing the detector shutters to close mid-experiment and no data to be collected until the shutters were reopened. The shutter trip occurred during half of the runs carried out, however, with the exception of one run, no data was lost as the capillary had already become empty. The exception was the 10g/100g solution with the 0.25 ^{o}C/min temperature cycle where the shutter tripped shortly after crystallisation had occurred and blocked the inlet and the detector shutter wasn’t opened until after the temperature cycle had finished.

8.2.1 Solution state

The solution state of the MEA myristate solutions at 50 °C show a consistent structure for the concentrations studied as shown by Figure 8.2. The scattering patterns of the 0.5 g/100g solution suggested that the MEA myristate solutions form worm-like micelles with a length larger than the length-scale covered by the detector. The slope at low q is equal to approx. -2, which corresponds to the self-avoiding walk of the chains, whilst at intermediate q the slope is equal to -1 corresponding to the rod-like behaviour – this behaviour is reported to correspond to wormlike micelles (1). The slope at intermediate q is not observed for the 2.5 g/100g concentration and above due to the increased concentration resulting in a broad scattering peak from the wormlike micelles mesh – the size of the pores between tangled wormlike micelles, related to the average distance between micelles (2). In Figure 8.2 the peak to the left at around q = 0.05 is likely the distance between micelles as it decreases with increasing solution concentration but increases in intensity; the distance is expected to decrease due to the greater number/length of micelles within a given volume which also results in greater scattering (3). The elbow in the pattern to the right, approx. q = 0.12, corresponds to the size of the cross-section of the wormlike micelles as it shows less dependence on concentration, which is to be expected for a wormlike micelle as increasing concentration will lead to more micelles or longer micelles rather than substantially wider micelles (4).

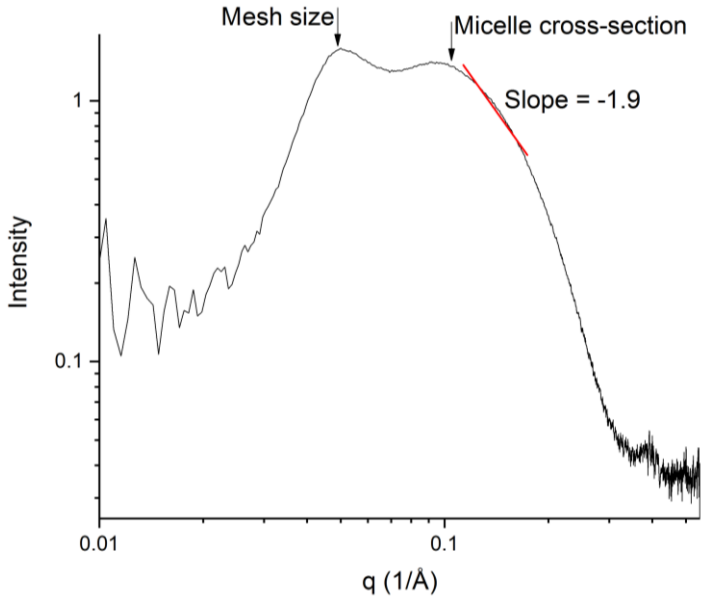

Figure 8.1: Example of data fit on a log-log plot of 2.5 g/100g MEA myristate solution at 50 °C, showing where the wormlike micelle mesh size and micelle cross-section size were extracted, along with the q-dependency.

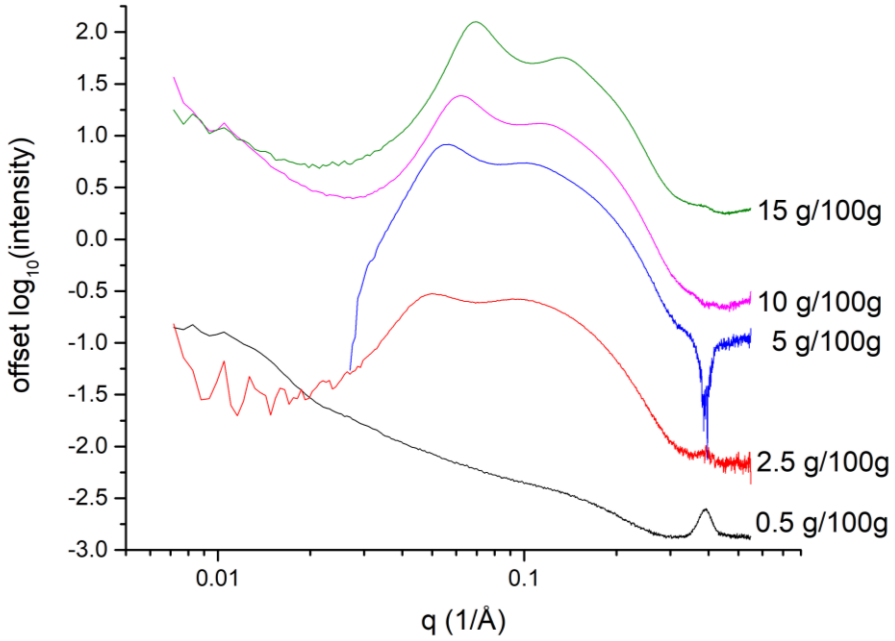

Figure 8.2: SAXS patterns of the solution state of MEA myristate solutions at 50 °C

The micelle cross-section size and wormlike micelle mesh size did show a degree of concentration dependence as summarised by Figure 8.3 below. The variation of the sizes with concentration showed a linear relationship for the concentrations of 2.5 g/100g and above.

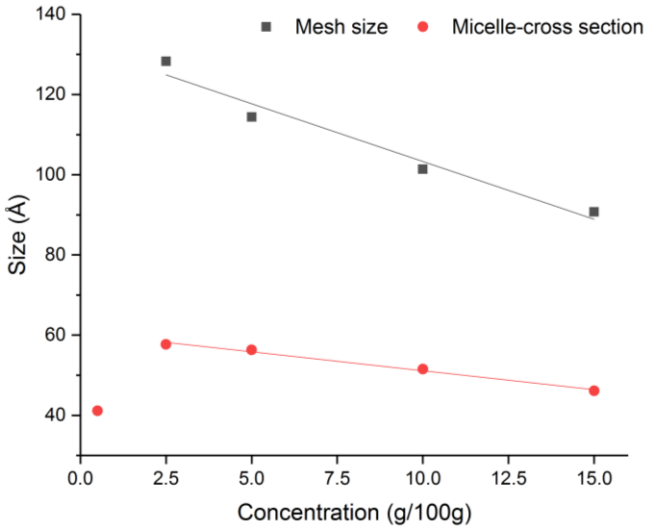

Figure 8.3: Wormlike micelle (WLM) cross-section size and mesh size determine from log-log plots of SAXS data

8.2.2 Micelle – crystal transition (1 °C/min ramp rate)

During cooling of the MEA myristate solutions, changes in the SAXS and WAXS patterns are observed corresponding to the transition from a micellar solution to a suspension of crystals. A cooling/heating rate of 1 °C/min was initially used to try shed light on the two-step dissolution behaviour observed

in the turbidity experiments for higher cooling rates in the previous chapter. However, no such two-step dissolution process was observed in the SAXS/WAXS data. The cooling data is presented here as the dissolution process during reheating showed the reverse of the behaviour observed on cooling.

The solution behaviour on cooling shows similar trends across the concentration range studied. At the onset of crystallisation, the 2D SAXS and WAXS images showed evidence of preferential orientation of the crystals by the presence of arcs in the pattern and higher intensity arcs on diffraction rings (5). Preferential orientation was to be expected given the high aspect ratio of the crystals and the tendency for them to become orientated as they flowed through the capillary cell and the sample lines.

8.2.2.1 0.5 g/100g MEA myristate solution

The SAXS patterns of the 0.5 g/100g MEA myristate solution showed changes during cooling. The slope of the scattering pattern in Figure 8.4 at low q is approx. -2 and -1 at moderate q, at the beginning on the cooling ramp, corresponding to a wormlike micelle solution state (1). On cooling, the slope of the scattering pattern remains constant until the onset of crystallisation at which the gradient increases to -3.5 as shown in the 10, 15, and 20 °C patterns. This represents a change from wormlike micelles to a combination of spherical micelles (slope of -4) and either rods (slope of -1) or platelets (slope of -2) (6, 7). The change in micelle structure was the result of the micelles breaking down to feed the crystallisation process. Changes were also observed in the WAXS pattern during cooling with a broad peak centred at q = 1.88 (d-spacing of 3.33 Å) appearing prior to the onset of crystallisation. The broad peak could be due to ordering within the solution, with d-spacing being approximate to that between adjacent alkyl chains in the crystal structure (8). The broad peak could therefore be due to alignment of alkyl chains prior to crystallisation.

The onset of crystallisation is indicated by the appearance of a series of sharp peaks in the SAXS pattern, whose d-spacing showed the characteristic ratios of a lamellar series - ratios of 1, 1/2, 1/3 (9). The n = 1, 2, 3 peaks were observed in the SAXS data and from these it was determined that the lamellar structure had a long-spacing of 41 Å. In the WAXS data the onset of crystallisation was characterised by the appearance of multiple sharp peaks, indicating a crystalline structure had formed (10).

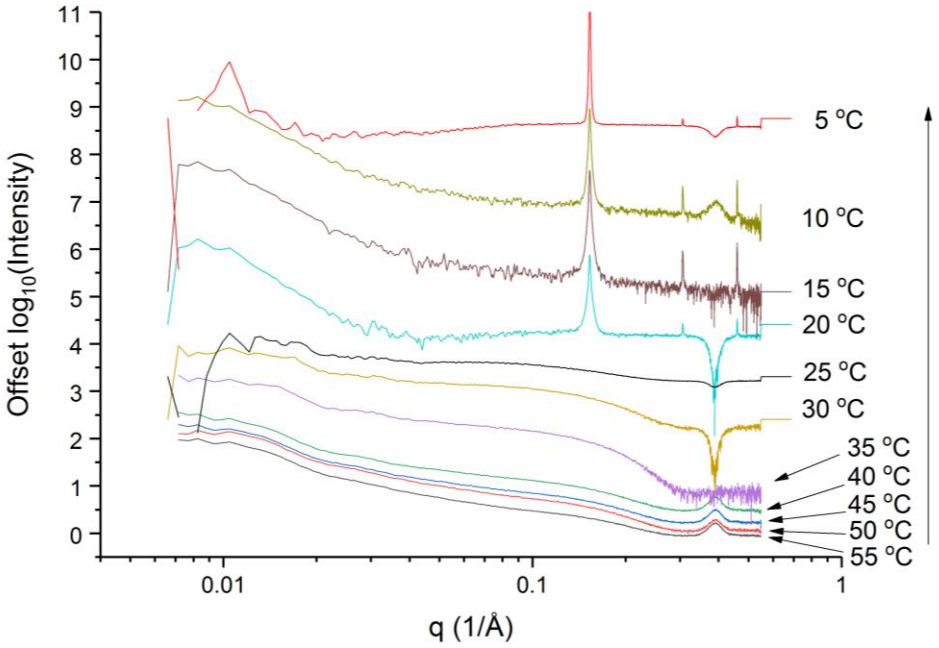

Figure 8.4: SAXS patterns (log-log) of 0.5 g/100g MEA myristate during cooling

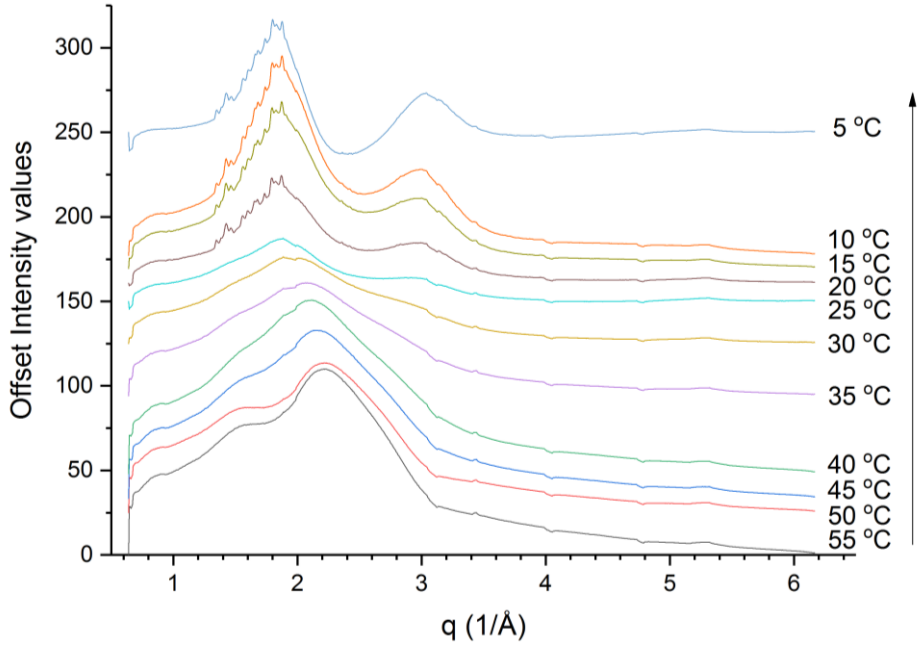

Figure 8.5: WAXS patterns of 0.5 g/100g MEA myristate during cooling

8.2.2.2 2.5 g/100g MEA myristate

During cooling of the 2.5 g/100g solution significant changes in the SAXS pattern only occurred close to the onset of crystallisation, which was characterised by the appearance of sharp peaks (n = 1,2,3) of a 41 Å lamellar structure at 13.5 °C. The gradient of the slope at low q increased during cooling of the solution from approx. -2 to -3.5 at 5 °C. This represents a change in solution structure from flexible wormlike micelles to more spherical particles (which have a slope of -4) (1, 6).

The changes in intensities of the broad peak centred on q = 0.049, the average distance between micelles, suggest that prior to crystallisation, the micelles began to breakdown by reducing in length and number resulting in an increase in the average distance between micelles and a decrease in repulsion between micelles (2, 3). This is further supported by the behaviour during crystallisation; as crystallisation begins and the sharp lamellar peaks increase in intensity, the peak at q = 0.049 decreases in intensity before the rest of the pattern changes. This represents the micelles being consumed by the crystallisation process with the micelles decreasing in length first, increasing the average distance between micelles, and the micelle radius only decreased once the micelles are almost fully consumed. Similar changes can be observed in the WAXS patterns, with the broad peak at q = 1.88 becoming more intense prior to the onset of the multiple sharp peaks that indicate a crystalline structure had formed (5). The increase of the q = 1.88 peak in intensity could represent a degree of structuring in solution as the lengthscale is approx. 3-4 Å, which is the approximate distance between adjacent alkyl chains in the crystal structure (7). The onset of the sharp peaks occurs simultaneously in SAXS and WAXS, indicating that crystallisation occurred directly without first forming a liquid crystal structure.

On reheating of the 2.5 g/100g MEA myristate solution, the reverse of the observed crystallisation process occurs; the lamellar peaks decreased in intensity and the scattering pattern of the micelle formed and increased in intensity until the crystal peaks are no longer visible. In the WAXS data, the sharp peaks reduce in intensity until no longer visible, returning to the broad peak at q = 1.88 which then falls in intensity shortly after dissolution after the solution temperature has risen further.

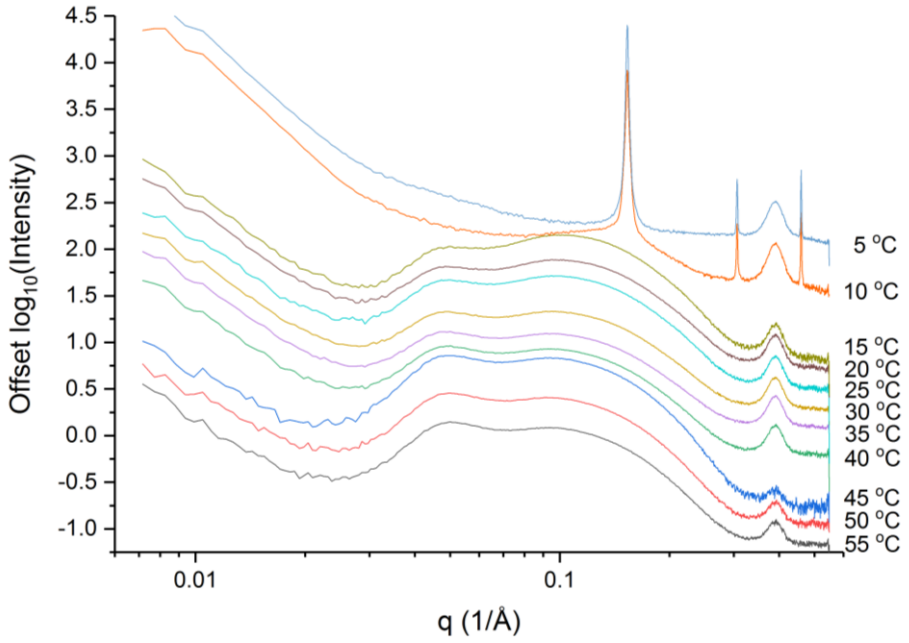

Figure 8.6: SAXS patterns (log-log) of 2.5 g/100g MEA myristate during cooling

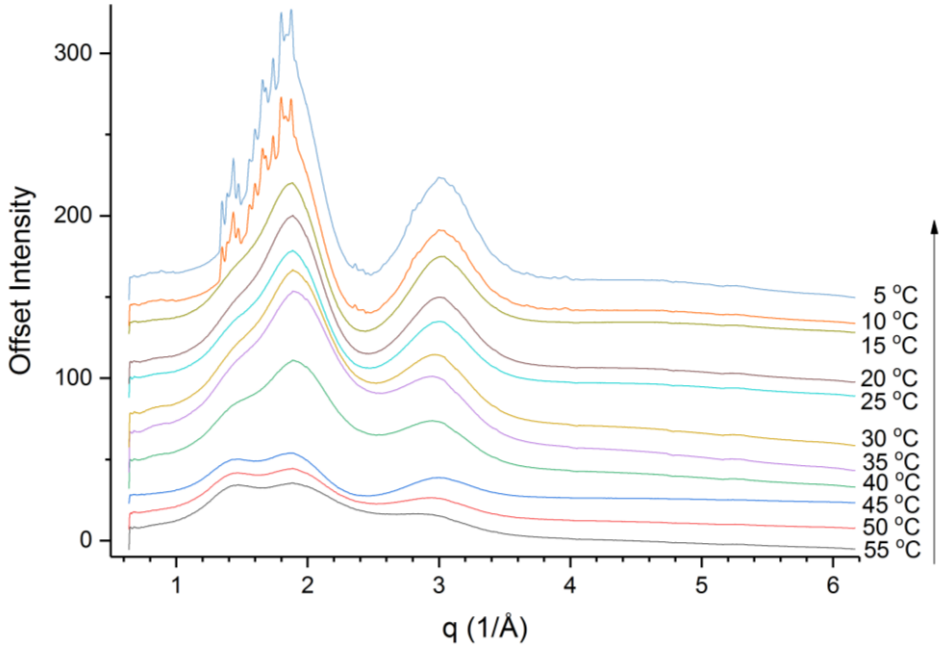

Figure 8.7: WAXS patterns of 2.5 g/100g MEA myristate solution during cooling

8.2.2.3 5 g/100g MEA myristate solution

The 5 g/100g MEA myristate solutions in Figure 8.8 showed similar trends to the 2.5 g/100g solution with the solution structure constant during cooling, including within the metastable zone width, and only showing changes immediately prior to the onset of crystallisation. At the onset of crystallisation at 21 °C, sharp peaks corresponding to a 41 Å lamellar structure were

observed (8). As the lamellar peaks increased in intensity, the broad peak at approx. q = 0.05 shifted to lower q and decreased in intensity, representing increased distance between micelles most likely due to a decrease in length as they are consumed by crystallisation. In the WAXS patterns in Figure 8.9, changes in scattering are observed from 45 °C with the intensity of the broad peak at q = 1.85 increasing as the solution is cooled. This change could be linked the shifting q = 0.05 peak in the SAXS data to lower q during cooling; micelles decreasing in length with the monomers starting to structure in solution.

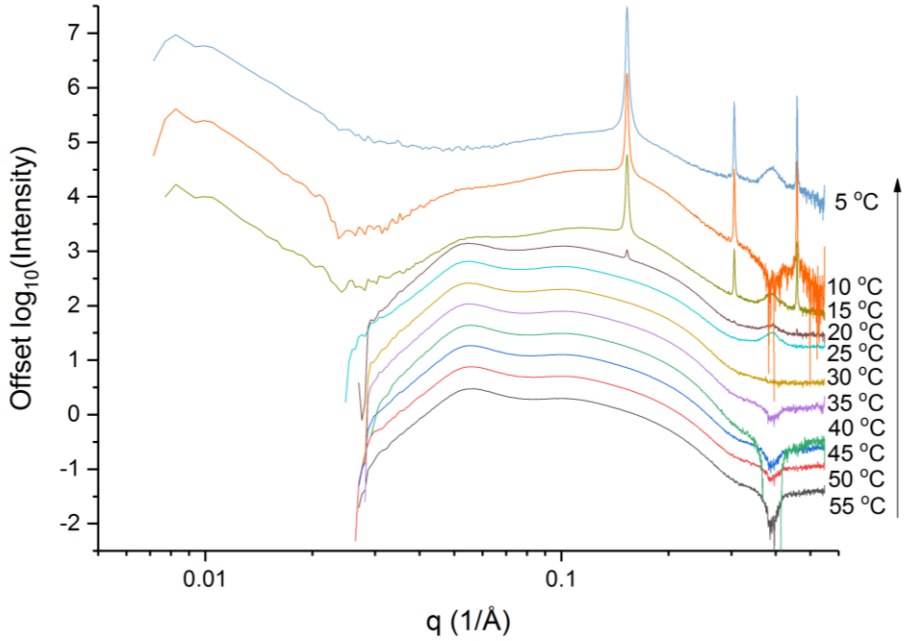

Figure 8.8: SAXS patterns of 5 g/100g MEA myristate solution during cooling

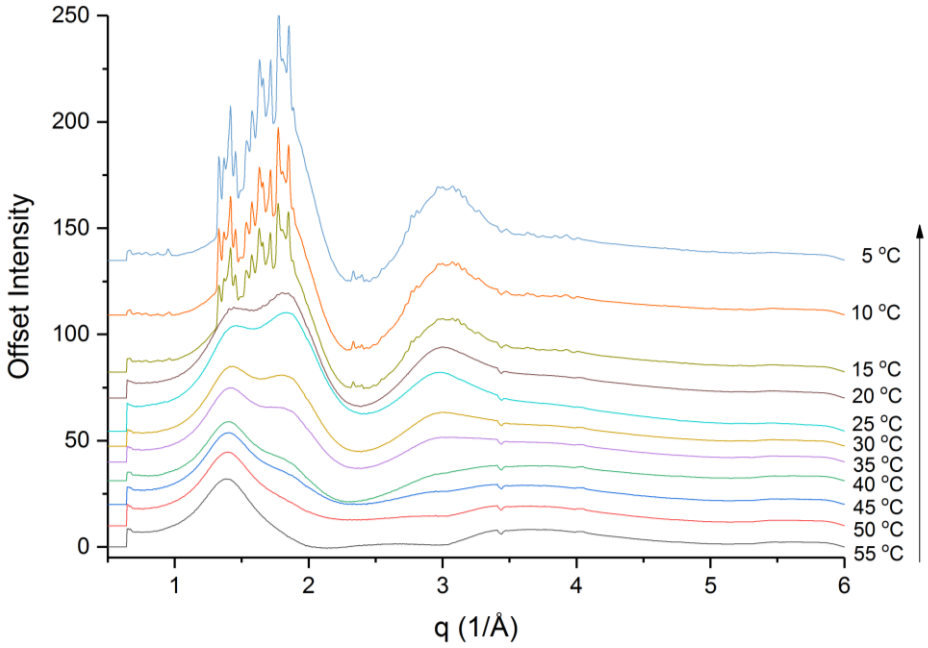

Figure 8.9: WAXS patterns of 5 g/100g MEA myristate solution during cooling

8.2.2.4 10 g/100g MEA myristate solution

The 10 g/100g solution follows the trends established by the lower concentrations, with limited changes in SAXS patterns shown in Figure 8.10, until the onset of crystallisation at 14.5 °C. The full cooling ramp wasn't captured however due to the capillary cell inlet becoming blocked shortly after crystallisation, causing the capillary cell to empty until the inlet unblocked after the onset of dissolution. The slope at low q was equal to -2 from 55 °C to 15 °C, whilst at 13.5 °C the slope was equal to -3.5, suggesting a wormlike micelle solution structure until the onset of crystallisation and consumption of micelles by crystallisation, resulting in a change to spherical micelles (1).

A 41 Å lamellar crystal structure was formed during cooling which the WAXS data in Figure 8.11 confirmed was a crystal rather than a liquid crystal due to the presence of sharp peaks. The solution structure showed changes prior to crystallisation during cooling, with the average distance between micelles increasing from approx. 100 Å at 55 °C to 105 Å at 15 °C. The WAXS data also showed changes during cooling with a broad peak emerging at q = 1.88 (d-spacing: 3.3 Å), that could be ordering of the alkyl chains in solution.

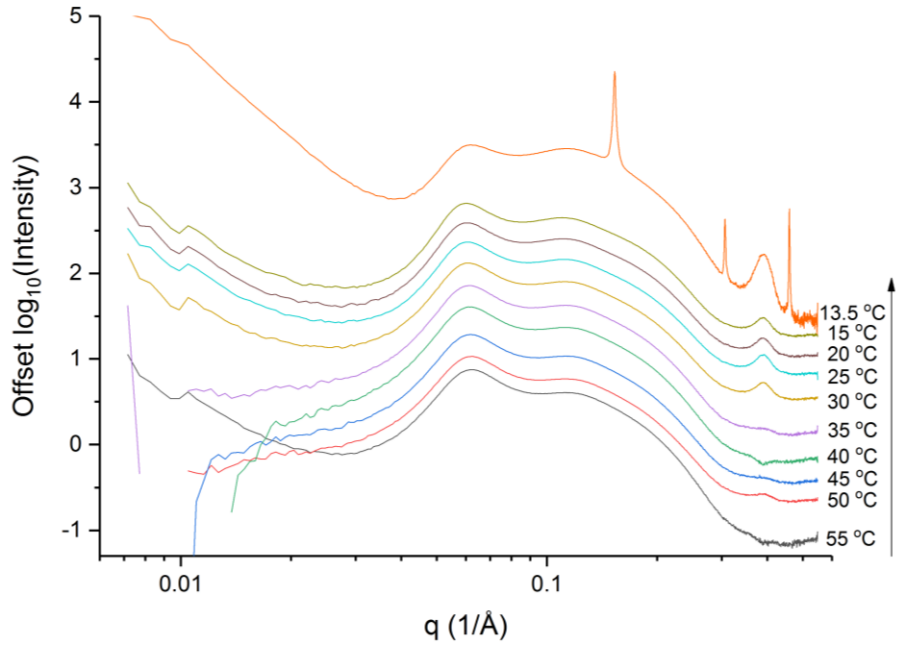

Figure 8.10: SAXS patterns (log-log) of 10 g/100g MEA myristate solution during cooling.

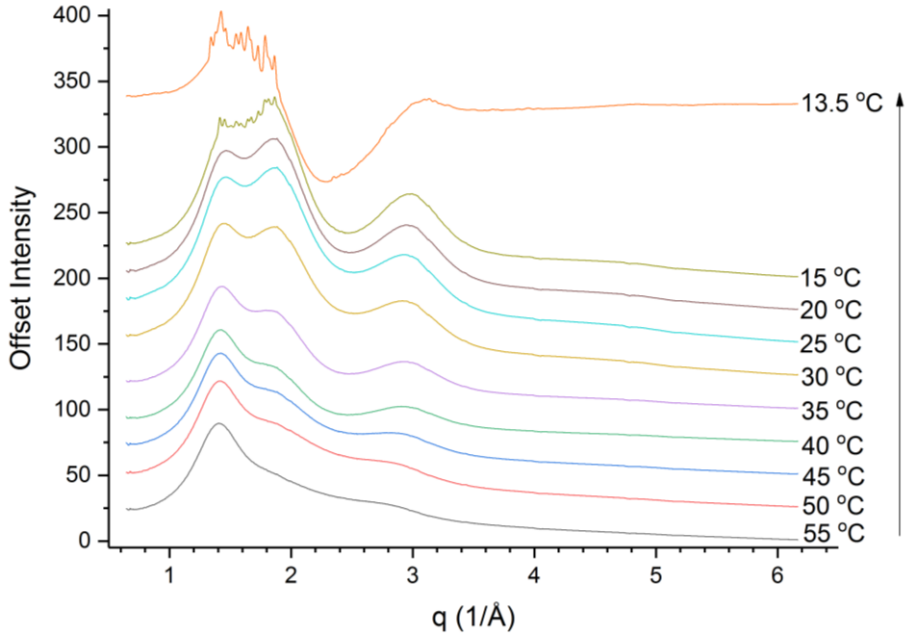

Figure 8.11: WAXS patterns of 10 g/100g MEA myristate solution during cooling.

8.2.2.5 15 g/100g MEA myristate solution

The 15 g/100g MEA myristate solution showed similar behaviour to the other concentrations with small changes in the SAXS and WAXS patterns before the onset of crystallisation at 11 °C. In the SAXS data the average distance micelles increased as the solution cooled whilst in the WAXS data a broad peak appeared at q = 1.88. This behaviour could be the gradual decrease in micelle length with the monomers in solution becoming structured. Similar to the 10 g/100g solution, the capillary cell inlet blocked and the cell emptied shortly after the onset of crystallisation. This resulted in the WAXS data not capturing the initial onset of crystallisation peaks.

The slope of the SAXS pattern at low q was approx. -1 at 55 °C, which corresponds to rod-like micelles (6). This could represent a change in solution structure compared to the lower concentrations, but it is more likely that due to the increased concentration and therefore increased length of micelles that the part of the scattering curve which has a slope of -2 that corresponds to the self-avoiding walk of the micelle was beyond the range observed (7).

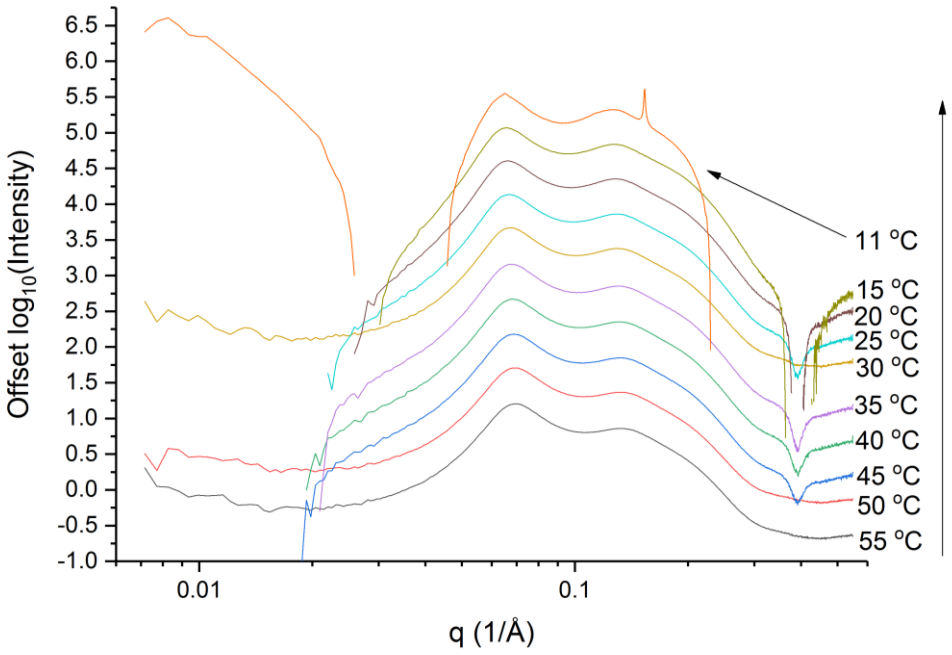

Figure 8.12: SAXS (log-log) patterns of 15 g/100g MEA myristate solutions during cooling

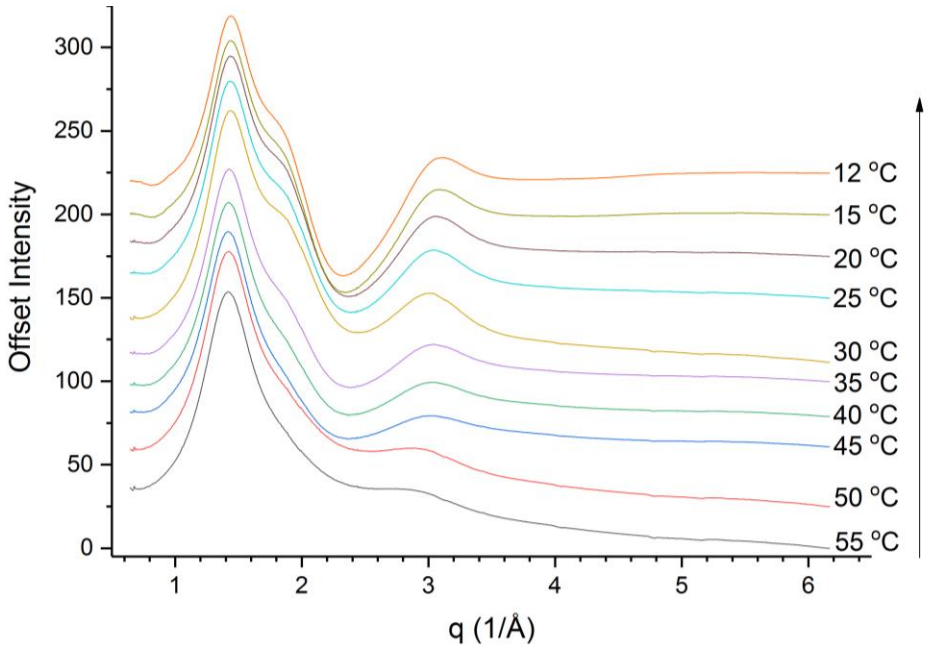

Figure 8.13: WAXS patterns of 15/g100g MEA myristate solution during cooling. Note: Capillary blocked and emptied due to crystallisation before WAXS pattern recorded of crystallised state.

8.2.3 Micelle-crystal transition (0.25 °C/min ramp rate)

The 5 g/100g MEA myristate solution cooled at 0.25 °C/min showed no significant changes in solution structure until the onset of crystallisation. The slope of scattering patterns in Figure 8.14 at low q was equal to -2, characteristic of wormlike micelles, between 55 °C to 25 °C (1). This indicates that there was no apparent change in solution structure on entering the metastable zone (below 34 °C) until crystallisation. After the onset of the sharp crystalline peaks of a 41 Å lamellar structure at 24 °C, the slope at low q increased in magnitude (reaching -3.25 at 5 °C) as crystallisation progressed, signifying a change in the solution structure as micelles are consumed by crystal growth (12).

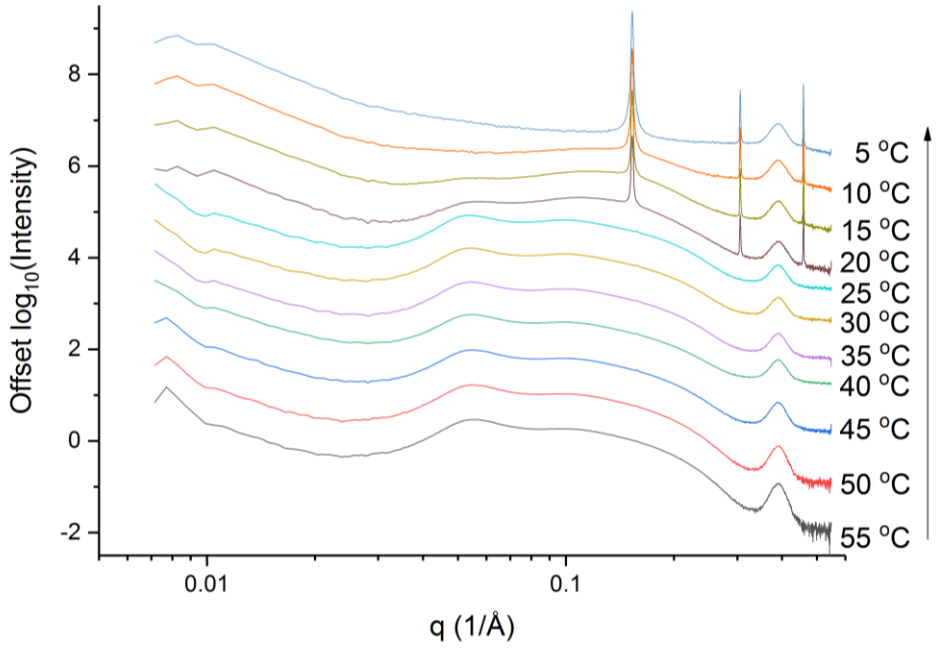

Figure 8.14: SAXS patterns of 5 g/100g MEA myristate during cooling at 0.25 °C/min

8.2.4 Crystallised state

For all the concentrations and cooling rates studied, there was only a single crystal structure observed and no observed phase transformation. The SAXS patterns showed a series of sharp peaks corresponding to a single lamellar structure with a long spacing of 41 Å (3). The corresponding WAXS patterns indicated that the structure was crystalline due to the presence of sharp peaks. The long spacing of 41 Å is close to that determined for the anhydrous 1:1 acid-soap of MEA myristate (39.7 Å) determined in previous chapters. However, it could also be due to hydration of MEA myristate with layers of water expanding its lamellar structure. Comparison of the SAXS/WAXS patterns with the PXRD patterns previously determined for the 1:1 acid-soap and MEA myristate show that the WAXS pattern is more similar to that of the acid-soap than MEA myristate. This would therefore prove that the 1:1 acid-soap does not form a hydrate, which is to be expected given the probable difficulty of water molecules being incorporated into the structure. The most likely point for a water molecule to bond would be around the headgroups where hydrogen bonding is possible, but in the acid-soap this region is likely to be congested due to interaction of the carboxylate, carboxylic, and ethanolammonium groups.

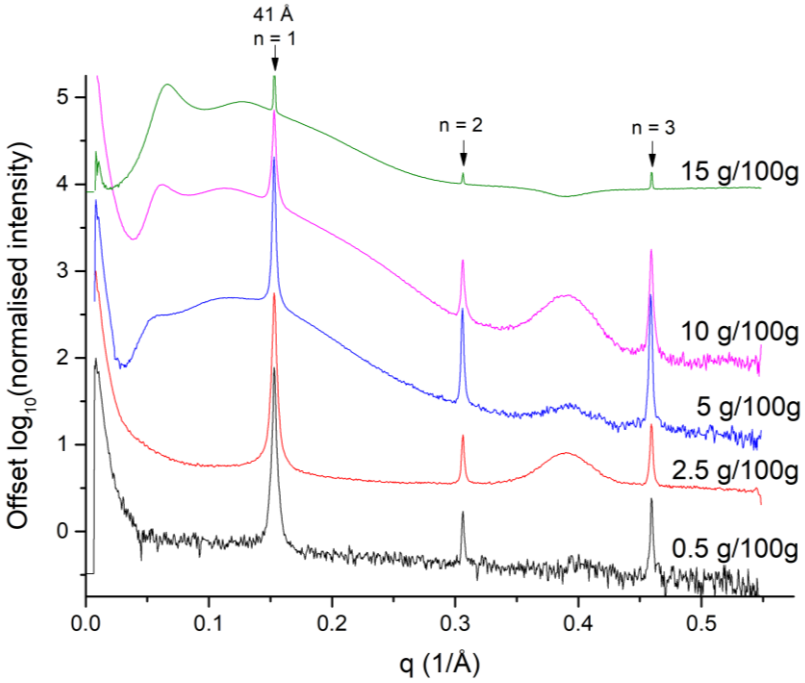

Figure 8.15: SAXS patterns of crystallised aqueous solutions of MEA myristate during cooling at 1 °C/min. The three peaks of the 41 Å lamellar structure are highlighted

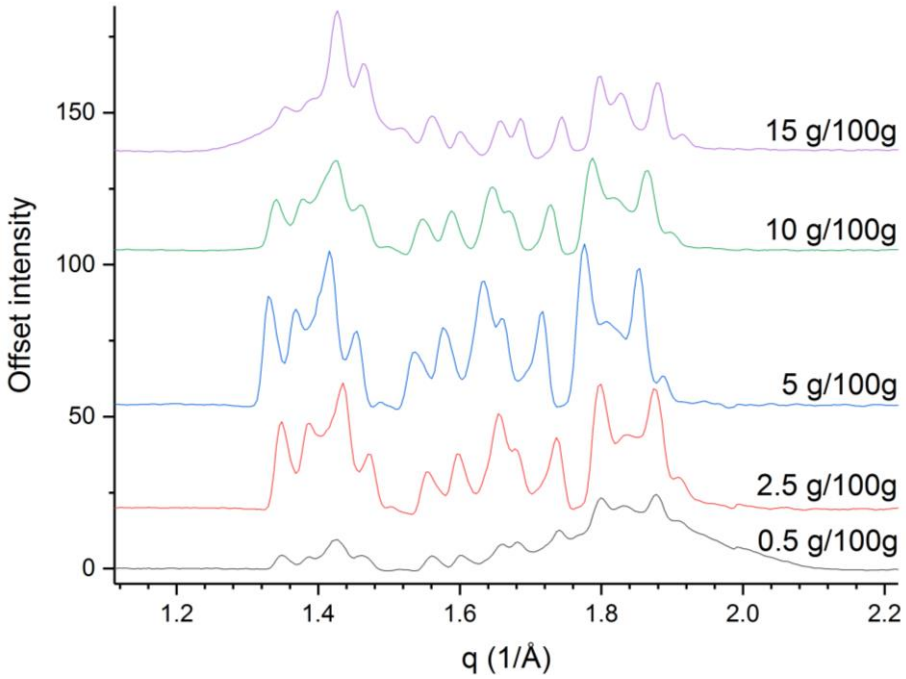

Figure 8.16: WAXS patterns of crystallised aqueous MEA myristate solutions during cooling at 1 °C/min

The WAXS patterns of samples from crystallised MEA myristate solution, shown in Figure 8.16, correspond to the spacing between adjacent molecules within the crystal structure. The WAXS patterns for the concentrations studied showed the same number and position of peaks across the concentration range. There are differences in relative intensities across the concentration

range but this was likely due to orientation effects – preferential orientation was observed during the crystallisation process due to the appearance of arcs and higher intensity arcs on diffraction rings in the raw 2D detector images for both SAXS and WAXS detectors (5).

8.2.5 Crystallisation and dissolution temperatures

Crystallisation and dissolution temperatures were obtained by both the SAXS/WAXS measurements with the flow cell and by turbidity via the probe in the reactor. Crystallisation was judged to have occurred at the onset of sharp peaks in both the SAXS and the WAXS patterns, corresponding to a crystalline structure. Dissolution was judged to have occurred when these peaks decreased in intensity and disappeared. Similarly, crystallisation and dissolution observed in the turbidity data by an increase and decrease in turbidity respectively. The transition temperatures observed by SAXS/WAXS and the reactor turbidity probe were consistent, with the turbidity data typically lagging the SAXS/WAXS data by a few degrees.

The crystallisation and dissolution temperatures of the MEA myristate solutions are shown in Figure 8.17, in which the trend with heating rate was not fully observed as there were issues during data collection of the 0.25 °C/min for the 10 g/100g and 15 g/100g samples. Comparing the crystallisation/dissolution temperatures with those determined in the previous chapter by turbidity showed that the transition temperatures had consistent overall trends i.e crystallisation and dissolution temperatures decreased with increasing concentration. The dissolution temperatures observed in the SAXS/WAXS experiments were slightly higher, but within a few degrees (maximum difference was 4.76 °C for the 10 g/100g concentration). The higher dissolution temperature is most likely due to the differences in experimental setup – a 1.8 ml vial vs an 80 ml reactor plus transfer lines and flow cell. Similarly, the flow cell set-up would have affected the crystallisation temperatures observed, with the increase in shear forces causing the higher crystallisation temperatures observed (13). The exception to this is the 0.5 and 2.5 g/100g solutions, whose crystallisation temperatures were outliers in the SAXS/WAXS data but in agreement with the crystallisation temperatures in the turbidity data. An explanation for this is that in the turbidity data the variation in crystallisation temperature was much greater for the lower concentrations, and therefore it is more probably in the SAXS/WAXS data to find outliers at the lower concentrations, particularly as each point is a single experiment.

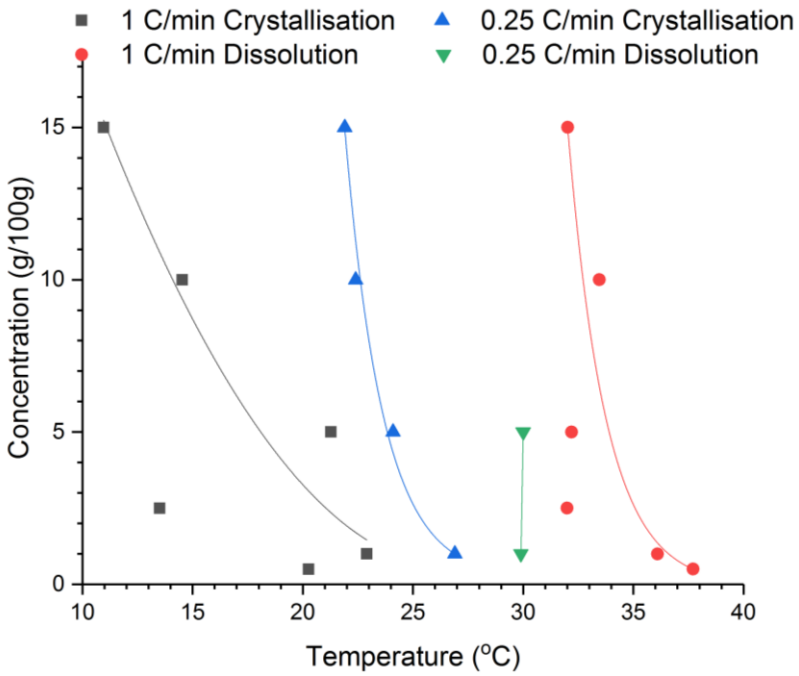

Figure 8.17: Crystallisation and dissolution temperatures of the MEA myristate solutions cooled at 0.25 °C/min and 1 °C/min.

The temperature profiles of the reactor temperature for the 5-55 °C runs at 1 °C/min show consistent temperature blips at 33 °C and 10 °C. The 33 °C and 10 °C 'blips' are consistent with an exothermic and an endothermic event respectively but there were no changes observed in either the turbidity, SAXS, or WAXS data. Similarly, these temperature 'blips' are not observed for the same concentrations subjected to temperature profiles with the same cooling rate in other reactor systems at the different scales used in previous chapters (80 ml HEL Ltd. AutoMATE, 500 ml HE Ltd. Simular).

8.3 SAXS/WAXS studies at BM28, ESRF

Simultaneous SAXS/WAXS studies were carried out at BM28 at ESRF on aqueous MEA carboxylate solutions in sealed capillary tubes.

As BM28 is not a dedicated SAXS/WAXS beamline compared to I22 at Diamond, the experimental set-up had larger air gaps, a purged beam tube rather than vacuumed, and physical restrictions on the placement of the detectors. The net result, whilst far better than anything possible using lab sources, was a compromise between time resolution and signal-to-noise ratio with a collection time of 10 s (plus an approx. 6 second dead time) giving a worse signal to noise than the individual 2 s frame within the Diamond multiframe captures. However, the main issue was that it was not physically possible to position the WAXS detector such that it would cover the q-range required, therefore the WAXS data will be omitted.

Temperature control was based on the circulators internal temperature rather than the capillary cell, resulting in cell temperatures that were slightly dependent on ambient conditions. The low and high temperature holds and the average heating/cooling rate achieved for each sample are listed in Table 8.1.

Table 8.1: MEA carboxylate chain lengths and concentrations used in the BM28 experiments with their temperature or temperature cycle used in the SAXS/WAXS measurements

Chain length	Concentrations (g soap/100 g deionised water)	Temperature cycle
Laurate (C12:0)	1	63 °C
	2.5	63 °C
	5	63 °C
	10	59 °C
	15	59 °C
Myristate (C14:0)	1	-7.5 – 52 °C @ 0.7 °C/min
	2.5	-7.8 – 52 °C @ 0.7 °C/min
	5	-7.8 – 52 °C @ 0.7 °C/min
	10	-8.7 – 52 °C @ 0.8 °C/min
	15	-7.8 – 52 °C @ 0.7 °C/min

8.3.1 MEA Laurate solutions

Solution state measurements were carried out on MEA laurate solutions held at 60 °C. As the log-log plot in Figure 8.18 shows, there is concentration dependence on the solution structure, with differences between solutions below and above 5 g/100g concentration. The more concentrated samples showed similar patterns to those collected for the MEA myristate solutions (2.5 g/100g and above), which was to be expected given the relatively small chain in chain length. The chain length however does have an effect on the solution structure behaviour with higher concentrations needed to obtain similar patterns; e.g 5-10 g/100g of MEA laurate compared to 2.5 g/100g of MEA myristate. This behaviour was likely due to the lower tendency for shorter chain lengths to aggregate into micelles, as evidenced by their higher critical micelle concentrations (14).

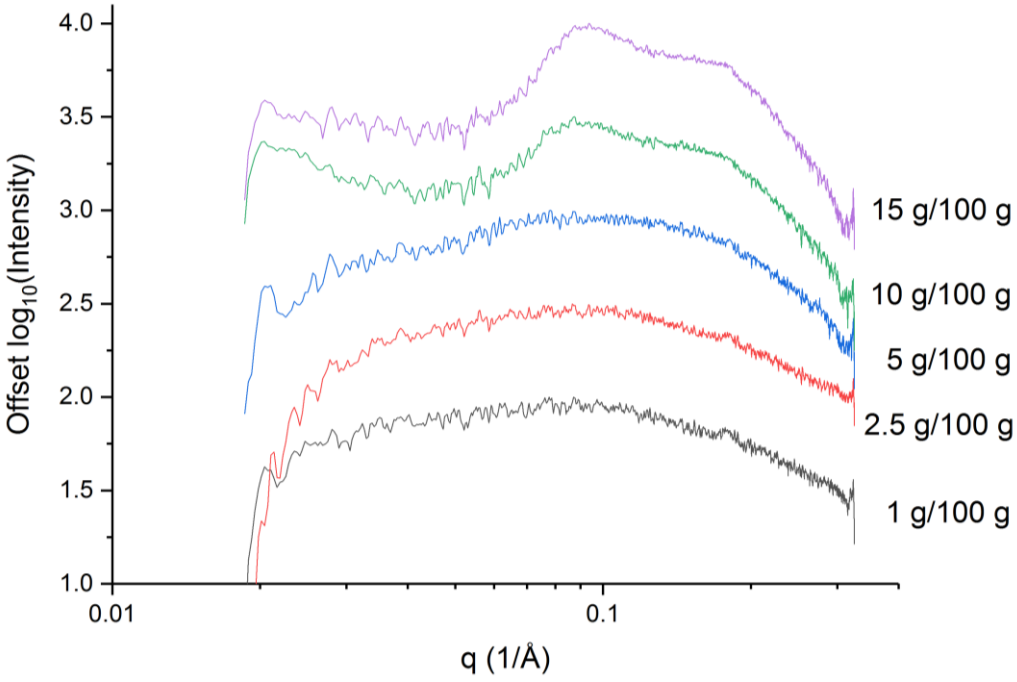

Figure 8.18: Log-log plot of SAXS of MEA laurate solutions at 60 °C

8.3.2 MEA Myristate solutions

8.3.2.1 Solution state

The SAXS measurements of the solution state of aqueous MEA myristate solutions in static capillaries at temperatures above 50 ^{o}C were in agreement with those recorded at I22, Diamond using the flow cell. The main difference between the patterns is that the ESRF data had a smaller q range covered by the detector, which means that it doesn't capture the low q data regarding the

solution structure. There was a degree of difference between patterns for the 2.5 and 5 g/100g solutions collected at ESRF compared to Diamond, though it is hard to determine whether this due to a difference in the pattern due to flow or whether it was due to the difference in background subtraction – the flow cell allowed for a much better background subtraction than the static capillary cells.

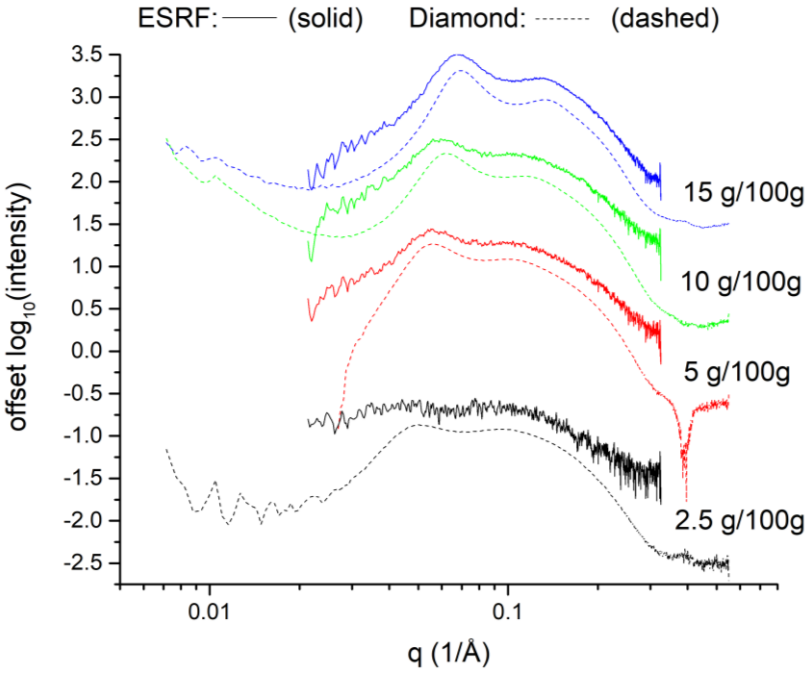

Figure 8.19: Comparison of the solution state of MEA myristate solutions at 50 °C by SAXS measurements recorded at Diamond (dashed lines) and ESRF (solid lines).

8.3.2.2 "Crystallised" state

The SAXS measurements on aqueous MEA myristate solutions under static conditions showed that there were pronounced differences in their behaviour during cooling compared to agitated conditions. For each concentration, series of evenly spaced peaks, corresponding to a lamellar structure, were observed on cooling (9). However, the long-spacing of the lamellar structure was concentration and temperature dependent and was much larger than the lamellar structures observed in the Diamond data. However, as the WAXS detector didn't cover the q-range required to observed the state of the alkyl chains, it cannot be determined whether the lamellar structure was crystalline or liquid crystal (10).

Figure 8.20 shows the long-spacing of the structures observed in each concentration and that the long-spacing of the structure appears to decrease with increasing concentration from 300 Å at 1 g/100 g to 118 Å at 15 g/100 g. Given the large size of the long-spacing, in excess of 100 Å, it is likely that

there were water layers within the structure, the thickness of which varying with concentration (9). This would mean that the structure formed was less likely to be a crystal but rather a liquid crystal. The decrease in thickness of the water layer, and hence long-spacing, with concentration could be due to the increased amount of MEA myristate (or acid-soap) crystallising out in a finite volume. These large lamellar structures also showed a temperature dependence, swelling and increasing in spacing as the solution temperature decreased. Throughout this chapter, these structures will be referred to by the size given in Figure 8.20 as a “representative” size due to the variation with temperature.

These large lamellar structures were not observed in the flow cell data collected at Diamond, which suggests that the difference is due to shear in the flow cell compared to the static conditions within the capillary (15). The mechanism for this is that the water layers in the large lamellar will be vulnerable to shearing and thus the stack of layers was not able to form in the flow cell setup.

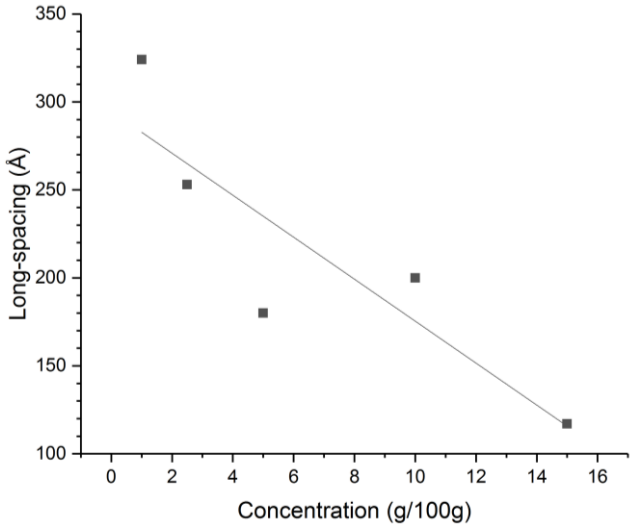

Figure 8.20: Average long-spacing of the lamellar structures observed by SAXS in the various MEA myristate solutions.

In addition to these large lamellar structures, a peak was observed at 40 Å that either did not fit the d-spacing ratios of the lamellar series of peaks or showed different behaviours, e.g changes in intensity whilst the other peaks do not. This peak could be the 001 peak belonging to the 1:1 acid-soap of MEA myristate, which would indicate that there are multiple components forming on cooling.

8.3.2.3 Micelle – crystal transition

The determination of crystallisation temperatures for the SAXS data was more difficult than the data from Diamond due to the lower time/temperature resolution – a frame every 0.175 °C during cooling – and noisier data that made identifying the onset of peaks more difficult. The issue of noisy data was more pronounced for the lower concentrations, particularly for the large 300 Å lamellar structure in the 1 g/100g solution. This structure was difficult to observe as demonstrated by Figure 8.21 in which each pattern is a three-frame average.

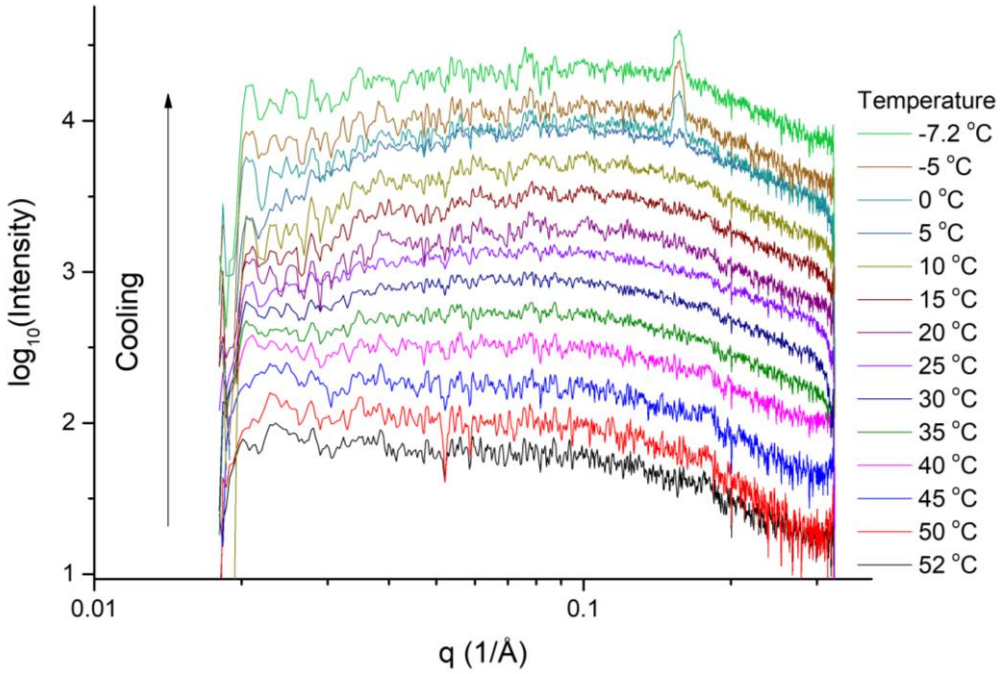

Figure 8.21: SAXS patterns during cooling of 1g MEA Myristate/100 g water solutions

The structure of the 1 g/100g MEA myristate solution shows limited changes at higher q (q > 0.1) as the solution cools and crystallises, but there are changes at lower q.

As Figure 8.22 shows, a large lamellar structure is formed on cooling of the 1 g/100g MEA myristate solution due to the presence of four broad peaks (9). Based on the d-spacing ratios of these peaks, these peaks are n = 2, 3, 4, 5 of an 317 Å (estimated) lamellar structure whose n = 1 peak is just beyond the q-range covered by the detector. These peaks are visible from 21 °C and below and exhibit temperature dependence; shifting to lower q as temperature decreases, the lamellar structure swelling to an estimated 330 Å. The much more intense and sharper peak at 40.1 Å appears at 6.1 °C, indicating that it is a separate structure to the larger lamellar structure. Based on the data for

MEA myristate and its acid-soap in previous chapters, the 40.1 Å structure is likely the 1:1 MEA myristate acid-soap with the small difference in d-spacing (0.4 Å) due to the broadness of the peak in the SAXS data. The large lamellar structure became harder to distinguish as the 40.1 Å peak increased in intensity, suggesting the larger structure was converting to the smaller structure.

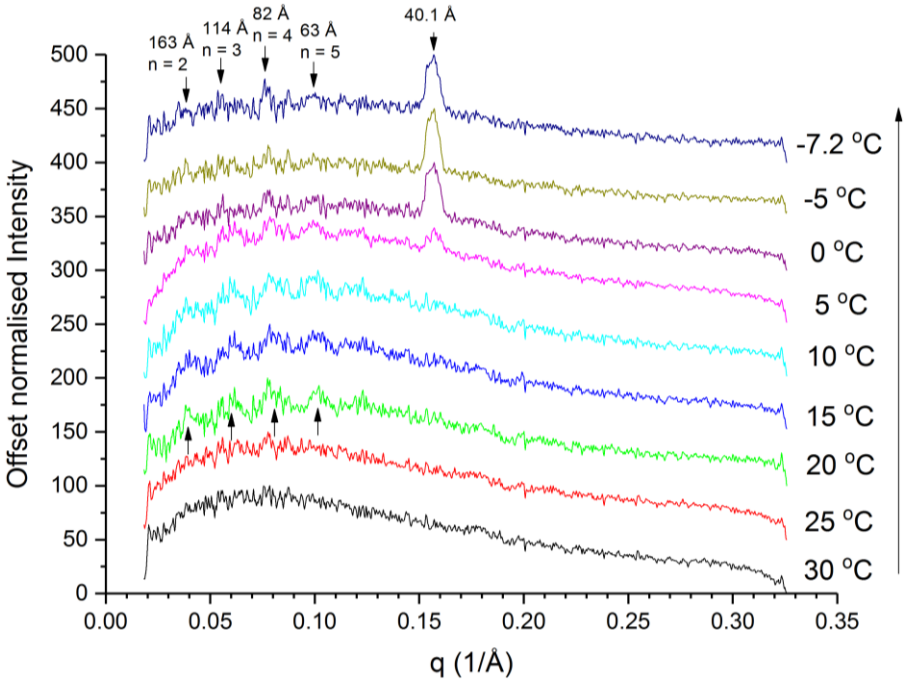

Figure 8.22: Detail view of onset of large lamellar structure during cooling of 1 g/100g MEA myristate solution

During reheating of the 1 g/100g MEA myristate solution, it isn't possible to observe the large lamellar structure and hence whether the swelling of the structure is reversible with temperature. There are a few possible explanations for the structures disappearance such as increased noise obscuring the weak broad peaks or that the large lamellar structure has converted to the more crystalline 40.1 Å acid-soap structure. As the solution was reheated, the 40.1 Å structure dissolved between 20-25 °C as shown in Figure 8.23. The effect of the dissolution on the solution structure appeared limited with no significant changes in the SAXS patterns recorded. There was a sharp peak in the SAXS pattern for 35 °C at 136.6 Å during reheating however, this was likely due to a "hot" pixel rather than the sample as the peak is far sharper than any other peak observed in the data and was at a position that didn't correspond to any crystal structure. In addition, looking at the raw 2D detector image there were no rings or arcs consistent with a structure, only a few scattered "hot" pixels (5,16) .

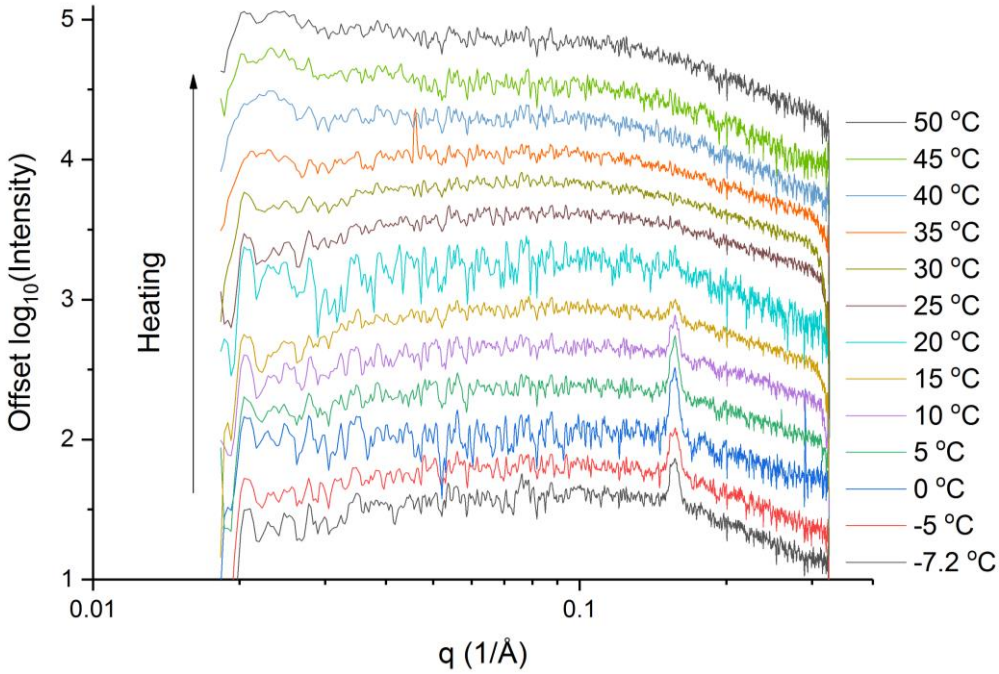

Figure 8.23: Heating of 1 g/100g MEA myristate solution

During the cooling of the 2.5 g/100g solution, a large lamellar structure with a spacing of approx. 243 Å formed at a lower onset temperature than for the 1 g/100g solution. The structure was highly ordered with 7 peaks of the lamellar series identifiable (9). The large lamellar structure swelled with cooling, increasing in long-spacing from 243 Å at 5 °C to 263 Å at -5 °C as shown in Figure 8.25. Unlike the 1 g/100g solution, the 1:1 acid-soap structure did not form in the 2.5 g/100g solution; the peak at 40.9 Å is part of the 248 Å lamellar series as it showed behaviour and shape consistent with the other peaks.

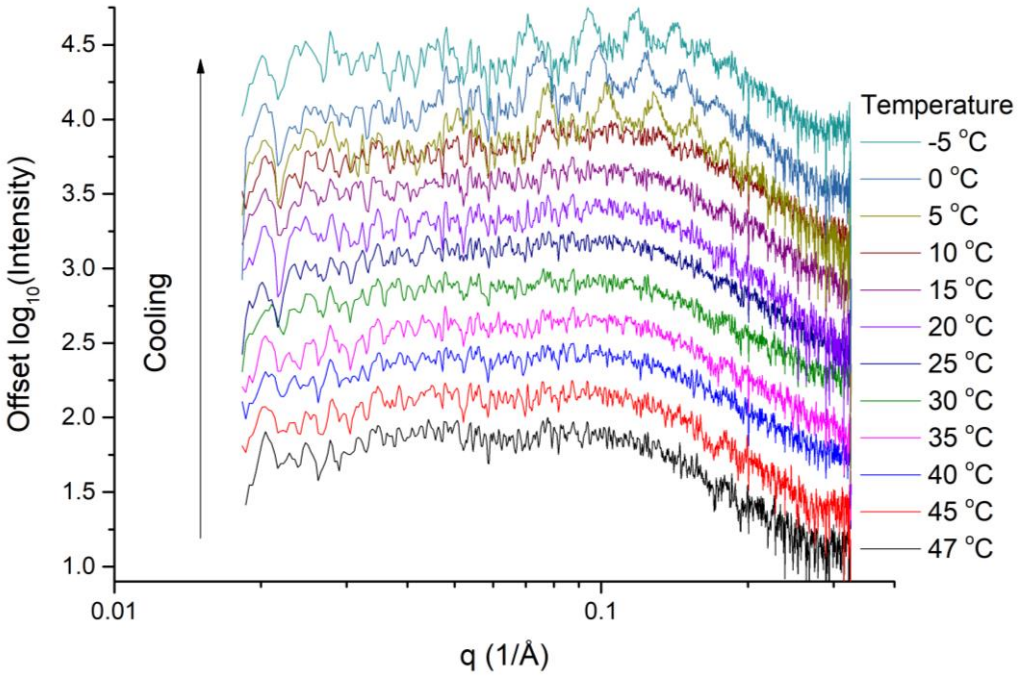

Figure 8.24: Log-Log SAXS pattern of 2.5 g/100g aqueous MEA myristate solution during cooling

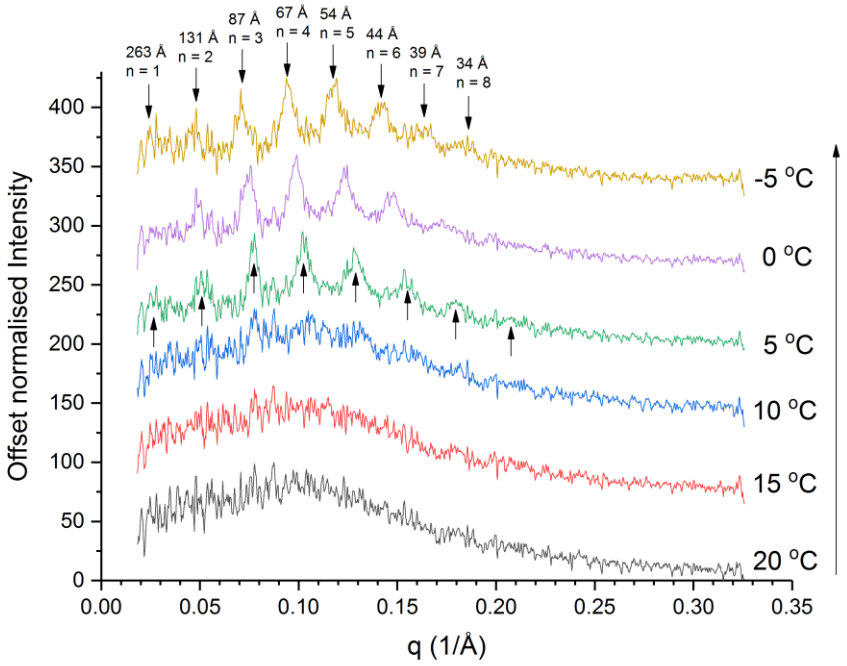

Figure 8.25: Detail view of the onset of the large lamellar structure in the 2.5 g/100g MEA myristate solution. The lamellar structure at 5 °C had a spacing of 243 Å and swelled to 263 Å on cooling to -5 °C.

There is a distinct change in the SAXS patterns for the 2.5 g/100g MEA myristate sample after the end of cooling ramp due to the removal, tapping, and reinsertion of the capillary tube. During the reinsertion, the tolerances of the cell and capillary tube were such that capillary tube became misaligned,

resulting in flaring around the beamstop as shown by Figure 8.26. The misalignment resulted in a change of the background and therefore affecting the background subtraction.

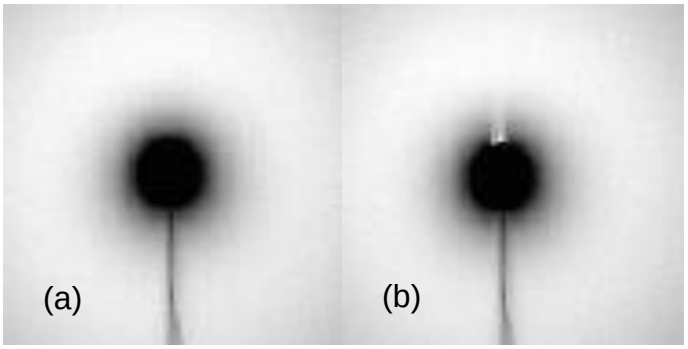

Figure 8.26: SAXS images (a) before and (b) after removal and reinsertion of the capillary tube. Flaring occurred after reinsertion due to misalignment of the beam and the capillary tube

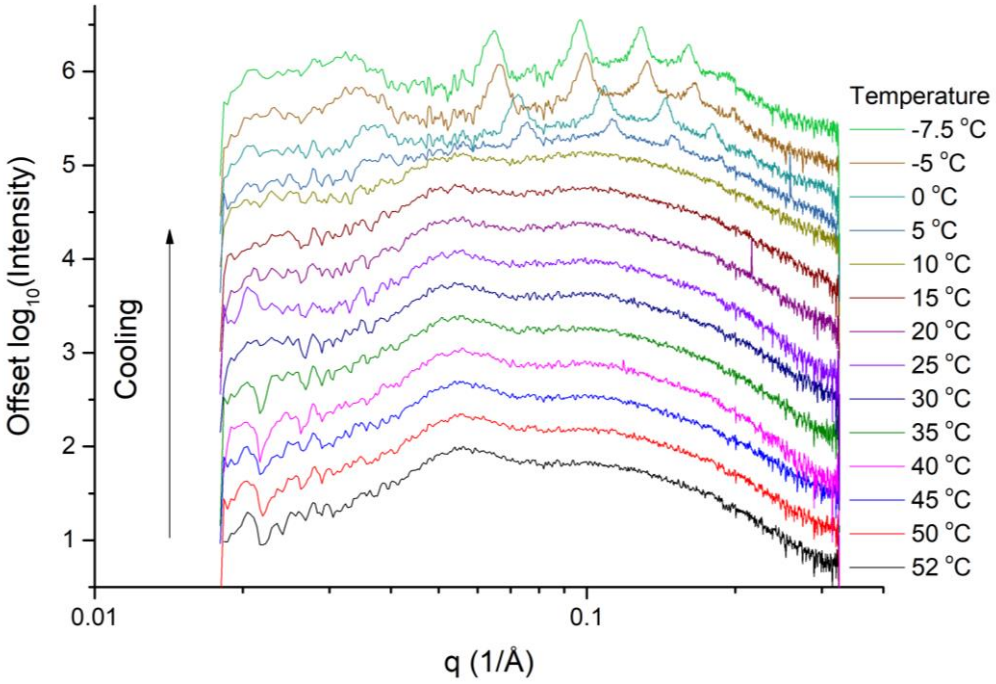

Figure 8.27: SAXS patterns of 5 g/100g MEA myristate solution during cooling

The 5 g/100g MEA myristate solution formed a large lamellar structure on cooling with the structure forming between 5-10 ^{o}C, continuing the trend of decreasing onset temperature with increasing concentration. The peaks of the large lamellar structure were sharper than for any of the other concentrations studied, indicating that it was more crystalline (5, 9). The large lamellar structure increased in long-spacing with decreasing temperature from 165 Å at 5 ^{o}C to 195 Å at -7.5 ^{o}C as shown in Figure 8.28.

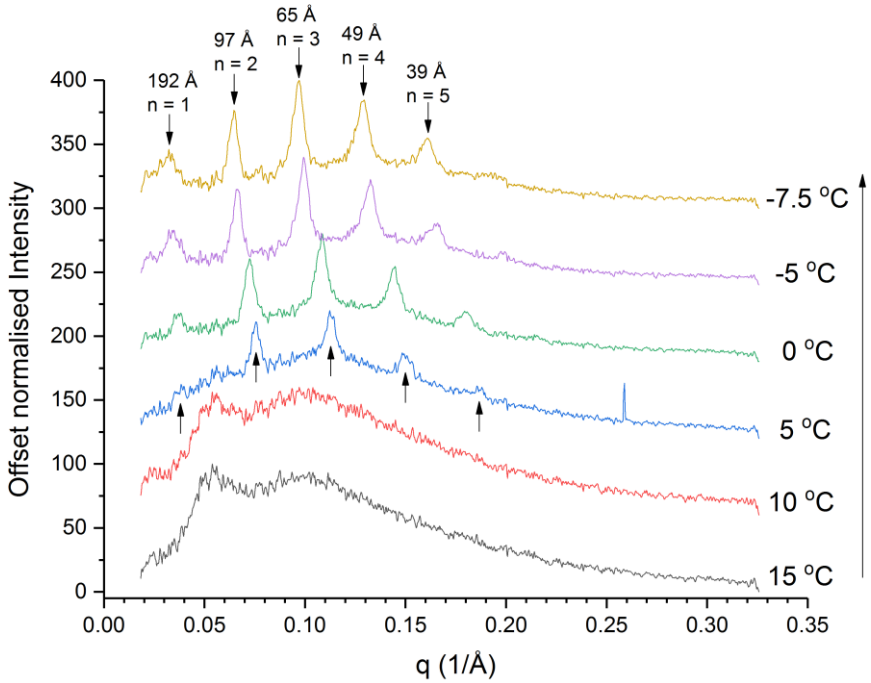

Figure 8.28: SAXS patterns of a 5 g/100g aqueous MEA myristate solution showing the effect on cooling on the d-spacing of a large lamellar structure

The 10 g/100g MEA myristate solution showed different behaviour on cooling compared to the lower concentrations. A large lamellar structure was observed at the low hold temperature, -8.66 °C, with weak, broad peaks that correspond to a structure of approx. 200 Å. The structure only appeared after perturbation of the capillary by tapping, however the removal and re-insertion of the capillary tube resulted in misalignment with the beam which resulted in a change in the background scattering. The background subtraction was therefore affected by this, particularly at low q, as demonstrated in Figure 8.30.

The pattern does show changes on cooling, particularly from 10 to 0 °C, indicating there was a change in solution structure which can be observed in the log-log plot in Figure 8.29. The scattering pattern of the micellar structure observed from 52-10 °C is less pronounced, particularly the left peak at approx. q = 0.06 (3).

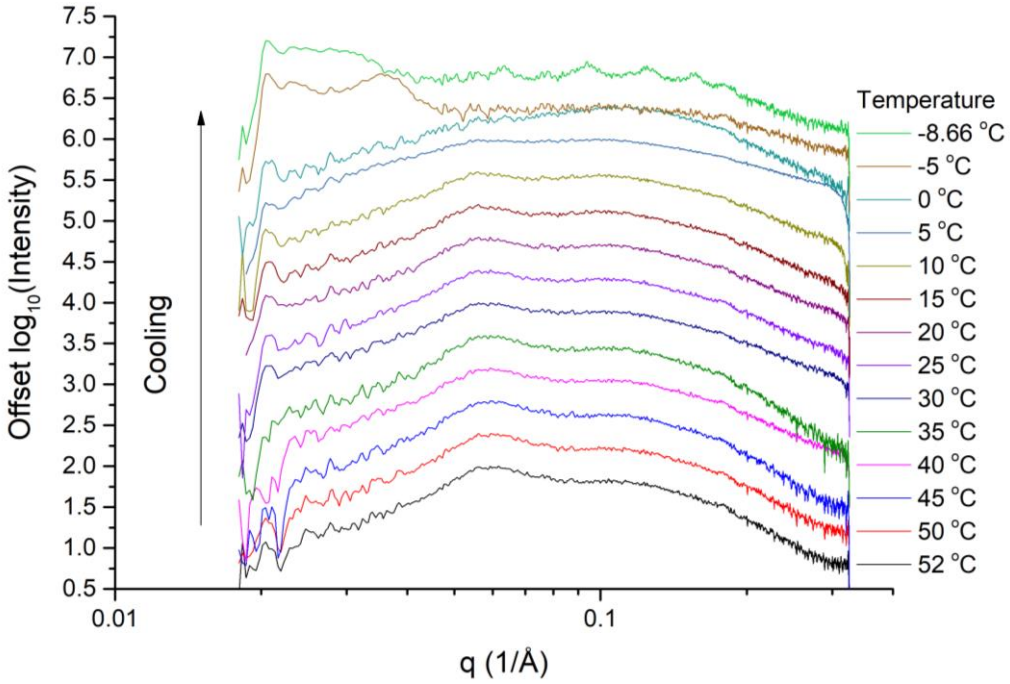

Figure 8.29 SAXS patterns of MEA myristate 10 g/100g solution during cooling

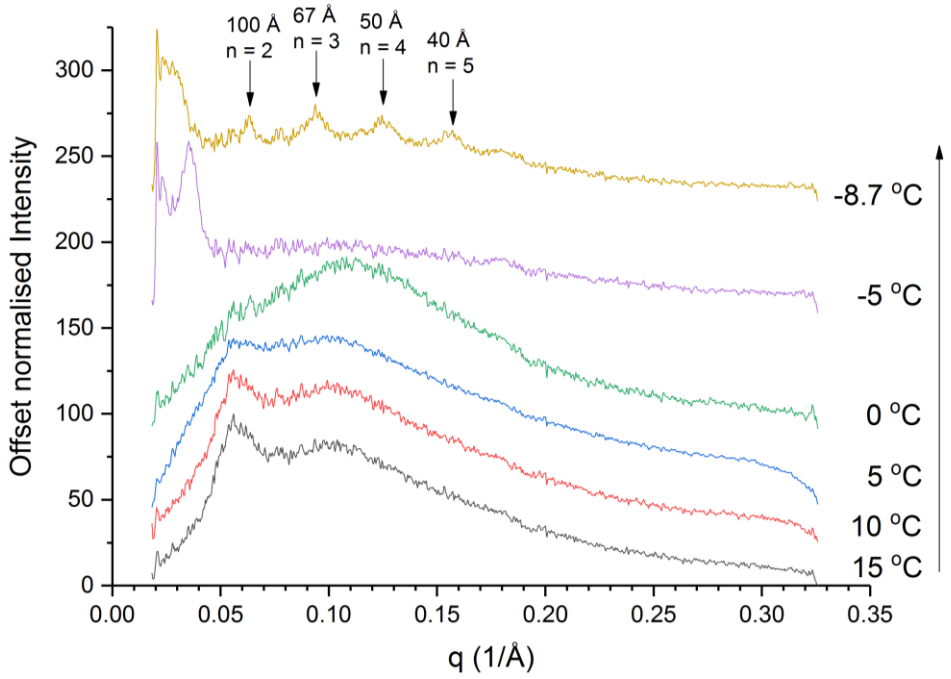

Figure 8.30: Detail view of the onset of the large lamellar structure during cooling of a 10 g/100g solution. The distinct change in pattern at low q (q < 0.03) is mainly due to flaring around the beamstop caused by misalignment.

Similar to the 10 g/100g MEA myristate solution, the 15 g/100g solution showed different behaviours compared to the lower concentrations. A large lamellar structure formed on cooling the solution, but whilst it was well ordered

with five peaks of the series visible the peaks were broad and relatively weak (9). The pattern recorded at 0 °C, shown in Figure 8.32, shows this series of five peaks which corresponded to a lamellar structure with a spacing of 117 Å.

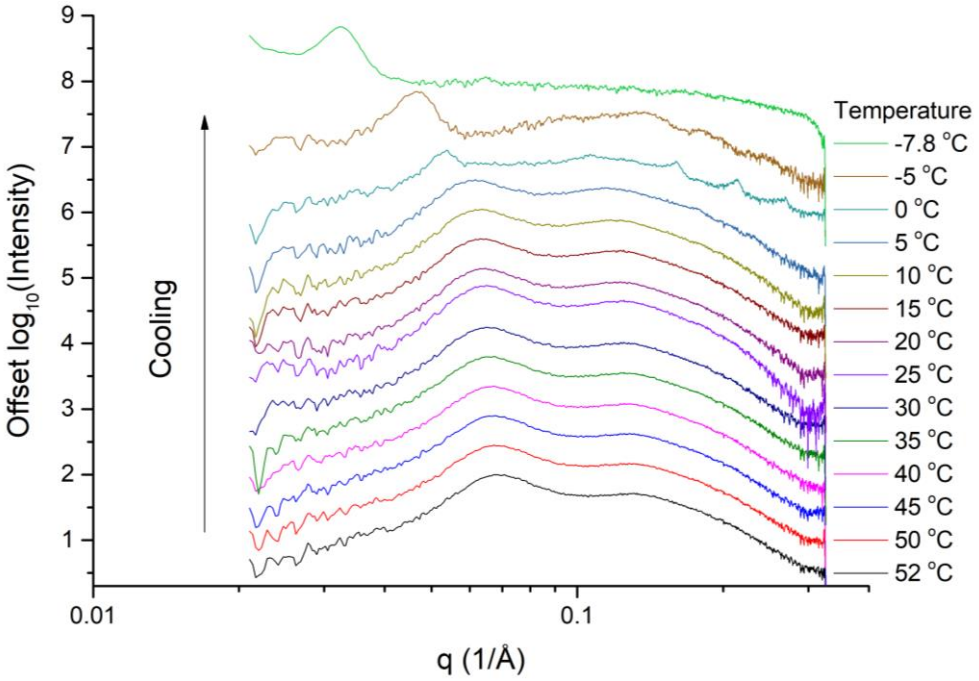

Figure 8.31: SAXS patterns of 15 g/100g MEA myristate solution during cooling

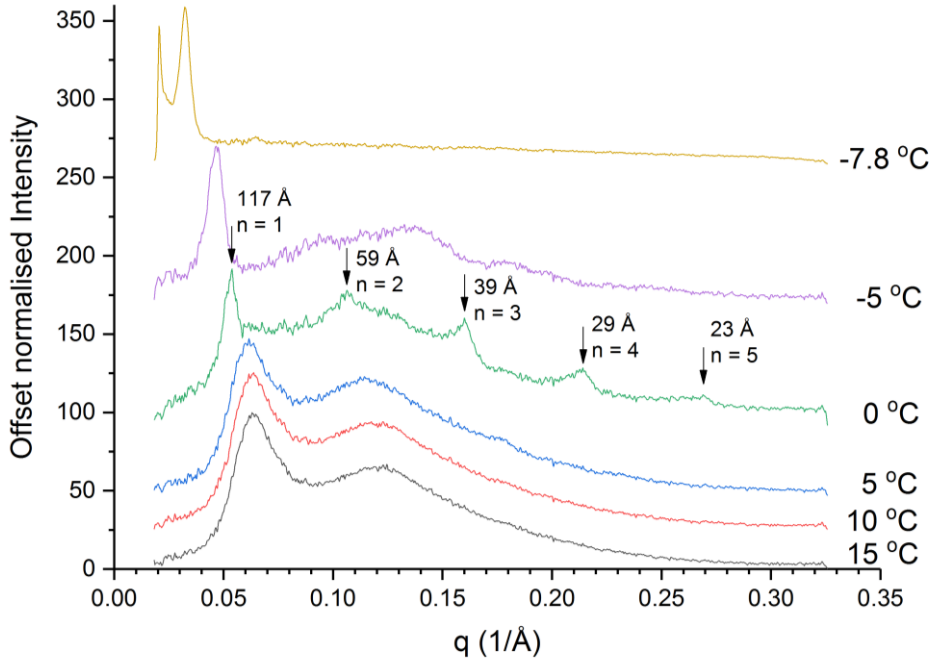

Figure 8.32: Detail view of the onset of a large lamellar structure during cooling of a 15 g/100g MEA myristate solution

8.4 Conclusions

Synchrotron SAXS/WAXS studies on aqueous MEA carboxylate solutions during temperature cycles showed differing behaviour depending on whether the solution was under flow or static conditions. Under flow conditions, MEA myristate solutions formed acid-soap crystals and the observe dissolution and crystallisation temperatures followed the trends established in the previous experimental chapters. Under static conditions, MEA myristate solutions formed much larger lamellar structures (> 100 Å) that swelled on decreasing solution temperature. Some static MEA myristate solution samples did form the 1:1 acid-soap structure on cooling, but at a much lower temperature than under flow conditions.

The difference in structures formed is due to the difference in shear; the large lamellar structures in the static capillaries are likely made up of layers of MEA myristate or its acid-soap separated by much larger layers of solution that can be easily sheared. Therefore in a flow cell with several sources of shear (magnetic agitator in reactor, pumping through transfer lines, and passing through the capillary cell) these structures would not be able to form and thus the crystalline state was reached instead (13).

The crystallisation and dissolution temperatures determined by SAXS/WAXS for the MEA myristate solutions under flow conditions further indicated that the unusual concentration-temperature trends are due to the solution state and the speciation within the solution.

8.5 References

1. DREISS, C.C.A. Wormlike micelles: where do we stand? Recent developments, linear rheology and scattering techniques. *Soft Matter*, 2007, **3**(8), p.956.
2. YANG, J. 2002. Viscoelastic wormlike micelles and their applications. Current Opinion in Colloid & Interface Science, 7, 276-281.
3. SHRESTHA, L. K., SHARMA, S. C., SATO, T., GLATTER, O. & ARAMAKI, K. 2007. Small-angle X-ray scattering (SAXS) study on nonionic fluorinated micelles in aqueous system. J Colloid Interface Sci, 316, 815-24.
4. JENSEN, G. V., LUND, R., NARAYANAN, T. & PEDERSEN, J. S. 2016. Transformation from Globular to Cylindrical Mixed Micelles through Molecular Exchange that Induces Micelle Fusion. J Phys Chem Lett, 7, 2039-43.
5. SEECK, O. H. & MURPHY, B. 2014. X-ray Diffraction Modern Experimental Techniques, New York, Pan Stanford.
6. FEIGIN, L. A. & SVERGUN, D. I. 1987. Structure Analysis by Small-Angle X-Ray and Neutron Scattering, New York, Plenum Press.
7. JENSEN, G. V., LUND, R., GUMMEL, J., NARAYANAN, T. & PEDERSEN, J. S. 2014. Monitoring the transition from spherical to polymer-like surfactant micelles using small-angle X-ray scattering. Angew Chem Int Ed Engl, 53, 11524-8.
8. BOND, A. D. 2004. On the crystal structures and melting point alternation of the n-alkyl carboxylic acids. New Journal of Chemistry, 28, 104.
9. RAND, R. P. & LUZZATI, V. 1968. X-ray diffraction study in water of lipids extracted from human erythrocytes: the position of cholesterol in the lipid lamellae. Biophys J, 8, 125-37.
10. WILLIAMS, W. P., CUNNINGHAM, B. A., WOLFE, D. H., DERBYSHIRE, G. E., MANT, G. R. & BRAS, W. 1996. A combined SAXS/WAXS investigation of the phase behaviour of di-polyenoic membrane lipids. Biochim Biophys Acta, 1284, 86-96.
11. NALLET, F., ROUX, D. & LAVERSANNE, R. 1993. Modelling X-ray or neutron scattering spectra of lyotropic lamellar phases : interplay between form and structure factors. J Phys II, 3, 487-502.
12. LUND, R., WILLNER, L., RICHTER, D., LINDNER, P. & NARAYANAN, T. 2013. Kinetic Pathway of the Cylinder-to-Sphere Transition in Block Copolymer Micelles Observed in Situ by Time-Resolved Neutron and Synchrotron Scattering. ACS Macro Letters, 2, 1082-1087.
13. SUMMERTON, E., BETTIOL, J., JONES, C., BRITTON, M. M. & BAKALIS, S. 2018. Understanding the Crystallization Process in Detergent Formulations in the Absence and Presence of Agitation. Industrial & Engineering Chemistry Research, 57, 16162-16171.

14. BERGSTROM, L. M. 2015. Explaining the growth behavior of surfactant micelles. J Colloid Interface Sci, 440, 109-18.

15. POULOS, A. S., NANIA, M., LAPHAM, P., MILLER, R. M., SMITH, A. J., TANTAWY, H., CARAGAY, J., GUMMEL, J., CES, O., ROBLES, E. S. & CABRAL, J. T. 2016. Microfluidic SAXS Study of Lamellar and Multilamellar Vesicle Phases of Linear Sodium Alkylbenzenesulfonate Surfactant with Intrinsic Isomeric Distribution. Langmuir, 32, 5852-61.

16. PAUW, B. R. 2013. Everything SAXS: small-angle scattering pattern collection and correction. J Phys Condens Matter, 25, 383201.

Chapter 9 Conclusions and future work

Conclusions from the work in this thesis are summarised and drawn together. The aims of the thesis are assessed and potential future work outlined.

9.1 Conclusions

9.1.1 MEA carboxylates and their 1:1 acid-soaps

MEA carboxylates were characterised by a number of techniques and were found to have similar structures across the chain length studied. Powder x-ray diffraction showed MEA carboxylates had a lamellar crystal structure, whose long-spacing was only approx. 3 Å longer than their approximate alkyl chain length. This, combined with the linear variation of long-spacing with chain length, indicate that the MEA carboxylate chains adopt either a highly tilted configuration, circa. 28° from the horizontal plane of the crystal layers, or a single, interdigitated structure with a tilt angle of 70°. FTIR and Raman spectra were consistent across the chain length range covered with the main differences in the IR spectra due to changes in the CH2 wagging behaviour.

The screen for acid-soap formation showed consistent trends across the chain length range and showed the formation of only one acid-soap structure; a 1:1 acid-soap. From the acid-soap screen, MEA carboxylate – fatty acid phase diagrams were constructed for the various chain lengths and showed similar transition trends. The MEA stearate – stearic acid phase diagram is consistent with that already in literature, but provides further insight into the material formed on cooling; above 50% neutralisation of the acid, mixtures of acid-soap and soap form whilst below 50% mixtures of fatty acid and acid-soap form. Characterisation of the acid-soaps formed showed little variation with chain length, particularly in the IR and Raman spectra. PXRD showed the acid-soaps had a lamellar crystal structure whose long-spacing is approximately twice the length of the alkyl chain. The variation of the long-spacing with increasing chain length indicated that the alkyl chains of the acid-soap were extended in a pseudo double-layer type arrangement i.e a linear molecule with MEA at the centre with carboxylate chain and the acid chains extending outwards, 180° apart, with the molecules vertical to the horizontal plane.

Comparison of the FTIR and Raman data for the fatty acid, acid-soap, and MEA carboxylate indicated that they could be differentiated, most easily by the position (or lack of) the carbonyl peak in the IR spectra; 1697 cm^{-1} in a fatty acid dimer, 1719 cm^{-1} in the acid-soap, and not present in the MEA carboxylate spectra.

9.1.2 Aqueous phase behaviour of MEA carboxylates

The metastable zone widths of aqueous MEA laurate and MEA myristate solutions were measured by turbidity and revealed non-typical crystallisation and dissolution temperature trends. The observed trends showed that with

increasing solution concentration, dissolution temperature decreased, which would suggest that crystallisation would occur by heating. However, crystallised occurred on cooling of the solutions. Results of off-line characterisation of crystallised material from the solutions showed that the crystals were predominantly the 1:1 acid-soap mixed with the MEA carboxylate. The crystal samples also showed a concentration dependence with the proportion of MEA carboxylate increasing in samples that were crystallised from solutions with a higher starting concentration. In-situ Raman measurements of MEA myristate solutions confirmed these findings, ruling out the possibility that the differences were due to filtering and drying process, and indicate that the transitions observed were due to the acid-soap crystallisation and dissolution.

Combining the results of the turbidity measurements, off-line characterisation, and in-situ Raman measurements the observed behaviours could be explained. The crystallisation and dissolution temperatures observed were not for a true binary MEA carboxylate – water system, but for a tertiary MEA carboxylate – acid-soap – water system in which the relative amounts of MEA carboxylate and acid-soap varied with total solution concentration. As the total solution concentration increased, the proportion of MEA carboxylate increased resulting in a decrease in dissolution temperature (as the MEA carboxylate will be more soluble than the acid-soap). The concentration dependence arises from the effect of the total concentration on the speciation within the solution due to MEA and fatty acids being a weak base and weak acids.

The MSZW of MEA myristate solutions with a 10% molar excess of MEA were therefore studied; the excess of MEA should shift the equilibrium towards MEA carboxylate formation rather than acid-soap and therefore reducing the dissolution temperature. The determined MSZW did show a shift towards lower crystallisation and dissolution temperature, however, the trends still showed non-typical behaviour and therefore two components were still being formed.

9.1.3 Solution structure and the micelle-crystal transition

Dynamic light scattering measurements of aqueous solutions of MEA laurate and MEA stearate were carried out to provide upper and lower bounds of the micelle size. The DLS results for 1 g/100g solutions of both MEA carboxylates showed large hydrodynamic radii, 82 – 103 nm for MEA laurate and 164 – 171 nm for MEA stearate, which indicated that the micelles had already become large and rod or wormlike. Larger particles, >1000 nm, were also observed in

solution, causing the solutions to become turbid, when more concentrated solutions at the same temperature were clear. These particles were precipitated fatty acid as at low concentrations in aqueous carboxylate soap systems, fatty acid precipitation is preferred over acid-soap or the carboxylate soap (1).

Time-resolved SAXS/WAXS studies of the behaviour of aqueous MEA myristate solutions during heating/cooling cycles were carried out under flow conditions. The SAXS/WAXS measurements at 50 °C, well above the dissolution temperature, showed wormlike micelle (WLM) solutions had formed with a length beyond the q range covered. For the 2.5 g/100g concentration and above, the patterns suggested the WLM were entangled and enmeshed with an average mesh pore size between 90.7 Å and 128.3 Å – decreasing with increasing solution concentration. On cooling, there was no observed change in solution structure until immediately prior to the onset of crystallisation, where the micelle mesh pore size increased and a broad peak at 3.3 Å emerged in the WAXS pattern. These represented a decrease in length of micelles and potentially ordering/alignment of the alkyl chains prior to crystallisation. Only the 1:1 acid-soap crystallised for all the concentrations and cooling rates studied and there was no observed phase transformation in solution. The crystallisation and dissolution trends were in agreement with those observed by turbidity and Raman in the earlier work in this thesis, indicating that the dissolution temperature trend was due to the differences in composition of the solution.

Time-resolved SAXS studies on MEA carboxylate solutions in static conditions in sealed capillary tubes during heating/cooling cycles showed the effect of shear. Static solutions of MEA myristate showed similar solution structures for a given concentration and temperature, but on cooling the static solutions formed large lamellar structures, with d-spacing >100 Å, that swelled with decrease temperature. Some concentrations did form the 1:1 acid-soap on cooling, but there was no clear trend observed with concentration.

9.2 Review of thesis aims

Considering the original aims of this project, the research in this thesis has made significant progress in characterising the crystallisation process of monoethanolammonium carboxylates from aqueous solution.

A screen for acid-soaps revealed that MEA carboxylates form a 1:1 acid-soap, whose formation is preferred over separate formation of fatty acid and soap.

MEA carboxylate – fatty acid phase diagrams generated build on existing work in literature. Metastable zone width studies by turbidity, Raman, and simultaneous time-resolved SAXS/WAXS have shown that MEA carboxylates have complicated aqueous solution crystallisation behaviour due to their tendency to hydrolyse and form acid-soap cocrystals. The SAXS/WAXS studies revealed that the formation of the 1:1 acid-soap occurs directly from solution without proceeding via any other phase and without significant change in solution structure until immediately prior to crystallisation.

However, the thesis objectives were not fully met, in particular characterising how the solution structure changes as it transitions from a micellar solution to crystals suspended in solution. This was mainly due to not being able to cover the full size range of the micellar solution during the SAXS experiments. In addition, the crystallisation behaviour of the MEA carboxylate itself in aqueous solution wasn't fully resolved – though how to do this isn't straightforward without adding additional components to the system e.g a strong base to prevent hydrolysis.

9.3 Suggestions for future work

The full dynamic transition from micelle to crystal could be characterised by further synchrotron study using simultaneous SAXS/WAXS. Small-angle neutron scattering (SANS) could be used as it provides more options for manipulating the contrast within the solution due to the ability to deuterate the solvent, MEA, or the fatty acid. However, SANS doesn't have the same time-resolution as SAXS/WAXS studies and as the crystallisation/dissolution transitions are quick, SAXS/WAXS is the more suitable technique.

The full transition could be probed by using a beamline such as ID02 at ESRF, which features a moveable SAXS detector, that would allow coverage of the complete length-scale necessary, albeit at the expense of time-resolution due to the need to move the detector (2). The experiment would require a flow cell for reliable background subtraction and could utilise a similar manner to that used in this work at I22 at Diamond. In addition, a Raman probe (or a probe such as that produced BlazeMetrics which combines microscopy and Raman (3)) could be inserted into the reactor to track the chemical changes in solution. This would allowed coupling of Raman and SAXS/WAXS data and therefore chemical and structural changes within the solution. The coverage of the full lengthscale would confirm how the micelle structure changes immediately prior to crystallisation and help shed light on the potential ordering within the solution observed in the WAXS data.

An alternative study could be to study the effects of shear on the crystallisation behaviour of MEA carboxylates from aqueous solution. Comparison of the ESRF and Diamond data in this thesis for MEA myristate solutions showed different behaviours on cooling with the primary difference in conditions being shear; Diamond was under flow, ESRF in static conditions.

9.4 References

1. KRALCHEVSKY, P.A., K.D. DANOV, C.I. PISHMANOVA, S.D. KRALCHEVSKA, N.C. CHRISTOV, K.P. ANANTHAPADMANABHAN and A. LIPS. Effect of the precipitation of neutral-soap, acid-soap, and alkanoic acid crystallites on the bulk pH and surface tension of soap solutions. *Langmuir*, 2007, **23**(7), pp.3538-53.
2. ESRF. *ID02 - Time-Resolved Ultra Small-Angle X-ray Scattering* [online]. 2018. [Accessed 17/09/2018]. Available from: http://www.esrf.eu/home/UsersAndScience/Experiments/CBS/ID02.html.
3. BLAZEMETRICS. *BlazeMetrics PAT InProcess Microscopy Particle Size Morphology Surface - Blaze400* [online]. 2018. [Accessed 17/09/2018]. Available from: https://www.blazemetrics.com/.